Queen Mary
University of London

# Experimental Study of Oxidation, Ignition and Combustion of Aluminum Based Nanomaterials

Fahad, Noor

The copyright of this thesis rests with the author and no quotation from it or information derived from it may be published without the prior written consent of the author

For additional information about this publication click this link.
http://qmro.qmul.ac.uk/jspui/handle/123456789/8777

Information about this research object was correct at the time of download; we occasionally make corrections to records, please therefore check the published record when citing. For more information contact scholarlycommunications@qmul.ac.uk

# Experimental Study of Oxidation, Ignition and Combustion of Aluminum Based Nanomaterials

by

**Fahad Noor**

School of Engineering and Materials Science

Queen Mary, University of London


A Thesis

Submitted in partial fulfillment of the requirements of the Degree

of Doctor of Philosophy at

University of London

May 2014

## *Declaration:*

I, *Fahad Noor*, confirm that the research included within this thesis is my own work or that where it has been carried out in collaboration with, or supported by others, that this is duly acknowledged below and my contribution indicated. Previously published material is also acknowledged below.

I attest that I have exercised reasonable care to ensure that the work is original, and does not to the best of my knowledge break any UK law, infringe any third party's copyright or other Intellectual Property Right, or contain any confidential material.

I accept that the College has the right to use plagiarism detection software to check the electronic version of the thesis.

I confirm that this thesis has not been previously submitted for the award of a degree by this or any other university.

The copyright of this thesis rests with the author and no quotation from it or information derived from it may be published without the prior written consent of the author.

**Print Name:** **Fahad Noor**

**Signatures:** .....

**Date:** .....

## Details of collaboration and publications

### Conferences

- **Noor, F**.; Song, P.; Ding, Y.; Korakianitis, T.; Wen, D.S., Exothermic Reaction of Energetic Nanomaterials and its Application in Energy Storage, *World Resources Forum (WRF)*, 2012

  **Noor, F.**; Zhang, H.; Zhang, K.; Wen, D.S., Oxidation and ignition characteristics of energetic nanomaterials, *4th UK-China Particle Technology Forum*, Shanghai, China, 2013.

### Journal Papers

- **Noor, F**.; Zhang, H.; Korakianitis, T.; Wen, D.S, Oxidation and Ignition Investigation of Aluminum Nanomaterials. *Phys Chem Chem Phys* 2013. *15 (46), 20176 - 20188*
- **Noor, F**.; Bandarra Filho, E. P.; Vorozhtsov, A.; Wen, D.S., Thermal-Chemical Characteristics of Al-Cu Nano-Alloys. Submitted to *Acta Materialia* 2013.
- **Noor, F**.; Wen, D.S., Exothermic Characteristics of Aluminium Based Nanomaterials, Submitted to *Powder Technology*, 2013.
- **Noor, F**.; Wen, D.S., Experimental study of thermal oxidation of nano-alloy of aluminum and zinc (nAlZn). Submitted to *Journal of Alloys and Compounds*, 2013.

# Abstract

Aluminum based reactive nanomaterials have extensive applications in many fields including solid propellants, pyrotechnics, and catalytic reactions. One recent example is the novel concept of using nanostructured energetic particles for energy storage where the controlled exothermic reaction is the key to control the energy release process. It is of primary interest to understand the thermodynamics, kinetics, morphological and structural properties of these particles during the exothermic reaction. While the physiochemical properties of the monometallic powders are determined only by their size, the properties of bimetallic nanoalloys can be also engineered by their constituent compositions. This thesis conducts a systematic experimental investigation of the oxidation, ignition, and combustion of nano aluminum particles (nAl) and nanoalloys such as nanoscale aluminium-copper (n-AlCu) and aluminium-zinc (n-AlZn). The oxidation experiments are conducted by a TGA/DSC system with detailed characterisation of particles before and after the experiments by scanning electron microscopy (SEM), transmission electron microscopy (TEM), the Nanosizer, Brunauer–Emmett–Teller (BET), energy dispersive X-ray spectroscopy (EDS) and powder X-ray diffractionmetry (XRD). In the TGA/DSC analysis, nanomaterials are oxidized either at constant temperature or under different heating rates in the controlled atmosphere of air or nitrogen. A unique early ignition reaction is observed at the high heating rates for nAl and n-AlCu, which is associated with the effect of polymorphic phase transformation of the alumina shell and the early melting of the aluminum core. Different to the conventional shrink-core concept, hollow structures, i.e. nanoholes, in the central regions of nAl are observed and a phenomenal model is proposed. The comparison of the thermal-chemical characteristics of different nanomaterials reveals some unique

features related to nano-alloys such as increased reactivity. A preliminary combustion experiment on feeding nanoparticles in a methane stream is performed with a Bunsen burner setup, where the burning characteristics of different nanoparticles are analysed.

**Keywords:** Oxidation, ignition, combustion, energetic nanoparticles, nanofuel, nano-alloys, STA, TGA, DSC, aluminum, aluminum copper alloy, zinc aluminum alloy, silicon.

*To my brother Shahid*

*&*

*My wife Ghazala*

# Acknowledgements

I would like to express my deepest appreciation to my research supervisor Professor Dr Dongsheng Wen for his continued guidance, encouragement and kind support for realisation of this dissertation.

I am very thankful to the laboratory in charge officers Dr Zofia Luklinska of NanoVision Centre, Dr R. M. Wilson of X-ray & neutron diffraction of materials lab, Dr Krystelle Mafina of School of Engineering and Material Science and Mr Balazs Ihracska of combustion laboratory for their help and assistance.

I would like to thank University of Engineering and Technology Lahore, Pakistan for funding this research. I would also like to say special thanks to Professor Dr Riaz Mirza for his love, guidance and the efforts he made to secure my PhD scholarship.

Finally, I would like to thank my father Noor Ahmad, my sons, Faraan Noor and Azlaan Noor for their patience and love, my brothers Zahid Hussain, Abid Ali, Asad Ali and their families, and my dear Dr Asif Mehmood and Akram Aftab for their out-and-out support, and my friends especially Dr Muhammad Sajid Kamran, Muhammad Farhan, Dr Zulfiqar Ali, Dr Shahid Imran, Zahid Anwar, Muhammad Asim , Zia ul Rehman, Shuakat ali, Jibraan Khaliq, Shabi-ul-Hassan, Dr Muhammad Imran, Rabia Shoukat and Maryam Amad Masood. All of them have always been incredibly supportive whenever I need any help. During this research, I realised that without their love and prayers, this work could never have been accomplished.

At the end, thanks London for making me learn ‘hard lessons’ which I could never learn elsewhere.

# Table of Contents

# List of Figures

# List of Tables

# Important Nomenclature

## Roman symbols

| | |
|---|---|
| A, b, c | Lengths of the planes |
| $\alpha$, $\beta$, $\gamma$ | Angles among the planes |
| å | angstrom |
| $A_{BET}$ | Specific area measured by BET method |
| a.u. | Arbitrary unit |
| C | Active aluminum contents |
| $c_p$ | Specific heat capacity |
| d-spacing | Distance (in angstroms) among the planes of the atoms |
| d | diameter of the particles |
| $D_p$ | Size of the crystallite |
| H | Enthalpy |
| h | Heat flow |
| $\Delta H/\Delta m$ | Specific heat release |
| $h_{pexo}$ | Peak heat flux during exothermic reactions |
| m | Mass |
| $m_f$ | Final mass |
| P | Peak |
| Pc | Centre of peak |
| Ro | Particle size including the shell thickness |
| st | Shell thickness |
| t | Time |
| $T_{01}$ | Temperature where rate of heat release of mass change is maximum |
| Tf | Final temperature of the thermobalance |

| | |
|---|---|
| $T_{f10}$ | Termination temperature for DSC-TGA test when β= 10 K/min |
| $T_{ig}$ | Ignition temperature |
| $T_{igAvg}$ | Average ignition temperature |
| $T_{on}$ | Onset temperature |
| $t_{oxide}$ | Thickness of oxide layer |
| $T_{pexo}$ | Peak temperature during exothermic reaction |
| $T_{endo}$ | Peak temperature during endothermic reaction |
| $V_{ox}$ | Maximum oxidation rate |

## Greek Symbols

| | |
|---|---|
| α | Degree of oxidation |
| $\beta$ | Heating Rate |
| $\mu$ | Viscosity |
| $\lambda$ | Wave length |
| Δ | Change |
| $\rho$ | Density of the particles |

## Abbreviations

| | |
|---|---|
| AP | Aluminum particle |
| BCC | Body centred cubic |
| BET | Brunauer-Emmett-Teller (absorption theory) |
| CRH | Constant rates of heating |
| DDSC | Derivative of DSC |
| DLS | Dynamic light scattering |
| DOM | Diffusion oxidation mechanism |

| | |
|---|---|
| DSC | Differential scanning calorimetry |
| DTA | Differential thermogravimetric analysis |
| DTGA | Derivative of TGA |
| EDS | Energy-dispersive X-ray spectroscopy |
| EEW | Electrical explosion of wire |
| FCC | Face centred cubic |
| FWHM | Full width half maximum |
| HCP | Hexagonal close-packed |
| HRSEM | High resolution scanning electron microscopy |
| HRTEM | High-resolution transmission electron microscopy |
| JCPDS | Joint Committee on Powder Diffraction Standards |
| MDM | Melt dispersion mechanism |
| nAl | Nano aluminum |
| NA | Nanoalloy |
| OS | Onset slop |
| PDF | Powder Diffraction File |
| PIV | Particle Image Velocimetry |
| PS | Power supply |
| PSD | Particle size distribution |
| XRD | Powder X-ray diffraction |
| RDX | Research Department Explosive |
| RT | Room temperature |
| SAED | Selected area electron diffraction |
| SAXS | Small angle X-ray scattering |
| SEM | Scanning electron microscope |

| | |
|---|---|
| SHS | Self-propagating high-temperature synthesis |
| SPMS | Single particle mass spectroscopy |
| STA | Simultaneous thermal analysis |
| TEM | Transmission electron microscopy |
| TGA | Thermogravimetric analysis |
| UFAP | Ultrafine Al powder |
| XPS | X-ray photoelectron spectroscopy |
| XRD | X ray powder diffraction |

# Chapter 1

# 1. Introduction

## 1.1. Background

Reactive metals such as Al, Fe, Cu, B, Mg etc. and their alloys have attracted widespread interest in various energy applications including propulsion systems, explosives, gun powders, propellants, pyrotechnics, metastable intermolecular composites (MICs) and thermites [1-3]. For instance, the thermite reaction, which involves the reduction of metallic oxides with aluminium to form aluminium oxide and metals or alloys, is widely used for metallurgical applications and combustion synthesis of new materials and explosives, and micrometre sized metal particles, including aluminium, boron and iron, have been used as solid fuel additives for enhanced propulsion, airbag igniters/boosters and aerial decoy flares [4-7]. The metastable intermolecular composites (MICs) are made by physical or mechanical mixing a metal and a metal oxide powder and are used as energetic materials (EMs) for various applications [8, 9]. These metallic materials are typically in powder form and are capable of storing a large amount of chemical energy, hence be termed as 'energetic particles'. Through oxidation or combustion, the chemical energy is converted to thermal energy, resulting in large exothermicity and high reaction temperatures [10-12], and the process is heavily dependent on the particle materials and morphology.

Increasing use of energies generated from renewable resources, including biomass, wind energy, hydroelectric power, and solar energy, will become viable where the geographical and climatic prerequisites are favourable, and pumped hydro, compressed /liquefied air, fly wheels, or super-capacitors have been conventionally proposed for

stationary energy storage applications. Such regions, however, seldom coincide with the areas of high energy consumption, namely industrial and city regions with a high population density. Alternative mobile energy storage media are required. Examples include hydrogen and batteries but both have significant problems to overcome. A novel energy storage concept by using nano-structured energetic materials, coined as 'nanofuel', such as aluminium, iron, silicon, and magnesium, was recently proposed [13]. The concept comprises three main elements: production, transportation and utilization of nanofuels. In a simplified version, primary or renewable energy resources are utilized to manufacture nanofuels from raw materials or captured end particles (production), which are then transported and stored in places requiring energy (transportation); heat or, indirectly, electricity/work is released through an oxidation or combustion process (utilization). The end products, oxidized particles, are recycled and processed back to metal form, thus closing the loop. Compared with either hydrogen or battery as the energy storage medium, nanofuel possesses a number of advantages: such as abundance, high energy density, **Figure 1.1**, and easy transportation, with many potential applications while reducing the carbon footprint and minimizing the formation of toxic and dangerous emissions. However conventional metals are difficult to use due to their high combustion temperature. One of the key requirements to achieve a controlled release of energy is to engineer the particle size to the nanoscale, where the particles exhibit strong size-dependent properties.

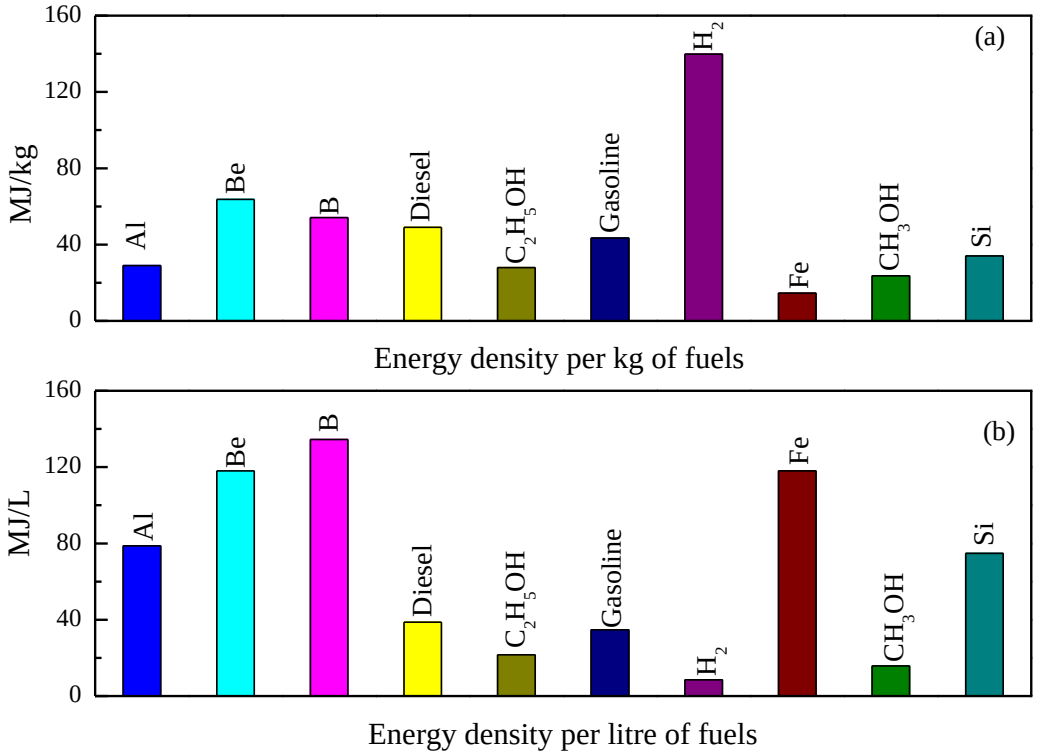


**Figure 1.1** Comparison of energy densities of various materials [13].

The physiochemical properties of energetic particles such as the ignition temperature, the burn rate and the specific impulse depend heavily upon the technique of powder production and the final particle parameters such as particle size, size distribution, particle shape, crystal structure and the initial amorphous oxide layer. A simple existence of some broken bonds on the particle surface would modify their physical and chemical properties significantly. According to the production method, the nanomaterials can be generally divided into three groups, 1) volume nanostructure materials such as nanoporous materials, 2) surface nanostructure materials such as surface coatings and 3) nano-structured particles including nanoparticles, nanocomposites and nanoalloys (NAs). In a broader term, these materials can be classified into two categories. The 1$^{st}$ *generation* nanomaterials are characterised by the presence of a natural passivation layer, mostly likely formed during the production and storage of the nanoparticles. To reduce the uncertainties, the 2$^{nd}$ *generation* particles actively control the initial oxide

layer by covering them with a material (organic or inorganic). For instance, for L-ALEX particles, palmitic acid ($CH_3$ $(CH_2)_{17}$ COOH) is used to protect the reactive core metal [14, 15]. Both categories have wide applications.

The energy conversion and transportation process at the nanoscale is expected to be quite different to that at the micrometre or bulk level. At the nanometer scale the properties of the particles, such as the thermal conductivity, enthalpy value, oxidation and ignition temperature, and combustion rate, exhibit a strong size-dependent behaviour. Clearly with the reduction of particle size, the specific surface area of the powders increases, which creates more contact points among the reactants and increases the homogeneity of the mixture that, in turn, increases the speed of the reaction. The specific surface area and the ratio of surface atoms to bulk atoms increase dramatically with the decrease of diameter of the particles as shown in **Figure 1.2** [16]. The co-ordination number also decreases with the decrease of diameter. When the co-ordination number becomes significantly lower, the whole particle would exhibit the properties of surface atoms, which, in turn, modifies many properties of interest such as increased reactivity, lower sintering, ignition and melting temperatures and higher catalytic properties as compared to micrometric and larger particles [17, 18].

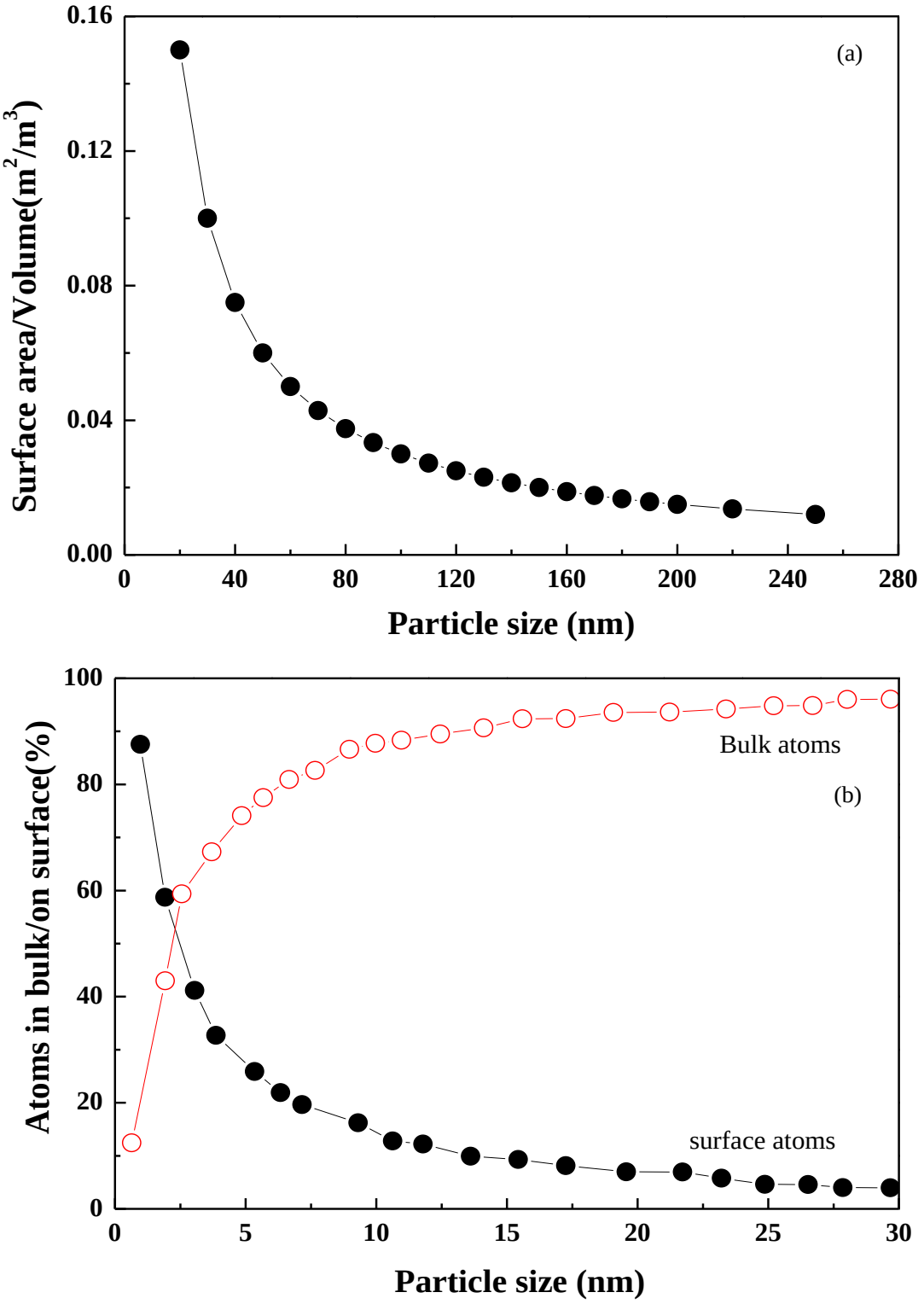


**Figure 1.2** Relationship of particle size with specific surface area and surface/bulk atoms

Metallic materials have high theoretical energy densities, **Figure 1.1**, but these combustion enthalpies cannot be achieved easily especially at the low temperature. The limiting factors of their usage as energetic materials include long ignition delays, low reaction rates and incomplete combustion. For example, aluminium melts before the start of ignition that increases the inter particle agglomeration which, in turn, increases the time to complete the reaction [19]. The current MICs are made by mechanically or physically mixing metal and metal oxide particles, which typically have the problems of nonhomogeneous mixing of fuel and the oxidiser, uneven distribution of the particles, and irregular patterns of contact points between the fuel and the oxidiser. The rate of reaction is also lowered due to the heterogeneous nature of the ions that are taking part in the ongoing chemical reaction at the metal/oxide interface [9, 20]. All these factors affect their performance by increasing the ignition delays and causing incomplete combustion. To overcome these problems and to have more controllability over the material's properties, some metals are alloyed by mixing with several other elements at the nanoscale [21-23]. Due to the synergistic effects of the constituent alloying materials, the physiochemical properties of the nanoalloys can be improved by chemical reordering and spatial redistribution of the atoms [24]. In addition, the alloying increases the surface area of the particles that will increase the rate of reaction and improve the reaction mechanism [9, 25, 26], which in turn shall improve the rate of heat release and the performance of propellants and thermites [27]. These alloys can be in the form of solid solutions, amorphous metallic phases or intermetallic phases [28].

Clearly advancing the understanding of the oxidation, ignition and combustion of energetic nanoparticles and nanoalloys is essential for all successful applications above.

## 1.2. Oxidation, Ignition and Combustion of Metals

The bulk metals are oxidized at a higher temperature but they can become unstable and can corrode at the room temperature at varying degrees depending upon the reaction kinetics [14]. Apart from the temperature, the oxidation of metals depends upon many factors such as its purity, the crystallographic structure, i.e., single crystal/ polycrystalline and the thickness of the oxide film. The oxidation of bulk metal is the interplay of one or combinations of many processes that include 1) inward diffusion of oxygen anions towards metal/oxide interface with outwards movement of electrons/holes etc. 2) outwards movement of metals cations and electrons 3) combinations of these processes [29]. With the diffusion of oxidant into the metal, the amount of metal oxide increases inside the metal and hence, gives rise to internal stresses. When these stresses are relieved, they produce more defects which, as a result, enhance the oxidation process.

According to Wagner, the transport property, such as the coefficient of diffusion of the growing film, can be related to its thickness [30]. For example, with the increase of the thickness of oxide film, the gradient force for driving the ions decreases. On the other hand, the Cabrera and Mott theory explains the oxidation growth in atomistic terms. They assumed that the oxygen molecules adsorbed at the gas/oxide interface could be ionized by the freely moving electrons from the metal to oxide/gas interface and the numbers of metallic available cations are consumed after their generation at the oxide/gas interface. The speed of electrons is higher than that of the ions whose diffusion across the film becomes slow and hence becomes the rate determining process [31].

The oxidation of particles is different from that of the bulk metals. It is found that the oxidation of the aluminium particles completes in two regimes namely, before and after the melting point, i.e., 660 $^{o}$C of aluminium. The first stage of oxidation is kinetically controlled and only a small amount of metals is oxidized. The second stage depends upon the diffusion of both metal and oxygen ions and the rate of growth increases with the decrease of diameter of the particle [32]. During the oxidation of aluminium particles, the passivation layer transforms from one polymorphic form to the other and thus controls the whole oxidation mechanism [33]. Because the effectiveness of the transport of oxygen towards the core, metal oxidation is strongly dependent on this passivation layer, the physical parameters such as thickness, roughness, specific surface area and the composition of this layer, which affects subsequently, the ignition temperature and ignition delay. Thermal analyses such as thermogravimetric analysis (TGA) and differential scanning calorimetery (DSC) are the fundamental techniques used for the study of the oxidation and ignition of the particles. The TGA trace gives weight increment due to the oxidation while the DSC curve quantifies all the energy evolved/consumed during the physical or chemical processes.

The physics of oxidation of fine particles (nanoparticles or sometimes micro-sized particles exhibiting size-dependent behaviours) have been found to be different to that of conventional-sized particles (i.e. > 50 micrometres) [34]. As the physical and thermodynamic properties of the fine powders are different, the models describing the oxidation of conventional-sized powders make certain assumptions such as that at any given instant the growth of oxide depends upon the diffusion of a single species etc. [35] . Such assumptions are not valid for the fine particles. For conventional-sized particles, the diffusion based oxidation is a good assumption, but for fine particles, the reaction is more likely to be kinetically controlled [34, 36].

The metals are normally ignited after achieving their boiling point. The volatility of the metal oxide relative to the metal and overall energy available for the gasification of both the metal and its oxide are very important factors in the phenomenological understanding of metal combustion. There are two possibilities for the combustion [37, 38] that 1) the metal relative to its oxide is volatile and the energy released during the reaction is sufficient to vaporize the oxide. This ensures that the combustion is homogenous and proceeds in the vapour phase via the diffusion of ions, 2) the metal relative to its oxide is non-volatile and oxidation energy is not enough to vaporize it. The combustion will be heterogeneous and proceed purely in the condensed phase. [39]. Von Grosse and Conway (1958) found that the flame temperature of the metal is limited to the volatilization-dissociation or boiling point of the oxide. If the oxide's volatilization temperature is higher than the boiling point of the metal, the combustion will proceed heterogeneously, i.e., in the condensed phase, on the surface of metal particles. On the other hand, when the heat of reaction is sufficient to transform both the oxide and the metal into gas, the combustion will proceed in the vapour phase. This is called Glassman's criteria for vapour phase combustion [58]. In this sense, the burn time for metallic particles can be related to its diametric length, i.e., the $d^2$ law, as the combustion of metallic particles is analogous to that of the hydrocarbon particles [40]. The law gives an approximate burn time in terms of diameter of the burning particles. It is assumed that the particle is spherical, its diameter regresses uniformly with the reaction, and no oxide layer generates on the surface of the particle. Practically, these assumptions are not possible. On the contrary, the particle is not spherical and an oxide layer having variable density is also developed during the reaction. It is also assumed that the final diameter becomes zero which is not possible [40]. Williams [41] has also summarized the combustion criteria for the metals and their oxides. His theory is based upon factors

related to energy and solubility of metals and metal oxides such as i) the amount of heat available is sufficient to heat and vaporize the metal oxide, ii) the available heat is higher than that is needed to boil the metal itself, and iii) the inter-solubility of metal and metal oxide.

For nanoparticles, two important mechanisms are proposed to explain the combustion mechanisms, namely, the Diffusion Mechanism (DM) and the Melt Dispersion Mechanism (MDM). When the heating rate is not high enough, e.g. below $10^3$ K/s, combustion takes place in a similar manner to that of micron sized particles. In this case, both cations and anions move towards each other and combustion proceeds while the layers of the oxide increases at the expense of the core metal. This mechanism is characterised by a slow speed of reaction that depends upon the oxide shell thickness, the radius of particle and the active metal contents [42]. On the other hand, when the heating rate of the nanoparticle reaches the order of $10^7$ K/s, the combustion becomes similar to detonation [43] and the combustion process cannot be explained by the traditional theory of oxidation [44]. This mechanochemical mechanism is characterized by the conditions of fast reaction rate and high heating rates, termed as the melt dispersion mechanism. Contrary to conventional-sized particles, a nanoparticle core would become melt before the fracture of the oxide shell. Hence the volume inside the shell is increased and causes internal stresses to develop. Subsequently, high rate of reaction and fast heating rate lead to dynamic fracture of the shell [45]. The major conditions [46] proposed for such reaction are: 1) the heating rate should be high such that the metal inside the core must melt before the fracture of the shell; 2) the oxide shell must fracture simultaneously which requires that there are no nano-voids, vacancies, defects, and damages etc.; 3) the pressure at the time of spallation must be

more that the cavitation pressure of the metal particle and there must be enough space around the particle so that these particle can move freely in the space.

Clearly the reduction of particle size to the nanoscale represents both opportunities and challenges. At the nanoscale, it becomes possible to engineer different melting, oxidation and ignition temperature of the materials by controlling the particle structure and morphologies to suit different applications. The increased specific areas at the nanoscale will lead to rapid oxidation and combustion, resulting in a fast release of the stored energy. However many challenges exist, which ranges from large-scale production of energetic particles, controlled oxidation and ignition of the materials, capture and regeneration of the burned fuels. From the physics aspect, many deviations from the established laws at the bulk scale have been reported. For instance, the ignition temperature of energetic nanomaterials is more sensitive to the passivation layer and the external heating conditions, and the burning time of nanomaterials is deviated from the conventional $d^2$ law [40, 47].

The above short review points out the large difference in the reaction mechanics between nanoparticles and conventional-sized particles. Concerning the wide scope of the work, detailed literature review of each topic will be presented in individual sections of the chapters.

## 1.3. Aims and Objectives

Clearly the oxidation, ignition and combustion of nanoparticles are essential to a number of applications, where a systematic investigation is still lacking. For nanoparticles, the exothermic reactions have to be related to the thermodynamic, kinetic, morphological and structural properties of these particles. Using aluminium as an example, this thesis

reports detailed experimental studies of the oxidation and ignition of nano aluminium particles (nAl) and nanoalloys (NAs) such as nAlCu and nAlZn. This is achieved by employing the Simultaneous Thermal analysis (STA), which is the combination of Thermogravimetric Analysis (TGA) and Differential Scanning Calorimetery (DSC). TGA and DSC are modern analytical techniques where the weight changes of the material and the energy released or absorbed by the particles undergoing some thermal treatments are recoded. The particles are oxidised at constant heating rates or isothermal conditions, in the controlled atmosphere of a gas such as air or nitrogen. With these techniques the oxidation and ignition mechanisms and relative reactivities of the nAl and NAs will be explored. The energy transfer and conversion at nanometre scale is also found. Detailed characterisation of particles before and after the experiments is carried out by scanning electron microscopy (SEM) and transmission electron microscopy (TEM) along with Nanosizer, Brunauer–Emmett–Teller *(*BET), energy dispersive X-ray spectroscopy (EDS) and powder X-ray diffractionmetry (XRD). In the other set of experiments, a preliminary combustion analysis on feeding nanoparticles in the methane stream using a Bunsen burner is performed. The particles are mixed with methane gas ($CH_4$) in the pre-combustion chamber. The aforementioned material techniques are used to understand the combustion behaviour and burning characteristics of various energetic nanoparticles.

## 1.4. Organisation of the Dissertation

This dissertation is divided into 5 chapters. The background information and the objectives are discussed in **Chapter 1.** Experimental procedures along with material synthesis and material physical characterisation methods are discussed in **Chapter 2.** The experimental results of the oxidation and ignition of the nano aluminium particles (nAl) are discussed in **Chapter 3**, where an interesting early ignition phenomenon and

the forming of hollow structured oxides are observed. Further detailed study in determining the temperature conditions at which the hollow-structured particles form and the relationship to the early ignition phenomenon are also presented. This chapter also reports the stepwise oxidation of the nano alloys (NAs), nAlCu and nAlZn respectively, with the help of various thermophysical characterisation techniques. This chapter also reports a preliminary comparative study of the combustion behaviour of aluminium, silicon and iron particles. In **Chapter 4,** the exothermic performance parameters such as its reactivity, ignition temperature, specific thermal energy and the thermal stability of pure nAl is compared with that of its nanoalloys. A brief summary and conclusion of the current research and future recommendations are presented in **Chapter 5**.

# Chapter 2

# 2. Materials and Methods

## 2.1. Materials Synthesis

Nano aluminum particles (nAl) as well as its nanoalloys, i.e., nAlCu and nAlZn were used in the experiments and were provided by Tomsk State University, Russia. These nanoparticles were fabricated with electrical explosion of wire (EEW) method which is shown schematically in **Figure 2.1** [48].

The constitutional elements were twisted in wires and the aluminum content in the explosion products was adjusted by varying the wire diameter. In brief, a high voltage power supply unit PS charges a capacitive storage C up to the required voltage monitored by a kilovolt-meter, mounted in PS. After the activation of discharger P, all accumulated energy is transferred to WE wires. The energy characteristics of EEW were calculated by a current oscillogram, obtained by means of current sensor $R_{sh}$, in accordance with the Kvartzkhava method [49]. The particles produced by this method typically have a wide range of size distribution (PSD) but with low level of contamination [50].

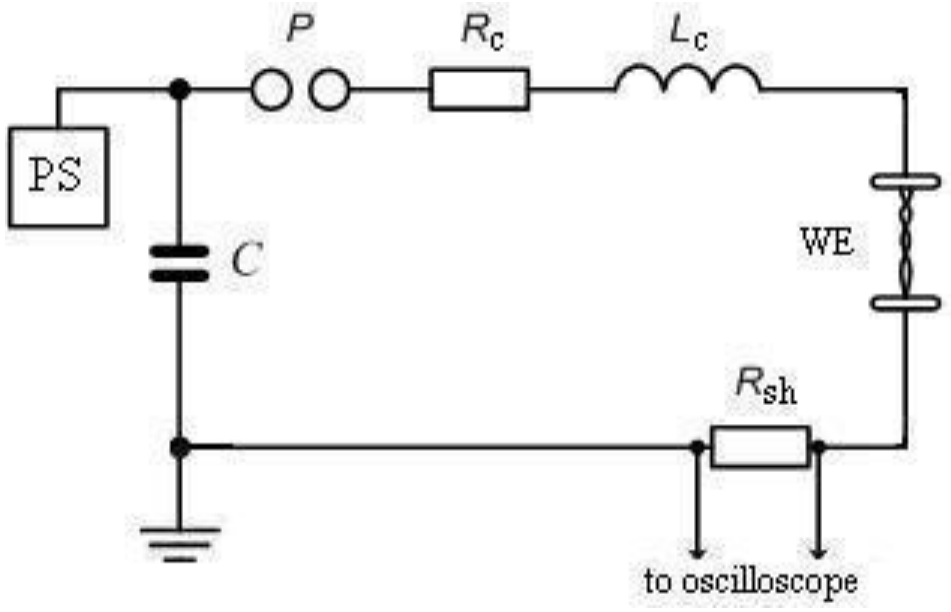


**Figure 2.1** Electrical schematic diagram of the unit *($R_c$* and $L_c$ – circuit resistor and inductor)

After their production, the particles were sealed in vacuum packs, and stored in an insulated vessel at room temperature. The prevention of its contact with air minimized the formation and growth of passivation layers.

## 2.2. Materials Physical Characterisation

The particle size distribution (PSD) and the mean diameter (MD) of the various particles were characterised by Nanosizer (Zetasizer Nano Zs, Make: Malvern, UK), which is based on the principle of dynamic light scattering (DLS). The powder samples were dispersed in the liquid medium of hexane and sonicated to reduce the particle agglomeration.

The morphology of the particles before and after experiments was observed with scanning electron microscopy (SEM) (Inspect F, FEI Company, EU) operating at 10 kV. The samples were sputter-coated with gold/carbon to enhance their electrical conductivity. This type of coating is desired to prevent the specimen from charging the electron beam and to improve the signal to noise ratio.

The elemental compositional analysis of the particles was performed by an Energy Dispersive X-ray Spectrometer (EDS, Oxford Instrument) equipped with INCA Energy 300 system. The particles were carbon coated before the inspection.

The microstructure, the oxide encapsulation and the sizes of voids, in relation to the temperature increase, of the nanoparticles particles were observed with ex-situ high resolution transmission electron microscopy (TEM) using a JEOL JEM 1020 microscope operating under 200 kV before and after the experiment. For that the samples were prepared in the solution of ethanol and were sonicated for 10 mins in the sonic bath to decrease the agglomeration among the particles. To ensure that the particles were de-agglomerised to a greater degree, the sonication process was interrupted after 5 mins for 15 seconds and after that the same process was repeated for another 5 mins. Carbon coated grids dipped in the solution and later dried at room temperature were used for the imaging. During the experiments it was found that the aluminum particles produced voids in their central regions after their oxidation. For that EDS spot analysis was performed on TEM.

The surface area of the particles was determined with the adsorption-desorption technique using a Gemini VII 2390p Surface Area Analyser from Micromeritics

Instruments Corp. Nitrogen gas was used as the adsorbate. Before each set of experimentation, the powder was degassed by using a Gemini FlowPrep degasser for three hours at 200 $^{o}$C and $10^{-2}$ Pa. This removed the foreign materials like $CO_2$, moisture, oil and grease adsorbed in the powder. After this, the samples were immersed in the liquid nitrogen at -196 $^{o}$C where a five-point isotherm in a relative pressure range of 0.05 to 0.30 was obtained. The Brunauer–Emmett–Teller (BET) equation was used for the calculation of surface area of the particles.

The crystalline structure of the nanoparticles before and after the heat treatment was examined with ex-situ XRD. The end products were cooled in the inert atmosphere of nitrogen gas and were preserved for their crystal structure analyses. Ex-situ powder X-ray diffraction (XRD) analyses were performed with XRD (Siemens, D5000 Diffractometer) operated 40 kV and 40 mA using CuK$\alpha$ radiation ($\lambda$ = 0.15418 nm. The diffraction pattern from $10^{o}$ to $70^{o}$ 2$\theta$ of each product was recorded and subsequently, used to identify the phase composition of the products of thermal treatment.

## 2.3. Experimental Procedures

### 2.3.1. Oxidation and ignition study

The oxidation kinetics, the ignition reactions, the intervening physiochemical reactions occurring at different temperature ranges, physical transitions and the thermal stabilities of the nanoparticles were studied using STA 1500 thermal analyser (Rheometric Scientific, Germany), similar to our previous studies [51, 52]. Simultaneous Thermal Analysis (STA) is an analytical technique used to monitor the behaviour of the matter

as a function of temperature. This technique (TGA/DSC) is often used to investigate the thermodynamic properties of the matter, due to its reliability as well as its simplicity. Thermogravimetric analysis (TGA) is an experimental technique where changes of the mass of the sample are recorded with respect to the temperature. The sample is loaded into a pan, made of platinum or alumina, placed in furnace whose temperature is controlled by a computer program. The temperature can be raised from room temperature to 1500 $^{o}$C. Microbalance having a resolution of 0.01 μg is used to measure the changes of weight. DSC is a thermoanalytical technique used to measure the energy emitted or absorbed by the sample. Endothermic or exothermic event will give rise to a peak in the DSC curve. A small amount of the sample is taken to ensure that within the sample the heat from the furnace to the sample is conducted homogenously without developing any heat barrier. To monitor weight and heat changes of the same process simultaneously, both DSC and TGA techniques are coupled into one set of instrument. Differential thermal analyses (DTA) can also be performed by taking the first derivative of the change of mass and heat, i.e., dm/dT and dh/dT. Various steps of reaction are analysed with the help of DTA. The atmosphere of the furnace is generated by a continuous supply of the gases such as air, $N_2$, CO, $CO_2$, $O_2$ and Ar. The atmosphere may be purged with an inert gas to prevent any reaction or desired gas to allow reaction to take place. The schematic diagram of the apparatus is shown in **Figure 2.2**.

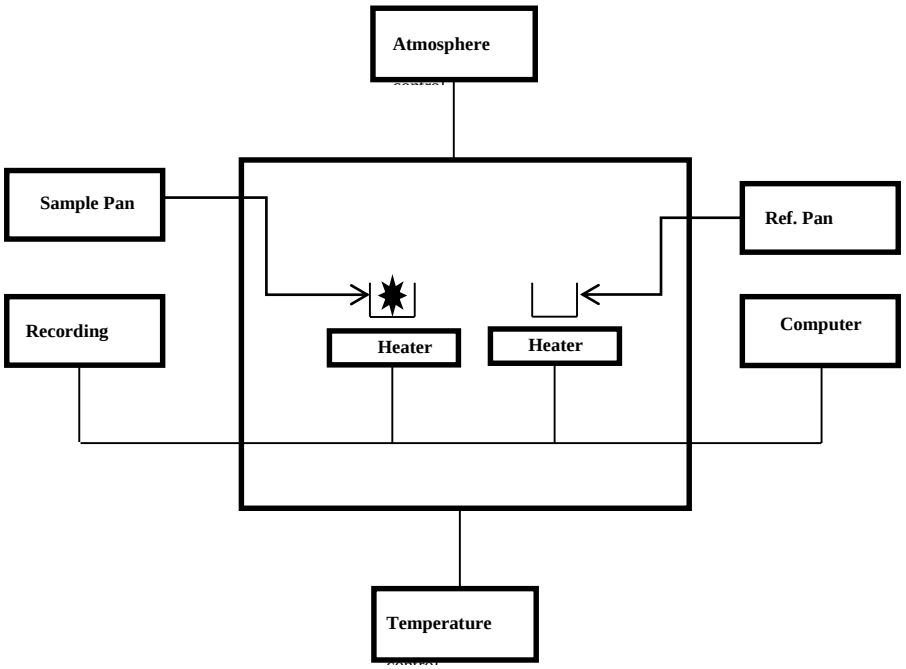


**Figure 2.2** Block diagram of thermobalance

Thermal oxidation and nitridation experiments were performed at the atmospheric pressure using dry air and nitrogen, respectively, **Table 2.1.** The changes of mass during the whole oxidation process were monitored with thermo-gravimetric analysis (TGA) and the changes of energy were surveyed with differential scanning calorimetery (DSC). Temperature calibration of the thermo-balance was conducted with the melting points standards of various metals (Zn, Sn, In, Pb etc.), and the weight calibration was done before the start of each experiment. A small amount (~6 mg) of the samples was loaded uniformly in the pan **Table 2.1**. With such a small quantity of the sample, the tendencies of developing the internal temperature gradient in the pan were reduced. Platinum crucibles were selected to ensure that there were no reactions between the pan and the products of on-going reactions. The pans were cleaned with 10% $HNO_3$ solution after each experiment to ensure that there were no residues left for the next experiment.

**Table 2.1** Experimental Conditions.

| Sample | $T_{iso}$ | $\beta i$ | t | $T_{f10}$ | $\beta$ | $T_f$ | m$i$ | Q |
|---|---|---|---|---|---|---|---|---|
| | $^oC$ | $K$min$^{-1}$ | Hrs. | $^oC$ | $K$min$^{-1}$ | $^oC$ | mg | ml/min |
| nAl | 400, 450, 500, 550, 720 | 30 | 10 | 525, 630, 665, 925, 1000, 1050, 1175, 500, 600, 700, 800 | 2-10, 12, 15, 18, 20, 30 | 1175 | 6 ± 0.05 | 20 ± 1 |
| nAlZn | 450, 500, 600, 650 | 30 | 10 | 400, 460, 625, 710, 910, 1200 | 2, 5-7, 10, 12, 15, 20, 30 | 1200 | 6 ± 0.1 | 23 ± 2 |
| nAlCu | - | 30 | 10 | 570, 900, 1100, 1200 | 2, 5, 7, 10, 12, 15, 20, 30 | 1200 | 6.1 ± 0.1 | 21 ± 2 |

Note:

$T_{iso}$ is isothermal temperature.

$\beta$ is heating rate or temperature ramp, $\beta i$ is initial heating rate to attain the required isothermal temperature conditions

$t$ is total experimentation time for one set of isothermal temperature conditions

$T_{f10}$ is the termination temperature for DSC/TGA test when $\beta = 10$ K/min

$T_f$ is the final temperature of the thermobalance m$i$ is the initial mass of the sample and Q is the flow rate of dry air.

To understand the effects of heating rate and temperature on the oxidation and the thermal stability of the aluminum nanoparticles and its nanoalloys, two sets of the experiments were performed in the thermal analyser. In the first set of experiments, the samples were thermally treated at heating rates of 2-30 K/min from room temperature to 1175-1200 $^{o}$C. This helped in understanding the effect of heating rate on the oxidation and the ignition process. In the second set of experiments, the samples were heated from the room temperature at a heating rate of 10 K/min and the reactions were terminated at '$T_{f10}$', **Table 2.1**. These temperatures were selected where sudden changes were observed on the TGA/DSC curves. This helped in revealing the various polymorphic phases of the products developed, the intervening oxidation steps and the path of the ongoing oxidation reaction. The products oxidation were cooled in the inert atmosphere of nitrogen for ex-situ XRD, SEM and TEM analyses. In addition to that, two sets of experiments were performed in the thermobalance to quantify the effects of the heating rate and the temperature on the changing morphology of the particles. In the first set, the particles were oxidized at a constant heating rate of 5 K/min and the temperature of furnace was raised from room temperature to 600, 700 and 800 $^{o}$C. This set of experiments was helpful in understanding the evolution of the voids in relation to the change of temperature and the physical state of the particles. It also reflects the effect of melting process on the development of the hollow structure. In the second set of experiments, the particles were heated at various heating rates (2, 8, 20 K/min). The products of oxidation were cooled in nitrogen gas and later analysed with TEM and the effect of the heating rate on the size and shape of the particles and the voids was studied. For each set of the experimentations, the parameters (i.e., reaction gas environment, crucible material and mass of the sample) that may affect the TGA/DSC experimental results were kept the same.

## 2.3.2. Combustion Study

### 2.3.2.1. Aerosol generation assembly

The experimental set up consists of a methane delivery system, a regulator, a meter valve, a particle dispersion system and a Bunsen type burner, **Figure 2.3.** The particles were mixed with methane gas and aerosolised in the aerosol generation assembly. The particles were mixed with the methane stream through a belt conveying system, where the particles were loaded from a hopper onto a belt, which was driven by an electric motor (12 V). The amount of particles added into the gas stream was adjusted by the speed of the motor. For the experimental results reported below, the amount of methane was regulated at 2 l/min to ensure the uniform flow rate of the gas.

### 2.3.2.2. Bunsen burner

Commercially available Bunsen type burner was used to analyse the combustion characteristics of the particles/methane/air. A continuous particle laden stream of methane gas from the feeder was supplied to the burner through a silicon tube having a diameter of 6 mm. Once the steady flow was achieved, the particles were ignited and were combusted under the atmospheric conditions. The burner was air cooled because the experiments were last only for a few minutes.

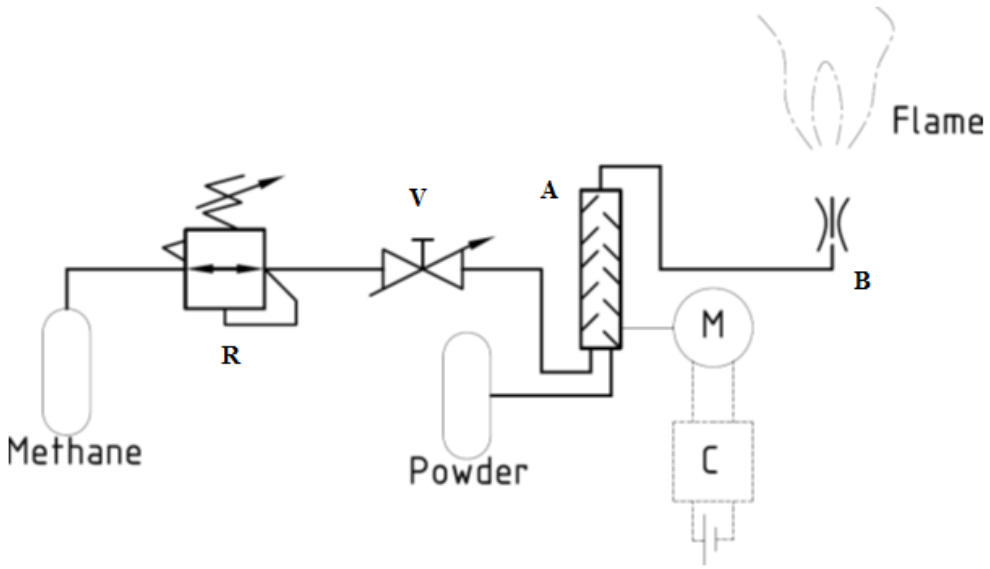


**Figure 2.3**. Schematic diagram of burner test set up (R-Regulator; V-Meter valve; A-Aerosol generation assembly; M- Driving motor; C- Control circuit and B-Bunsen burner.

### 2.3.2.3. Image capture

The combustion of the particles was recorded and subsequently interpreted with the help of a high speed video camera (Phantom V2.3) recording at a frequency of 1000 Hz with 256 by 128 pixel array. The recording was started once the flame became stable. The distance to pixel ratio (spatial resolution) was calculated as 14.5, 14.9 and 16.7 for Si (720 nm), Si (1 μm) and Fe (45-75 μm), respectively. The capture time in all experiments was maintained constant at 1 ms. The captured images were binarised using J-image software.

### 2.3.2.4. Particle image velocimetry (PIV) measurement

The combustion velocity, burning times and reactivity/ignitibility of various particles are quantified with the particle image velocimetry technique. The velocity profile and

flow vectors of the combusted particles were processed using the PIVview2C software. To achieve time-averaged results with higher quality, the average speed of the particles was calculated by processing 100 images (50 image pairs). Only axial component of the velocity was determined. For image pair data processing, a window size of 32x32 (pixel) having a step size of 16x16 (pixel) was used. Images were evaluated with a direct cross (non-FFT) correlation. Multiple pass interrogation method with number of iterations 3-passes was used. The velocity vector and particle flow field was smoothed with a smooth kernel width (in nodes) of 1.0. No filtering or interpolation was done to fill in the missing vectors.

# Chapter 3

# 3. Results and Discussions

## 3.1. Oxidation and Ignition Study of Aluminum Nanoparticles

Nano aluminum particles (nAl) can improve the combustion characteristics of energy materials and are being used as additives in propellants, pyrotechnics and explosives. Their unique properties such as high specific surface area coupled with high energy density makes them good choices for many energy applications, especially in high specific thrust and high pressure conditions [48, 53-55]. Due to their unique properties such as lower ignition temperature (<660 $^{o}$C) and a higher reactivity (i.e., 5-10 times faster), nAl possesses many features non-comparable by the micron sized counterpart [56]. However, the physiochemical phenomena responsible for their better performances are still unclear [57, 58].

The utilization of nAl is usually the exothermic reactions through oxidization and ignition; hence it is of the primary interest to investigate these processes. Many experiments have been conducted in the last decade to understand the oxidation of nano aluminum, NAP-composite in the presence of air, nitrogen or oxygen. The effect of particle size, particle size distribution, and passivation layers have been discussed. A comprehensive survey of the literature is summarized in

**Table 3.1** Summary of oxidation/ignition related study using aluminum nanoparticles

| Authors (Year) | Materials | Technique used | Exp. conditions | Oxidizer | Major Findings |
|---|---|---|---|---|---|
| Mench et al.[59] (1998) | nAl, μAl (20 μm) | TGA-DTA | Up to 1300 °C @5 K/min | Air, He, $O_2$, $N_2$ | i) Size effect is explored and the higher reactivity of Al is due to its smaller size |
| Jones et al.[60] (2000) | Alex (nano)/ micron | TGA/DSC SDT/ARC | 400-600°C @ 0.5 K/min | $N_2$, He, Air | i) $c_p$ values of micro and nano Al are similar<br>ii) the mass changed has an inverse relation with the heating rate β |
| Il'in et al.[61] (2001) | Various Ultrafine Al Powder (UFAP) | Derivatograms of TGA/DSC | RT-1000 °C 10 K/min | Air | i) The reactivity should be defined by $T_{on}$, $v_{ox}$, maximum oxidation rate, α degree of oxidation and S/Δm specific heat release<br>ii) Particles having similar metallic contents have different reactivity due to difference of size, shape and PSD |
| Kwon et al.[62] (2002 | SFAP, coated with $AlB_2$ & $Al_2O_3$, $Al(OH)_3$ | TGA/DTA | RT-1000 °C @10 K/min | Air | i) $T_{on}$ increase by 30-40 °C when $AlB_2$ coating is used. Both thermal stability but and total metallic contents are improved.<br>ii) 40% mass is oxidized in the second stage at temperature 660-1000 °C |
| Dokhan et al.[63] (2002) | Aluminized Composites propellants | Visual/high speed camera | Rocket motor pressure (1.38-6.9 MPa) | Air | i) Composites having finer aluminum particles burn fast<br>ii) The burning rate of AP increase with the addition of nAl having a bimodal particle size distribution. |
| Jones et al.[64] (2003) | Alex, Als, Alss, Alsstef & GAP/AND/RDX | TGA/DSC/DTA | RT-1400 °C @ 0.5 K/min | Air, $N_2$, Ar, | i) The reactivity depends not only on diameter but also on shell thickness<br>ii) The onset decomposition temperature of GAP/RDX was reduced with addition of Al. |
| Gromov et al.[65] (2006) | nAl (coated with organic and metallic materials) | TGA/DSC /DTA | Up to 1000 °C @10 K/min | $N_2$, Air, $H_2O$ | i) The coated Al powders show increased stability to oxidation/nitridation. |

| | | | | | |
|---|---|---|---|---|---|
| | | | | | ii) Non-oxide coating have higher combustion enthalpy as compared to the oxide coating. |
| Gromov et al.[66] (2006) | Nano and micro Al Coated with NC/boron/alumina/ oleic/stearic acid | DTA-TGA | RT-1300 $^{o}$C @10 K/min | Air, $N_2$ | i) The type of coating, particle size and ageing have direct link with the thermal stability |
| Rufino et al.[58] (2007) | nAl (160 nm) μAl (1.2, 17 μm) | HTGA/DSC | Up to 1000 $^{o}$C @10 K/min | Air, Ar | i) The oxidation rate depends upon particle size<br>ii) The thickness of alumina layers produced during the 1$^{st}$ stage is independent of the particle size |
| Kwok et al.[67] (2007) | NAP uncoated/ Coated with polymers | TGA/DSC/DTA | Up to 1300 $^{o}$C @20 K/min | Air | i) The reactivity depends not only upon the particle size but also on particle size distribution, specific surface area, composition and thickness of the passivation layer |
| Chen et al.[68] (2009) | nAl 50nm | TGA/DSC/DTA | Up to 1200 $^{o}$C 5,10,20 K/min 30/50/90K/min | Dry $O_2$ | The effect of heating rate (β) is explored<br>i) No trend of $\Delta m_1$, $\Delta m$ with β<br>ii) Tp/To increase with β<br>iii) S/Δm remains constant<br>iv) ΔH increase with β |
| Gromov et al. [69] (2009) | Explosives + NPs Al, Fe, W ,Ni, Cu | TG-DTA | Up to 750 $^{o}$C @10 K/min | $N_2$, Ar, | i) NPs have a strong effect of on the decomposition temperature of the explosives |
| Pantoya et al.[70] (2009) | nAl (15-50 nm) + Teflon | TGA/DSC | Up to 750 $^{o}$C @20 K/min | Ar | i) With the decrease of size, reaction kinetics improves and rate of pre ignition reaction increases |
| Reber et al.[71] (2010) | Al clusters anions with water | Various | N/A | N/A | i) The role of geometry on the reactivity at nanoscale is important |
| Korshunov [72] (2011) | Alex (92 nm) and μAl (20 μm) | TGA/DSC | Up to 1200 $^{o}$C @5 K/min | $N_2$ | i) The effect of powder dispersion, composition and structure of oxide shell and core metal with temperature rise is important |
| Mohan et al.[73] (2012) | NAP having no protective coating | Cabrera-Mott reaction mechanism | Thermal run away is | Air | i) Particle smaller than 68 nm are able to ignite at room temperature without initial preheating. |

| | | | | | |
|---|---|---|---|---|---|
| | | | considered as ignition | | |
| Sossi et al.[74] (2012) | nAl (coated with organic materials) + HTPB based fuels | TGA/DSC | Up to 1500 $^{o}$C @10 K/min | $O_2$ | i) The regression rate of several fuels are investigated<br>ii) Direct correlation of ballistics characterization by powder physical anAlysis and DSC/TGA cannot be made |
| Sun et al.[75] (2006) | nAl (30-160nm), μAl(3-4.5μm) | TGA-DSC | Up to 830 $^{o}$C @ 3, 5, 10, 20 K/min | $O_2$/Ar | i) The reactivity depends on the PSD but maximum reaction rate depend on size only |
| Levitas et al.[76] (2009 | nAl (17-202nm), μAl(12μm) | TGA-DSC | 20- 800 $^{o}$C @10 K/min | $O_2$/Ar | i) Melting temperature decreases with the particle size, whose value is higher than theoretical value due to pressure build up in the core. Damaging the shell reduces the melting temperature. |
| Sun & Simon[77] (2007) | nAl (8-50 nm) | TGA-DSC | DCS 670 $^{o}$C @5 K/min<br>TGA 830$^{o}$C @5 K/min | $O_2$/Ar | i) The melting temperature and heat of fusion decrease with the decrease of particle diameter due to the increase of the crystal defects at the nanoscale |
| Chen et al.[78] (2009) | nAl (20-50 nm) | DTA-TGA | DTA 800 $^{o}$C @10 K/min<br>TGA to 1000$^{o}$C @10 K/min | $O_2$/Ar | i) Particles having defects in their lattice structure are characterised with higher oxidation energy and a higher peak temperature during 1$^{st}$ exothermic reaction. |
| Pivkina et al.[79] (2006) | nAl (43 nm), doped with Ba, benzene and silicone rubber μAl(10 μm) | TGA/DSC/DTG | Up to 1100 $^{o}$C @10 and 2 K/min | Air | i) Thermal behaviour of powders depends upon the method of production<br>ii) The chemical activity of Ba-doped Al is enhanced during its storage due to the degradation of the oxide layer. |
| Schoenitz et al[80] (2010) | μAl(3-4.5μm) | TGA/DSC/DTG | Up to 1200 $^{o}$C @5-500 K/min | $O_2$/Ar | i) The activation energies are insensitive to the heating rates and a refined oxidation model is built at the high heating rates.<br>ii) The refined model can interpret the particle ignition in the laser beam experiment. |
| Wang et al.[81] (2011) | nAl (50-200 nm) passivated with nitrocellulose | DTA-TGA | Up to 800 $^{o}$C @5 K/min | Air , $N_2$ | i) Nitrocellulose is effective material of passivation for stabilizing and protecting the core metal. |

| | | | | | |
|---|---|---|---|---|---|
| | | | | | ii) Coating decreased the ignition temperature of nAl compared to the bulk Al and decreased the reaction temperature for Al/CuO thermite reaction. |
| Ivanov et al.[48] (2003) | nAl with other metals having various sizes | DTA-TGA | Heated at 10 K/min | Air , $N_2$ | i) Various metallic nano particles are manufactured with EEW method and their reactivities are calculated. Metallic powders produced in N2 environment is characterised with higher reactivity in oxygen. |
| Kwon et al.[82] (2007 | Eleven samples of nAl coated with gas, liquid and solid materials | DSC-TGA | Up to 1400 $^oC$ @10 K/min | Air | i) The effect of coating materials on the energetics of nAl was characterised<br>ii) The powders produced in Ar+$CO_2$ passivated by boron, air and CO2 showed improvements in the energetics of the nAl/ whereas coating with organic reagents was not profitable. |
| Eisenreich et al.[32] (2004) | nAl (100-150nm), μAl (0.3-25μm) | DSC-TGA | Up to 1000 $^oC$ @5 K/min | Air | i) The effect of size on the reactivity is studied.<br>ii) The oxidation completed in two steps, first step is dominated by chemical kinetics and passivation layer of 6-10 nm is formed regardless of the size of the particle, 2$^{nd}$ step is dominated by the diffusion and chemical reaction.<br>iii) γ- and θ-alumina is formed in first step whereas in the second step they transformed to α-alumina |
| Ilyin et al.[83] (2002) | Various e.g. UFAP, nAl and μAl | DTA-TGA | Up to 1000 $^oC$ @10 K/min | Air | i) The effect of size, shape, distribution, specific surface area etc on the above mentioned four reactivity parameters is calculated. |
| Cheng et al.[84] (2009) | Nano-Ni (100 nm) coated μAl (50 μm) | DSC-TGA | Up to 1400 $^oC$ @20 K/min | Air | i) The effect of coating composition is determined. It was found that the onset temperature of particle decrease with the increase of Ni amount. During 2$^{nd}$ exothermic reaction 10%Ni sample having high enthalpy might be due to |

| | | | | | |
|---|---|---|---|---|---|
| | | | | | due to its optimum composition, which decreases the intensity of the agglomeration during this reaction.<br><br>i) The polymorphic transformation of alumina (amorphous-γ–δ–θ–α) produced controls the diffusion of oxygen and is responsible for the stepped oxidation. |
| Trunov et al.[85] (2005) | Spherical (3-14μm) flakes(-325 mesh) | DSC-TGA-DTGA | Up to 1500 ºC @5-40 K/min | $O_2$ | |

Among those, Trunov et al. [33] suggested that the oxidation process of aluminum proceeded in four stepwise oxidation stages. During the oxidation of nAl, the passivation shell (product of the oxidation) goes through several intermediate metastable polymorphs according to the temperature conditions. The route for the amorphous film of alumina to the stable alpha alumina is typically shown as amorphous→ $\gamma$→($\delta$→ θ)→ α-alumina [86]. The speed of the reaction and the rate of energy release are dependent upon the mass and energy transport dictated by the porosity and permeability of the oxide shell. The whole oxidation process can be then explained according to the changing properties of the external alumina layer [87]. Rai et al. [34] found that the oxidation was due to the diffusion of species, which took place in two regimes separated by the melting temperature of the metal particle. The first regime was slow and happened before the melting whereas the second regime was fast occurring after the melting. They also found that solid particles turned hollow when the temperature was raised above 1000 $^{o}$C. Henz et al. [88] suggested that the built-in electric field in the shell enhanced the diffusion coefficient and was responsible for the rapid oxidation process. Rosenband [7] argued that the heterogeneous oxidation process was driven by the pressure, which was induced in the shell due to the density or thermal expansion coefficient differences between the molten metal and the oxide, and the oxidation proceeded through several polymorphic phase transformations. According to Rufino et al. [58] there were no apparent differences in the lattice expansion before and after the melting as the shell was not thick enough to produce the pressure in the core. The pressure induced by the transformation of alumina could be mitigated by the thickening of the ductile shell.[89] Several theories, such as the diffusion oxidation mechanism (DOM) and recently, melt dispersion mechanism (MDM), have also been proposed for the oxidation of nAl [43].

There are, however still many questions still remain unanswered. Many of these studies are related to some applications such as in combustion and explosion, and were conducted under one or a few heating rates. Comprehensive study of the oxidation mechanism, supported by elemental, structural and crystallography information, and the influence of heating rate is rare. Perhaps the most detailed work is from Dreizin's group and Eisenreich's group [32, 85] where the reported staged oxidation scenarios were supported by detailed phase transition information. However, both studies were focused on the oxidation pheneomenon only and did not contain any information about the particle ignition. No study has ever reported on the detailed charactersiation of both oxidation and igntion phenomena that are decided by the heating rate.

On the ignition study, several models have been proposed that include stress in the oxide layer model, fixed ignition temperature model and exothermic growth of oxide film model. There is however still lack of consistency in these models. The predicted ignition temperature would occur over a wide range of temperatures even for the same materials, i.e. 575 –2000 $^{o}$C for aluminum. Relative agreement has been reached for conventional large particles, and the ignition temperature tends to approach a fixed value around the melting temperature of the alumina shell. The combustion is similar to the liquid droplet combustion, obeys the $d^2$ law, and significant oxidation occurs after the melting of the outer oxide layer. There are, however, still strong debates for the ignition temperature of small particles (below a few micrometres). While some studies suggested that it was a fixed value around the melting temperature of the aluminum particles [90, 91], many others suggest that the ignition temperature is not only a material property but also depends upon the environmental variables, such as the heating rates [43, 92, 93], particle size [35], specific experimental conditions or methods employed, [94, 95] and

instruments used [94, 96, 97]. It is still debatable if the ignition of aluminum nanoparticles occurred before or after the melting temperature of aluminum.

### 3.1.1. Physical Characterisation

The morphology of the particles and size distribution before the thermal treatment are shown in **Figure 3.1**(**a-d**) and **Figure 3.2**, respectively.

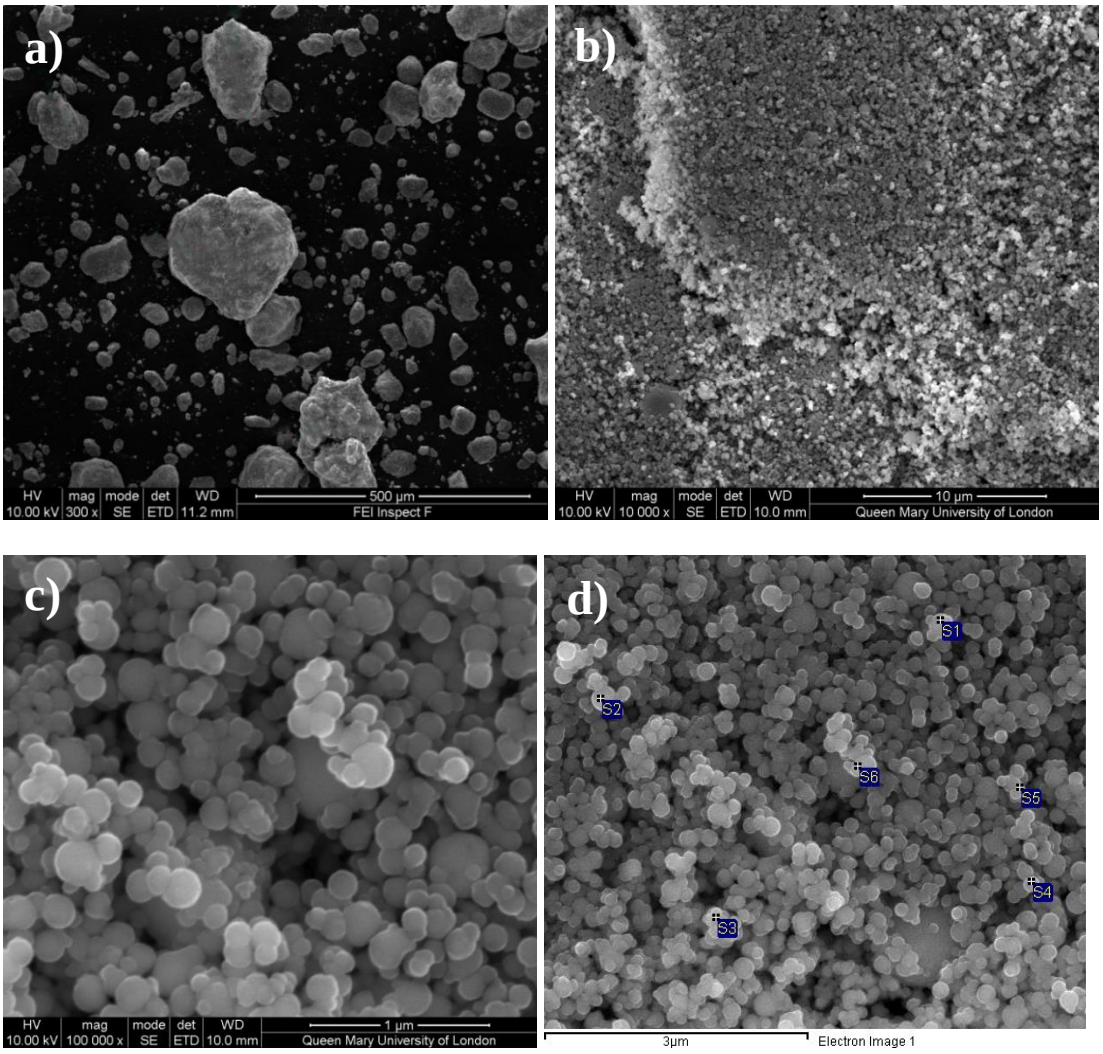


**Figure 3.1** SEM micrographs showing general morphology of the particles; a) at x300, showing soft agglomeration; b) at x10 k; c) at x100 k, showing particle are spherical and physically connected by Van der Waals forces; d) at x50 k, for micro-compositional analysis at various points

SEM image shows that particles are spherical with an average diameter of ~150 nm. The particles are loosely agglomerated.

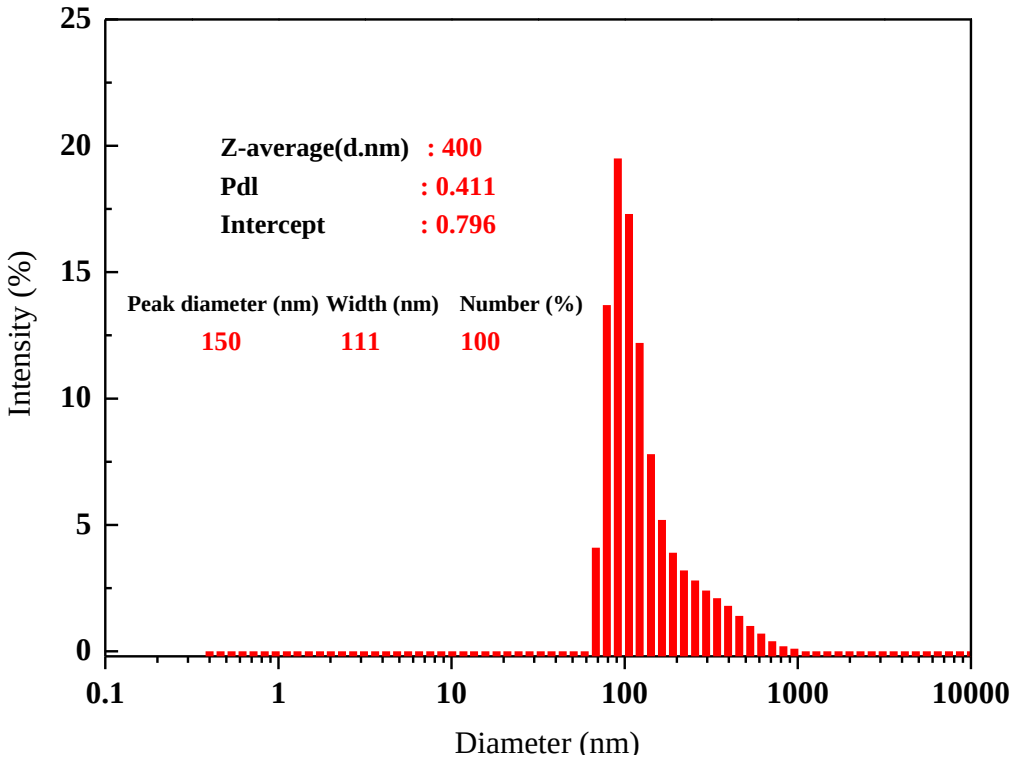


**Figure 3.2** Particle size ditribution (PSD) of nAl (before oxidation)

The particle size distribution of the nAl are measured by the dynamic light scattering (DLS) technique after dispersing the dried particles into an aqueous medium, which shows a uniform size distribution, peaking at 150 nm with a range of 111 nm with Z-average diameter of 400 nm. This average diameter is different from the observed by the electron microscope as DLS measures the hydrodynamic diameter. Though it inevitably contained some agglomerates, it would still provide useful information regarding the particle size distribution. The micro-chemical analysis (EDS) of the sample was performed to calculate the mass of the active aluminum and its surface oxide layer. For the elemental compositional analysis, various points were selected on the particles and the results showed that the sample contained 11.09 % oxygen, which corresponds to

23.57 % of $Al_2O_3$ (initial oxide) and 76.43 % of active aluminum, and presented in **Figure 3.3 .**

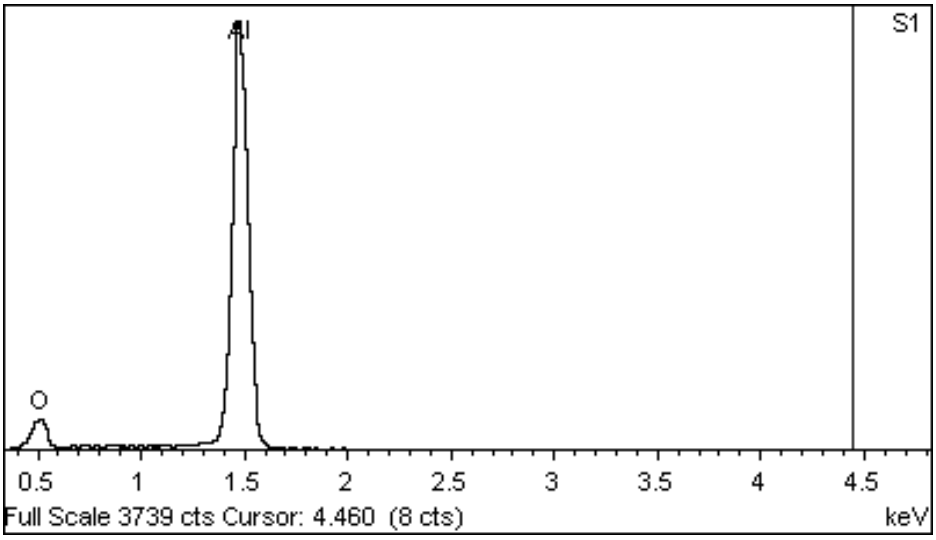


**Figure 3.3** Energy dispersive X-ray spectrometer (EDS), micro chemical compositional analysis of nAl showing relative strength of Al and O peaks

**Table 3.2** EDS analysis of nAl shown in **Figure 3.1(d)** (before oxidation)

| Spectrum | O | Al | Total |
|---|---|---|---|
| | % | % | % |
| 1 | 11.39 | 88.61 | 100.00 |
| 2 | 12.18 | 87.82 | 100.00 |
| 3 | 12.84 | 87.16 | 100.00 |
| 4 | 12.06 | 87.94 | 100.00 |
| 5 | 8.34 | 91.66 | 100.00 |
| 6 | 9.72 | 90.28 | 100.00 |
| Mean | 11.09±1.72 | 88.91 | 100.00 |

The Brunauer–Emmett–Teller (BET) model based on adsorption-desorption of nitrogen gas is used to find the specific surface area of the particles. It is assumed that the particles have uniform spherical shapes. **Figure 3.4** shows the adsorption isotherm of the nAl obtained at -196 $^{o}$C. The BET surface area of the particles is 10.48m$^2$/g and is used to find the BET equivalent diameter ($d_{BET}$) with the following relationship [98],

$$\mathbf{A_{BET} = 6/ (\rho d_{BET})} \quad (3.1)$$

$A_{BET}$ is the specific area measure by BET technique and ρ is the density of the particles (2.7 g/cc) and $d_{BET}$ is the equivalent diameter of the particles calculated as 211 nm.

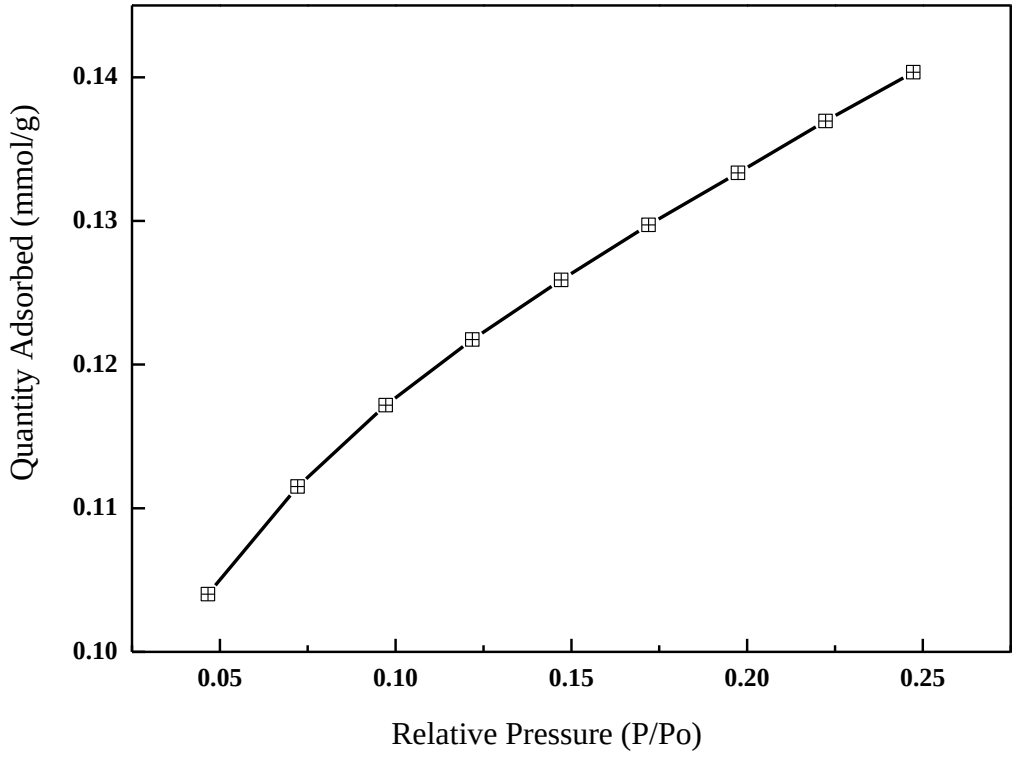


**Figure 3.4** Isotherm of the nAl showing the relationship of the relative pressure and the quantity of $N_2$ adsorbed

The chemical composition of the particles (EDS) shows the sample pure contains Al and O elements. The oxygen present in the sample indicates that the particles are passivated with alumina. The thickness of the oxide layer can be calculated by the mass balance [77] as,

$$\boldsymbol{t_{oxide} = d\left[1 - \left(\frac{\rho Al2O3C}{\rho Al + C(\rho Al2O3 - \rho Al)}\right)^{1/3}\right]} \quad (3.2)$$

Where $t_{oxide}$ is the thickness of oxide passivation layer, $d$ is the particle size including the shell thickness, $C$ is the active aluminum content, $\rho Al_2O_3$ (3.05 g/cc) and $\rho Al$ (2.7 g/cc) are the densities of amorphous alumina and aluminum respectively. From the above **Eq. 3.2** the value of the shell thickness is calculated to be ~5.1 nm which is consistent with the elemental analysis and that observed with TEM, **Figure 3.5** , and is in good agreement with the result from Rufino et al. [58].

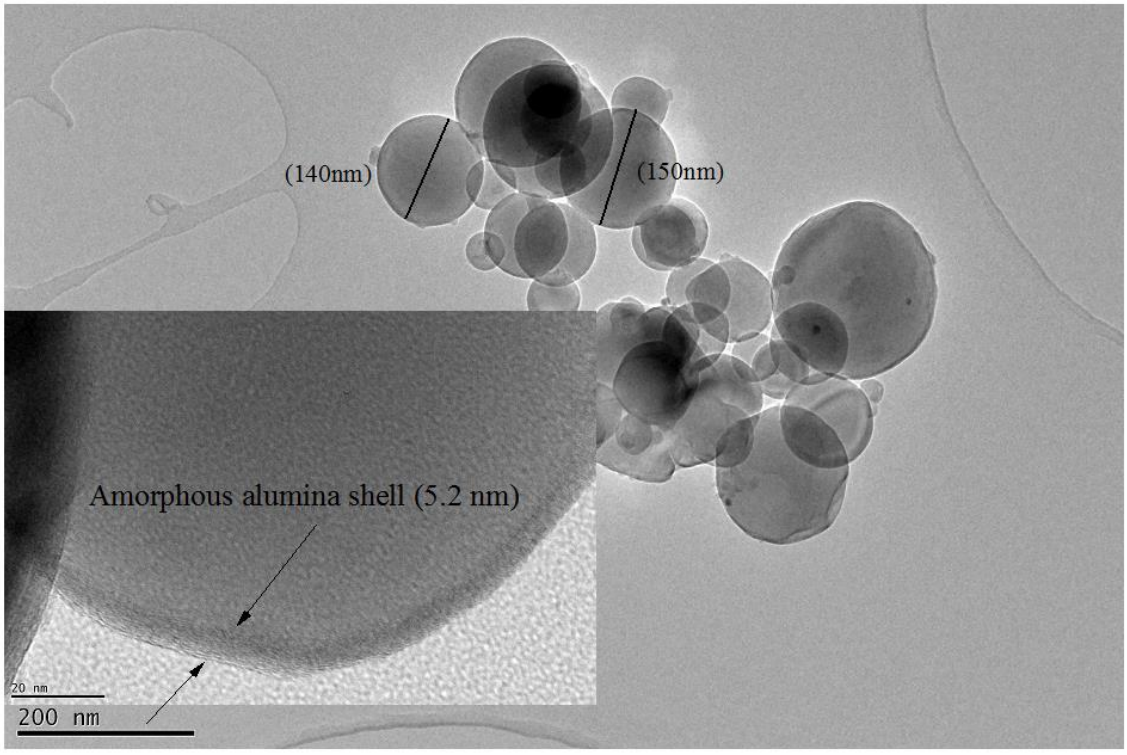


**Figure 3.5** TEM micrograph showing the amorphous alumina layer of ~ 5 nm

Crystalline structure of nAl, was found with diffraction peaks at 38.42$^{o}$ (111), 44.66 $^{o}$ (200) and 65.06 $^{o}$ (220), **Figure 3.6** . The obtained XRD trace was compared with the PDF card # 04-0787 of aluminium metal and found to be consistent with it. No peaks of Alumina are found which suggests that $Al_2O_3$ is in the amorphous state. This observation is consistent with that of the TEM. No peaks of other impurities are detected which means the nAl have high purity.

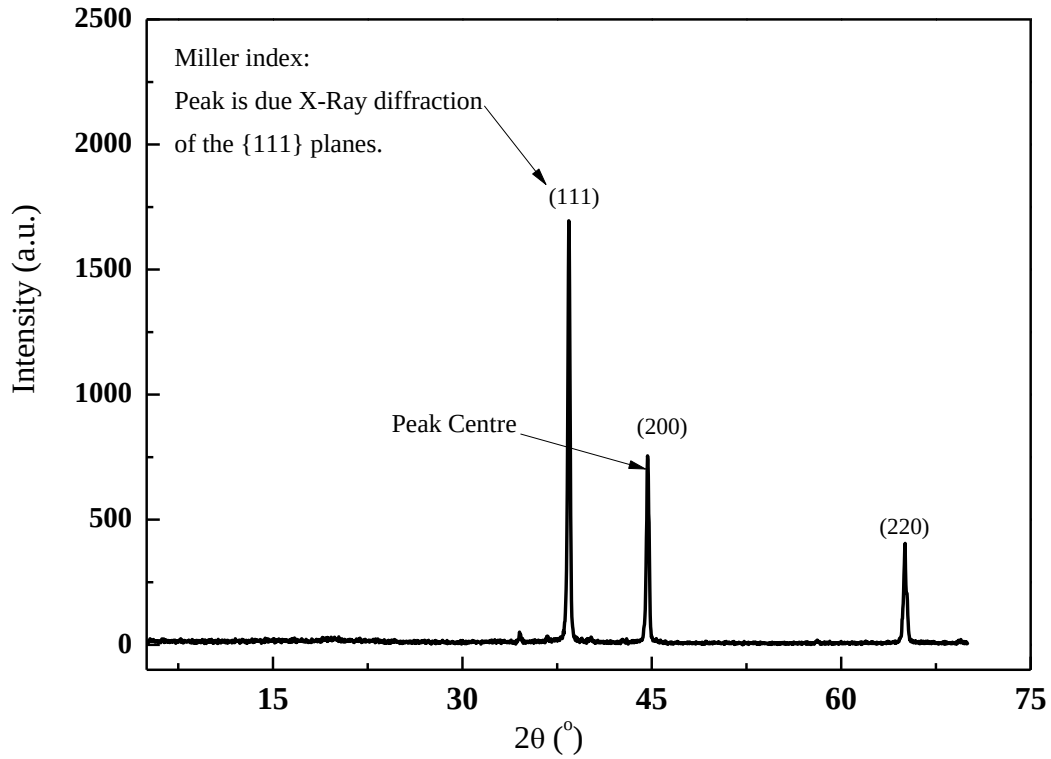


**Figure 3.6** Powder X-ray diffraction (XRD) analysis of nAl shows no peaks of $Al_2O_3$ , suggesting that it is in the amorphous state

The crystallography information was identified by XRD as the products still keep their crystalline form even after being cooled [99]. Ex-situ X-ray diffraction was performed with Siemens (D5000) diffraction meter using CuKα radiation (λ = 0.154187 nm). The average crystallite sizes of nAl were measured from X-Ray line broadening based on the

Scherer's formula ( $D_p = \frac{0.94*\lambda}{(FWHM*Cos\theta)}$) [100]. Other lattice parameters such as the distance between the planes of atoms, i.e. d-spacing, the length and intervening angle of the side, were calculated with the Bragg's Law ($d = \frac{\lambda}{(2*sin\ (\theta/2)}$) , illustrated in **Table 3.3**. To analyse various metastable polymorphs of alumina developed at various temperatures, the diffraction pattern of all recovered samples were recorded from 5$^o$ to 70$^o$ 2θ and identification of phases of all the samples are done with Jade 5 from MDI (Materials Data, Inc.,)

**Table 3.3** XRD analysis of the nAl (before oxidation, **Figure 3.6**) and estimation of crystallite size with Scherer's formula.

| Peaks | *FWHM* | | $P_c$ | | $D_p$ | *d* | *(a ,b ,c)* | *(α, β, γ)* |
|---|---|---|---|---|---|---|---|---|
| | ($^o$) | rad | ($^o$) | (rad) | nm | a$^o$ | nm | ($^o$) |
| P1 | 0.212 | 0.00370 | 38.42 | 0.3354 | 41.47 | 2.343 | 4.0586 | 90 |
| P2 | 0.247 | 0.00430 | 44.66 | 0.3899 | 36.41 | 2.029 | 4.0586 | 90 |
| P3 | 0.279 | 0.00486 | 65.06 | 0.5680 | 35.35 | 1.434 | 4.0553 | 90 |

Note:

P1, P2, P3 are the 1st, 2nd and 3rd peaks on XRD curve,

FWHM is Full width half maximum and is found with Origin software,

*P*c is centre of the peak on XRD trace,

$D_p$ is size of the crystallites,

*d* is the distance (in angstroms) among the planes of atoms found with the Bragg's Law,

*(a, b, c)* are the lengths of the planes,

*(α, β, γ)* are the angles among the planes.

### 3.1.2. Thermal Characterisation

Thermal characterization of the nAl was done with the simultaneous thermal analysis (STA). During the experiment, the flow of heat from and to the samples, and the corresponding mass change are recorded simultaneously until the complete oxidation curves are obtained.

Very interesting results were obtained regarding the effect of the heating rate. The experiments fall into two distinct types: low heating rate ($\beta$ = 2-7 K/min) and high heat rate ($\beta \geq 8$ K/min). For the low heating rate, the oxidation process completes without any sudden change of heat or mass. For the high heating rate, there is a sudden increase of mass and heat flow due to the early ignition. Both oxidation types have some distinctive features and are explained separately, below.

### 3.1.3. Sample TGA/DSC curve at low heating rate (no ignition)

Simultaneous curve of TGA/DSC of nAl at heating rate of 2-7 K/min shows similar characteristics and a heating rate of 5 K/min is selected as an example.

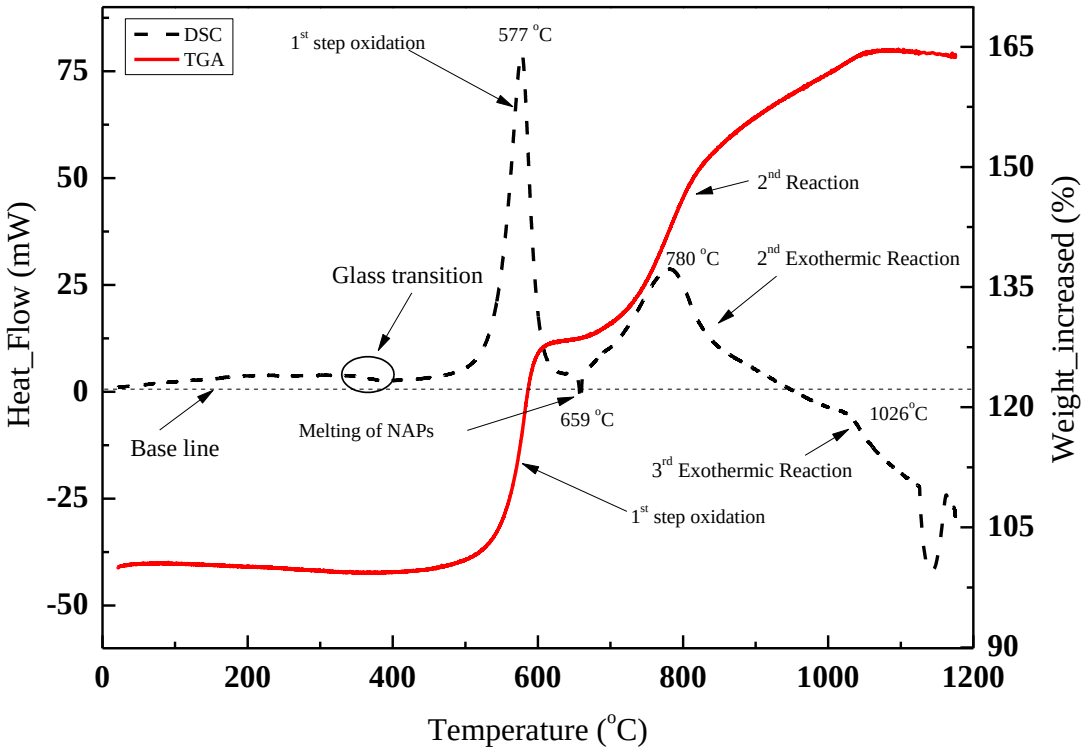


**Figure 3.7** Example of TGA / DSC curve under low heating rate (no ignition)

**Figure 3.7** shows that the whole oxidation process completes in three stages, one before and two after the melting of the particles. With the start of thermal treatment, the heat flow is continuously increasing, albeit at a small magnitude, until it reaches around 380 $^{o}$C. The heat flux dips in the 400 $^{o}$C region that is associated with the glass transition, where the amorphous alumina begins to crystallize and the shrinkage of the shell is started [101]. The weight of the sample is decreased by ~ 1 % when it reaches at 400 $^{o}$C. This decrease of weight is due to the thermal decomposition of the sample above 100 $^{o}$C. This could be due to the loss of moisture (dehydration), at about 100 $^{o}$C, or the loss of adsorbed $CO/CO_2$, at relatively higher temperatures. There are possibilities that the amorphous alumina layer, being hydrophilic, have some water ions attached to it and are lost at this temperature range [102]. The extrapolated onset temperature for this first stage reaction is 487 $^{o}$C. The slow oxidation process starts even earlier than the onset temperature that thickens the amorphous passivation alumina shell. The initial oxidation

process is similar to the work of Trunov [103] but with additional features at the high temperature, as analysed below.

The first stage oxidation process peaks at 577.7 $^{o}$C and occurs in the temperature range of 500-620 $^{o}$C. It is characterized with a considerable mass change of ~27 % and a heat release of 5.64 kJ/g. The chemical reaction can be expressed as

$$\boldsymbol{4Al + 3O_2 \rightarrow 2Al_2O_3} \tag{3.3}$$

This reaction is taking place before the melting process in a heterogeneous process. The 1$^{st}$ derivative of thermo-gravimetric analysis (DTGA) and 1$^{st}$ derivative of differential scanning calorimeter (DDSC) were also computed to locate the temperatures where the rate of change of mass ($T_{01}$=$\left(\frac{dm}{dT}\right) max1$ =579.5 $^{o}$C) or the rate of heat released ($T_{01}$=$\left(\frac{dh}{dT}\right) max1 = 567$ $^{o}$C) is the maximum, which are slightly different from the peak temperature ($T_{pexo1}$ = 577.7 $^{o}$C). DTGA and DDSC traces are shown in **Figure 3.8** and **Figure 3.9**.

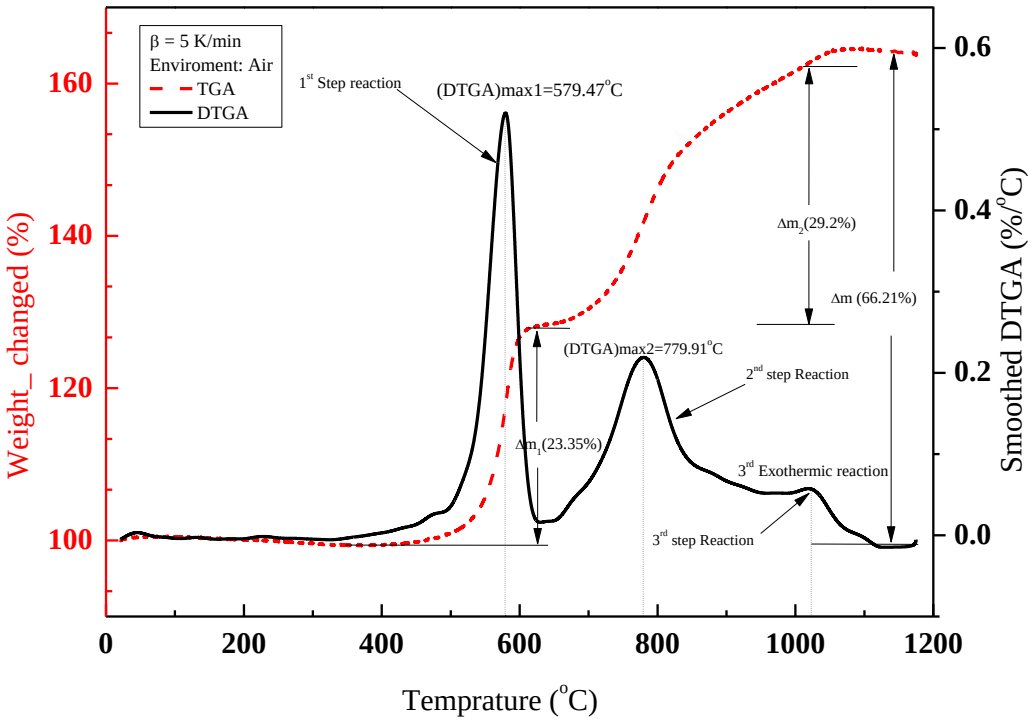


**Figure 3.8** DTGA of nAl at β =5 K/min shows different steps of reactions and amount of weight changed

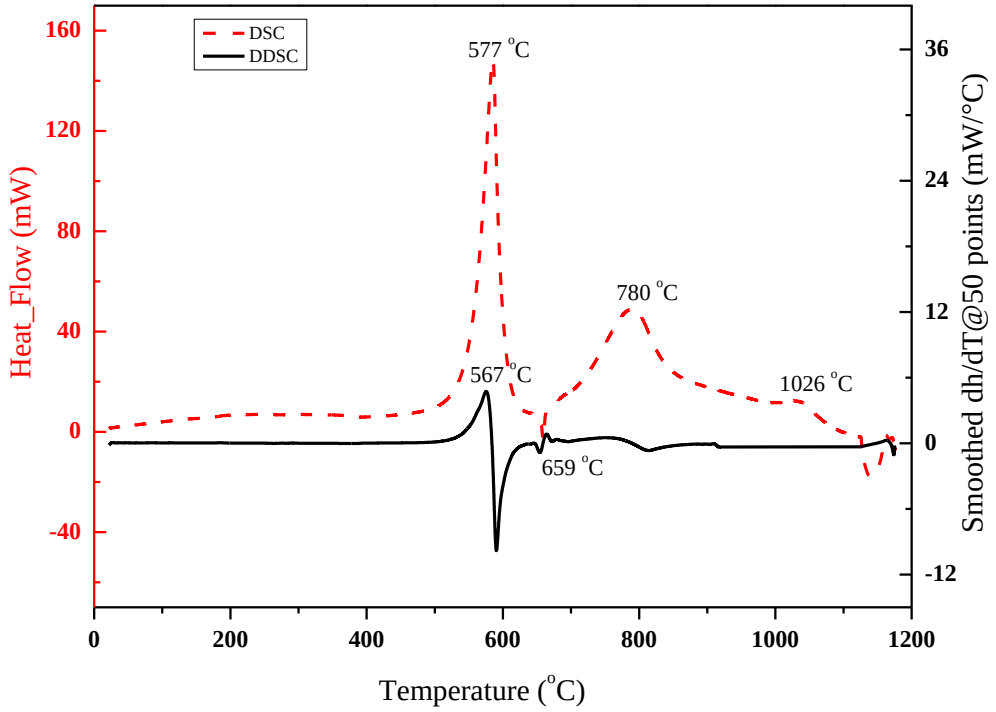


**Figure 3.9** DDSC of nAl at β =5 K/min shows different steps of reactions

After attaining the rapid weight increase, the rate of the reaction decreases and the reaction goes towards an endothermic process, which starts at ~649 $^{o}$C, peaks at ~659 $^{o}$C and completes at 662 $^{o}$C. This endothermic process can be attributed to the melting of the remaining nAl. For the particles over 100 nanometer, the melting depression phenomenon is not obvious. The melting temperature ~660 $^{o}$C is similar to that of the bulk aluminum and other observations, Mei et al. [104] After the melting of the aluminum core, the second stage oxidation occurs in the temperature span of 665-900 $^{o}$C. During this stage, the metal core is in molten state and the mobility of its molecules increases. This diffusion based exothermic reaction is characterized by the movement of both metal cations and oxygen anions towards each other. It is also known that at higher temperatures, e.g. > 500 $^{o}$C, nitrogen may react with aluminum, but the XRD results did not detect any peak related to the formation of AlN compound. This, however, still cannot exclude the possibility that traces of AlN would be formed during the oxidation experiments as the activation energy to form AlN at high temperatures was not significantly higher than the formation of $Al_2O_3$, i.e. the range of 200-230 kJ/mol [60]. If AlN was indeed formed in the experiments, it is assumed that the aluminum nitride could be re-oxidized to $Al_2O_3$. The likely reactions that were taking place could be the combination of the following reactions [60],

$$\mathbf{2Al + N_2 \rightarrow 2AlN} \tag{3.4}$$

$$\mathbf{4AlN + 3O_2 \rightarrow 2N_2 + 2Al_2O_3} \tag{3.5}$$

The weight increases during the second stage is ~27.5 % and the heat released is 5 kJ/g. The exothermic reaction peaks at 782.8 $^{o}$C after which the rate of reaction decreases. The third stage oxidation is observed after 900 $^{o}$C. It becomes clear that~ 1000 $^{o}$C, the heat flow of the reaction increases once again suggesting a third exothermic reaction.

After this reaction, there are no changes in TGA/DSC curves, which indicate that the reaction is completed. The cumulative TGA and DSC curves are consistent with one another for heating rates of 2-7 K/min and shown in **Figure 3.10** and **Figure 3.11 .**

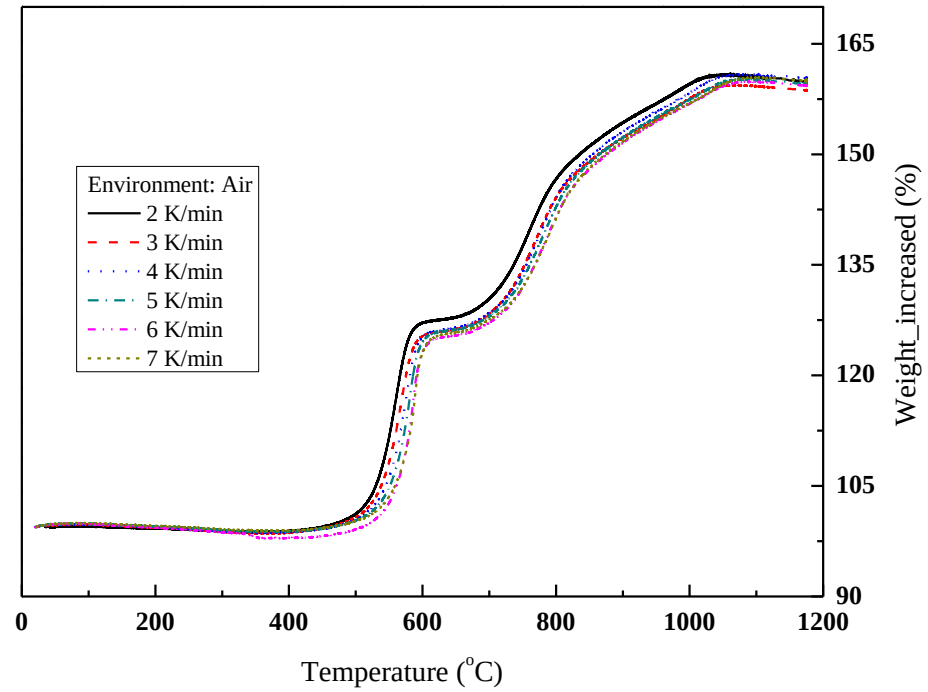


**Figure 3.10** Cumulative TGA trace of nAl at the heating rates of 2-7 K/min

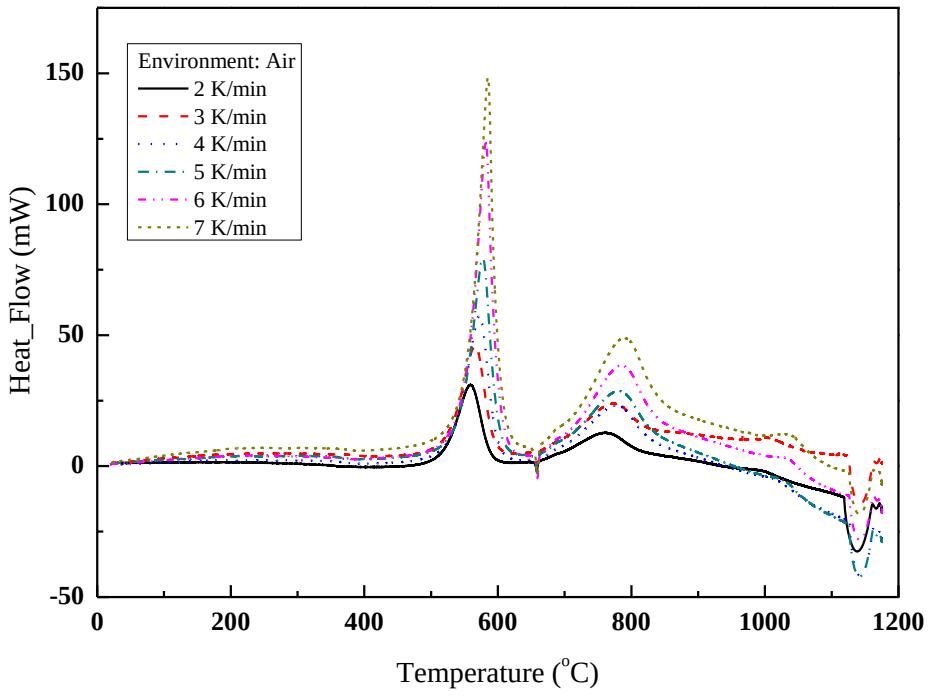


**Figure 3.11** Cumulative DSC curve of nAl at the heating rates of 2-7 K/min.

The slight drop of heat in the end of DSC diagram (**Figure 3.11**) is showing that the reaction is ending. It does not show any physiochemical reaction. These three oxidation stages can be observed by taking first derivatives of TGA/DSC. The example curves are shown in **Figure 3.12** and **Figure 3.13**

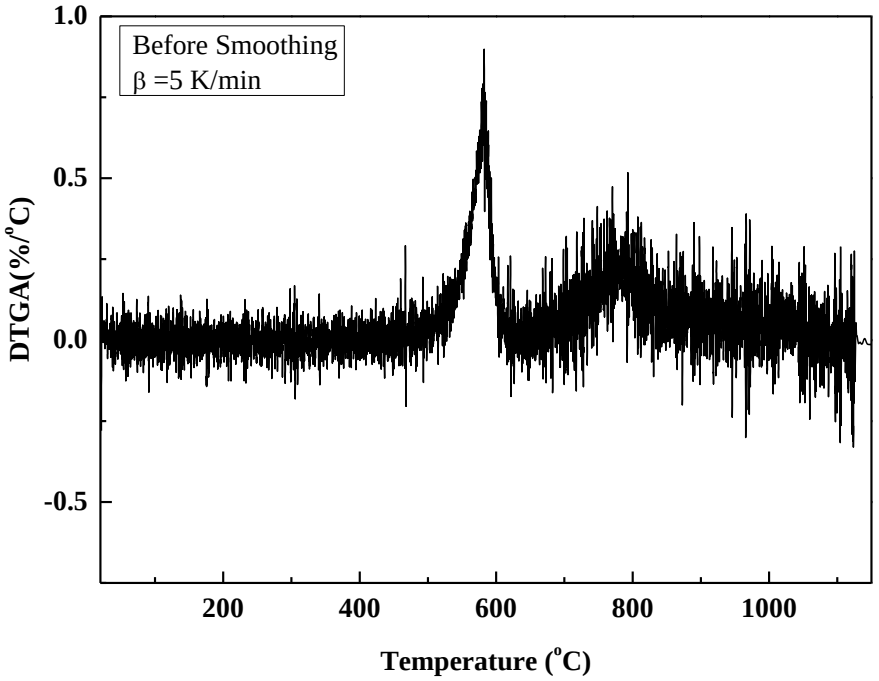


**Figure 3.12** DTGA of nAl particles at 5 K/min (raw data, no smoothing)

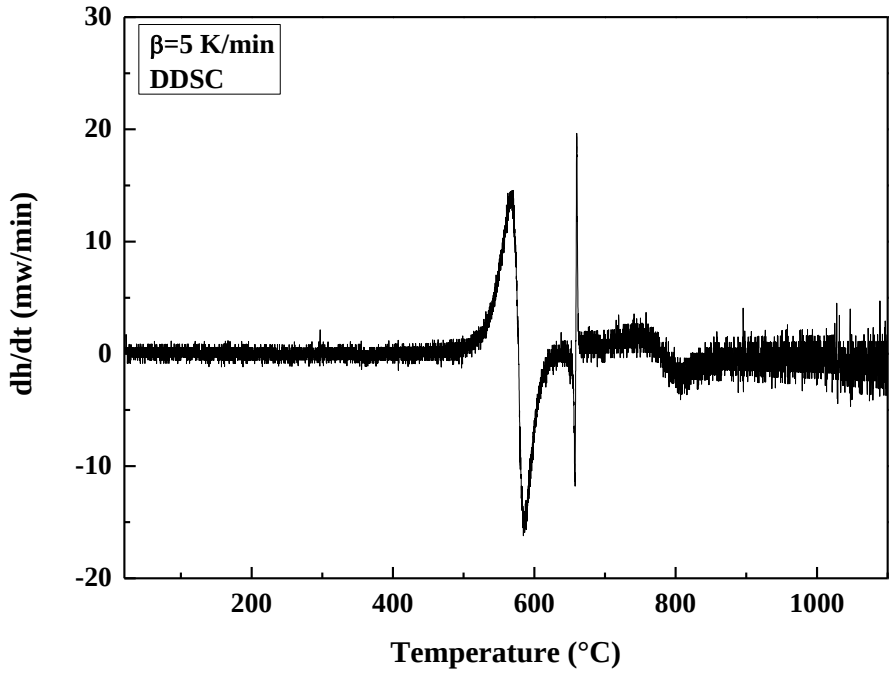


**Figure 3.13** DDSC of nAl particles at 5 K/min (raw data, no smoothing)

For clarity, the curves are smoothed by reducing the noise by employing the Fast Fourier Transformation (FFT) using 250 data points and shown in **Figure 3.14** and **Figure 3.15**.

.

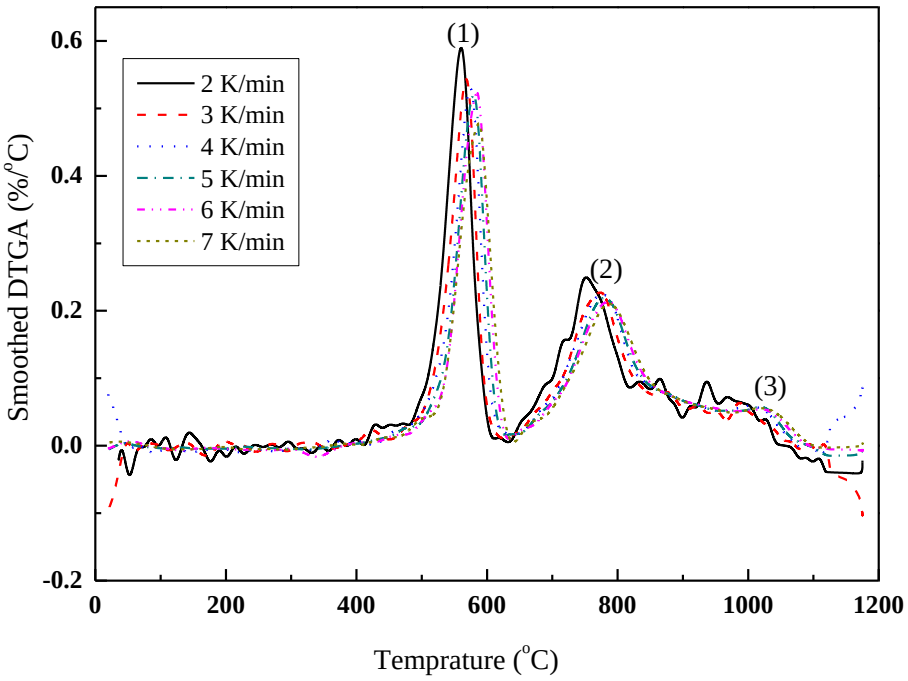


**Figure 3.14** DTGA of nAl particles at various heating rates (smoothed)

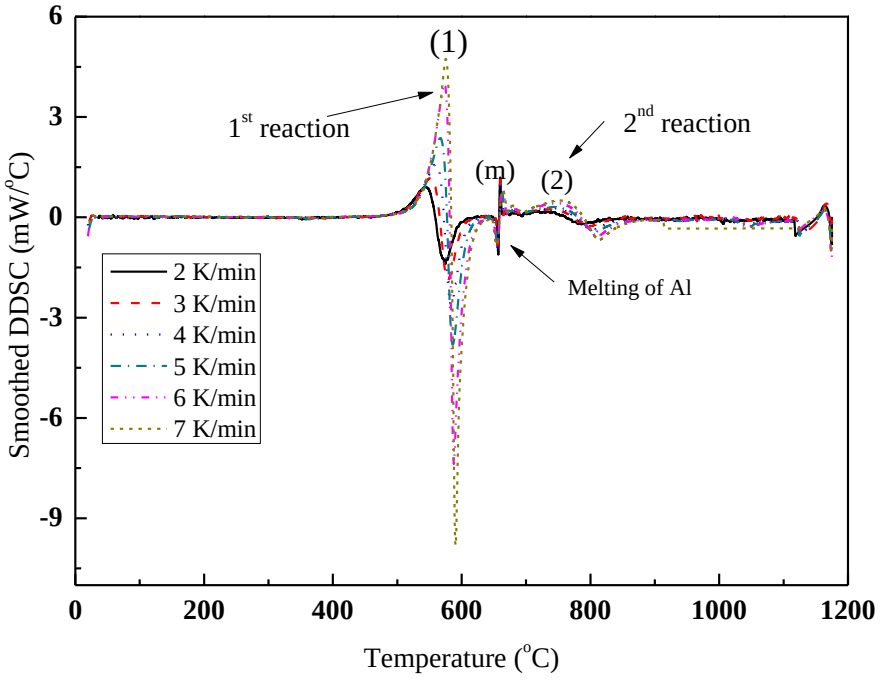


**Figure 3.15** DDSC trace of nAl particles at various heating rates (smoothed)

Theoretically, the weight increase for the complete oxidation of pure aluminum is 88 % but only 65.5 % of weight increase is obtained in this case. This reduced amount of the product is because of the initial amorphous shell of alumina ($Al_2O_3$). Through the elemental compositional analysis (EDS) it is found that 11 % of oxygen is present in the sample that corresponds to 23% of $Al_2O_3$ and 77% of active aluminum. The estimated alumina thickness is ~ 5 nm, which is in the right region as reported by other studies [58]. The value of the weight increment (65.5%) is nearly the same as that from the oxidation of active aluminum contents of the sample (68% increase). Similar oxidation scenario is observed for heating rates of 2-7 K/min. The diffractograms of the particles under these conditions are shown in **Figure 3.16**.

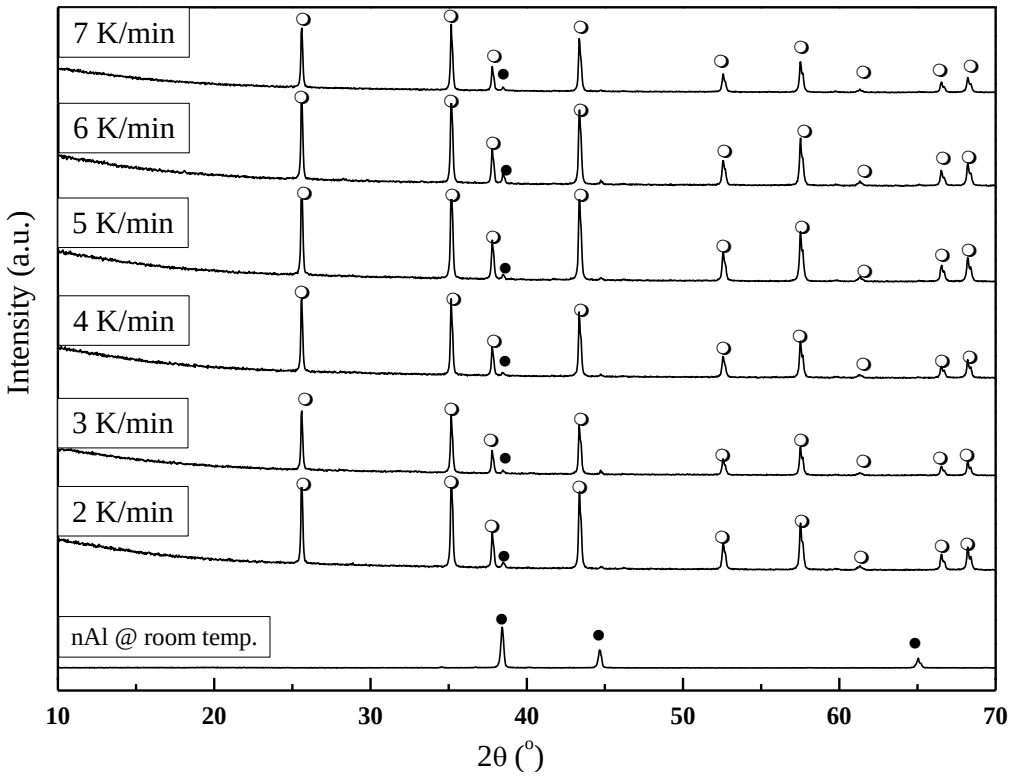


**Figure 3.16** XRD analyses of nAl after their heat treatment at the heating rates of 2-7 K/min (no ignition) (solid dot = Al and hollow dot = α-$Al_2O_3$)

### 3.1.4. Sample TGA/DSC curve at high heating rate (with ignition)

The exothermic heat release during the first step oxidation reaction increases with the increases of the heating rate. As the heating rate becomes ≥8 K/min, the large amount of heat released becomes far more than that can be absorbed by the purge gases, which results in a rapid increase in the particle temperature. Consequently the slope of heating rate (dT/dt) is shifted to a high value for a short interval of time and the temperature of the sample becomes even higher than that of the furnace. The sample undergoes a fast reaction with a sharp increase in the weight and a rapid release of heat in a very short period of time. This temperature run away process is regarded as the ignition point and is due to the self-heating of the particles [105, 106]. The simultaneous TGA/DSC curve at 10 K/min is taken as an example to illustrate its characterization, **Figure 3.17**.

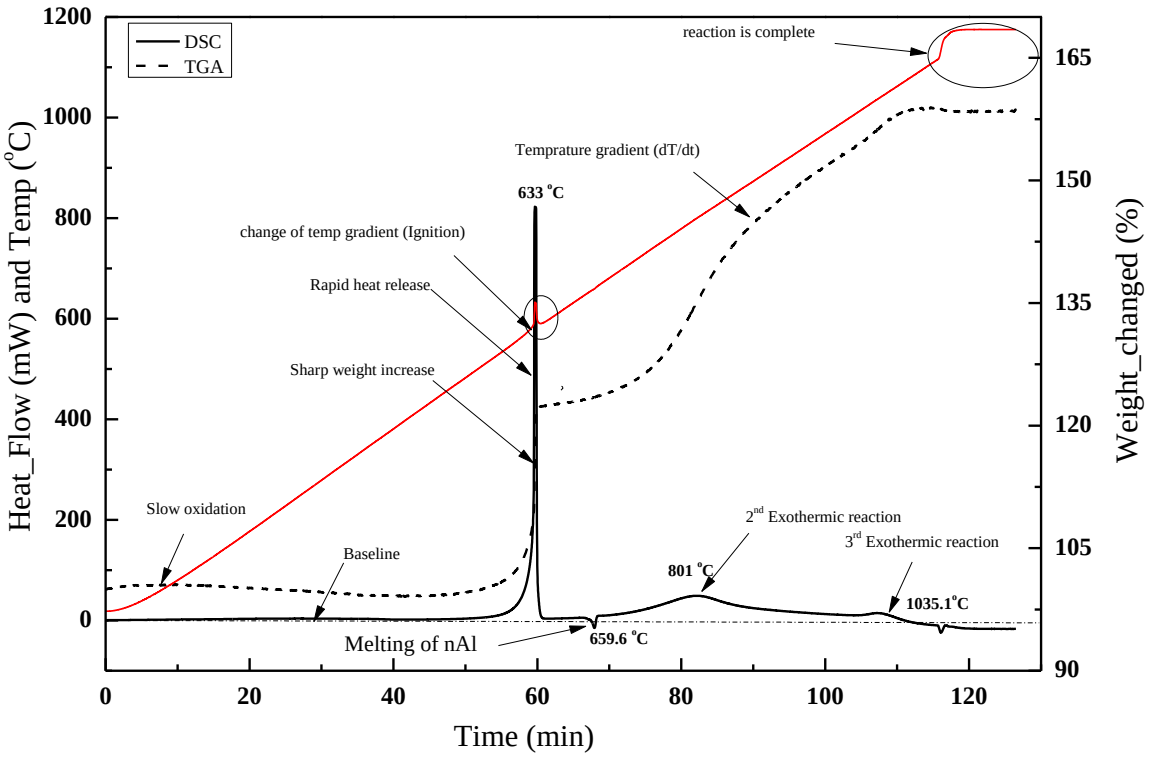


**Figure 3.17** Example of TGA / DSC curve under high heating rate (with ignition).

The initial oxidation process, similar to the previous example i.e. at 5 K/min, starts at a slow pace, which is due to the slow diffusion of oxygen molecules from the amorphous layer of alumina. This increases the thickness of the pre-existing shell of amorphous alumina. The sample lost ~1% of the mass due to the physiochemical processes such as dehydration of water and dehydroxylation of aluminol groups presenting in the hygrophilic layer of alumina [102]. The first non-baseline signal is produced at 460 $^{o}$C which can be regarded as the onset temperature. The first oxidation reaction happened within a very short span of temperature (525-591 $^{o}$C). This reaction is characterized by a sharp weight increase (23.25 %) with a rapid rate of heat release (5.6 kJ/g). The particle temperature becomes more than that of the furnace. This temperature run away process is due to the ignition reaction caused by the self-heating of the particles. It shall be noted that such an ignition would not cause a global combustion event of the sample, but to accelerate the following oxidation process. Such a process occurs before the registered melting temperature of the aluminum core.

To understand this process, separate experiments were conducted where the oxidation experiment was discontinued at 525 $^{o}$C (before the ignition point) and 630 $^{o}$C (after the ignition point) and analysed by the XRD. The radiograph at 525 $^{o}$C shows no peak other than the metallic Al, **Figure 3.18**, but on the thermograph, the mass of the sample has increased. This suggests that there must have some growth of amorphous layer of alumina before the first stage reaction. The XRD at 630 $^{o}$C shows that the aluminum has been transformed into a number of polymorphs including θ-alumina due to this fast reaction.

Such a co-existence of polymorphs under low temperature is unexpected and different to the observation from Trunov et al. [35] where a continuous transition of the phase from amorphous→$\gamma$→($\delta$→$\theta$)→$\alpha$–alumina was reported with the increase of the temperature, which is thermodynamically favourable. This is true only for the low heating rates. It is believed that at the high heating rate, the ignition, which leads to a partial particle combustion, is responsible for the co-existing of different phases, initiating at low temperature (before melting) and spanning over a wide range of temperature.

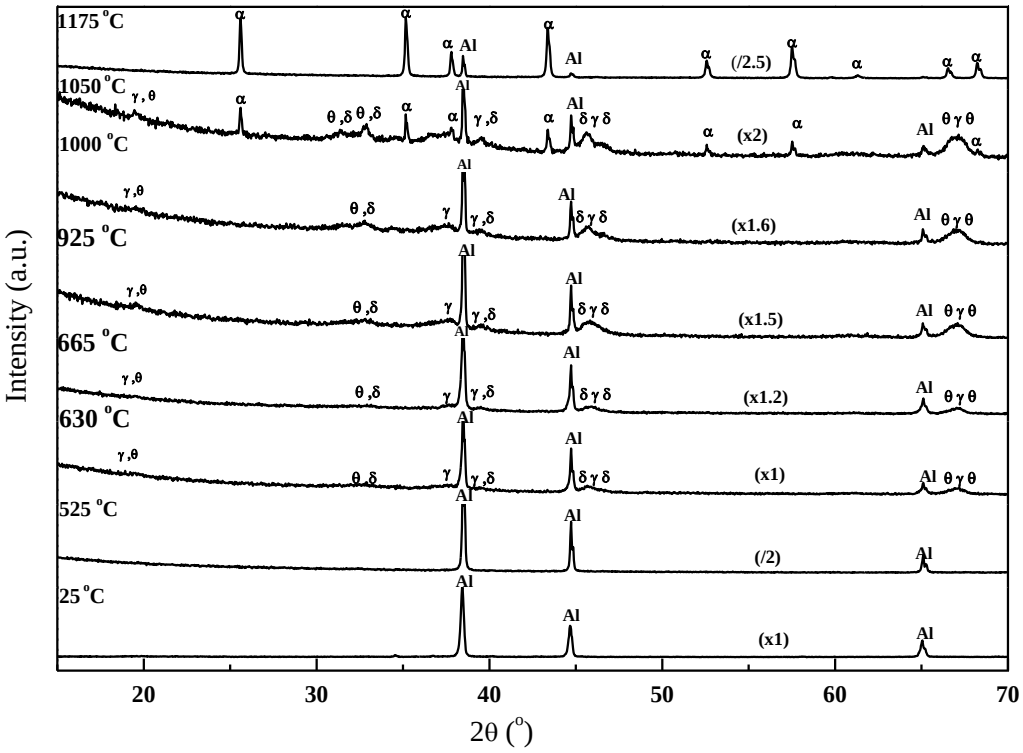


**Figure 3.18** Ex-situ XRD analysis shows that the various polymorphs of alumina coexisted and transformed from one state to the other state at different temperature ranges

According to Rosenband [7], the ignition was initiated by the melting of nAl. Due to the melting, the volume of the core would increase by 6 %, which creates some pressure on

the shell of the alumina, increasing the porosity (or producing some cracks in certain local locations) of the shell that leads to the ignition. It is clearly shown that in our experiments, the ignition happens before the melting temperature as recorded by the TGA device. However it shall be cautious to interpret this temperature. The TGA measures the pan's temperature, which will have some difference to the real temperature of the heated particle. It is possible that at the registered ignition temperature (i.e., 592 $^{o}$C for 10 K/min), the temperature of the particle is higher than that of the melting temperature. The active aluminum part might be in a molten stage contained by the solid oxide layer. The transition to melting would still play a role for the observed ignition event. Different to what was proposed by Rosenband [7] , this ignition does not lead to a sustained burning event. On the other hand, the phase transformation should also be considered. As analysed earlier, the growth of amorphous alumina and its transformation to gamma happened simultaneously. The density differences (i.e., $\gamma$-alumina has higher density than that of the amorphous alumina) would also cause the discontinuities in the shell that increases the porosity of the shell. This in turn would decrease the diffusion resistance of oxygen and accelerates the diffusion of oxygen towards the core, which leads to the rapid oxidation i.e. ignition. During this phase transition process, the particle is still in the solid phase and such a reaction could not lead to a self-sustaining combustion. The reaction would lead to the formation of one of the polymorphs with simultaneous transition into other phases, which subsequently would seal the cracks / high porous shell produced during the first stage transition. Our XRD result, **Figure 3.18** which shows the co-existence of $\gamma$, $\delta$, θ-alumina (after the ignition temperature and before the registered melting temperature of the aluminum core), also supports our hypothesis above. As the oxidation continues, less active mass of aluminum becomes available for the ongoing reaction and less the discontinuities are

left. This would increase the diffusion resistance of the oxygen and subsequently slows down the reaction. After this reaction, the particles go through an endothermic process i.e. melting, which starts at 647 $^{o}$C, peaks at 659.5 $^{o}$C and completes at 665 $^{o}$C.

It still cannot be ascertain which mechanism is responsible for the early ignition phenomenon at this stage. The lack of accurate particle temperature measurement is the major reason. However the phase transition process, as analysed above, shall be carefully considered. The likely reason for the early ignition would be a combination of both particle melting and phase transition of the oxide layer, and the exact reason require some further studies.

After the melting process the particles go through second step oxidation reaction with a temperature span of 683-993 $^{o}$C. This is wider as compared to that of the first reaction. The sample gained 29.2 % of the weight and 4.9 kJ/g of the heat produced during the reaction. Again to understand the phase transition process, separated experiments were conducted where the oxidation tests were terminated at a number of characteristic temperatures, i.e., 665, 925 and 1000 $^{o}$C, and the sample were then analysed with the XRD, **Figure 3.18**. It is found that there is no change in the polymorphs, which suggests that the growth/transition of polymorphs is going on. After attaining the peak at 801 $^{o}$C the reaction is slowed until ~1000 $^{o}$C.

The third exothermic reaction is observed at high temperature with span of reaction (1010-1050 $^{o}$C). Only 3 % of the weight changed, with 94 J/g of heat produced, is observed during this reaction. XRD trace at 1050 $^{o}$C shows that the peak of α-alumina is also present, **Figure 3.18.** As the density of α-alumina (4.05 g/cc) is higher comparing

to that of $\gamma$, $\delta$, θ-alumina (3.58, 3.6, 3.65 g/cc), the shell once again contracts and breaks the continuity and which consequently, increases the porosity of the shell. The reaction completes at 1175 $^{o}$C, evidenced by the horizontal line of the TGA curve. XRD at 1175 $^{o}$C (after the whole thermal treatment process) shows that all the polymorphs have been transferred to α-alumina. Traces of un-reacted aluminum are also seen in the sample. All the DSC and TGA curves for heating rates between 8–30 K/min are shown in **Figure 3.19** and **Figure 3.20,** respectively.

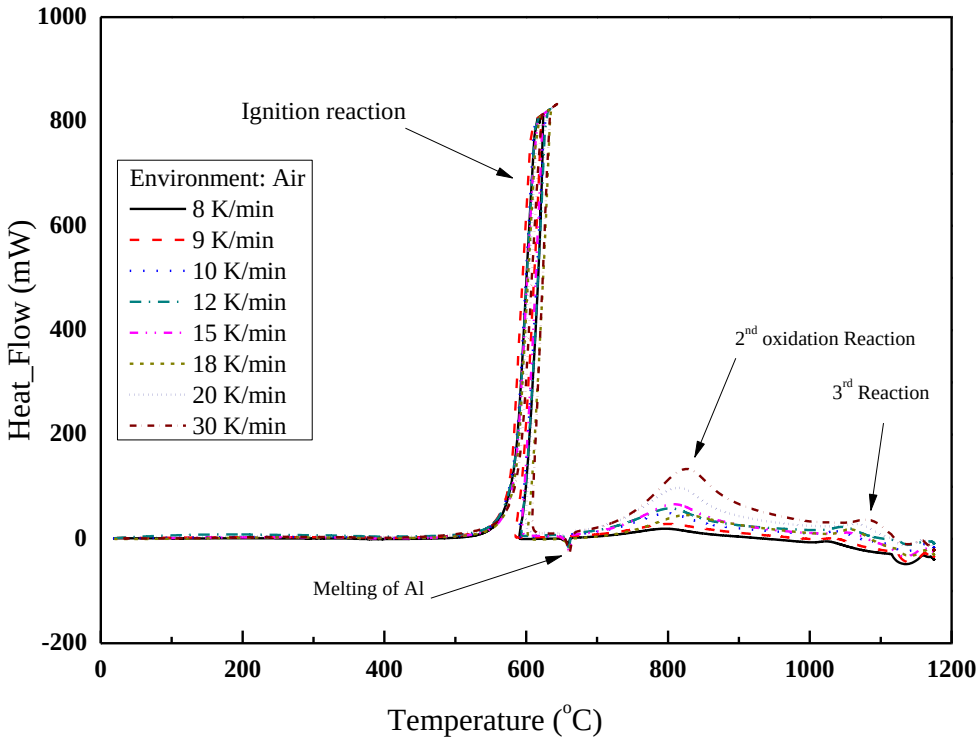


**Figure 3.19** All DSC trace of nAl particles at high heating rates (ignition)

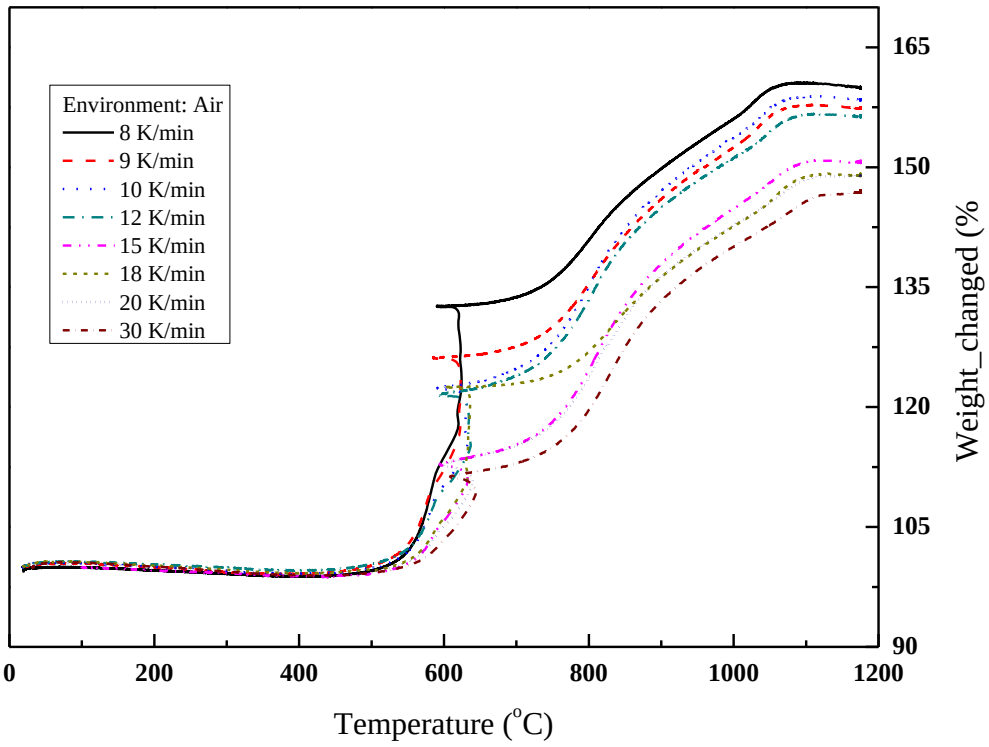


**Figure 3.20** All TGA trace of nAl particles at high heating rates (ignition)

The XRD trace of the particles under these conditions are shown in **Figure 3.21**.

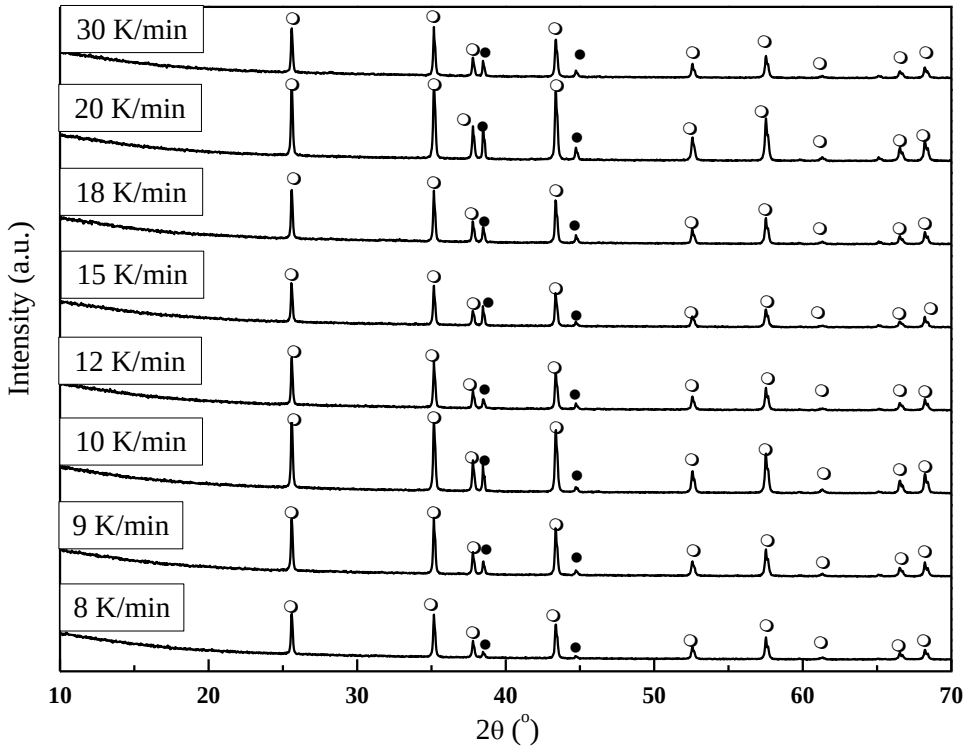


**Figure 3.21** XRD analyses of nAl after their heat treatment at the heating rates of 8-30 K/min ( ignition); shows the rise of the intensity peak of the Al metal with the heating rate (solid dot = Al and hollow dot = α-Al2O3)

### 3.1.5. Effect of Heating Rates

#### 3.1.5.1. Ignition temperature and peak heat values

It is worth noting that, in the first oxidation step, the peak values of the heat flux changes with the heating rate in a monotonous way, i.e., it increases from 31 mW at 2 K/min to 148 mW at 7 K/min, **Figure 3.22.**

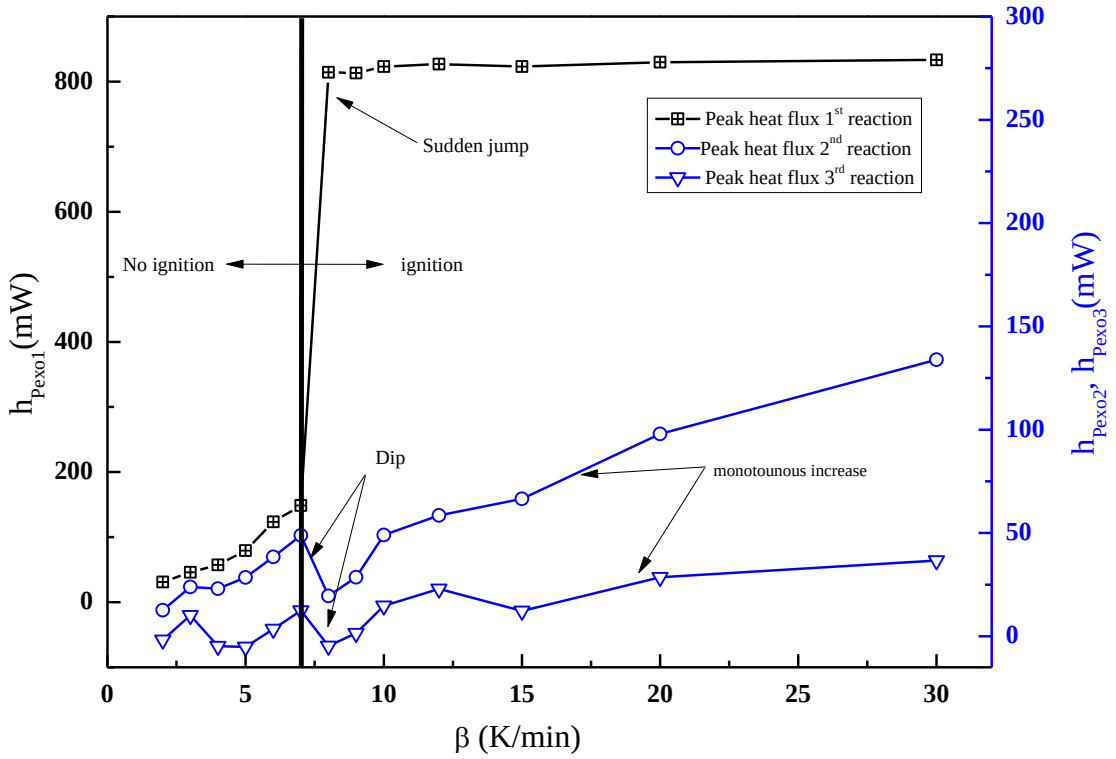


**Figure 3.22** Peak heat flux values of three exothermic reactions show the sudden jump during the first reaction when heating rate is increased to 8 K/min, peak heat values of 2nd and 3rd reactions increase monotonously, after a dip, just after the ignition criteria was met.

However as the ignition reaction is observed, a sudden jump in its values is observed. The heat release rate remains a similar value and is in the region of 800 mW for all heating rates above 8 K/min. This suggests that the ignition event is similar under all

these heating rates, and releases similar amount of heat. The peak heat flux values of the 2nd and 3rd exothermic reactions also change with the heating rate but the trend is different to the 1st reaction shown in **Figure 3.22.** There is a decrease of the heat release as the ignition happened. For instance, the peak heat value of the 2nd exothermic reaction at 2 K/min is 12.7 mW and increases to 45.9 mW at 7 K/min. The peak heat value decreases to 19.52 mW when the ignition happens at 8 K/min, and then increases monotonically, reaching 134 mW at 30 K/min.

The ignition temperature can be identified by both the TGA and DSC curve, i.e., defined by $T_{igTGA}$ and $T_{igDSC}$. These values are obtained by the 2nd derivative of TGA and DSC curves, respectively. The difference for the ignition temperature calculated by these two methods is in the range of ~ 1 K and the average value, $T_{igAvg}$ is used as the ignition temperature. The ignition temperature clearly shows some dependence with the heating rate. There is a general trend of the increase of ignition temperature with the increase of heating rate, **Figure 3.23.**

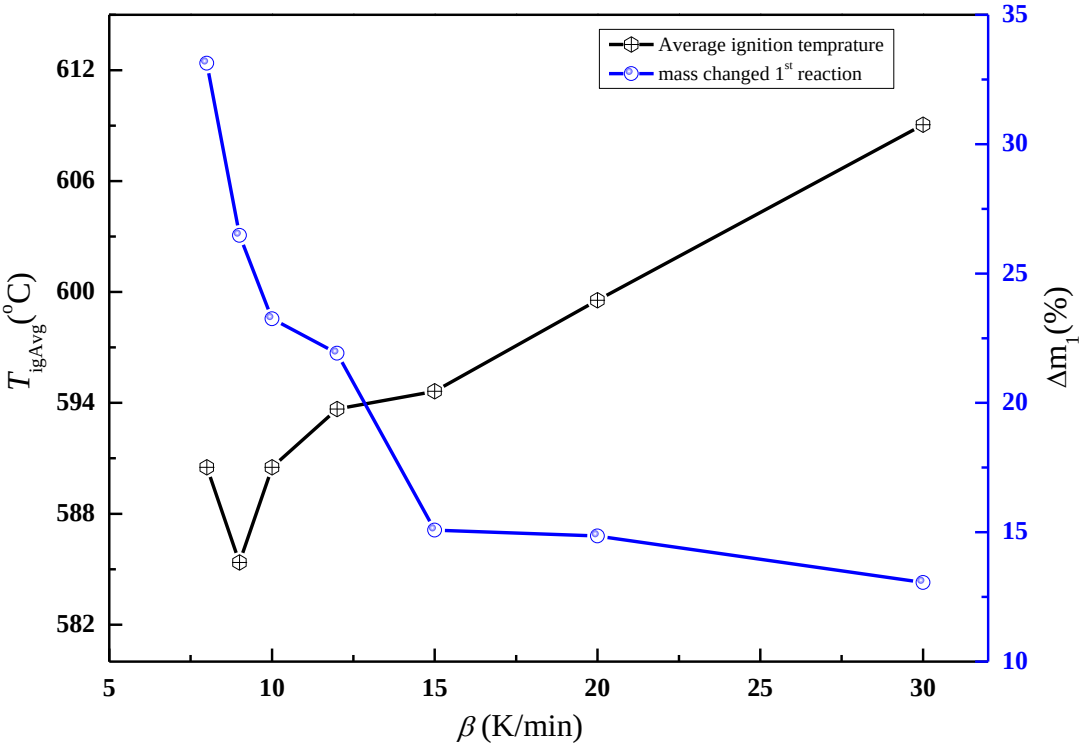


**Figure 3.23** Average ignition temperature values increase with the heating rate

For example, the ignition temperature is 585 $^{o}$C at 9 K/min and increases to 609 $^{o}$C at 30 K/min. Such an observation is different to the studies [90, 91], where it was reported that the ignition temperature of aluminum nanoparticle was a constant value, around the melting temperature of the core. However our study shows a good agreement with a few other studies [95], which shows that the ignition temperature is not a material property, but depends on the operational conditions. For instance, the ignition temperature of Ni/Al pellet (4 μm Al, 800 nm Ni) was found to be 550 $^{o}$C at a heating rate of 0.5 K/min and the value increase to 620 $^{o}$C at a heating rate of 40 K/min [11]. Though not for the same reaction, such a comparison did suggest that the ignition can occur well before the melting temperature of the aluminum. For ignition to occur at low temperature and low heating rates, a few conditions need to be met, which may include 1) the thickening and subsequent breaking of amorphous alumina shell 2) sufficient amount of reactive metals is available 3) the diffusion of oxidant gas through the protective layer of alumina and 4) the amount of heat released is much higher than the amount of heat removed through the sample pan.

For lower heating rates i.e. 2 K/min the nAl melt at 658.7 $\pm$ 0.3 $^{o}$C whereas in the case of ignition, they melted at 659.9 $\pm$ 0.6 $^{o}$C, so heating rate has a little effect on the melting temperature, **Figure 3.24**.

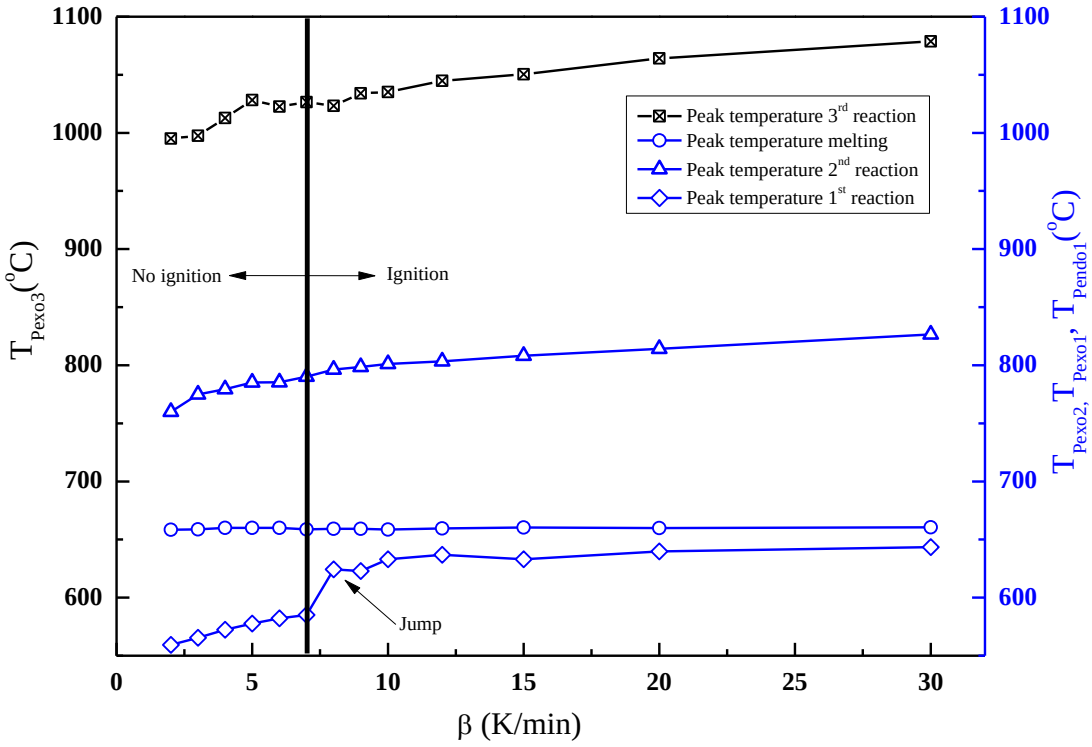


**Figure 3.24** The peak temperatures values for 2nd and 3rd reaction increases with heating rate monotonously. The peak temperature values of melting remains same. During the 1st reaction, there is a jump in its values when the ignition is observed.

### 3.1.5.2. Characteristics of Different Oxidation Stages

Here we will use the total weight change to characterize the three-stage oxidation process, and reveal the influence of heating rate and the ignition. For the first stage oxidation reaction, the mass changed is decreasing with the increase of heating rate, **Figure 3.25**. For instance, an increase of 28 % of the sample weight is observed for β = 8 K/min and only 13.06 % mass increase is observed at 30 K/min. One possible explanation to the trend of mass decrease can be given that the reaction is kinetically controlled. With the increase of heating rate, the available time to the sample decreases and consequently, less time is available for the sample to react with air, resulting lower weight increase at higher heating rates.

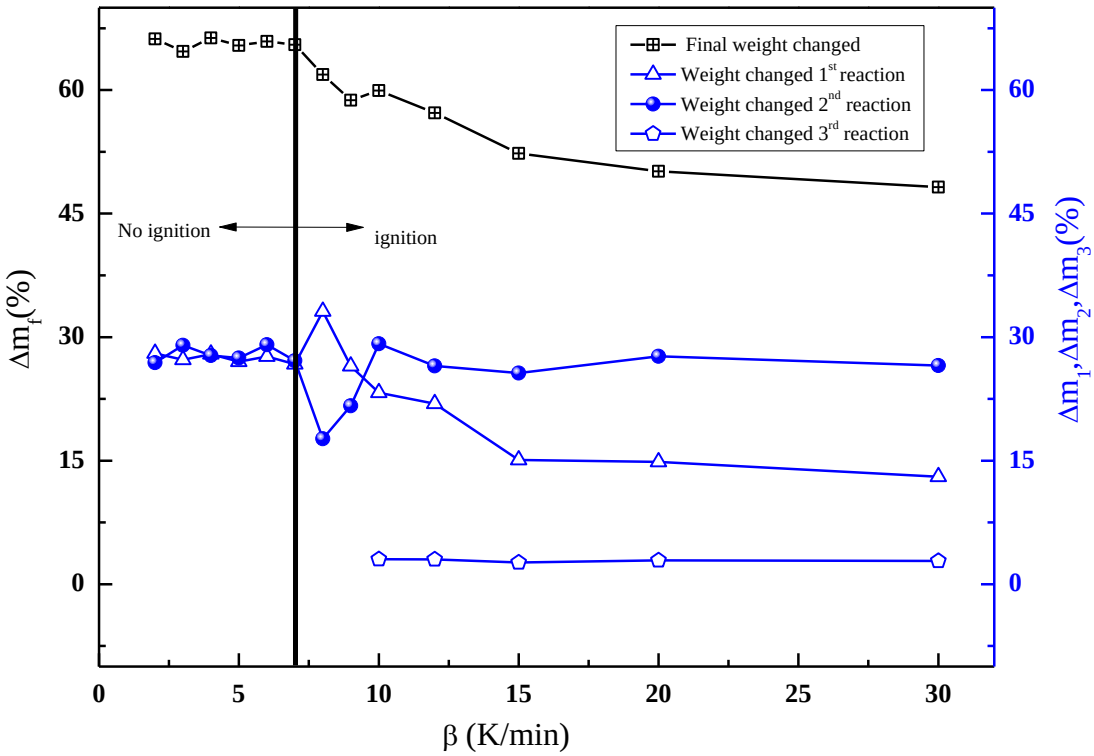


**Figure 3.25** Relationship of weight changed with heating rates, during various oxidation steps

It is noteworthy that the ignition reaction influences not only the mass changed during the first reaction ($\Delta m_1$), but also the final mass of the products. It is evident from **Figure 3.25** that during the whole oxidation process, when no ignition happened, similar weight change is observed and the final weight increase ($\Delta m_f$) remains 65.7 ± 0.6 %, which indicates that the heating rate has a little effect. On the other hand, when ignition is observed i.e. $\beta \geq 8$ K/min, the amount of final weight decreased with the heating rate. For instance when β is 8K/min, an increase of 61.9% of the sample weight is observed and only 48.21% mass increase is noticed at 30K/min. This trend of mass change can also be evidenced by the XRD graphs as shown in **Figure 3.16** and **Figure 3.21.**

The heating rate has little effect on the mass changed during the 2nd and the 3rd reaction. For example when β is 2 K/min, 26.9% of the mass increased is seen and at 30 K/min

when ignition is observed, similar mass changed (26.54%) is observed. Nearly 3 % of mass is being increased during the 3rd reaction. it can be suggested that the mass changed during this reaction is independent of the amount of active mass left, lower mass changed is because of the crystallization of alumina that is slowing down the diffusion process.

## 3.1.6. Nitridation of Nano Aluminum Particles

### 3.1.6.1. Simultaneous TGA/DSC trace

The simultaneous TGA/DSC trace is shown in **Figure 3.26**. The sample goes through the glass transition at 350 $^{o}$C after which it assumes the first non-baseline signal showing the start of the first reaction. The onset temperature for this nitridation reaction is ~ 400 $^{o}$C. The slope of the first exothermic reaction remains constant until the particles go through melting. The chemical reaction can be represented as in **Eq 3.4**.

The endothermic peak showing the melting process starts at 643 $^{o}$C attains maxima at 659 $^{o}$C and ends at 666 $^{o}$C. After melting of the nAl, the mobility of Al has increased. The rate of the chemical reaction should also increase but interestingly, contrary to that it is decreased. This decrease of the slop continues to 730 $^{o}$C where the rate of reaction increases once again and peaks at 780 $^{o}$C. This shows the 2nd exothermic reaction. The slope of this reaction is steeper than that of the reaction before the melting.

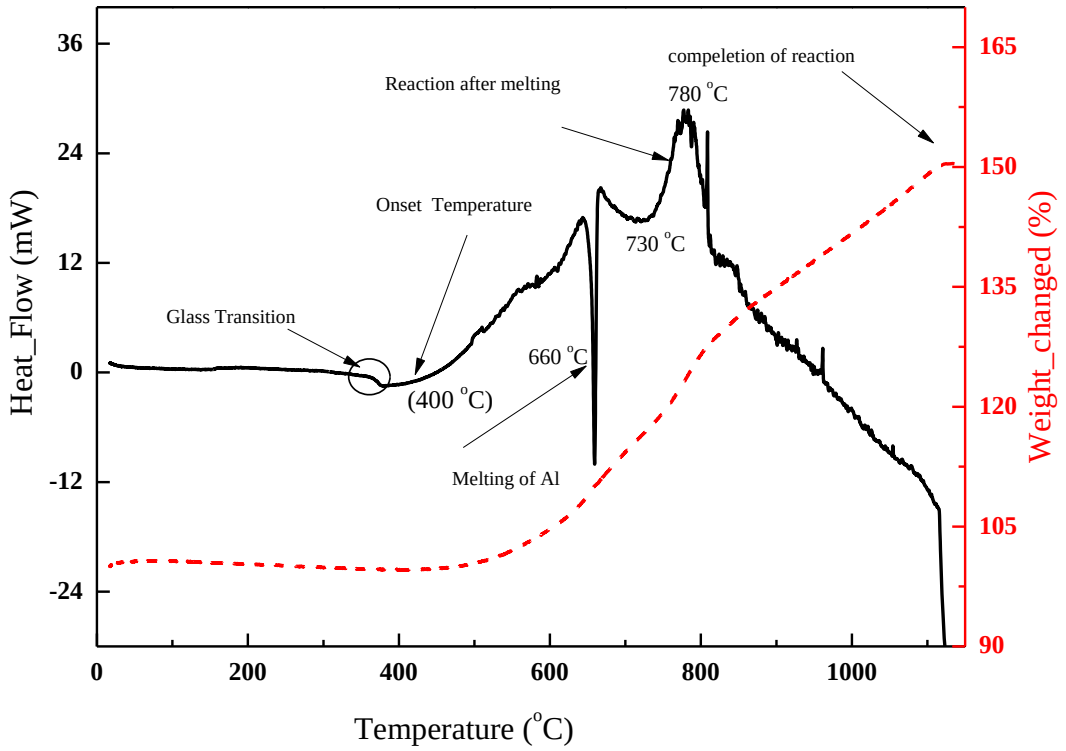


**Figure 3.26** Simultaneous TGA/DSC trace in $N_2$ at β =10 K/min

This can be understood in the following way that the AlN is a hard substance and makes a strong passivation shell over the active aluminium core. The reaction is going on even the particles are melting and the thickness of nitride shell is continuously increasing. Just after the melting temperature, the shell has attained the thickness that hinders the diffusion of nitrogen into the oxide which, consequently, slows down the rate of the reaction. With the increase of temperature, the molten metal produces pressure that is building inside the core. At 730 °C there develops a rupture in the shell, due to increase of pressure. This initiates the second reaction at higher rates. Metallic molecules are no more in the solid state but in the liquid form having a higher mobility that, in turn, enhances the rate of the reaction. That is why the slope of this reaction is steeper than the first step reaction. After attaining the peak at 780 °C the reaction slows down because the ruptured shell is healed now. The TGA curve shows that the sample is gaining weight

and the DSC curve is shifting downwards. The nitridation reaction completes at ~ 1100 $^{o}$C where the TGA curve has become flat.

### 3.1.6.2. XRD analysis of the nAl heated in Nitrogen

The XRD trace of the particles after nitridation is given in **Figure 3.27.** It can be seen that the particles contain γ– , α–$Al_2O_3$ along with AlN and Al. The presence of γ– , α–$Al_2O_3$ can be linked to the passivation layer of amorphous alumina. During the thermal treatment the amorphous alumina has transformed into γ– and α–$Al_2O_3$. AlN is a hard substance that blankets the aluminum core; consequently, some unreacted Al is left [59].

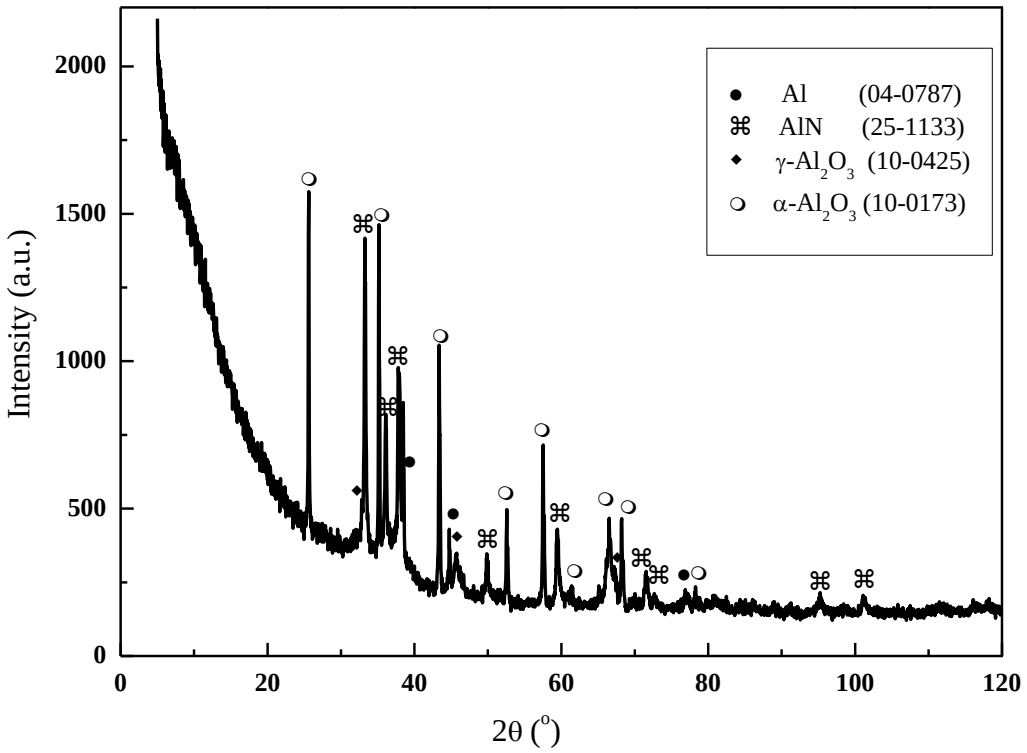


**Figure 3.27** XRD trace of nAl heated in the atmosphere of $N_2$ showing the peaks of γ–$Al_2O_3$ and α–$Al_2O_3$ along with AlN and Al. The polymorphs of alumina are transformed from the amorphous alumina passivating the nAl.

### 3.1.6.3. Comparison of the air and $N_2$ environments

No thermal runaway is observed in the nitridation case. Melting of the particles peaks at ~ 660 °C. It starts at 643.8 °C and 648 °C in the nitrogen and air, respectively. The peaks of the exothermic reactions in both cases are also different. DSC peaks in air are much higher than that in the nitrogen. The rate of the 2nd exothermic process, after the melting process, has an increasing trend in the air. Contrary to that, it is has a decreasing trend in nitrogen until it is reached at 730 °C, **Figure 3.28**.

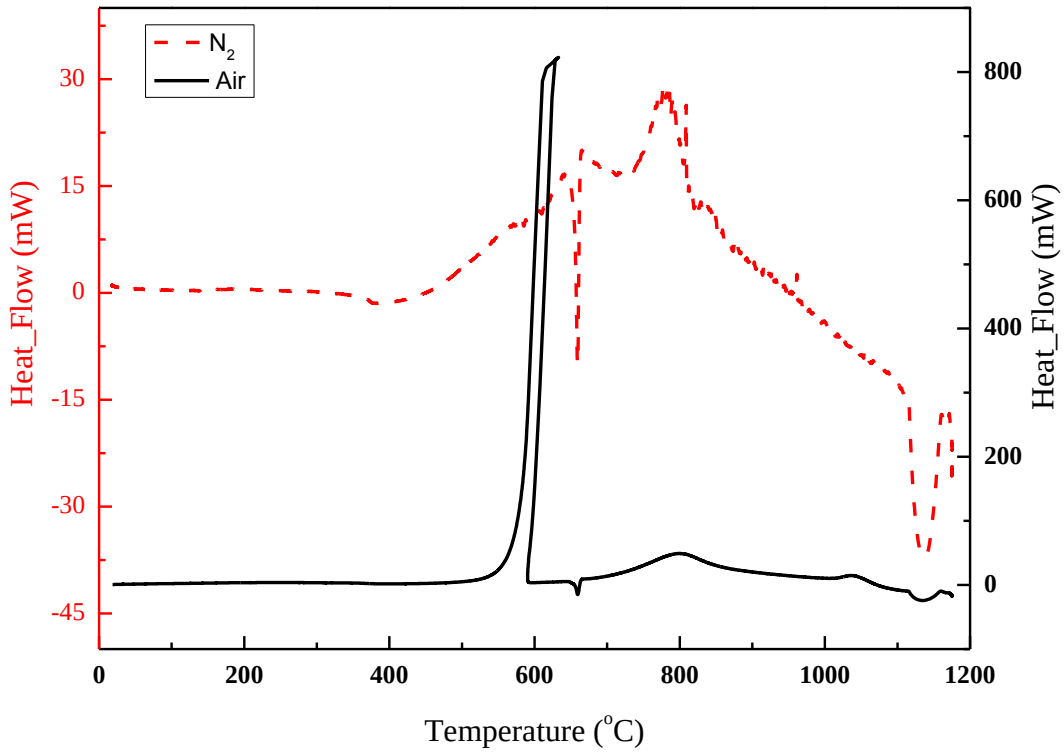


**Figure 3.28** Comparison of DSC curves of nAl particles in air and $N_2$ environments

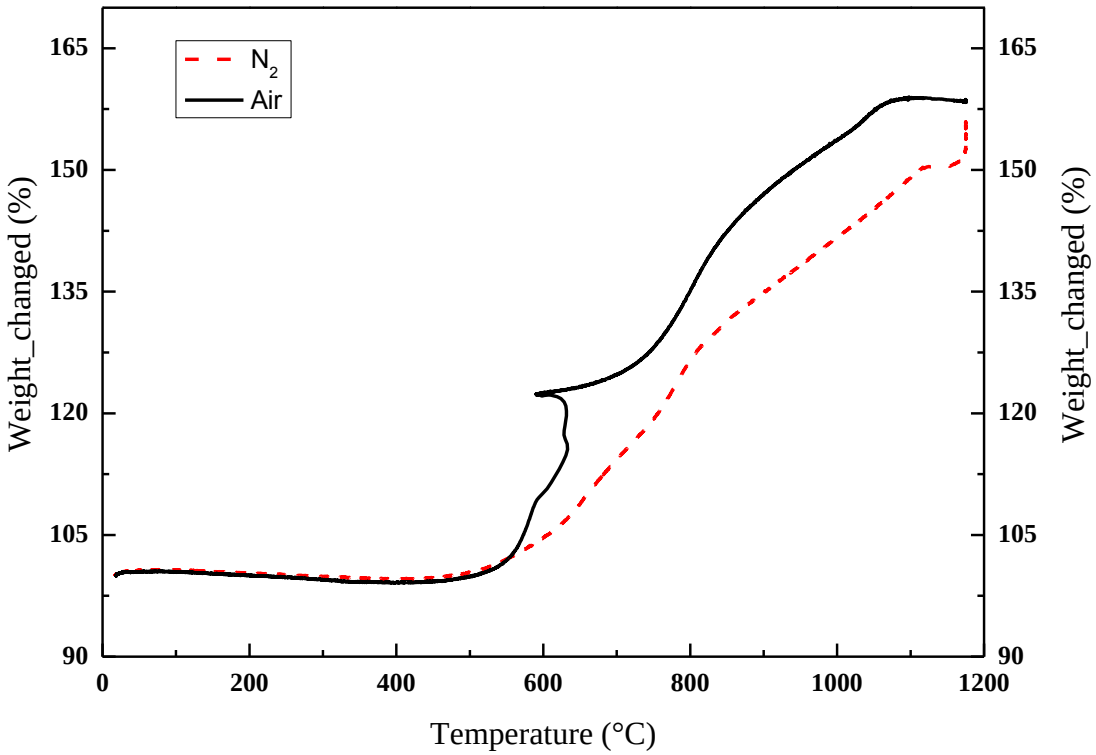


**Figure 3.29** Comparison of TGA curve of nAl in air and $N_2$ environments at a heating rate of 10 K/min

The weight gained by the sample in air is 58.7 % compared to 46.5 3% in nitrogen as shown in **Figure 3.29**.

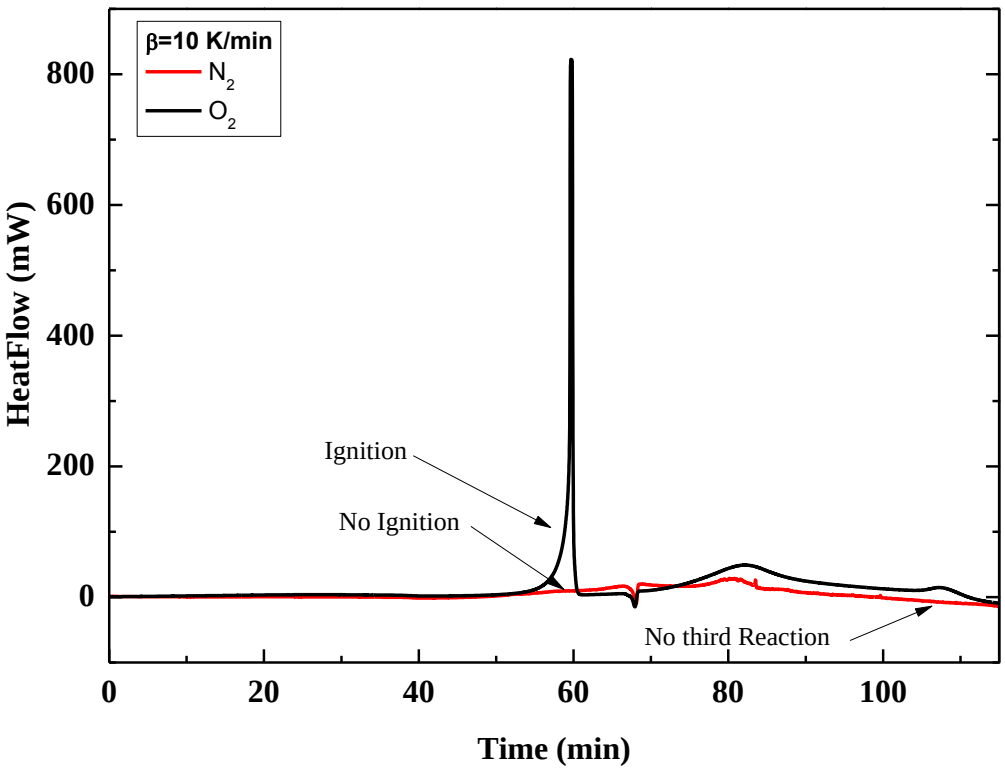


**Figure 3.30** Comparison of DSC curves shows that under the similar conditions of heating rate and the flow of purge gases, nAl do not ignite and there is no third exothermic reaction, in the atmosphere of $N_2$.

The particles go through ignition in air at 10 K/min but no such reaction is seen in the nitrogen environment, **Figure 3.30**. This is because the aluminum has more affinity towards oxygen as compared to nitrogen. Secondly, the AlN produced during the nitridation is much harder than the alumina layer produced during the oxidation. This alumina layer is also transforming from one polymorphic state to the other, making it porous and enhancing the diffusion of oxygen. On the other hand, the diffusion of nitrogen is slower. These factors lead towards the ignition reaction in air and a slow reaction in nitrogen.

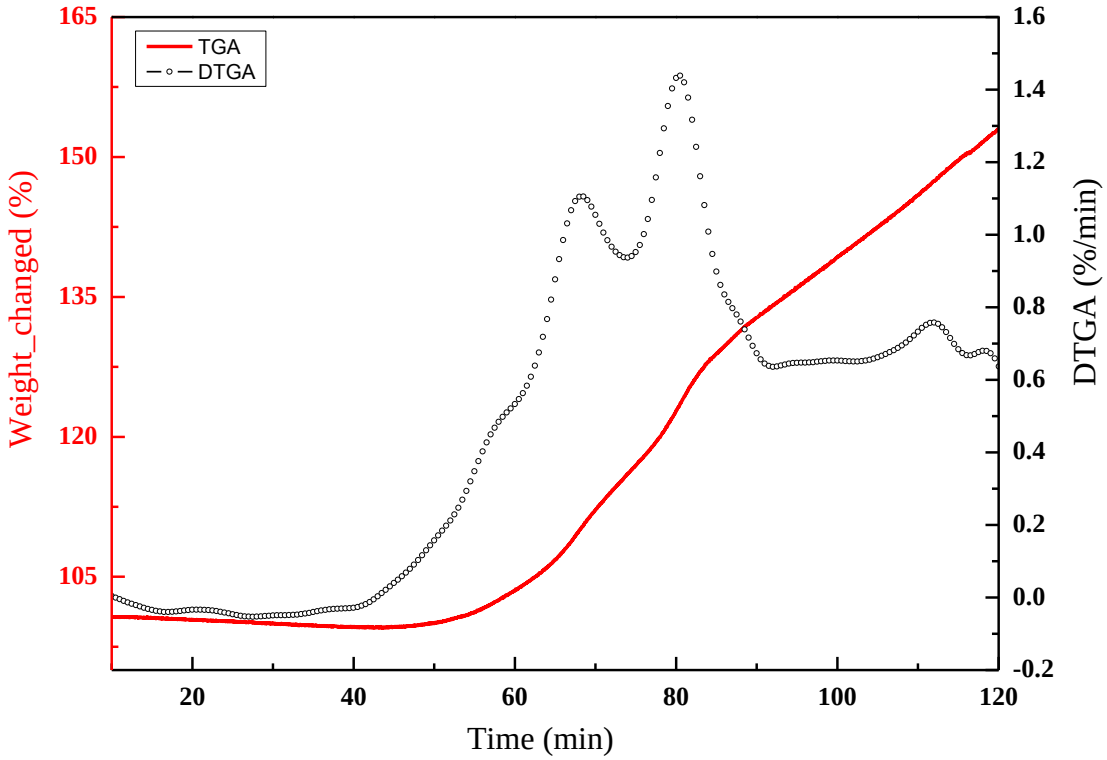


**Figure 3.31** A DTGA trace of nAl in $N_2$ environment

It is found with DTGA analyses that the oxidation of nAl completes in three exothermic reactions, whereas the nitridation completes in two steps as shown in **Figure 3.31**.

### 3.1.6.4. Comparison of heat released in air and nitrogen environments

The total heat produced can be estimated by integrating the area under the DSC curves, with reference to the baseline. The amount of heat produced during the oxidation in the air (15.42 kJ/g) is three times the heat produced during nitridation (5.52 kJ/g) in the nitrogen. In both environments, the heating rate is kept constant at 10 K/min and all other experimental parameters are also similar. The baseline is chosen where the flow of heat has become steady which happened approximately at 50 $^{o}$C, in both cases.

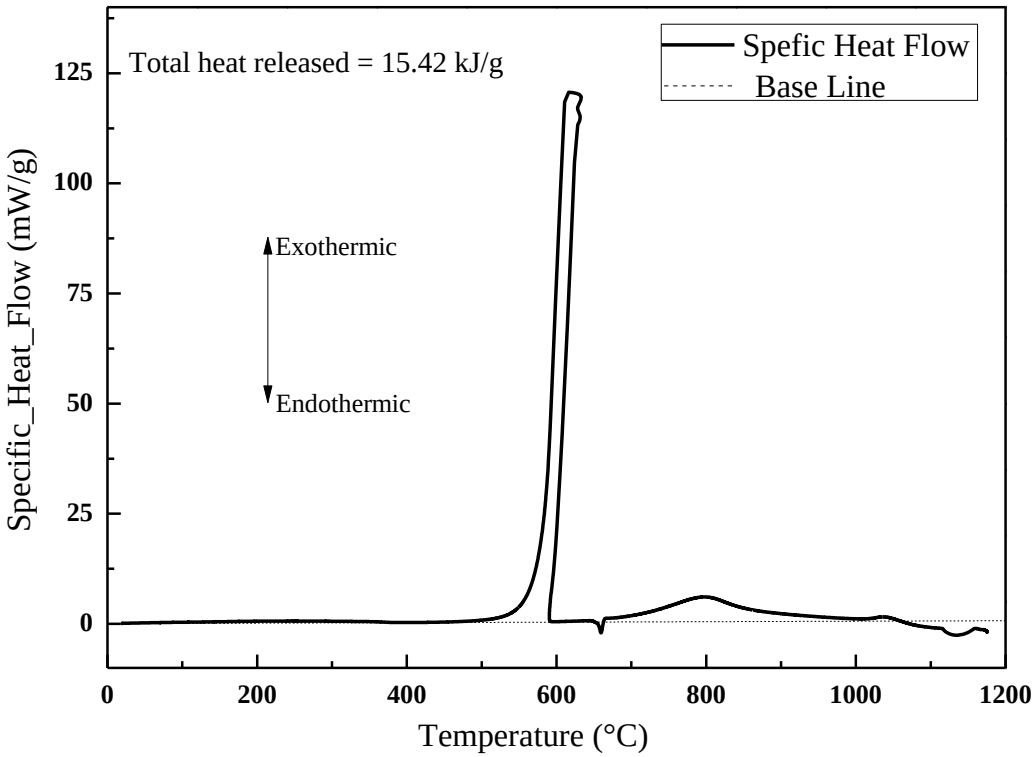


**(a)**

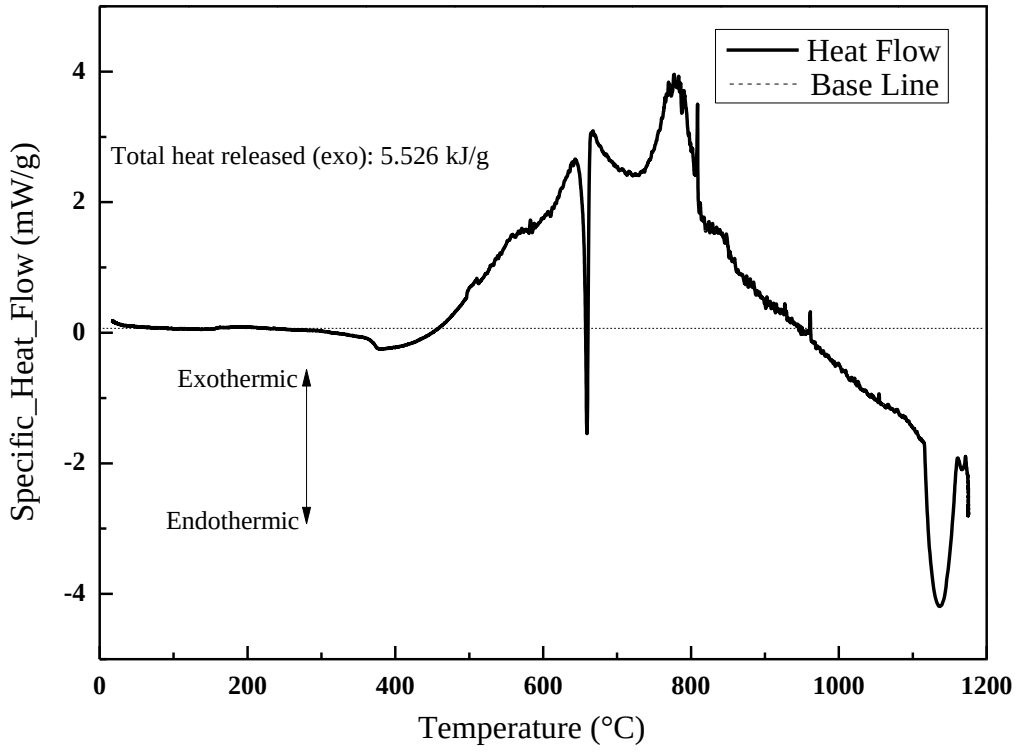


**(b)**

**Figure 3.32** Comparison of the total heat released in environments of the air (a) and $N_2$ (b) under similar experimental conditions (β = 10 K/min)

The enthalpy of formation ($\Delta_f H^o$) of AlN is -7.758 kJ/g and of $Al_2O_3$ is -16.428 kJ/g. The amount of specific heat produced in the air is more than that in the nitrogen. Under the environment of air, the sample undergoes ignition which produces more heat as shown in above **Figure 3.32(a)**. On the other hand, no ignition is observed in case of nitrogen which, in turn, produced less heat. Secondly, the melting caused the rupture in the alumina and consequently, more aluminum is reacting with the oxygen in air hence more heat is being released. On the other hand, no such increase of the reaction rate is seen in nitrogen environment, due to which, less amount of heat released is observed.

## 3.2. Formation of hollow structures

A lot of attention has been paid to enhance the practical usefulness of nano aluminium particles in various applications [107, 108]. Much research has been devoted to the phenomenological understanding of the oxidation process of nAl, being the key element for the realisation of whole energy production scheme. It is well known that the oxidation process of nAl is not a single step but a multiple step process. The rate of reaction of each intervening oxidation step depends upon various factors such as the physical state of the nAl i.e. the solid or liquid (molten) form. Secondly, the polymorphic phases of the alumina produced during the reaction [33, 35, 59]. The information of morphological evolution such as the change of shape, size, density, crystallanity and the shell thickness during each oxidation step is of the paramount importance for understanding the oxidation mechanism. Recently, it is discovered that the oxides of various materials such as polymers, inorganic, carbon, non-metallic and oxides of metallic nanoparticles including, Ti, Cu, Zn, Fe, Co, and Al form hollow structures after their oxidation [34, 109-112].

The main studies of the hollowing behaviours of NPs are related to the size of the particles and void, the reaction regimes and the role of surface diffusion of the species [113-115]. For example, Rai et al. [34] studied oxidation of nAl having a mobility size of 100 nm and found that the particles after their oxidation were hollow. In their research, the particles were oxidized from 500 $^{o}$C to 800 $^{o}$C in a furnace. It was found that the density of particles increased from 2.7 g/cc to 3.85 g/cc. Under these conditions the particles were in the solid state. When the temperature of the furnace was increased to 1100 $^{o}$C, the density decreased, which suggested that the particles formed voids in the centre. Ma et al. [109] synthesized hollow AlN nanospheres with diameters ranging from 20 nm to 200 nm with a shell thickness of ~10 nm. They observed that the formation of hollow nanosphere started at temperature of 800 $^{o}$C. At this temperature, the particles were a mixture of hollow nanospheres and partially or un-altered Al particles. These particles were turned into complete hollow structures at 1200 $^{o}$C. Brandstadt et al. [116] studied the oxidation process of nano aluminium particles with diameters of 38 nm and 45 nm using simultaneous thermal analysis (STA) in an atmosphere of $CO_2$ at a heating rate of 5 K/min. The diameter of the particles was increased when the temperature of the furnace was increased from 500 $^{o}$C to 800 $^{o}$C but particles remained solid. The particles developed a hollow structure at temperature of 1000 $^{o}$C. They theorised, as the diffusion distance of these particles was small, Al atoms moved towards the outer side of the particle that developed an empty hole in the central region of the particles. In these studies, the nanoscale Kirkendall effect was used to explain the formation of the hollow spheres. The void formation was started near the metal/oxide interface due to the creation and aggregation of the vacancies by the differences of diffusion rate of ions moving to and from the centre of the particles. Nakamura et al. [110] investigated the formation mechanism of nanoholes of Al (6-8 nm) at temperature ranging from 22 to

150 $^{o}$C. They argued that because the diffusivity depended upon the temperature and at such a low temperature the difference of diffusivities of oxygen and aluminium was not sufficient to create a vacancy in the centre. They explained the formation of nanospheres of aluminium oxide with the help of Carbera and Mott theory.

It is clear that the mechanism and kinetics of formation of void in nanosized particle are not well understood. The barriers lie in the difficulty of manipulating sample particles at the nanoscale and the insufficient characterisation of the morphology and intermediate products. To understand the formation mechanism, this section aims to provide a detailed investigation of the void formation in nAl during the oxidation.

### 3.2.1. Morphology of nAl after oxidation

In the previous section it was shown that the oxidation of nAl completes in three exothermic steps. These steps are distinct from one another. The energy produced and mass changed during each step depend upon the rate of the reaction, which is related to the state of the nAl, i.e., whether they are in the solid or in the liquid (molten) state, as well as the polymorphic phases of alumina shell. In this  it is observed that there are two modes in which the oxidation proceeds. In the first mode, the particles complete oxidation in the thermobalance without being ignited. This occurs when the heating rate is relatively low, i.e., 2 to 7 K/min.  In the second mode, the particles go through ignition reaction. This reaction happens when the heating rate becomes equal to or higher than 8 K/min. In this case, the particles are ignited in the furnace before reaching the theoretical melting temperature (660 $^{o}$C) of aluminium. The morphology of the particles after oxidation under both conditions are described in  **Figure 3.33(a, b, c, d)**

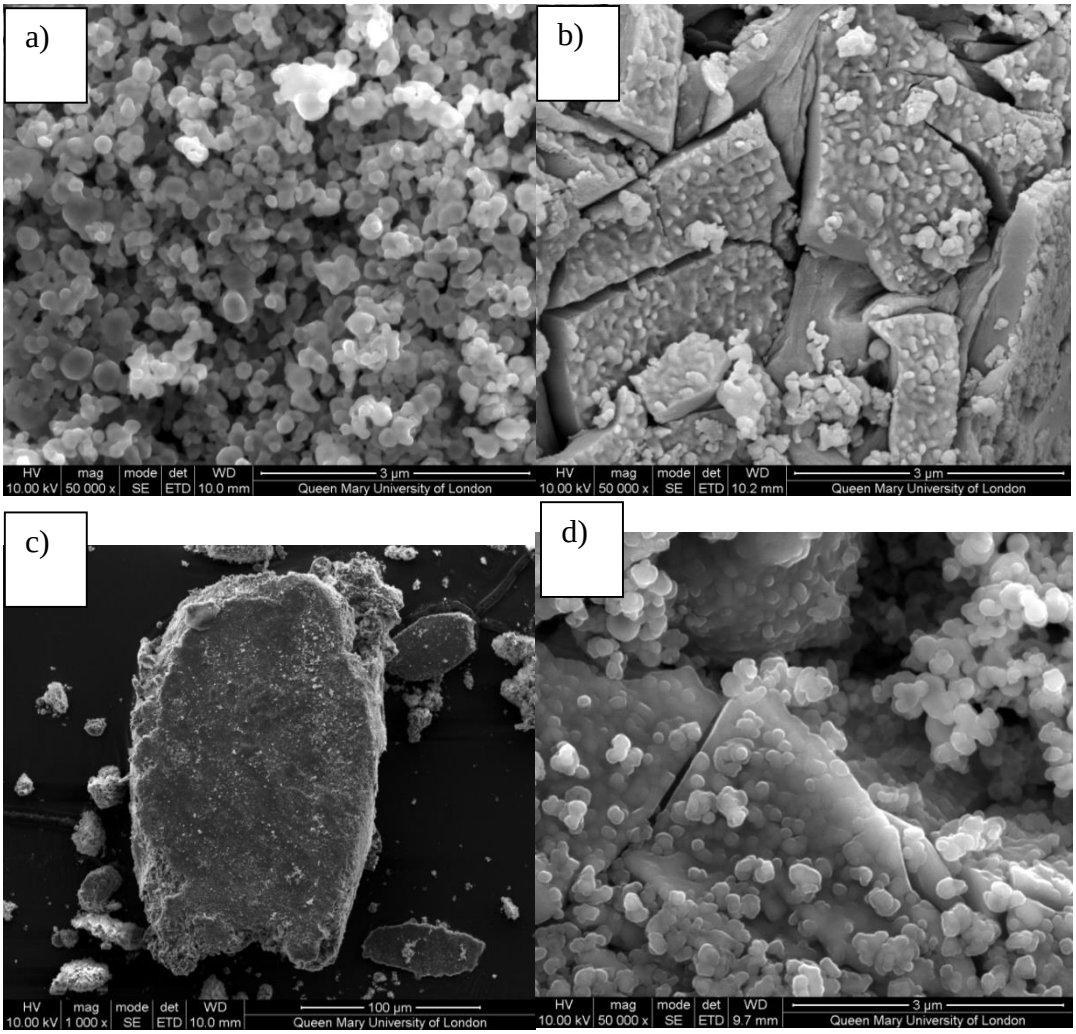


**Figure 3.33** SEM micrographs showing morphology of the particles (after oxidation) a) at x50 k, at heating rate of 2 K/min (no ignition), showing that the particles are spherical in shape; b, d) at x50 k, at heating rate of 10 K/min and 30 K/min, respectively; c) at x10 k at heating rate of 20 K/min (ignition), showing particles are losing their shape and inter-particle and inter-agglomerate sintering can be observed.

It can be observed from **Figure 3.33(a) (**no ignition), the particles are losing their sphericity but the major structure of the product is spherical-shaped. The particles are separated by considerable distances. Partial inter-particle sintering can also be observed. On the other hand, **Figure 3.33(b, c, d)** shows the morphology of the particles after they are ignited ($\beta$ = 10, 20 and 30 K/min). The particles are heavily agglomerated. The level of agglomeration among the particles and agglomerates is higher as compared to that

when no ignition happened. Big aggregates having micrometric sizes can be seen as well. The particles are closely packed and the distance among them is reduced. This hard agglomeration is due to the strong chemical forces produced by the chemical bonds between the particles. This can be explained by the ignition process that occurred during the oxidation process. Due to ignition the particles go through fast oxidation. As a result the thickness of alumina layer produced during this quick reaction is also small. The particles are melted, subsequently at 660 $^{o}$C, and increased the volume of the core. Due to the smaller thickness of the shell, it is easy for the molten metal to rupture it. The molten aluminium would be poured out of the particles and be oxidised in the vicinity of the neighbour molecules. This accelerated the inter-particle sintering and consequently hard agglomeration is developed.

### 3.2.2. The evolution of voids

With the help of TEM, it is found that the particles develop a void in their central region. From **Figure 3.36** it is clear that the particles have a lighter contrast in the central regions and a dark in the outer shell areas. This suggests that the thickness of the central regions is smaller than that of the outer regions, i.e., the formation of hollow nanostructures after the oxidation. To confirm that the difference in the contrast is due to the void developed inside the particles, the position of the sample holder was tilted by 15$^{o}$ shown in **Figure 3.36(b)**. It was observed that the outer shell consistently exhibited a higher contrast than that of the inner core. The relative amount of aluminium and oxygen on the various regions of the particle was found with the help of EDS. Three regions, namely, the outer edge, inner edge and the centre of the particle were selected. The aluminium and oxidation concentration profiles are summarised in **Table 3.4.**

**Table 3.4** EDS spot analysis at three regions on the particles (β = 20K/min)

| Regions | Elements | | |
|---|---|---|---|
| | O | Al | Total |
| | % | % | % |
| Edge | 58.6 | 41.4 | 100.00 |
| Inner Edge | 57.0 | 43.0 | 100.00 |
| Centre | 66.4 | 33.6 | 100.00 |

It is evident from **Table 3.4** that the regions nearer to the edge (oxide/metal interface) have more aluminium than that in the central region. This tendency of decreasing Al amount towards the centre also indicates that the particles are hollow [117]. TGA and XRD confirm that a very small amount of active aluminium is left in the particles. The lighter contrasted region can be due to the un-reacted aluminium but the ratio of void size to the size of particle is large. This means, the lighter contrasted central region is not due to the un-reacted aluminium but is a void developed during the oxidation process. The outer peripheral regions have darker contrast due to the higher densities.

### 3.2.3. Effect of temperature

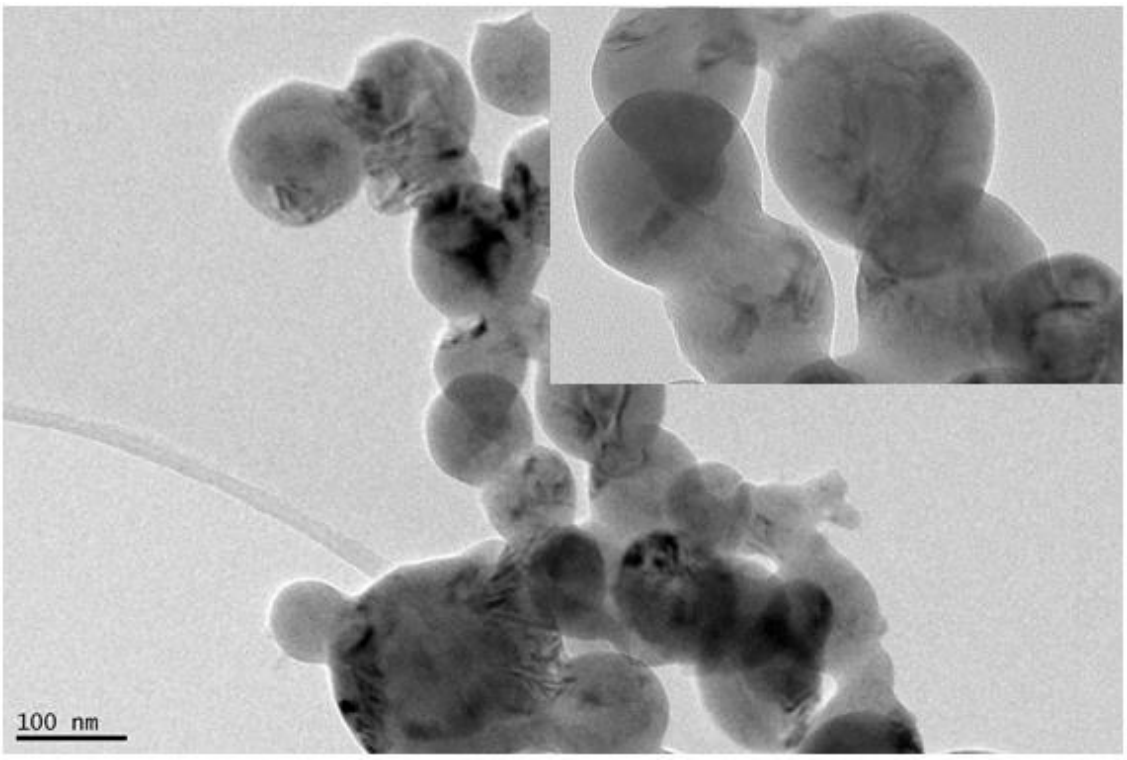


**Figure 3.34** TEM image at the heating rate of 5 K/min at a terminal temperature of 600 $^{o}$C (after first oxidation step and before the melting of nAl: all particles are solids)

It can be observed from **Figure 3.34** (particles oxidised to 600 $^{o}$C) that the particles have not yet developed a hollow structure as no visible indication for cavity formation is found. This means that after the first oxidation step, which occurred before the melting of the particles, they retained their sphericity without developing into hollow structures. The particles are sintered into chain-like necking structures made by the diffusion of atoms in the surface boundary areas of the adjacent particles.

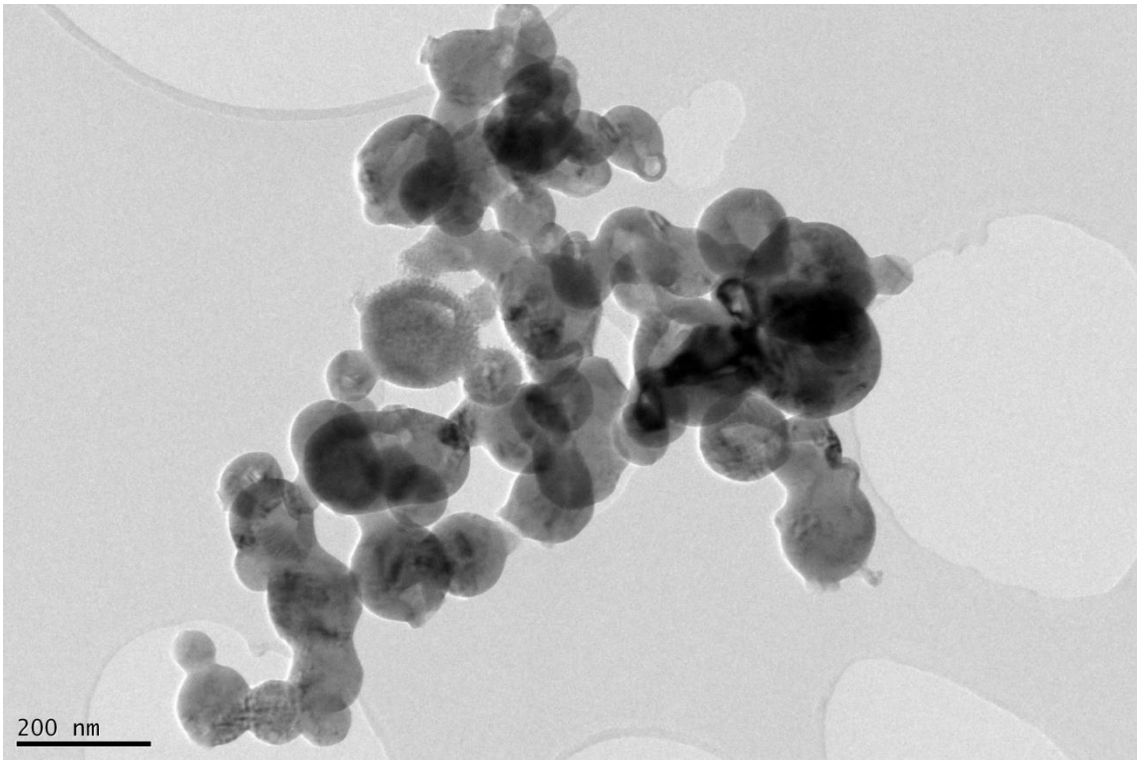


**Figure 3.35** TEM image at the heating rate of 5 K/min at a terminal temperature of 700 $^{o}$C (after the melting of nAl and the beginning of the 2$^{nd}$ oxidation step: a mixture of solid and hollow particles)

**Figure 3.35** shows the TEM image of particles at 700 $^{o}$C, i.e., the beginning of the 2$^{nd}$ oxidation step when all Al has been melted. At this temperature the oxidation is still incomplete. The particles have developed partial voids of small sizes in their central regions. The TEM image shows that the particles are the combination of solid as well as hollow particles. For statistics purpose, one hundred and twenty particles are examined and out of which thirty particles have developed the hollow structure, at this temperature conditions.

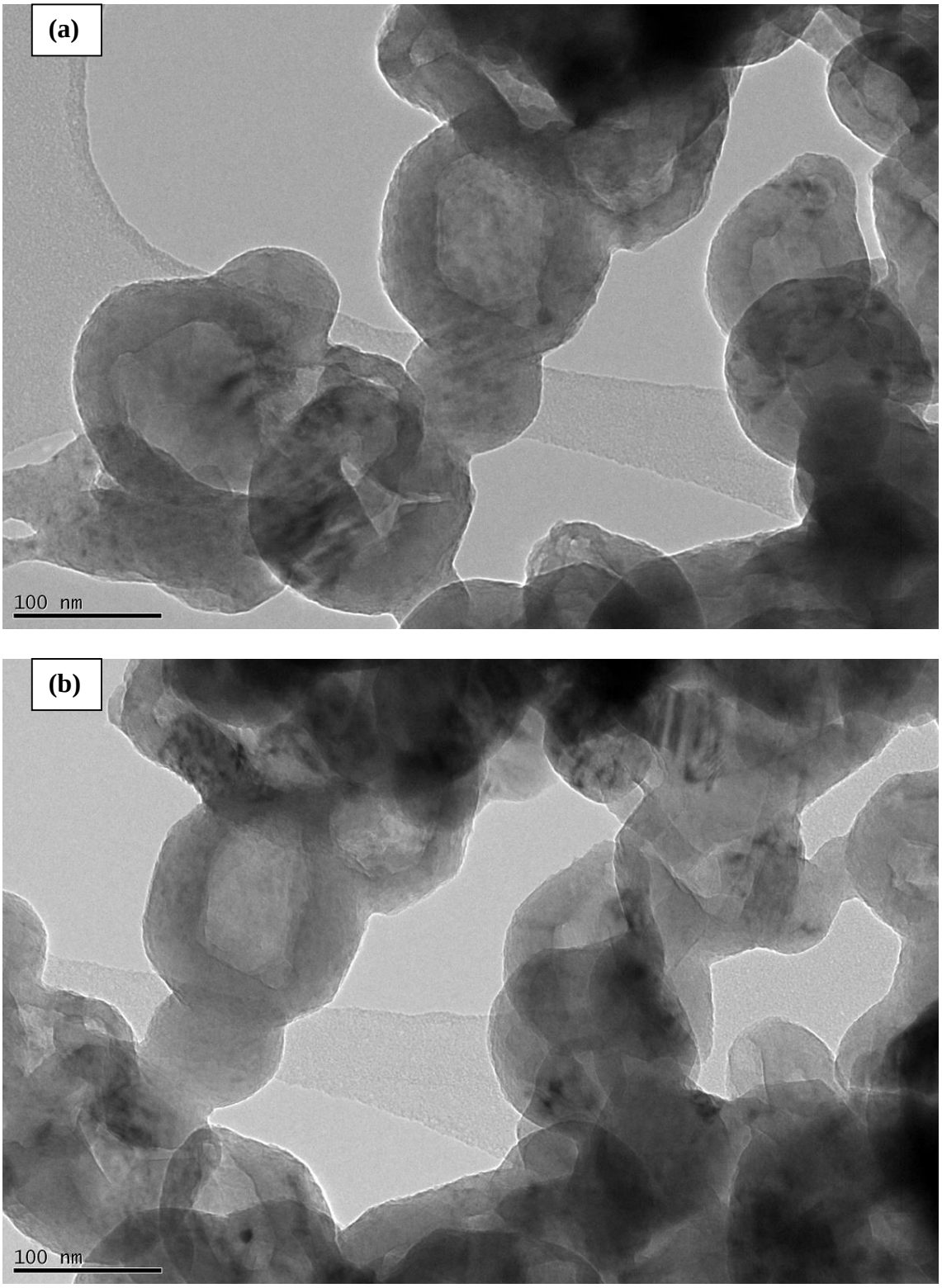


**Figure 3.36** TEM image at the heating rate of 5 K/min at a terminal temperature of 800$^{o}$C (after melting, end of 2$^{nd}$ oxidation step); a) without tilt; (b) with sample holder tilted at 15$^{o}$.

**Figure 3.36** represents the particles oxidized to 800 $^{o}$C, i.e., near the end of the second oxidation step. It can be easily discerned from the **Figure 3.36** that the particles have developed the voids in their central regions. Almost all the particles have the hollow structure. The sizes of the voids are bigger than those developed by the particles at 700 $^{o}$C. It can be concluded that the hollow structure development process is completed by this temperature. As discussed earlier, to confirm the central bright contrast is due to the void inside the particle the sample holder was tilted by 15$^{o}$. The particles still have the lighter contrast in the central region and a darker near the boundaries, suggesting the particles are hollow [117].

TEM analyses shows that after developing the void in the central region, the mean particles diameter has been increased. TEM analyses of particles at various temperature conditions are summarised in **Table 3.5.**

**Table 3.5** Showing increase in the mean diameter of particles after developing voids.

| T | N | $d_{mean}$ | $\sigma$ | $d_{min}$ | $d_{max}$ |
|---|---|---|---|---|---|
| $^{o}$C | Count | nm | nm | nm | nm |
| 25 | 280 | 106 | 41.6 | 35 | 356 |
| 600 | 84 | 115 | 47.7 | 33 | 329 |
| 700 | 120 | 112 | 53.1 | 12 | 318 |
| 800 | 89 | 148 | 44.8 | 70 | 384 |

Note:

d is the diameter of the nAl

$d_{min}$, $d_{max}$, $d_{mean}$, are the minimum, maximum and mean observed diameter of the particles

$\sigma$ is the standard deviation

T is the temperature conditions

N is the total number of particles examined

The mean diameter of the nAl before oxidation was 106 nm. After the oxidation of the particles at 600 $^{o}$C and 700 $^{o}$C its values changed to 115 and 112 nm. These values are nearly the same as that of the particles before the start of the oxidation. It is interesting to note that its mean value increased to 148 nm after the generation of the void. The diameter of the hollow cavities ranges from 31 to 269 nm with a standard deviation of 37 nm. The average value of the shell thickness is estimated ~32 nm.

The relationship of the shell thickness and the diameter of the voids are shown in **Figure 3.37(a).** Both values increase with the increase of the particle diameter. Cavity diameter distribution is also shown in **Figure 3.37(b)**. The histogram shows that the length of the voids developed by most of the particles range from 50 to 100 nm.

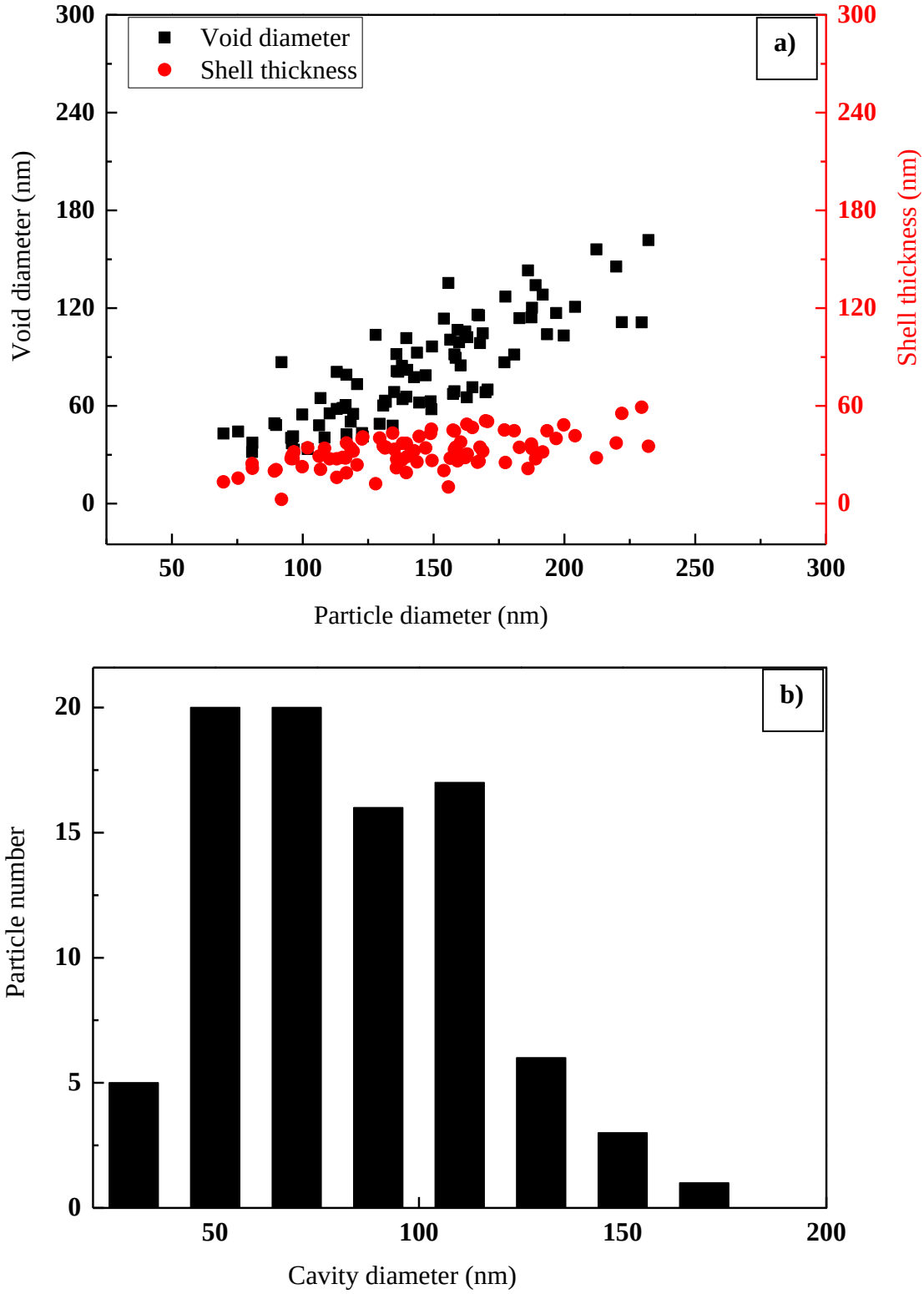


**Figure 3.37** a) shows the relationship of shell thick and diameter of the void; b) void diameter distribution of nAl (β = 5 K/min, T=800 $^{o}$C)

### 3.2.4. Effect of heating rate

The effect of the heating rate on the morphology of the particle is also studied. Two examples are shown here. The first is for higher heating rate (β >7 K/min) that the particles go through the ignition in the thermobalance and the second is under low heating rates (β ≤ 7 K). Both are explained below.

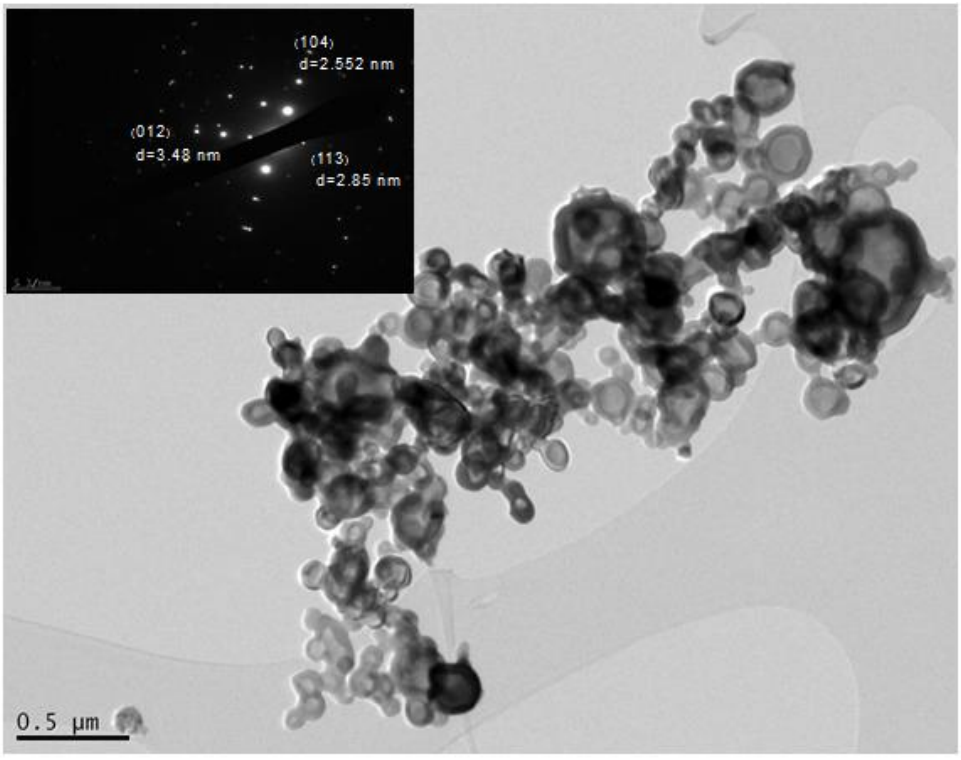


**Figure 3.38** TEM image at heating of 2 K/min showing the particles are hollow and spherical shaped (no ignition).

**Figure 3.38** shows TEM image of the particles at the heating rate of 2 K/min. It is evident that the particles are spherical and have a hollow structure. The particles are totally oxidized. The SAED pattern shows three peaks (104), (113) and (012) of alumina (PDF card No. 10-0173) (in the inset) as well.

The morphology of the particles heated at 8 K/min and 20 K/min is shown **Figure 3.39**. It is clear from TEM images that the particles have lost their spherical shapes and have agglomerated. The particles have transformed into elliptical shapes and the voids have also been elongated. The particles are pressed upon each other and joined with each other.

It can be discerned from **Table 3.6** that the mean diameter of the particles heated at 2 and 5 K/min are similar (no ignition). The value has increased from 149 nm to 173.6 nm when the particles are ignited. The diameter of the void has also increased from 83.1 to 106.7 nm. The values of shell thickness are similar with one another in all cases.

**Table 3.6** Showing increase in the mean diameter of particles with increase of heating rate

| $\beta$ | N | $d_{mean}$ | $d_{hmean}$ | $st_{mean}$ |
|---|---|---|---|---|
| K/min | Count | nm | nm | nm |
| 2 | 150 | 149.2 | 83.1 | 33.1 |
| 5 | 89 | 147.6 | 83.1 | 32.2 |
| 8 | 78 | 173.6 | 106.7 | 33.4 |

Note.

$d_{hmean}$ is mean diameter of the cavity

$st_{mean}$ is the mean shell thickness

(at $\beta$ = 5 K/min , the mean diameter of particle at 800 $^{o}$C is taken (not at 1175 $^{o}$C) as the hollow structures are stable once they are developed [117]).

The relationship of cavity diameter and shell thickness with the diameter of the particles for both conditions is shown in **Figure 3.40(a, b)**.

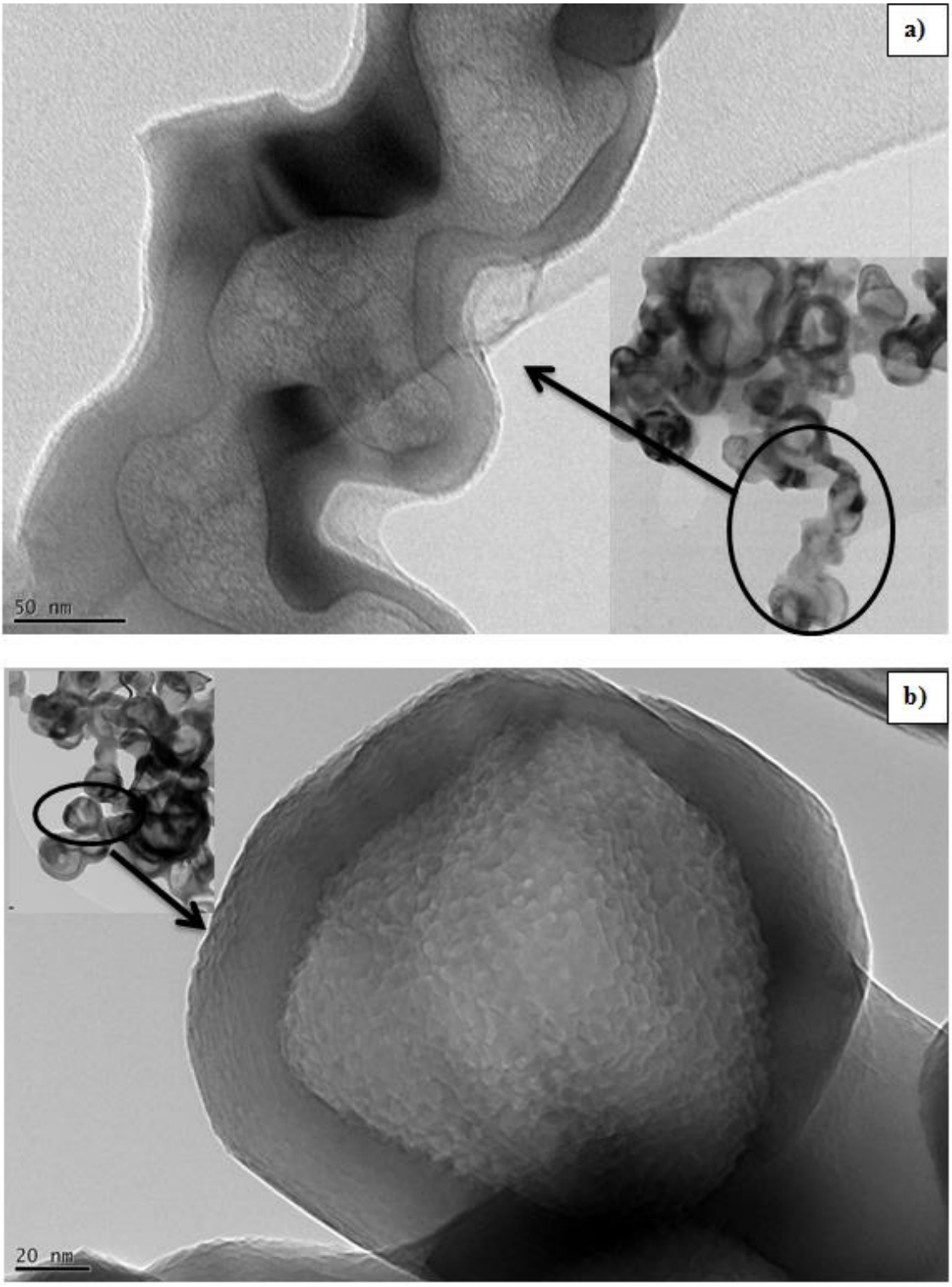


**Figure 3.39** a) TEM image of nAl treat at heat rate of 8 K/min shows the joining of individual particles; b) TEM image of nAl treat at heat rate of 20 K/min shows an individual particle joined with the other particles (ignition).

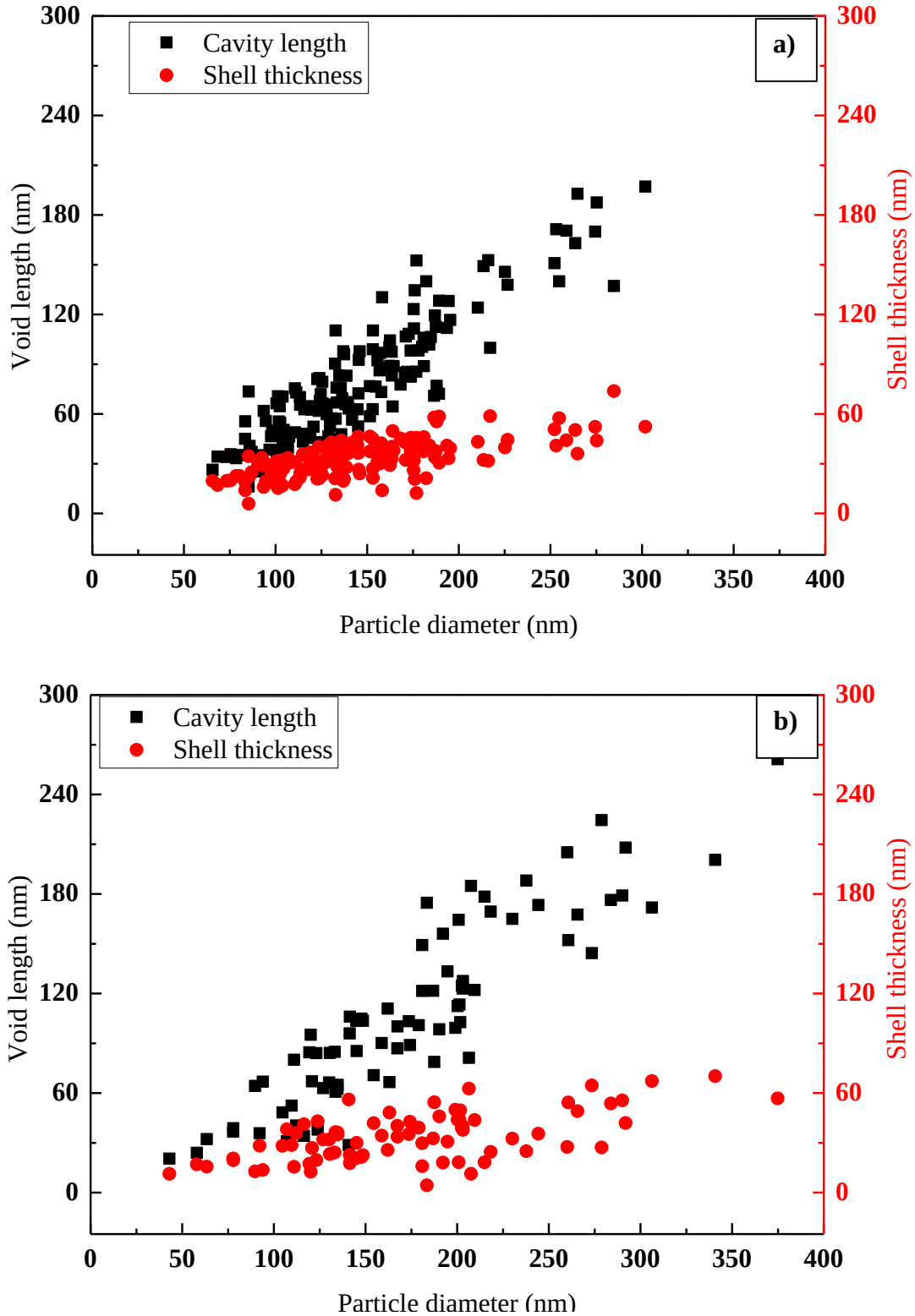


**Figure 3.40** Shows the relationship of shell thickness and diameter of the void; when β = 2 K/min (no ignition); b) when β = 8 K/min (ignition)

### 3.2.5. Mechanism of formation of the voids

It is observed that the cavity formation started after the melting process and completed ~ 800 $^{o}$C. The formation of void inside the particles can be explained in the way as shown in **Figure 3.41** and **Figure 3.42**. At the start of oxidation, the nAl had a core-shell structure, **Figure 3.41(a)**. Amorphous alumina is covering the metallic aluminium core. The first oxidation step starts at 500 $^{o}$C, peaks at 570 $^{o}$C and completes at 630 $^{o}$C. With the start of the oxidation, the layer of amorphous alumina changes to γ-alumina. Due to the polymorphic phase transformation, the γ-alumina layer becomes dense and shrinks which, subsequently, has become porous. The core aluminium is exposed to the oxygen. This is the start of the first oxidation step. Due to oxidation the thickness of the alumina layer has increased and the core aluminium has shrunk as it is consumed, **Figure 3.41(b)**.

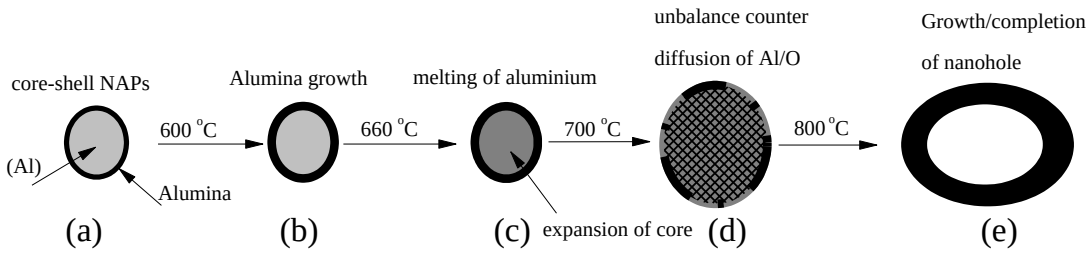


**Figure 3.41** Schematic diagram of the evolution of the hollow alumina during the oxidation of nAl; a) core-shell structure of nAl before oxidation where amorphous alumina is coating active aluminium; b) after first oxidation step the particles oxidised to 600 $^{o}$C where core shrank and alumina layer stretched; c) at 660 $^{o}$C where aluminium core melted; d) the solid alumina layer became barrier for the molten aluminium to react with air and subsequently molten aluminium reacted with oxygen via nanoscale Kirkendall diffusion process (700 $^{o}$C) ; e) growth of alumina layer and formation of hollow alumina particles (800 $^{o}$C).

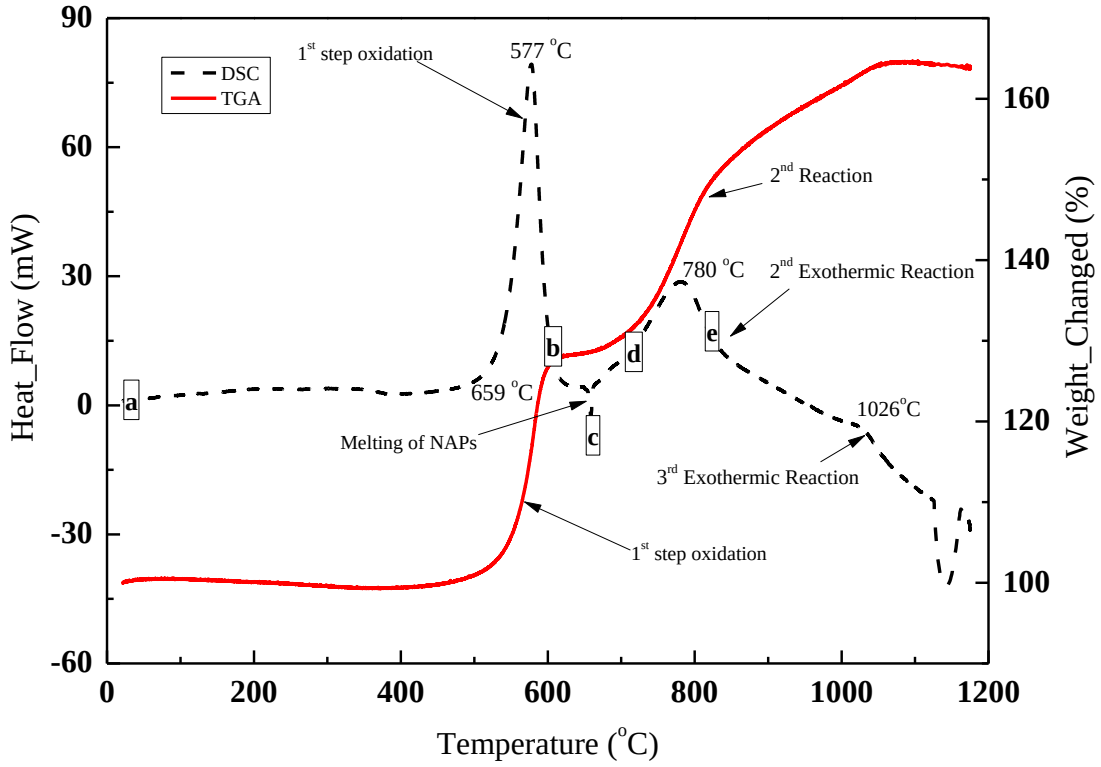


**Figure 3.42** TGA/DSC curve of nAl at 5 K/min showing the development of the void with the change of temperature

To understand the morphology after the first oxidation step, the particles are heated to 600 °C. It can be observed from **Figure 3.34** that the particles are still solid. The average diameter of the particles has increased from 106 to 115 nm. This increase of diameter is due to the addition of alumina produced during the first oxidation step. The rate of oxidation has decreased because the shell of alumina has become a barrier between the active aluminium and oxygen, also indicated by TGA/DSC curves, **Figure 3.42**. At 660 °C, the remaining active aluminium has melted that has increased the volume of the core. This pushed the alumina shell, which produced cracks in the layer. This is the start of the second oxidation step. The cracks of alumina are plugged with further oxidation of oozing molten aluminium that renders it into a solid structure. Now the less porous layer of alumina became barrier between the air and the active aluminium and the ongoing

oxidation is happening due to the nanoscale Kirkendall effect [117-119]. The aluminium species diffused outward to react with the oxygen and increase the thickness of the shell. The diffusion rate of Al atoms towards the shell is much higher than that of the oxygen species towards the core [120]. This is because the size of oxide anions is much bigger than the size of the metallic cations. The metallic cations are consumed fast while traversing through the metal/oxide interface. Due to the differences of the diffusivities there develops a net outward flux of the cations. To balance this, an inward vacancy flux in created. The gradual evacuation of aluminium from the core gives rise to a void in the central region. Similarly, Yin et al. [121] and Ma et al. explained the formation of nanoscale hollow cobalt sulphide and nanoscale hollow aluminium nitride with the same mechanism. TEM image of the product at 700 $^{o}$C (**Figure 3.35**) shows that the particles are the combination of hollow and solid structures. At this stage, the particles are going through the second oxidation process which peaks at 783 $^{o}$C. The average diameter of the particles at 700 $^{o}$C is similar to that at 600 $^{o}$C as shown in **Table 3.5**. Due to small diffusion distances the outwards diffusion of molten aluminium caused the formation of the voids. At this temperature, TEM image (**Figure 3.35)** shows that the particles have developed partial holes. This process of making the hollow structure completes at 800 $^{o}$C as shown in **Figure 3.36**. At this temperature conditions, the average diameter of the particles has increased to 148 nm from 112 nm. The mean cavity diameter is ~83 nm and the mean shell thickness is ~32 nm.

It is also observed that the heating rate also affects the shapes of the cavity and of the shell. The particles are oxidised at high heating rate, i.e., $\beta$ = 8 K/min at which the ignition is observed. Large portion of nanoparticles have changed to irregular morphologies having empty spaces in their central regions. The average diameter of the

nano cavities has become 173.6 nm. This is higher than that (149.2 nm) of the particles heated at 2 K/min where no ignition is seen.

Most of the particles are ellipsoids. The relationship of the cavity diameter, shell thickness and the particle diameter of the both cases is shown in **Figure 3.40(a, b).** The morphology of the particle is very sensitive to the motion of the molten aluminium during the oxidation process. At higher hearing rate, the after melting process, the pouring aluminium exerted more pressure on the shell distorting it into an ellipsoid shape. The cavity elongated without causing much changes in the thickness of the shell. The mobility of aluminium is increased and it poured out of the particles and oxidised in the vicinity of other particles. This increased the magnitude of the agglomeration as well.

## 3.3. Thermal-Chemical Characteristics of Al-Cu Nano-Alloys

Metal based energetic materials (EMs) have been used in many applications including thermites, explosives and pyrotechnics [2, 3]. Aluminum is a favourite choice for such applications because of high reaction enthalpy, high energy density, abundance, low cost, nontoxic nature, developed procurement market, and the technological maturity for the manufacturing [10-12, 54]. Monometallic EMs have high theoretical energy densities yet difficult to achieve in practice due to the limitations of long ignition delays, low reaction rates and incomplete burning [19]. To have more controllability over the material properties, aluminum is usually alloyed by mixing with several other elements. Due to the synergistic effects of the constituent alloying materials, the physiochemical properties of the alloys can be improved by chemical reordering and spatial redistribution of the atoms [24]. In addition, the alloying increases the surface area of the particles that will increase the rate of reaction and improve the reaction mechanism [9, 25, 26], which in turn improves the rate of heat release and the performance of propellants and thermites [27].

Many studies have been conducted in the last a few decades to investigate the thermo-mechanical and chemical activities of aluminum based alloys. For instance Shoshin et al. investigated the ignition and combustion characteristics of aluminum rich Al-Ti and Mg alloys having micrometric dimensions (10-14 μm) [28, 122, 123]. It was found that the flame speed of the alloy aerosol was higher than those produced by Al, Ti and Mg aerosols individually, and the ignition temperature of the alloy was decreased with the increase of concentration of Ti and Mg. Wang et al. [21] showed that with the increase of Mg concentration, the brittleness of the MgAl alloy (0.75 μm-6.64 μm) increased, and the particles were ignited at ~ 620 $^{o}$C, even lower than the theoretical melting

temperature (660 $^{o}$C) of aluminum. The amount of heat produced and weight increased during the process had a direct linkage with the composition of the alloy.

For alloys made from micro-sized particles, the main tool to modify the alloy property is to vary their constitutional compositions, which have their own limitations. It has been well known in the physics domain that as the particle size reduces to the nanoscale, it will exhibit a unique size-dependent property phenomenon due to the increase of specific surface areas. Consequently for any alloys, their physiochemical properties will not only depend on the constitutional compositions, but also the particle size. These properties can be consequently tuned and engineered according to the specific requirements by varying the elemental compositions, internal structures, particle size distributions as well as the sizes of the particles [124-126]. However the investigation of nano-alloys (NA) is still very limited. For instance, investigated by the TGA/ DSC method, Singh et al. [127] observed a reduction in the ignition delay for bimetallic nanoalloys of Ni mixed with Cu, Co and Zn. Some studies have shown that nano aluminum (nAl) in combination with copper possessed some excellent properties and can be widely used for various applications including resistance welding electrodes, electrical connectors, lead frames and the metastable intermolecular composites (MICs) [81, 128-130]. At the bulk scale, the thermodynamic and kinetic stability and the coexistence of different phases such as CuO, $Cu_2O$, $CuAl_2O_4$ and $CuAlO_2$ during the oxidation of Al-Cu system have been reported [131-133]. However there is still no detailed study of the thermal-chemical kinetics of nano alloy (NA) of copper and aluminum (nAlCu). Their properties in relation to the bulk behaviour and the individual compositional element are still unclear. In this section, the oxidation and ignition

behaviour of nAlCu in the atmosphere of air will be investigated with the help of thermo-gravimetric analysis (TGA) and differential scanning calorimetery (DSC).

### 3.3.1. Particle size, morphology, and phase composition

The morphology of the nano alloy (NA) is evaluated with SEM and is shown in **Figure 3.43.** It can be observed that the particles are agglomerated and are spherical in shape. These particles are uniformly distributed with considerable distances among them. The agglomeration is soft as the particles are coagulated by the low intensity physical forces such as Van der Waals forces, surface tension and electrostatic forces [134].

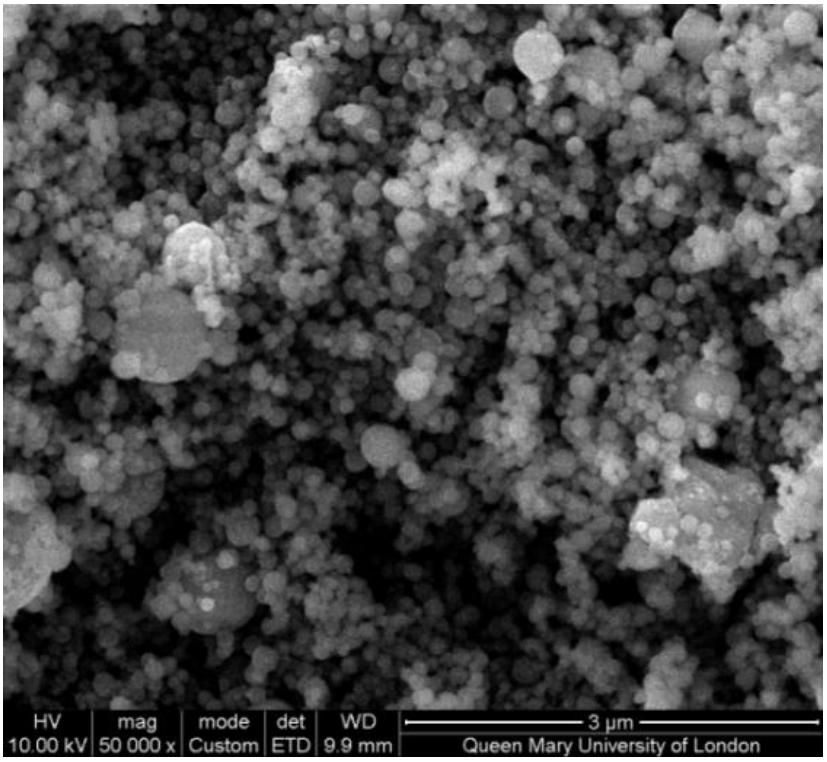


**Figure 3.43** SEM image of the particles of nAlCu Alloy (before oxidation)

**Figure 3.44** shows that the particle size distribution is monomodal having a polydispersity index of 0.33. The peak diameter is 211 nm with a z-average diameter, i.e., the cumulate mean of 343 nm and a width of 95.8 nm. The peak diameter is bigger

than that observed with TEM because the DLS measures the hydrodynamic diameter, which is the apparent size of the hydrated molecules.

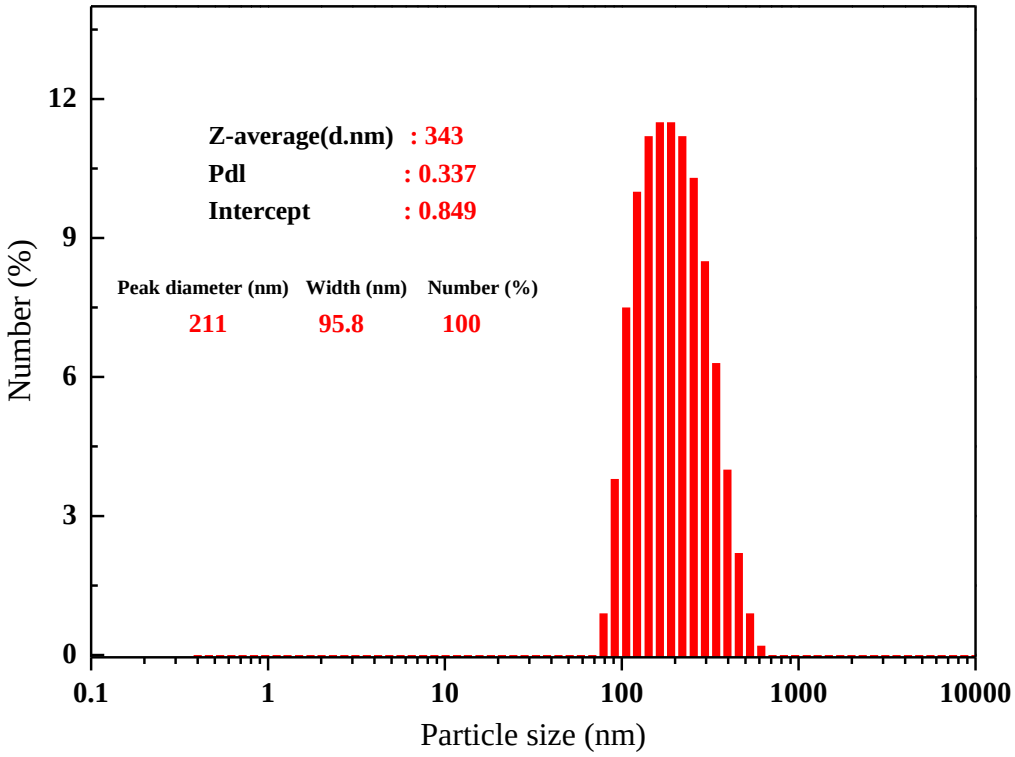


**Figure 3.44** Particle size distribution (PSD) of nAlCu Alloy

The chemical composition of the particles before and after the thermal treatment is found with EDS. It is found that the sample (before oxidation) contains Al, Cu and O as its major constitutional elements, **Figure 3.45** (a). No peaks of any other element are seen which suggests that the sample is free of any contaminations. The same analysis is also done on the end products of oxidation. Various points were selected on the micrograph. It is found that the amount of O, Al and Cu are not uniformly distributed. For instance, at point s1 the amount of Cu is 47.22 % whereas it value at s2 is only 3.85 %, **Figure 3.45** (b). This suggests that a variety of the compounds are present in the sample which is later confirmed by the X-ray diffraction analyses. EDS of both cases are given in the **Figure 3.45 (a-d)** and their weight percentages are summarised in **Table 3.7**.

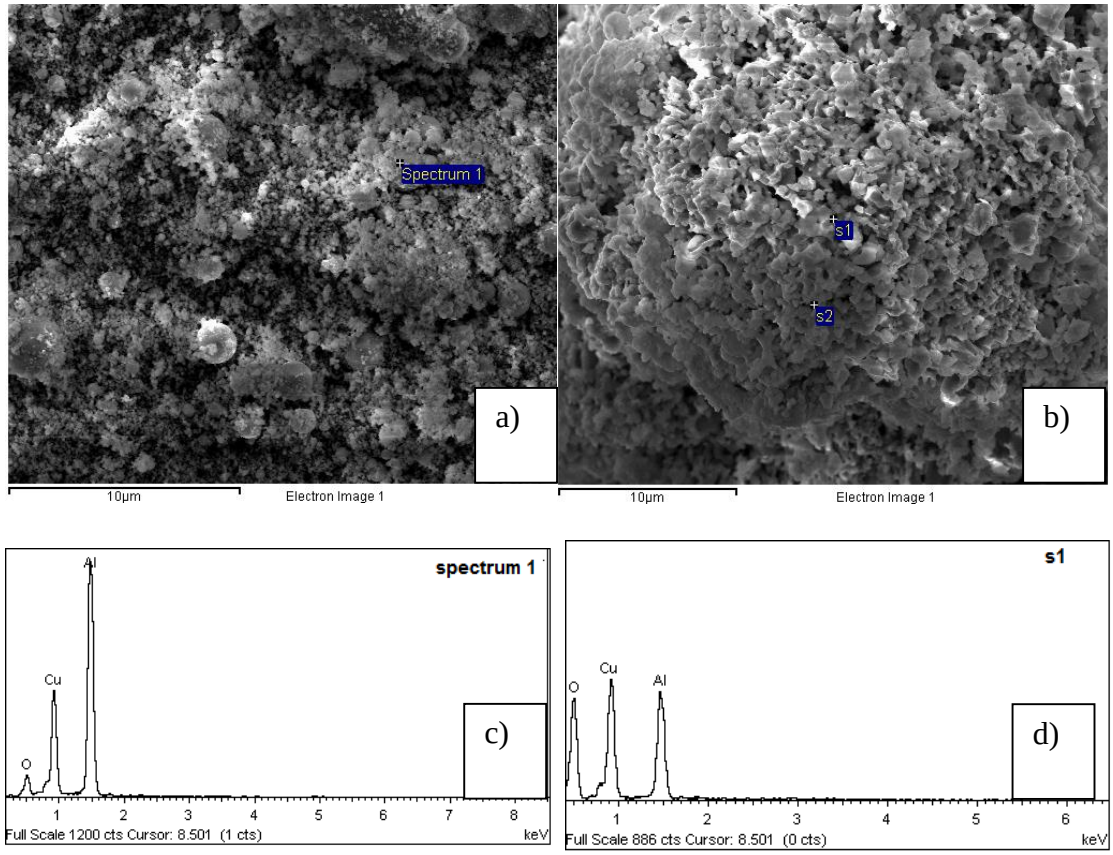


**Figure 3.45** (a) and (b) show the micrographs of the particle before and after oxidation whereas (c) and (d) show the corresponding spectrum representing peak intensities of the elements.

**Table 3.7** EDS analysis of nAlCu before and after the oxidation

| State of the sample | Points | O | Al | Cu | Total |
|---|---|---|---|---|---|
| | | Weight % | Weight % | Weight % | Weight % |
| Before Oxidation | 1 | 5.95 | 56.14 | 37.91 | 100 |
| After Oxidation | 1 | 29.89 | 22.89 | 47.22 | 100.00 |
| | 2 | 44.00 | 52.15 | 3.85 | 100.00 |

The sample contains oxygen which is in the oxide form and is passivating the particles, as revealed with TEM. It is found that the thickness of oxide passivation layer is ~ 3-4 nm, **Figure 3.46**.

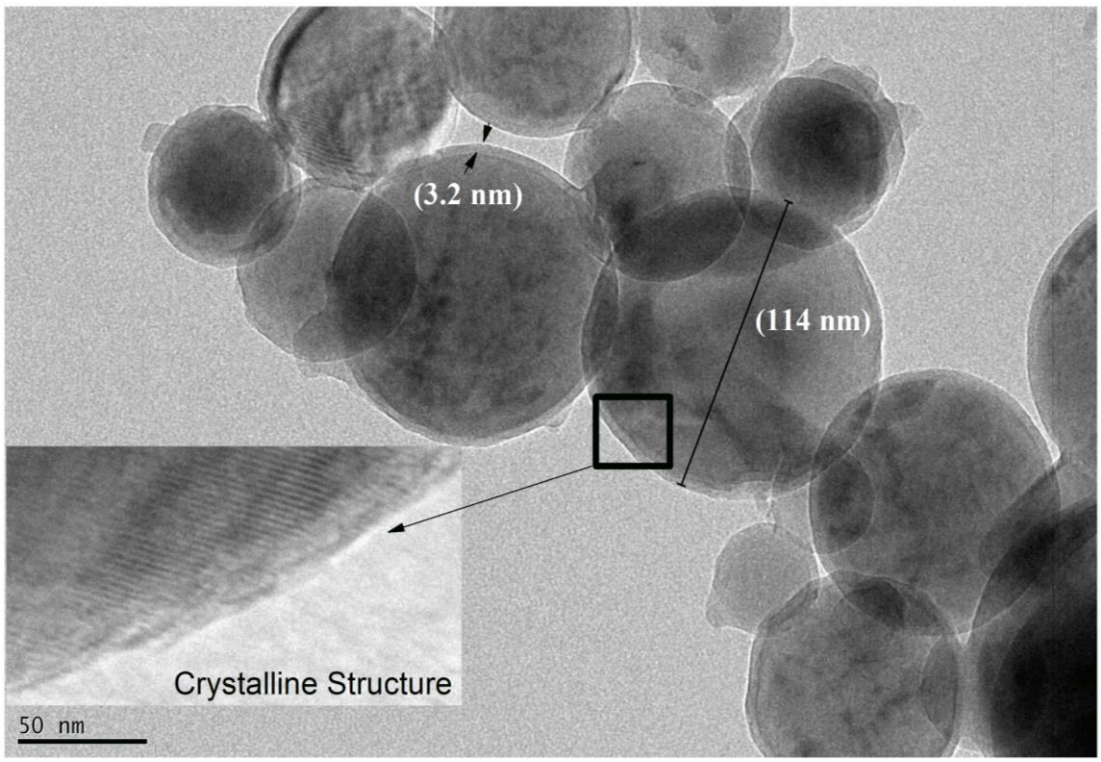


**Figure 3.46** TEM image of the NA showing passivation layer (*inset* enlarged view showing crystalline structure)

With the help of powder X-ray diffraction (XRD), the crystalline structure of the sample is revealed (**Figure 3.47**). The analysis shows that the sample contains pure Al (JCPDS card no. 04-0787), and intermetallic compounds $CuAl_2$ (JCPDS card no. 25-0012) and $Cu_9Al_4$ (JCPDS card no. 24-0003). On the diffractogram of the sample, no peaks of oxide are detected, which means that the passivating oxide layer is in the amorphous phase. No peaks of copper are identified.

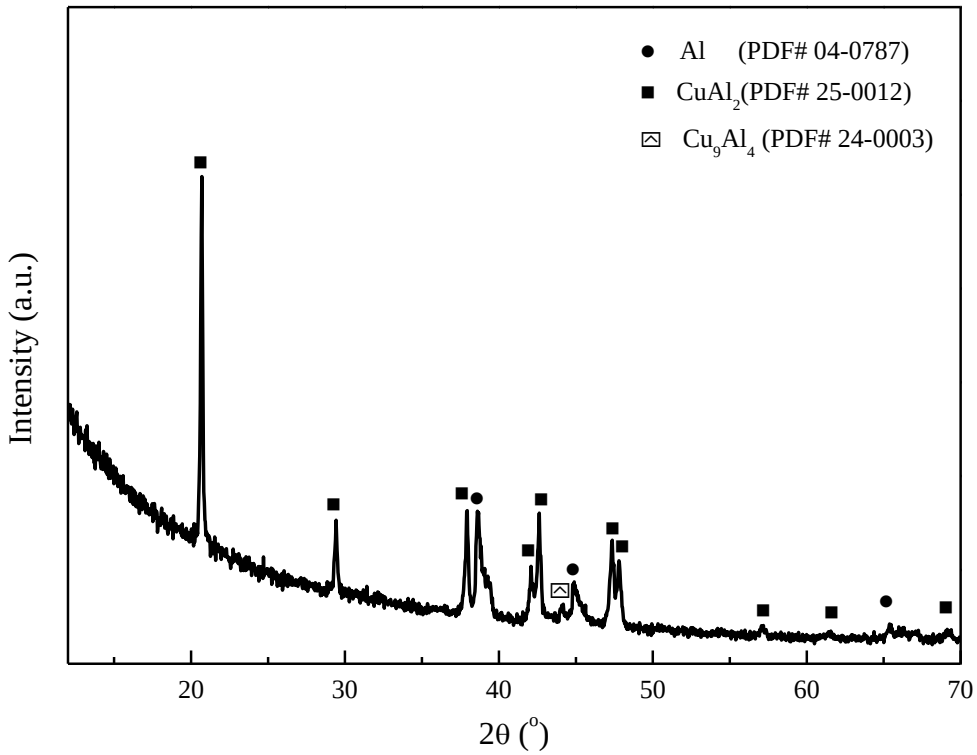


**Figure 3.47** XRD trace of NA before thermal heat treatment

After the thermal treatment of the particles at various heating rates, the shape profile is assessed with SEM, **Figure 3.48(a-f),** and following observations can be found 1) the particles have lost their spherical shape in their entirety and are morphed into flakes, crystals, spongy and needle like structures, 2) the particles are sintered and inter particles and inter aggregates agglomeration are appearing. The agglomeration is hard due to the chemical bonds of high strength among them, 3) the most striking aspect of SEM images is the variety of the particle sizes, e.g., some particles are very small while others are much bigger than the sample's original size, and 4) big round globular and wedge shaped aggregates of the order of several micrometres are also observed. These are made with the assemblages of small crystals and needle-like particles.

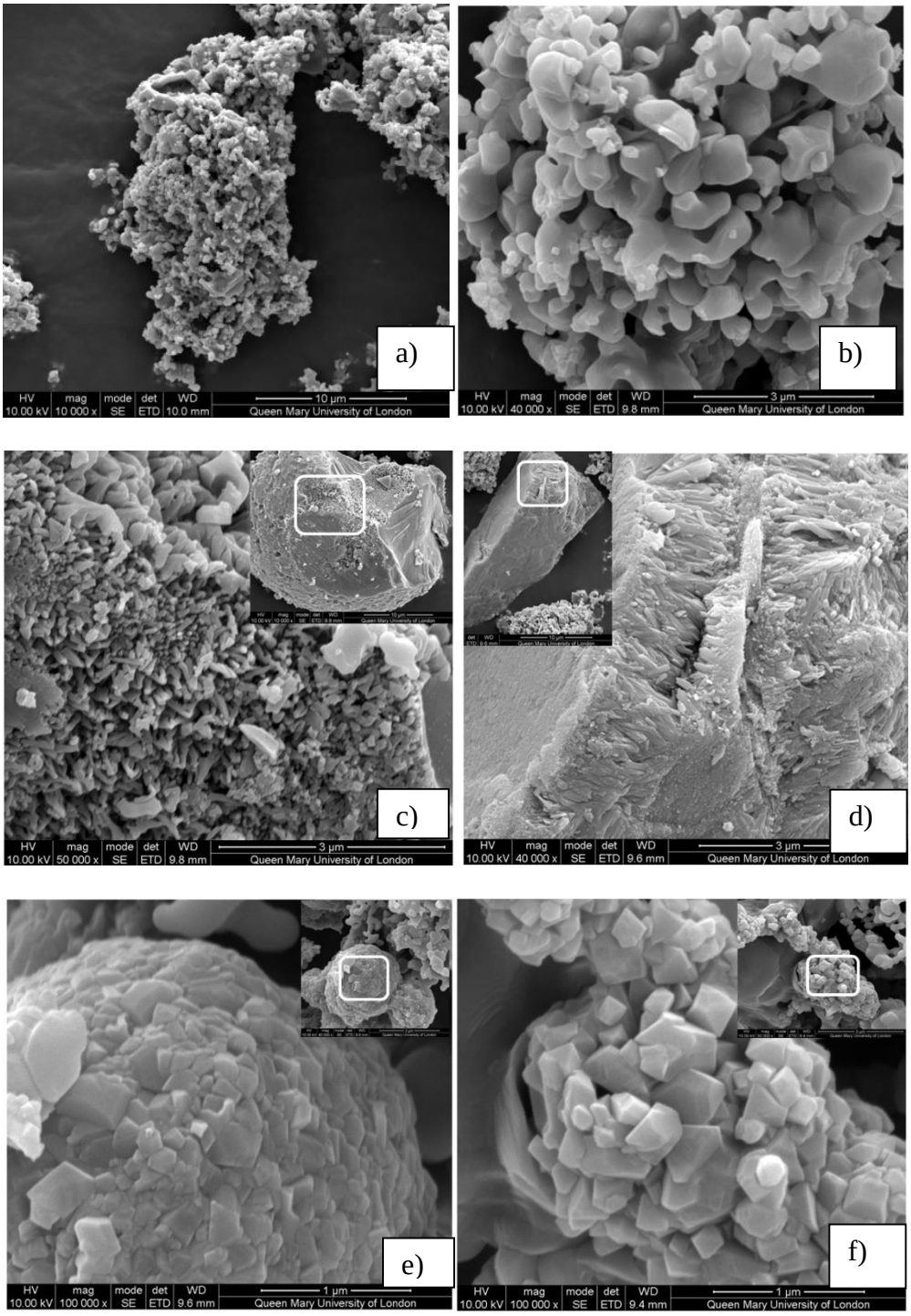


**Figure 3.48** SEM images of nAlCu after oxidation at various heating rates conditions.

### 3.3.2. Thermal analysis and reaction kinetics

Thermal characteristics such as thermal reactivity, ignition temperature, peak temperatures of various physiochemical reactions of nAlCu are evaluated by TGA/DSC.

The particles are heated in the thermobalance from room temperature to 1200 °C under various heating rates (2-30 K/min) in the atmosphere of air. During the experimentation, the amount of heat flow and mass change are recorded simultaneously. It is observed that the heat flow patterns of the particles changed significantly with the heating rates. The experiments fall into two distinct types: low heating rate (β = 2-7 K/min) and high heat rate (β >7 K/min). For the low heating rate, the oxidation process completes without any sudden change of heat or mass. For the high heating rate, there is a sudden increase of mass and heat flow, indication of an early ignition. Both oxidation types have some distinctive features and are explained separately.

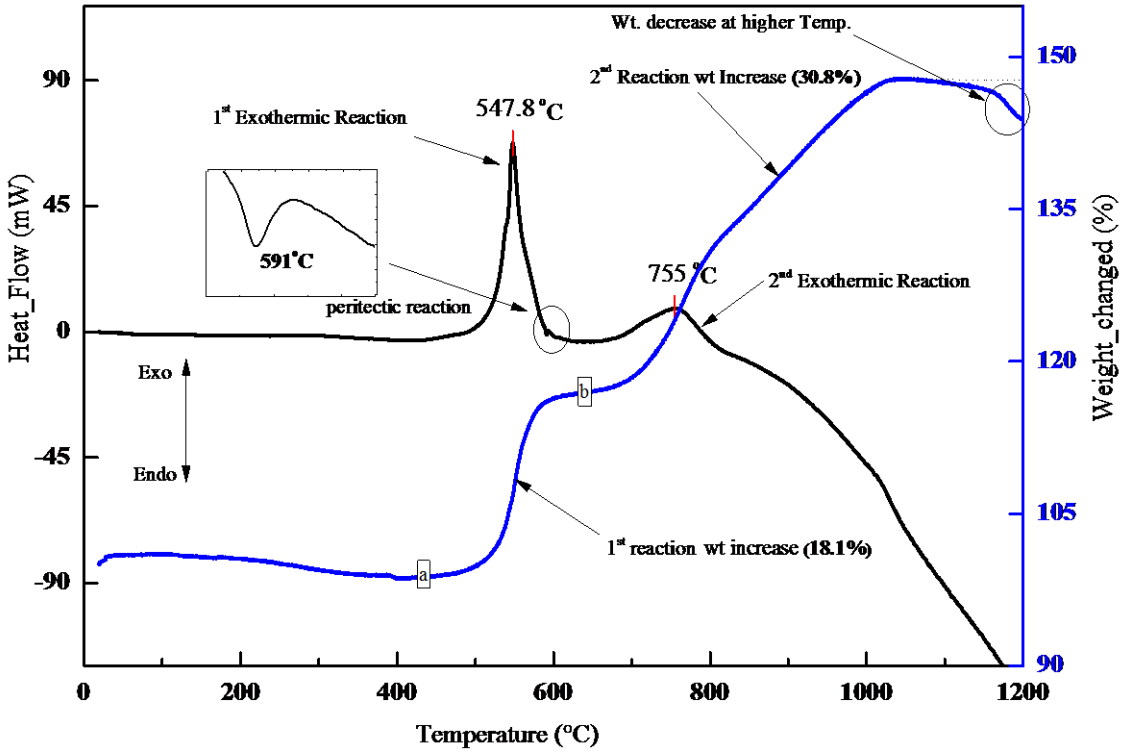


**Figure 3.49** Example TGA/DSC curve of nAlCu at 7 K/min (no ignition)

**Figure 3.49** shows simultaneous TGA/DSC traces at the heating rate of 7 K/min. It can be observed that the mass of the sample gradually decrease to point 'a' (450 °C). This can be ascribed to the desorption of the adsorbed moisture and $CO_2$ in the sample [102]. The first exothermic process starts at 525 °C, peaks at 547.8 °C and ends at 590 °C.

During the reaction, an increase of 18.1% of the mass and 2.3kJ of energy produced is observed. The endothermic peak is seen at 591$^{o}$C, which is due to the peritectic reaction [135], as shown in the phase diagram of AlCu binary system in **Figure 3.50**.

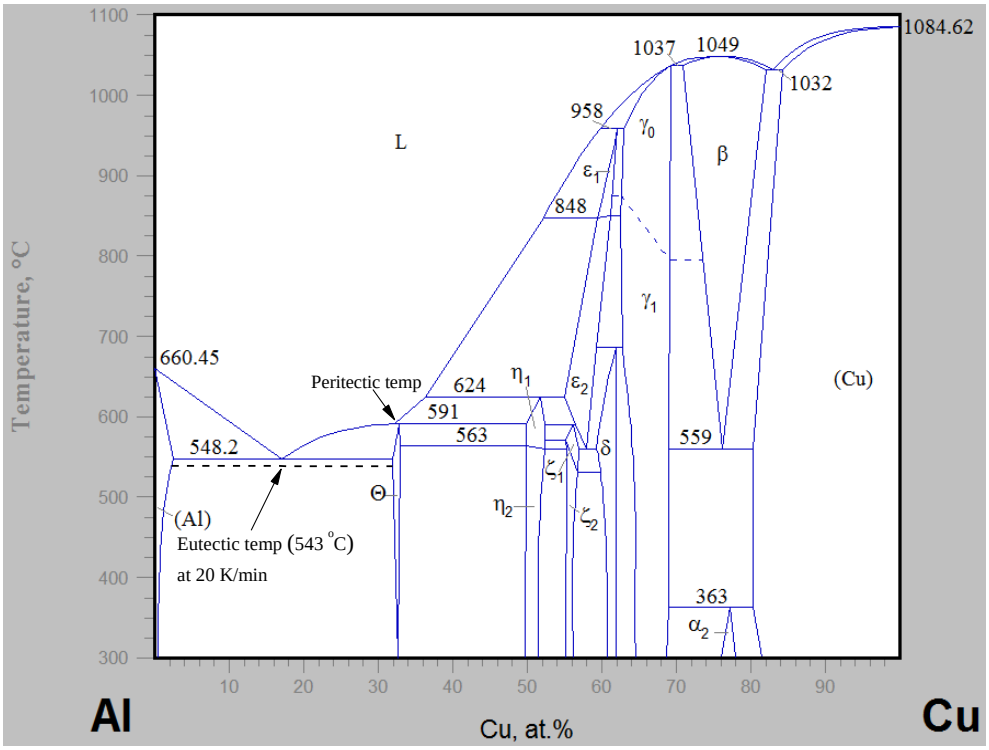


**Figure 3.50** Phase diagram of Al-Cu alloy binary system [136]

The second exothermic process peaks at 755 $^{o}$C, after which the rate of the reaction decreases and the sample goes through an endothermic process till the experiment ends at 1200 $^{o}$C. During this reaction, the weight of sample increases linearly and the TGA trace becomes a straight line near 1000 $^{o}$C. An increase of 30.8 % of the weight is seen during this reaction. At temperature ~ 1150 $^{o}$C, the weight of the sample begins to decrease (~ 4 %) till it reaches 1200 $^{o}$C. Similar oxidation scenario is observed for heating rates of 2-7 K/min, as shown in **Figure 3.51**.

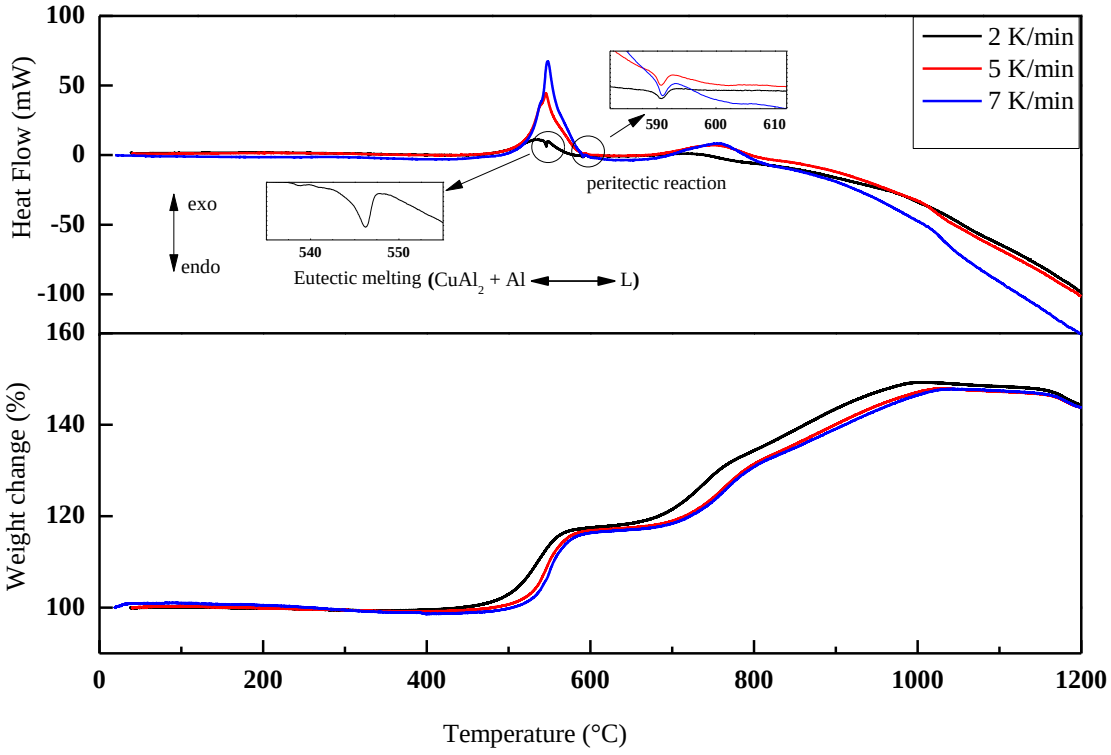


**Figure 3.51.** TGA/DSC of nAlCu at heating rates of 2-7 K/min (*inset* showing eutectic and peritectic reactions)

In the second example when the heating rate is 10 K/min, the particles go through an exothermic reaction which is characterized with a rapid rate of heat released and a sharp weight increased. This occurs during the first exothermic reaction when the amount of heat produced by the particles becomes more than the amount absorbed by the purge gases. The temperature of the particles becomes higher than that of the furnace. The temperature gradient (dT/dt) during the experiment remained constant but for a very short interval of time, it becomes higher than its set value. This run away of temperature is regarded as the ignition reaction [33, 90].

The simultaneous TGA/DSC curve at 10 K/min is taken as an example to demonstrate its characterization, **Figure 3.52** , and all the TGA/DSC curves for heating rates of 10–30 K/min are shown in **Figure 3.53.**

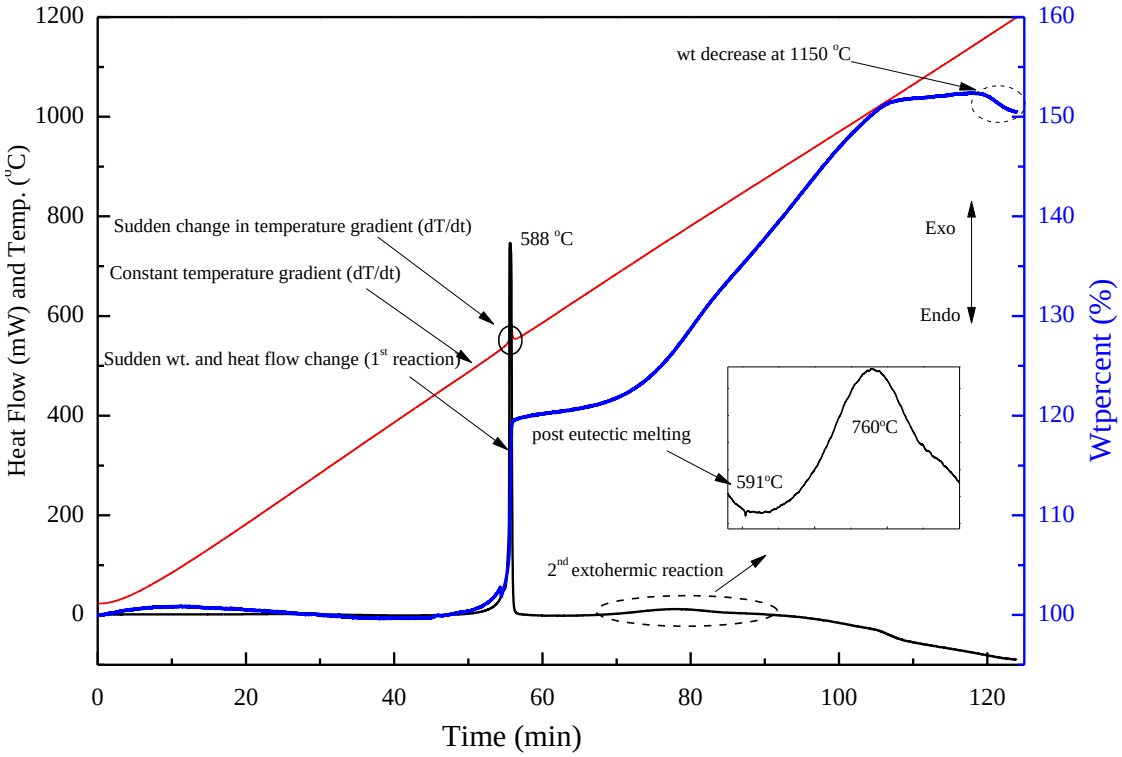


**Figure 3.52** Example TGA/DSC of nAlCu at 10 K/min (*inset* showing peritectic reaction and 2nd exothermic reaction)

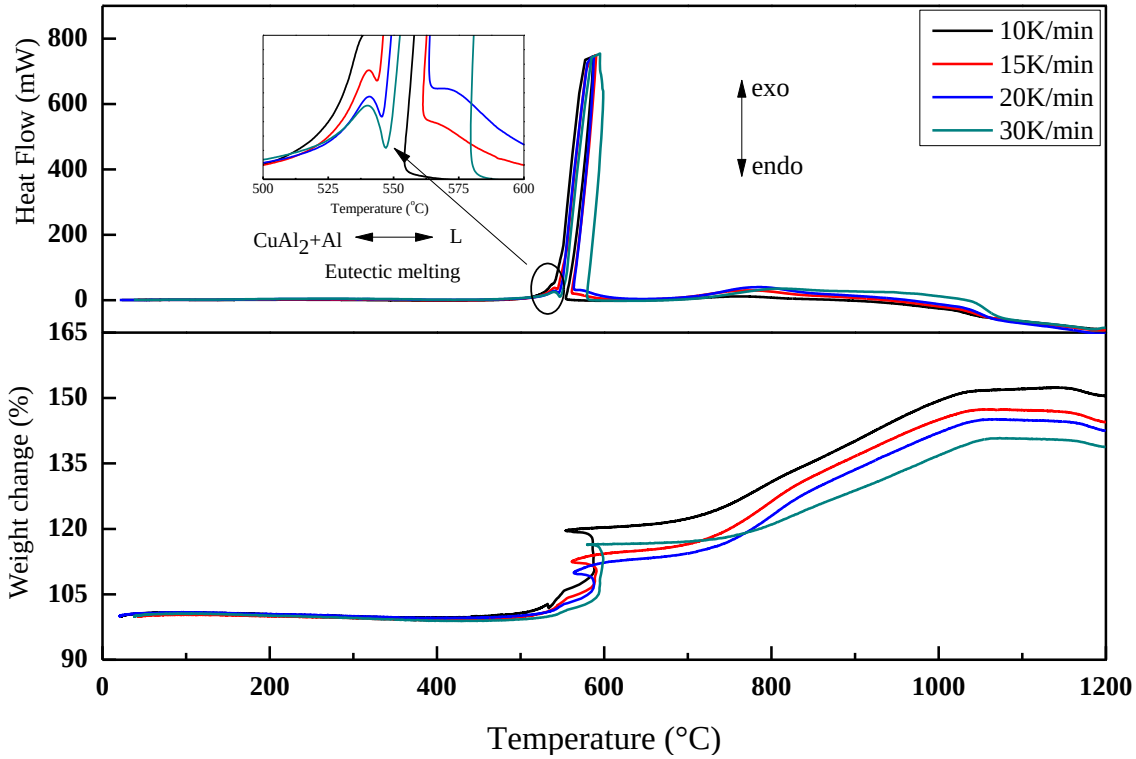


**Figure 3.53** TGA/DSC of nAlCu at heating rates of 10-30 K/min (*inset* showing eutectic melting reaction before the ignition)

From the TGA/DSC profile, it can be observed that the onset temperature for the first exothermic reaction is 500 $^{o}$C and it completes at 560 $^{o}$C. To investigate the early ignition reaction and the intervening chemical reactions, a separate experiment is performed. The particles are heated to 570 $^{o}$C in the TGA under the same conditions. The products of oxidation were then preserved and analysed with XRD ex-situ, shown in **Figure 3.54.** The peaks of δ-alumina (JCPDS card no. 04-0877) appeared on the radiograph at 2θ = 37.3$^{o}$ and 45.9$^{o}$.

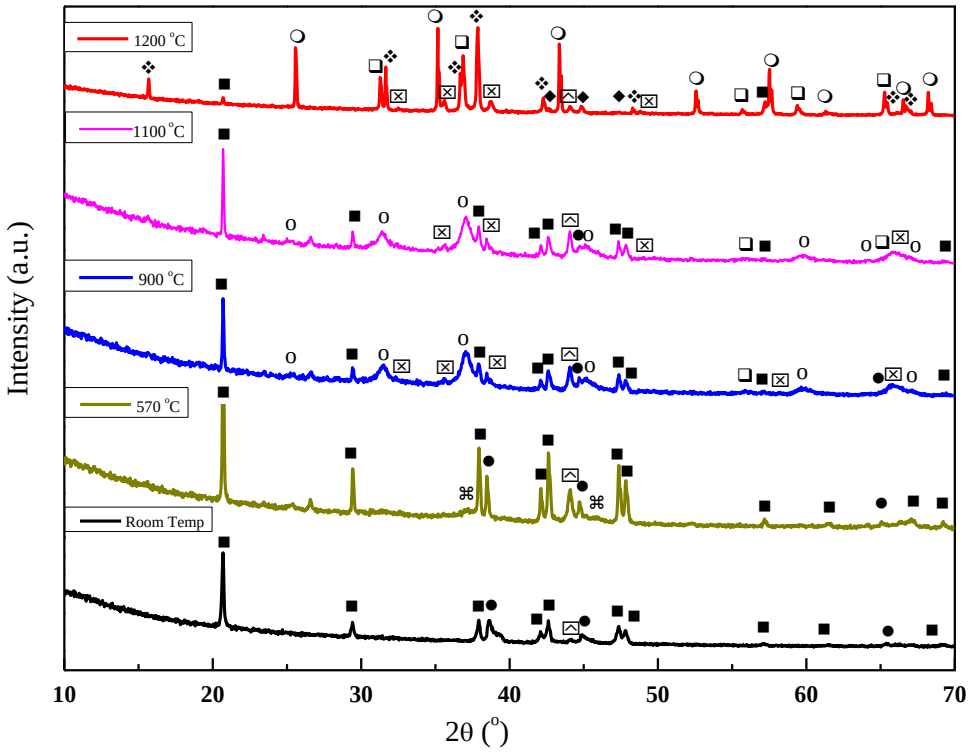


**Figure 3.54** XRD analyses of nAlCu at various temperature conditions at10 K/min (● Al, ■ $CuAl_2$, ❍ $Al_2O_3$, ☒ CuO, ❖$CuAlO_2$, ❑$CuAl_2O_4$, 🜲 $Cu_9Al_4$, o θ-$Al_2O_3$, ⌘δ-$Al_2O_3$, ◆$Cu_2O$)

The chemical reaction in the temperature span of 500 $^{o}$C ~ 600 $^{o}$C can be identified as

$$\mathbf{4Al + 3O_2 \rightarrow \delta\text{–}2Al_2O_3} \qquad (3.6)$$

During this reaction, 19.5 % of the mass increased and 4.4 kJ/g of heat produced is observed. Like pure metals, some mixtures of elements in alloys are liquefied (or solidified) at a single invariant temperature called the eutectic temperature [137]. The eutectic temperature for the Al-Cu alloy in its bulk state is 548.2 $^{o}$C. Nearly the same value for the nano alloy is found from the current experiment, 545.6 $^{o}$C ± 1.4 $^{o}$C, **Figure 3.50.**

From the DSC curve shown in **Figure 3.53** (e.g. $\beta$ = 15 K/min), it can be seen that immediately after the eutectic melting reaction, the particles go through a rapid exothermic reaction. Supported by some preliminary analysis, the melting of the particles is believed to play a major role for the early ignition of the material [138]. For pure nanoparticles such as nAl, it has been suggested that the early ignition could be associated with the melting of nAl [7]. Due to the melting, the volume of the core would increase and creates some pressure on the alumina shell, increasing the porosity (or producing some cracks in certain local locations) of the shell that leads to the ignition. From the DSC/TGA data, it appears plausible that similar scenario may happen for the nano Al-Cu alloy.

The second peak on DSC trace starts at 625 $^{o}$C and reached the maxima at 760 $^{o}$C after which the rate of energy released decreased constantly. The span of this reaction is wider as compared to the first reaction. During this reaction the weight of the sample is increased by ~31.8 % until 1040 $^{o}$C where the TGA trace becomes flat. To characterize this peak and the associated reactions, the particles were oxidized from room temperature to 900 $^{o}$C and 1100 $^{o}$C, and XRD measurements were arranged to examine the oxidation products. The spectrograph of the particles heated to 1100 $^{o}$C is similar to

that obtained at 900 $^{o}$C. From the XRD data analyses of the products at 900 $^{o}$C, the peaks of copper oxide CuO (JCPDS card no. 48-1548) and θ-$Al_2O_3$ (JCPDS card no. 11-0517) are identified. Various minor phase peaks of complex aluminum oxide such as Copper Aluminate spinel $CuAl_2O_4$ (JCPDS card no. 01-1153) produced by the chemical reactions between copper oxide and δ-, θ-alumina are also found [139-141]. The likely reaction paths in the temperature range of 600 ~ 1100 $^{o}$C can be proposed as

$$\delta\text{-}Al_2O_3 \rightarrow \theta\text{-}Al_2O_3 \quad (3.7)$$

$$CuAl_2 + 2O_2 \rightarrow Al_2O_3 + CuO \quad (3.8)$$

$$Al_2O_3 + CuO \rightarrow CuAl_2O_4 \text{ (weak peaks)} \quad (3.9)$$

The formation of complex aluminum copper oxide at atmospheric pressure conditions, i.e., $p_{O2}$ = 0.21 atm, and the relationship of CuO-$Al_2O_3$ system can be understood by the phase diagram reported by Gadalla and White [131], which was further refined by Jacob and Alcock [132]. In the Cu-Al system, the peaks of $CuAl_2O_4$ are common at temperature above 1000 $^{o}$C, and its formation has been reported to near 615 $^{o}$C by Jacob and Alcock [132] based on the electrochemical methods. The diffusion of metallic ions at 900 $^{o}$C is slow hence its formation is not favourable, which explains the weak peak observed in our experiment (**Eq. 3.9**). Such an observation is consistent with the observations of Gadalla and White [131] who found the formation of $CuAl_2O_4$ by the thermo-gravimetric method at a temperature in the range of 1000 $^{o}$C.

When the temperature of the sample reached above 1150 $^{o}$C, the weight of the particle was decreased by ~ 4 %. To investigate such a process, XRD analysis of the particles oxidized at 1200 $^{o}$C was studied. Various phases of complex aluminum oxides are identified in the products of the oxidation reaction. These oxides are produced by the chemical reactions between CuO and alumina. The radiograph shows the peaks of a variety of the products, which includes Al, $CuAl_2$, CuO, $CuAl_2O_4$, $\alpha$-$Al_2O_3$ (JCPDS card no. 46-1212) and $Cu_2O$ (JCPDS card no. 35-1091). The peaks of multi oxide form of Cuprous Aluminate Delafossite $CuAlO_2$ (JCPDS card no. 35-1401) are also observed. Hence the complicated ongoing reactions at over 1100$^{o}$C can be proposed as,

$$\theta\text{-}Al_2O_3 \rightarrow \alpha\text{-}Al_2O_3 \quad (3.10)$$

$$Al_2O_3 + CuO \rightarrow CuAl_2O_4 \quad (3.11)$$

$$2CuAl_2O_4 \rightarrow 2CuAlO_2 + Al_2O_3 + 0.5O_2 \text{ (liberated)} \quad (3.12)$$

Or

$$4CuO \rightarrow 2Cu_2O + O_2 \text{ (liberated)} \quad (3.13)$$

$$Cu_2O + Al_2O_3 \rightarrow 2CuAlO_2 \quad (3.14)$$

And

$$4CuAlO_2 + O_2 \rightarrow 2CuO + 2CuAl_2O_4 \quad (3.15)$$

$$4CuAlO_2 + 2Al_2O_3 + O2 \leftrightarrow 4CuAl_2O_4 \quad (3.16)$$

According to the temperature-pressure phase fields boundaries of CuO-$CuAlO_2$-$CuAl_2O_4$ system [133], $CuAlO_2$ is thermodynamically stable only above 950 $^{o}$C in air.

Below this temperature it transforms to $CuAl_2O_4$ following the pathway of **Eq. 3.15**. In the rich mixture of alumina, the Cuprous Aluminate Delafossite $CuAlO_2$ is metastable in air between 1050 $^oC$ and 1170 $^oC$ and changes to Copper Aluminate spinel $CuAl_2O_4$ following a reversible reaction **(Eq. 3.16)** [141, 142]. The formation of $CuAlO_2$ is thermodynamically feasible only at a temperature of 1175 $^oC$ [131, 132]. The decrease of the weight above 1175 $^oC$ can be attributed to the oxygen produced during the reduction of CuO to $Cu_2O$ as in the reaction **(Eq. 3.12)** or **(Eq. 3.13).**

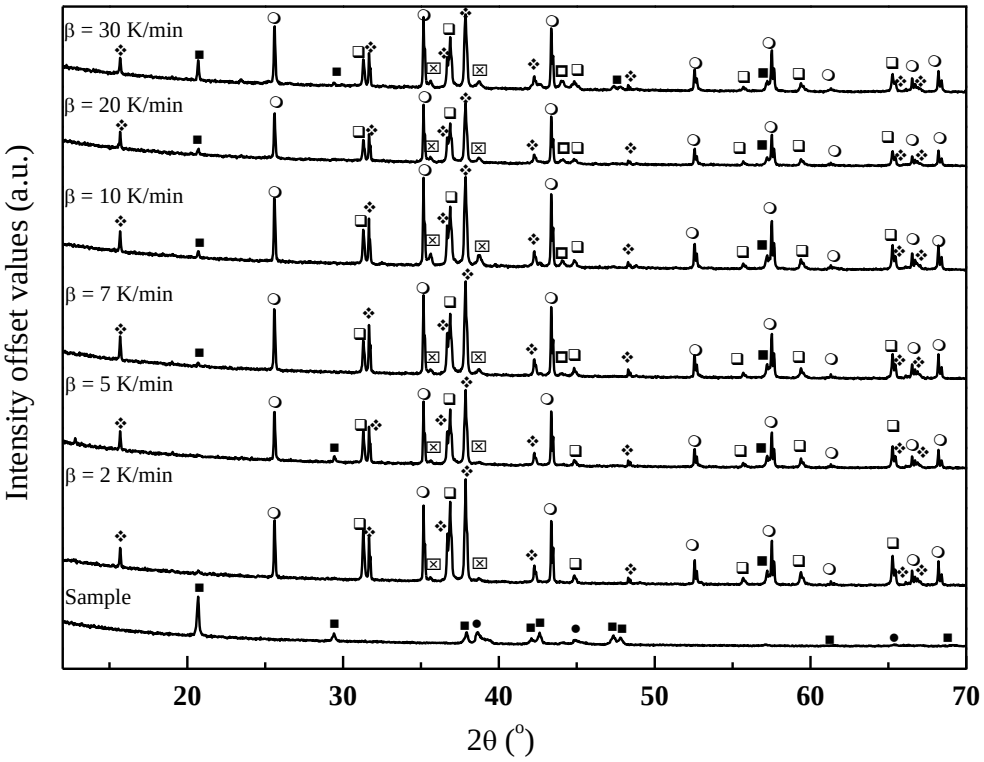


**Figure 3.55** XRD analyses of nAlCu at various conditions of heating rates ( ● Al, ■ $CuAl_2$, ❍ $Al_2O_3$, ☒ CuO, ❖ $CuAlO_2$, ❑ $CuAl_2O_4$, ⛛ $Cu_9Al_4$, o θ-$Al_2O_3$, ⌘ δ-$Al_2O_3$, ◆ $Cu_2O$ )

The peaks of α-alumina have gain strength due to the crystallographic transformation of theta-alumina at high temperature. Overlapping peaks of $Cu_2O$ (JCPDS card no. 35-1091) with alumina and delafossite are also seen at 1200 $^oC$. Throughout the sequence of thermal treatment the intensities of the peaks of $CuAl_2$ and Al are decreased with the

temperature. No elemental Cu peaks are observed. The XRD analyses of the powder under various heating rates are shown in **Figure 3.55**. It can be seen that the strength of Al peak is increasing with the heating rate which suggests that the amount of unreacted Al is increasing with it.

## 3.4. Experimental Study of Thermal Oxidation of Nano-alloy (NA) of Aluminium and Zinc (nAlZn)

Metallic particles such as aluminium and zinc have important applications in many industries, and alloying is usually used at the bulk scale to improve the performance. Due to the synergistic effects of the constituent alloying materials, the physiochemical properties of the alloys can be improved by chemical reordering and spatial redistribution of the atoms [24]. In addition, the alloying increases the surface area of the particles that will increase the rate of reaction [9, 25]. AlZn alloys have been found good application in thermal spraying, soldering, and anti-corrosive agency [143, 144]. Many of these applications involve heating and oxidation reaction, which requires to be carefully controlled either to inhibit or to accelerate the process.

The oxidation mechanism of bulk metals has been well understood, which is diffusion-controlled where the growth rate of oxide film depends upon the diffusion coefficients of the reacting species [30, 145]. At the nanoscale, as the particle size is smaller or comparable to the mean free path of air, deviations from the conventional laws are expected. For instance, the oxidation process may change from the diffusion-controlled to the kinetically-controlled mode [32]. At the nanoscale, it also becomes possible to engineer different properties by controlling the particle structure and morphologies to

suit different applications. The oxidation characteristics of individual components of AlZn alloy particles have been widely investigated in the past decade [32, 146, 147]. For aluminium nanoparticles, several theories including the diffusion oxidation mechanism (DOM) and melt dispersion mechanism (MDM), have been proposed. At low heating rates, the oxidation could be described by a shrink-core model, which proceeded by four stages as the temperature increases and controlled by the distinctive phase transition of the oxide and the melting [85]. The oxidation process of Zn powders under various environments has been studied by many authors. For instance, Delalu et al.[148] showed that the isothermal oxidation of zinc particles obeyed the parabolic growth law for micrometre-sized zinc particles (65-375 μm). Zhou et al. [149] and Alivov et al. [150] observed that the transformation of Zn powder to ZnO was independent upon the duration of the oxidation and the crystallanity of ZnO was dependent on the temperature. Aida et al. [147] suggested that the oxidation of zinc powder was controlled by the diffusion of oxygen ions in the zinc matrix hence the temperature and species mobility played vital roles in the oxidation kinetics. Ma and Zachariah [151] reported two reaction regimes for Zn nanoparticles in the size range of 50-100 nm, with a slower reaction regime at lower temperatures, followed by a faster oxidation regime occurring at higher temperatures. The oxidation process is again diffusion controlled and can be described by the shrink core model. The reactivity was observed to increase with the decrease of particle size, i.e. the oxidation onset temperature was 250 $^{o}$C for 50 nm, and ~300 $^{o}$C for 100 nm particles.

Some studies have shown that aluminium nanoparticles (nAl) in combination with copper possessed some excellent properties and can be potentially used in resistance welding electrodes, electrical connectors, lead frames and the metastable intermolecular

composites (MICs) [81, 128-130]. However there is still no detailed study of the thermal-chemical kinetics of AlZn nanoalloys (nAlZn). Their properties in relation to the bulk behaviour and the individual elements are still unclear. In this section, details of results of oxidation of AlZn nanoalloy (nAlZn) are discussed.

### 3.4.1. Powder characterisation

The morphology of the nAlZn at various temperature conditions is evaluated with SEM. The SEM image of the particles before the oxidation is presented in **Figure 3.56**. Particles have spherical shapes and a soft agglomeration due to weak physical forces like surface tension, van der Waals forces and electrostatic forces can be observed [134].

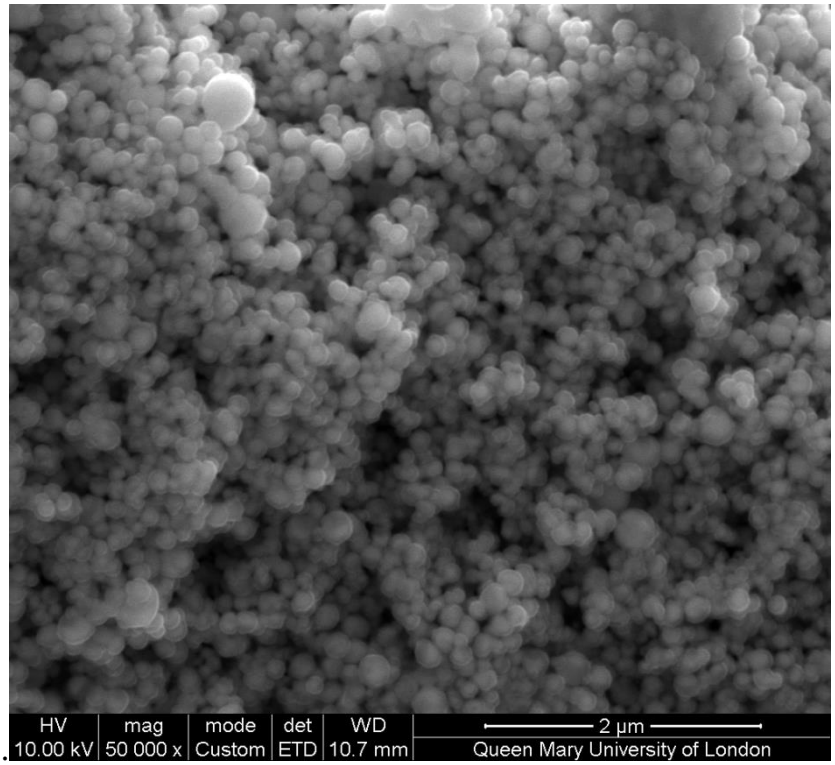


**Figure 3.56** SEM micrograph showing the particles of nano alloy of Zn and Al are spherical and agglomerated

The chemical composition of nAlZn is estimated with the Energy-dispersive X-ray spectroscopy (EDS). It is found that the sample contains 4.8 % of oxygen, 18.3 % of Al and 76.9 % of Zn, i.e., in the molar ratio of 1:2.25:3.91 for O, Al, and Zn respectively. The EDS spectrum shows a weak signal of oxygen, **Figure 3.57(b).**

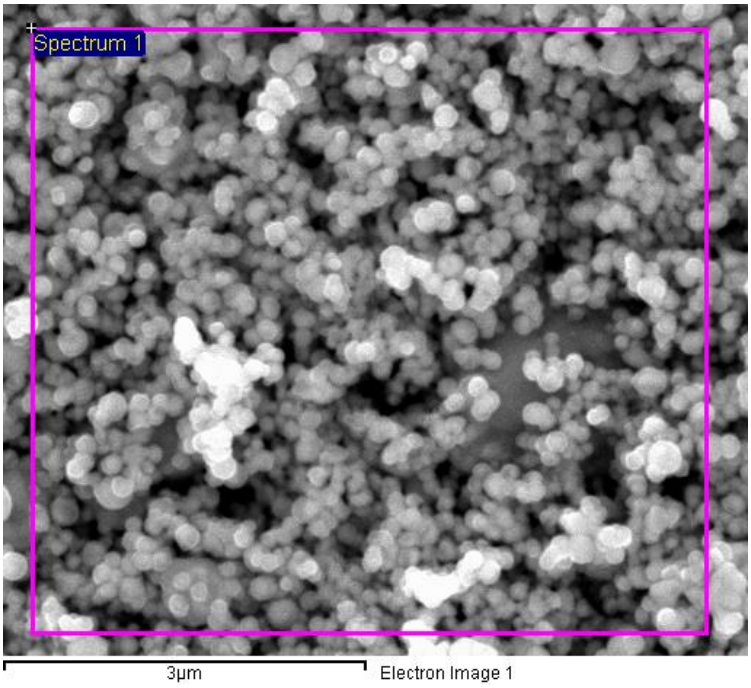


**(a)**

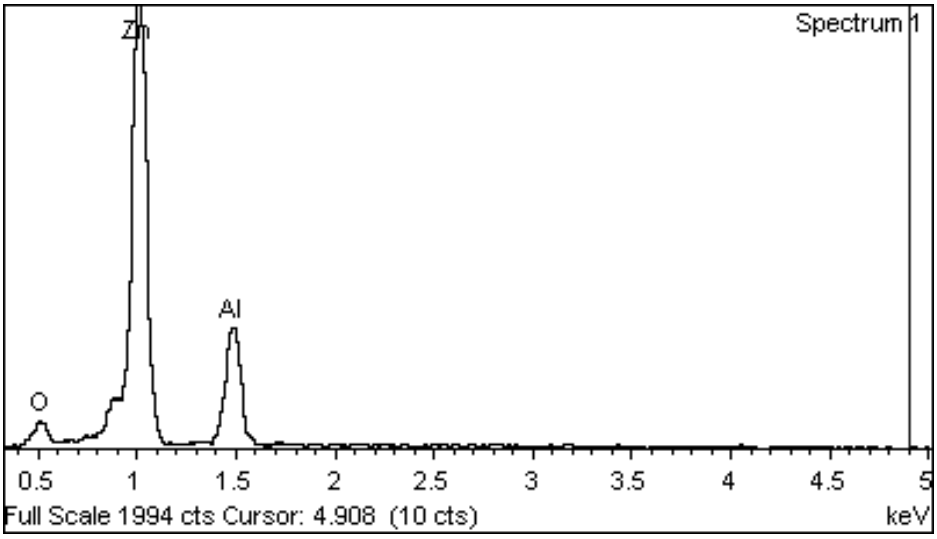


**(b)**

**Figure 3.57** EDS analysis of the sample showing a weak signal of Oxygen.

Diffractogram of the particles does not show any peak of the oxide compound. This suggests that the oxide contained by the particles is in the amorphous phase. However it is unclear about the exact form of the oxides, i.e. ZnO, $Al_2O_3$ or some other compounds. The active metal content enclosed inside the oxide layer could be in the regime of

80%~94% of the metal content. With the help of TEM it is found that the particles are blanketed by a passivation layer having a thickness of ~5-6 nm. TEM image shows that the diameter of the particle ranges from 28 to 240 nm, **Figure 3.58.**

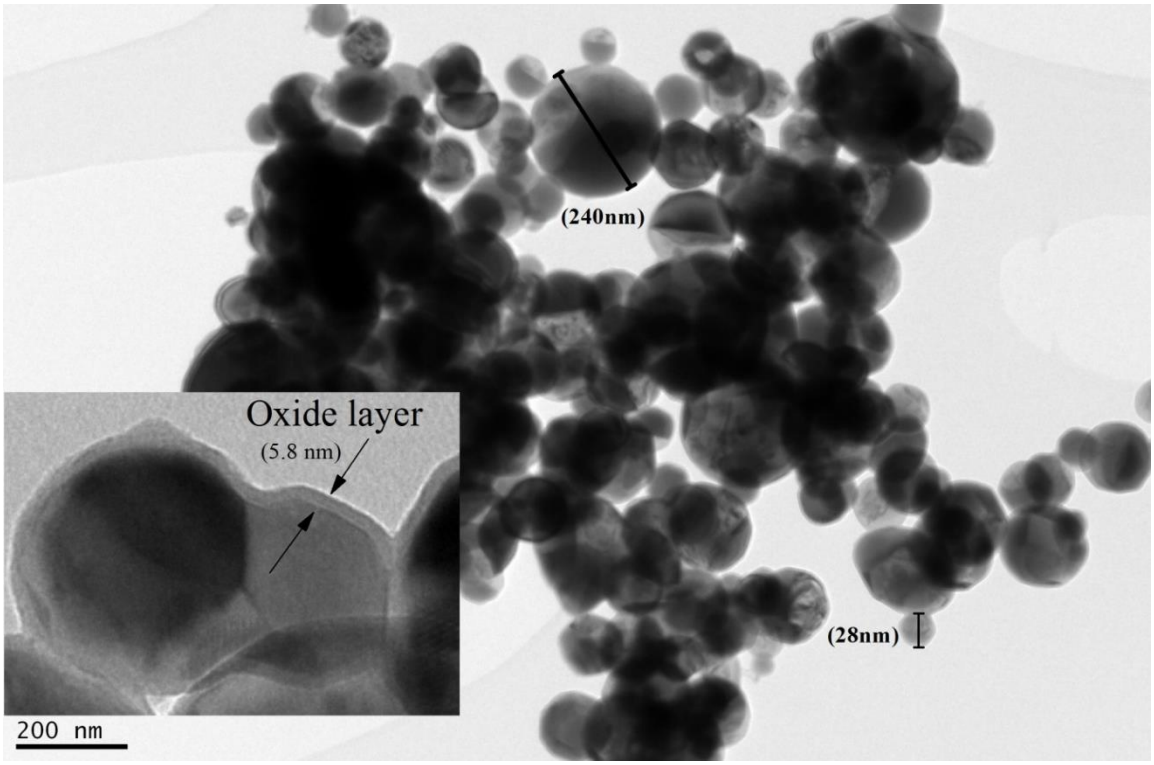


**Figure 3.58** TEM image showing that the particles diameter ranges from 28 to 240 nm and is encapsulated with an oxide layer of 5.8 nm thickness.

X-ray diffraction (XRD) of the sample shown in **Figure 3.59** reveals that the nAlZn is in the solid solution form. No peaks of any intermetallic compounds of Zn and Al, which should be formed with definite stoichiometric ratios, are observed. XRD pattern shows the peaks of aluminium (JCPDS No. 04-0787) at $2\theta = 38.52^{o}, 44.80^{o}, 65.21^{o}$ and of zinc (JCPDS No. 04-0831) at $2\theta = 36.31^{o}, 39.0^{o}, 43.26^{o}, 54.33^{o}, 70.09^{o}$ and $70.66^{o}$. No peaks of any other material are observed, which means that the sample is in the pure form.

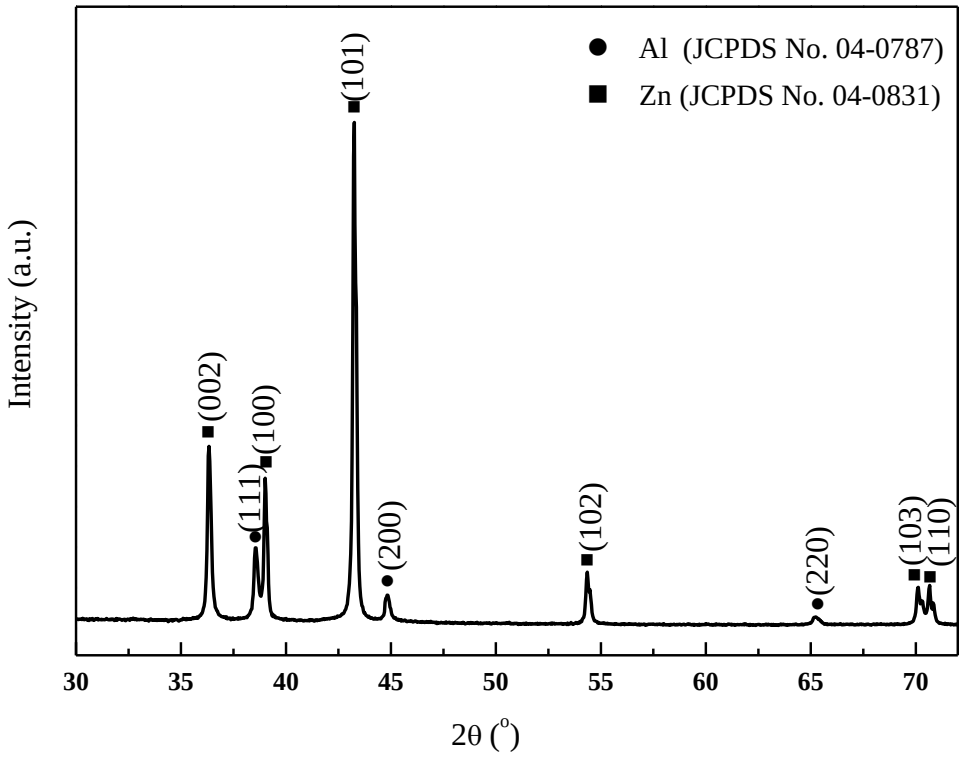


**Figure 3.59** XRD showing that the NA does not make intermetallic compounds

The BET surface area of the sample particle is determined as 7.73 $m^2/g$. Assuming that all particles having smooth spherical shapes, the BET equivalent diameter $d_{BET}$ is calculated with the relationship $A_{BET} = 6/(\rho * d_{BET})$ [152], where $A_{BET}$ is the specific area, $\rho$ is the density of the particles (taken as 5.5 g/cc) and $d_{BET}$ is the equivalent diameter of the particles. The calculated equivalent diameter is 141 nm, which is in the range of TEM observation. **Figure 3.60** shows the adsorption isotherm of nAlZn.

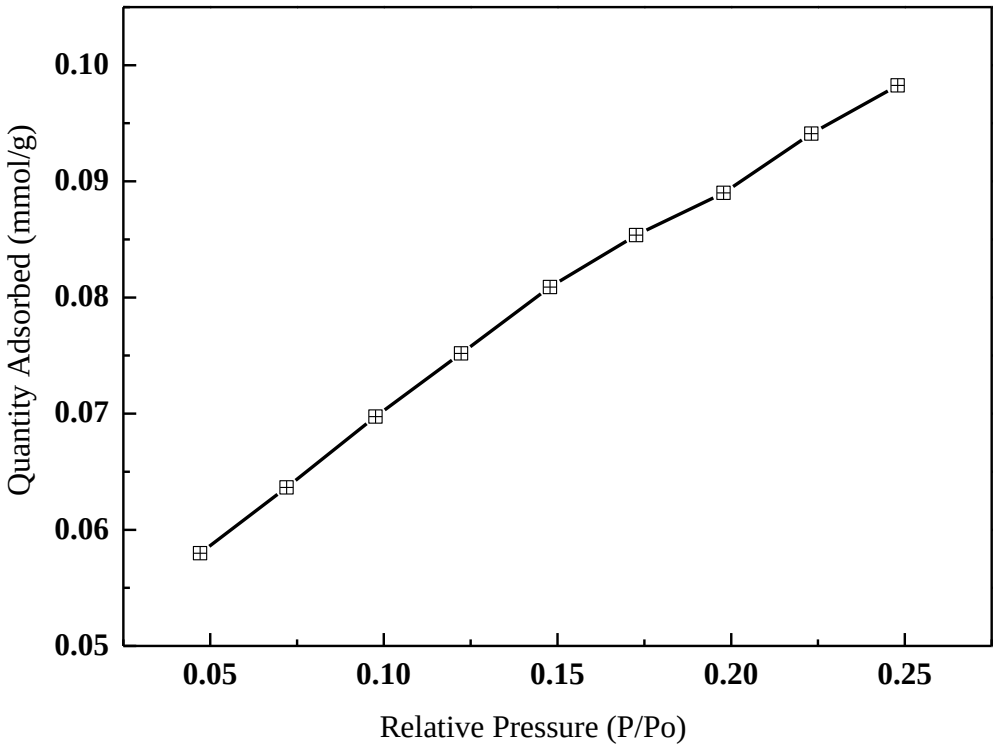


**Figure 3.60** Isotherm of the nAlZn showing the relationship of the relative pressure and the quantity adsorbed

## 3.4.2. Thermal chemical characteristics

The samples are oxidised in the atmosphere of dry air using a thermobalance (STA1500), and thermogravimetric (TGA) and differential scanning calorimetery (DSC) analyses are performed simultaneously. The oxidation characteristics of n-AlZn are similar under all the heating rates investigated. Heating rate of 10 K/min is taken as an example to illustrate the thermal behaviour and oxidation kinetics of the nAlZn from 25 to 1200 $^{o}$C. Simultaneous TGA-DSC curve is shown in **Figure 3.61** together with marks showing distinctive characteristic points. According to alteration of the energy flow and the mass of the sample, the whole heating process can be generally divided into three stages as the temperature increases. The first stage starts from the room temperature (RT) and ends at 390 $^{o}$C, the second stage is from 390 to 725 $^{o}$C, and the third stage begins from

725 ºC and extends to the completion of heat treatment process at 1200 ºC. These three stages are explained separately

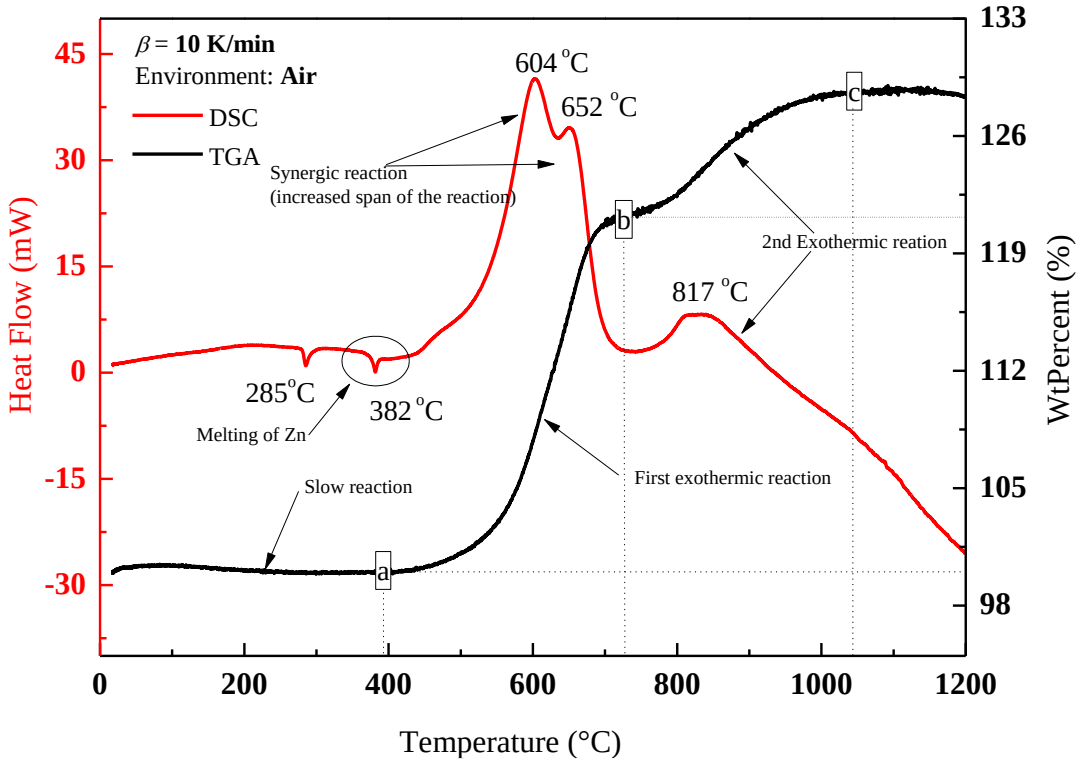


**Figure 3.61** DSC/TGA curve of nAlZn at a heating rate of 10 K/min (RT-1200ºC) showing interesting features.

### 3.4.2.1. Stage 1 (RT- 390 ºC)

During this temperature range, two endothermic reactions are observed in the DSC curve. The first peak is observed at 285 ºC and the second peak is emerged at 382 ºC. In this zone no weight gain is observed on the TGA curve. This suggests that both endothermic reactions are related to the physical changes occurring in the particles. It is believed that the first endothermic peak is related to the phase transition of the alloy and the second one is due to the eutectic melting, which are explained below.

It is known that Zn and Al metals do not make intermetallic compounds due to the weak interaction between their atoms, but Zn is soluble in Al [153] , which is also shown by the XRD result, **Figure 3.59**. The solubility of zinc in the aluminium increases with the increase of the temperature. AlZn is characterised with two phases of alloy as shown in phase diagram, **Figure 3.62.**

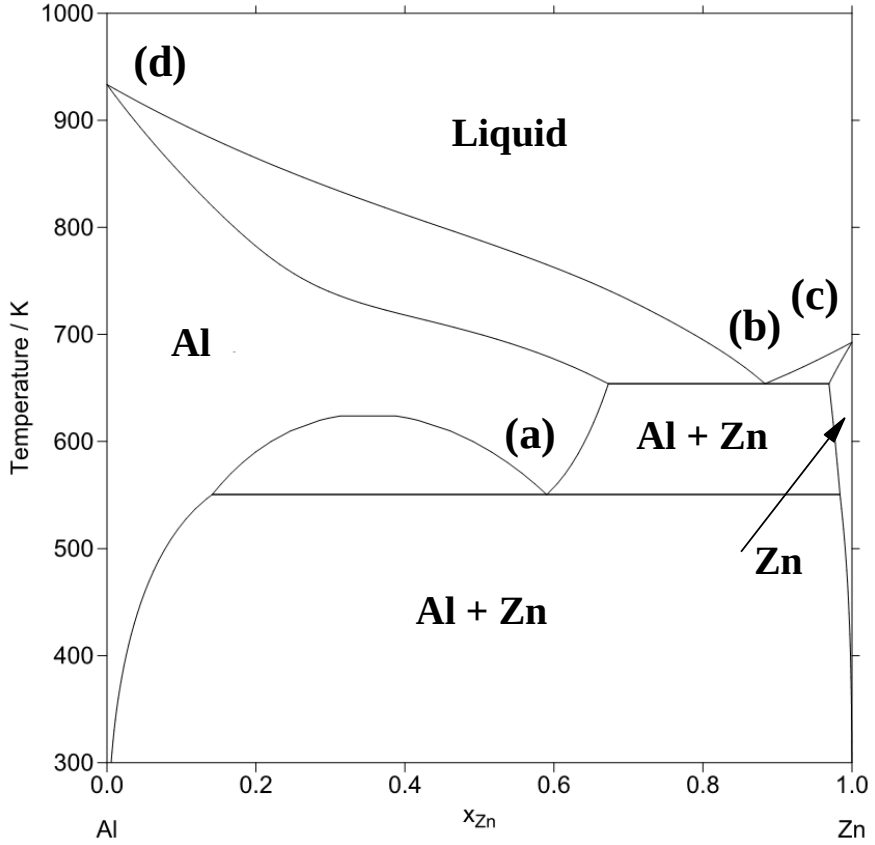


**Figure 3.62** Phase diagram of AlZn alloy showing important physical transformation temperatures [154].

The first one is face centred cubic (fcc) structured, which is the α–phase (contains ~1% Zn, ~99% Al), and the second is a hexagonal close packed (hcp) structured, the β–phase (contains ~ 99% Zn, ~ 1% Al). Both phases of AlZn alloy slowly but gradually reach the equilibrium state. The capacity to attain the equilibrium increases with the increase

of temperature. When the temperature reaches 285 $^{o}$C, there is a transformation of β-phase (hcp) → α–phase (fcc) [155, 156]. This transformation is an endothermic process and is believed to be associated with the first endothermic peak of DSC curve at 285 $^{o}$C. To examine whether this phase transformation is reversible or not, a separate experiment is performed, where the particles were heated to 400 $^{o}$C at the heating rate of 10 K/min and then cooled to room temperature in the atmosphere of nitrogen, under the same heating rate. The DSC curve is shown in **Figure 3.63**.

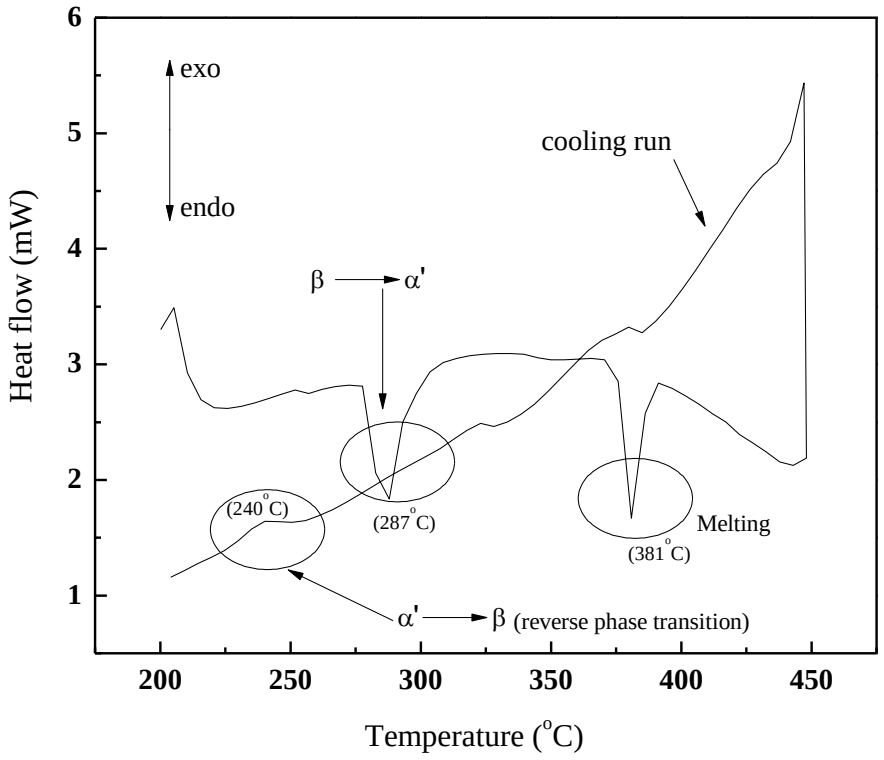


**Figure 3.63** DSC showing endothermic transformation of β-phase to α'-phase of nAlZn and the reverse process during cooling run shows the sample exhibited a temperature hysteresis.

During the heating process, the particles go through a phase transformation, associated with a peak emerged ~ 287 $^{o}$C. On the cooling run, the reverse transition from α

(fcc) → β (hcp) is observed near 240 °C, which is 47 K below the transition temperature, showing the temperature hysteresis.

The second peak at 382 °C is identified as the eutectic melting of the AlZn alloy. The phase diagram of AlZn alloy, **Figure 3.62,** shows the important transformation points at 277 °C, 381 °C, 420 °C and 660 °C. Point (a), which shows the transformation of phases, is at 277 °C in the phase diagram, and appears at 285 °C in the DSC curve. This upward shift of temperature is believed to be associated with reduction of particle size to the nanometer scale. Point **(b)** is the eutectic melting temperature of the alloy. There is no difference of eutectic melting point, ~382 °C, of the alloy in its bulk and nanometer scales. The points **(c)** and **(d)** represent the melting temperatures of Zn and Al, respectively.

### 3.4.2.2. Stage 2 (390 °C - 725 °C)

Stage 2 is the first exothermic zone that characterised with various interesting points. On the TGA curve, this zone starts from point 'a' and ends at point 'b'. During this step of oxidation, a total weight change of 21.2 % is observed and two exothermic peaks were emerged shown in the DSC curve. The DSC curve deviated for the first time at ~430 °C, showing the start of the oxidation reaction. The first peak attained the maxima at 604 °C and ended at 635 °C. The second peak emerged at 635 °C gained maxima at 652 °C and ended at 725 °C. During the first peak, 13 % weight of the sample was increased. To understand the path of the oxidation, two separate experiments were performed where the samples were heated from the room temperature to 625 °C and 710 °C respectively, under the same heating rate. The products were cooled in the

atmosphere of nitrogen gas and XRD and EDS were arranged. The XRD traces of the products are given in **Figure 3.64(d)** and **(e).**

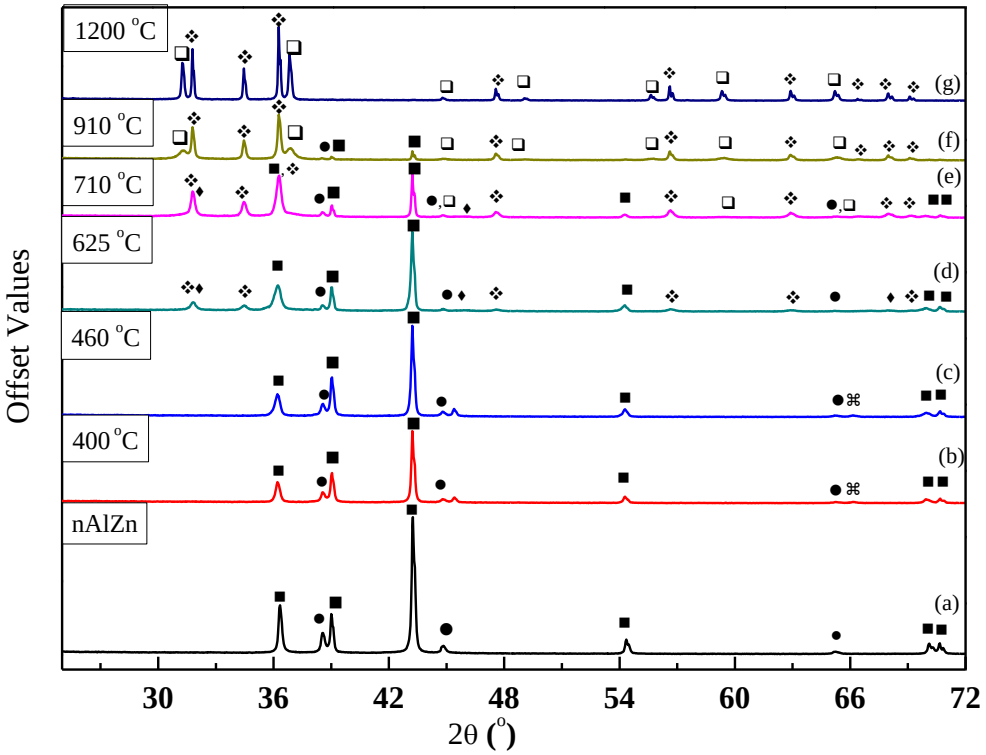


**Figure 3.64 (a-g)** XRD peak patterns of the NA at various temperatures at the heating rate of 10 K /min (● Al, ■ Zn, ❖ ZnO, ♦ γ-$Al_2O_3$, ❑ $ZnAl_2O_4$)

The peaks of ZnO (JCPDS card no. 36-1451) are emerged at 625 °C which shows the oxidation of zinc. XRD also shows the weak peaks of $\gamma$-alumina (JCPDS card No. 10-0425), which can be attributed to the combined effect of reaction of aluminum with oxygen and the transformation of amorphous alumina. As also suggested by the EDS and TEM, the particles are covered with a passivation layer of amorphous oxide. Consequently, the chemical reactions taking place in the temperature range of 430~635 °C are proposed as,

$$\mathbf{2Zn + O_2 \rightarrow 2ZnO} \quad (3.17)$$

$$\mathbf{2Al + 3/2\ O_2 \rightarrow \gamma\text{-}Al_2O_3} \quad (3.18)$$

$$\mathbf{Amorphous\text{-}Al_2O_3 \rightarrow \gamma\text{-}Al_2O_3} \quad (3.19)$$

XRD trace of the products at 710 $^oC$ shows the intensities of ZnO peak is increased whereas the intensities of Zn and Al peaks are decreased. Weak peaks of $ZnAl_2O_4$ (JCPDS card No. 05-0669) have also emerged at this temperature. Peaks of ZnO and Zn overlap at $2\theta = 36.3^o$.

The reaction pathways in the temperature range of 635~ 725$^o$ C are therfore proposed as the combination of reactions (**E.q. 3.17**), (**E.q. 3.18**) and (**E.q. 3.20**) below:

$$\mathbf{ZnO + \gamma\text{-}Al_2O_3 \rightarrow ZnAl_2O_4} \quad (3.20)$$

The second stage is characterised with two interesting peaks, particularly the second one. In order to interpret both peaks and their relationship with the physical state of Al, the sample was heated from room temperature to 700 $^oC$ in the environment of nitrogen under the heating rate of 10 K/min. The results of DSC curves attained in both environments, i.e., air and nitrogen are compared in **Figure 3.65.**

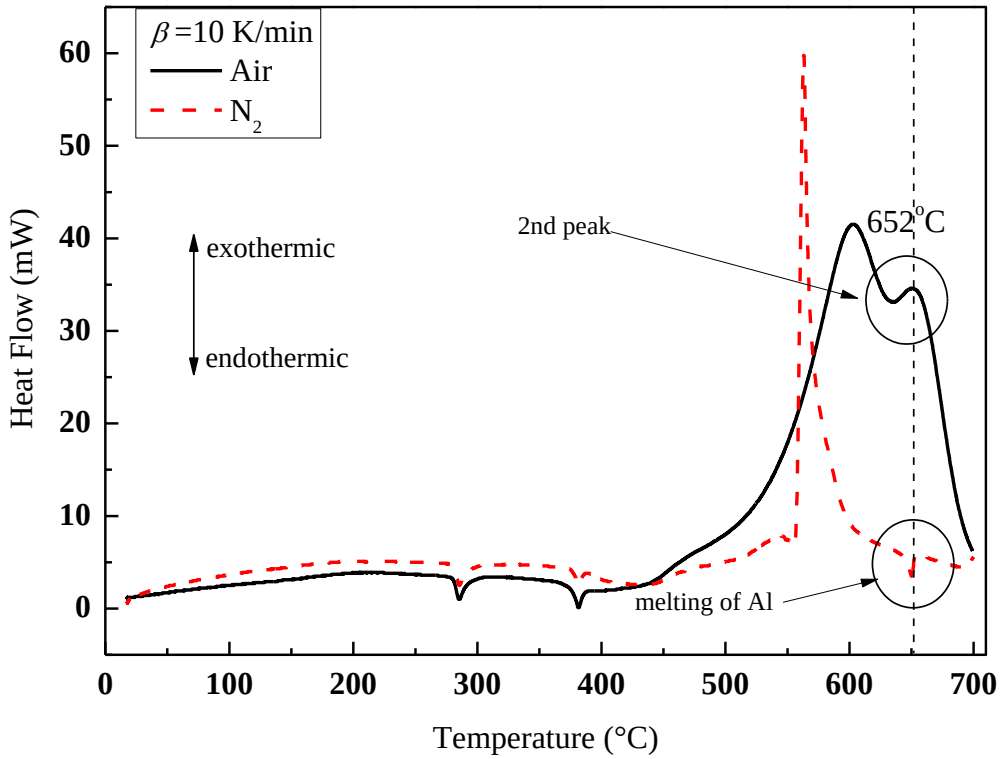


**Figure 3.65** DSC curve of the particles in air and nitrogen environments shows that the second oxidation peak in air coincides with the endothermic peak (melting of Al) in nitrogen

It is interesting to note that the endothermic peak of the DSC in nitrogen environment coincides with the rise of the exothermic peak in the air. Consequently this shows that first peak happens when some part of the Al is in the solid state and Zn is the in liquid state. The second peak occurs after the melting of the remaining Al in the alloy. Due to the increased mobility of Al in its molten state, the reaction between Al, oxygen and ZnO is accelerated that ultimately forms $ZnAl_2O_4$, as shown in **Figure 3.64 (d)** and **(e)**. Due to this 'synergic reaction' the span of the reaction is increased and more heat is produced.

It is shown from the phase diagram, **Figure 3.62**, that all the alloy transform into a molten state at point (d), 660 $^oC$. For nAlZn used in this work, the full melting is

observed at 652 $^{o}$C, which is due to the nano size effect of the particles. After attaining the 2$^{nd}$ peak, the rate of the reaction decreased once again, and 8.2% weight is increased during this sub-step.

### 3.4.2.3. Stage 3 (725 $^{o}$C-1200 $^{o}$C)

Stage 3 is the 2$^{nd}$ exothermic zone where the rate of oxidation is increased from 725 $^{o}$C and peaks at 817 $^{o}$C. After attaining the peak, the rate of the reaction decreases till it reaches 1200 $^{o}$C where the experiment ends. During this stage, 7.2 % of the weight of sample is increased. The TGA curve becomes flat at 1045 $^{o}$C, which suggests that the reaction is complete. Similarly two additional experiments were conducted by heating the samples from room temperature to 910 $^{o}$C and 1200 $^{o}$C respectively, at $\beta$ =10 K/min in order to identify the crystalline structure and elemental information. XRD shows that the peaks of Zn and Al are weakening at T~ 910 $^{o}$C, **Figure 3.64 (f)** and **(g).**

Different to the oxidation of pure nAl where the phase transition, i.e. forming various polymorphs of alumina ($\gamma$-, $\delta$-, $\theta$-, and $\alpha$-$Al_2O_3$) as the temperature increase, is dominant [157], we did not observe any other forms of the alumina for nAlZn, probably due to the small portion of the Al atoms in the alloy. The peak of $\gamma$-$Al_2O_3$ can not be observed at the 3$^{rd}$ stage **,** which suggests that the alumina has been reacting with ZnO forming $ZnAl_2O_4$ . As the temperature increases, the peaks of ZnO and $ZnAl_2O_4$ are getting strong. Consequently the proposed reaction pathways remain the same as **Eqs. 3.17, 3.18** and **3.20**. After reaching 817 $^{o}$C, the rate of reaction decreases. The TGA signal becomes flat at point 'c' in the TGA-DSC curve, i.e., 1045 $^{o}$C, which shows that the reaction is complete and all the nAlZn has been consumed. The end products are ZnO and $ZnAl_2O_4$.

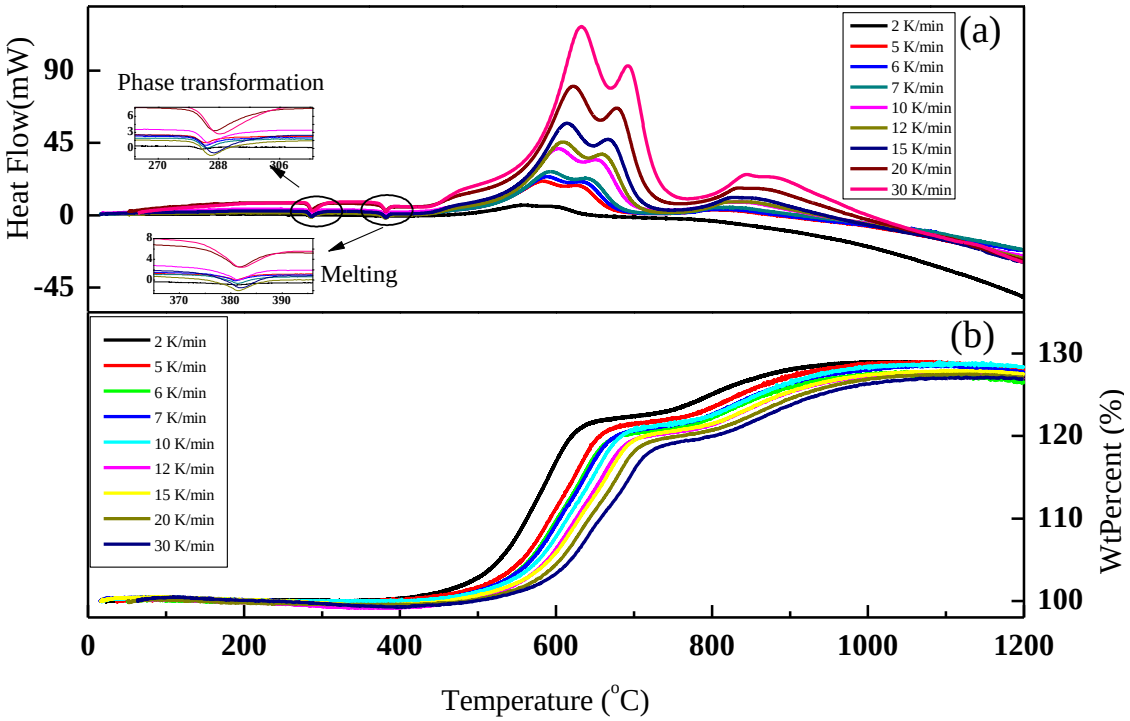


**Figure 3.66. (a)** and **(b)** showing the DSC and TGA curves of the NA under heating rates of 2-30 K/min, respectively

As shown in **Figure 3.66**, the final weight gain after the full oxidation changes slightly at different heating rate. If taking an average final weight increase ~29%, the molar ratio of ZnO to $ZnAl_2O_4$ can be estimated as ~5:1 accordingly. This is consistent qualitatively with the XRD result, **Figure 3.64(f)**. The increase of the $ZnAl_2O_4$ ratio in the 1200 °C temperatue might be associated with the effect of the evaporation of part zinc at high temperature and continuous convertion of ZnO.

During the oxidation process, the morphology of the particles changes at different temperatures, **Figure 3.67**.

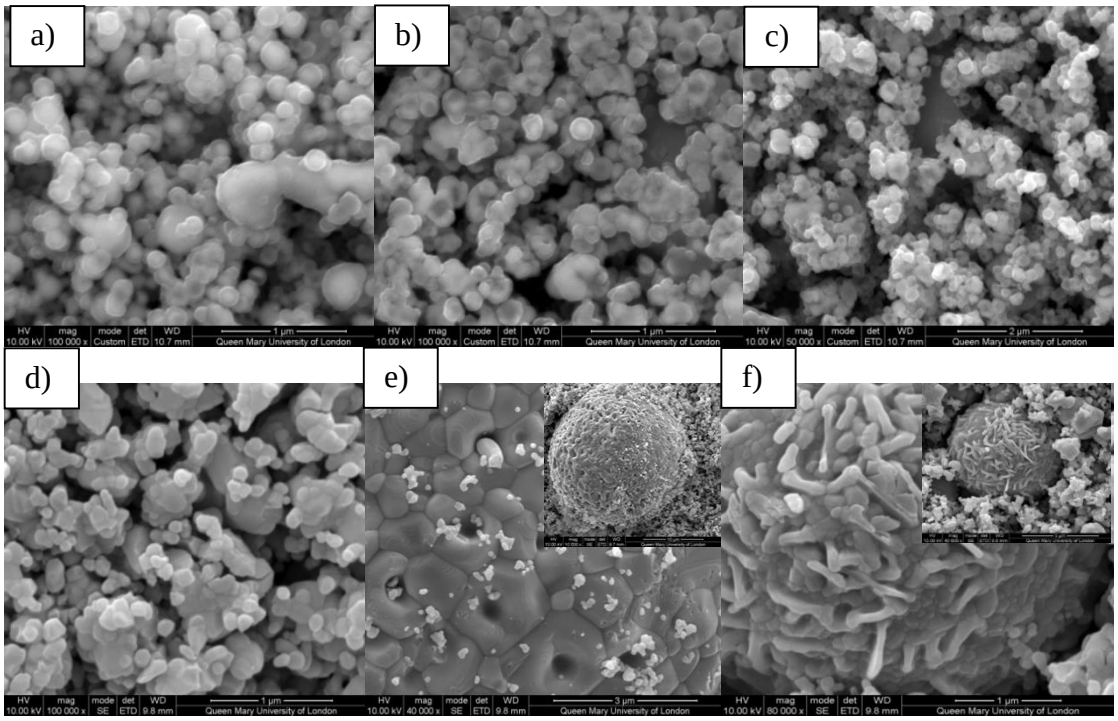


**Figure 3.67.** SEM observations at (**a**) 625 $^{o}$C (100 k); (**b**) 710 $^{o}$C (100 k); **c**) 910 $^{o}$C (50 k); (**d, e, f**) 1200 $^{o}$C (100 k, 40 k, 80 k, respectively) at 10 K/min

The particles retain their spherical shapes while went through various oxidation steps, **Figure 3.67(a), (b)** and **(c).** Significant morphological changes are observed at higher temperature ~ 1200 $^{o}$C where some particles are agglomerated into big structures of multigonal crystals and needle-like fibrous structures, **Figure 3.67 (d), (e)** and **(f)**. This type of morphology is not observed for the oxidation of pure aluminium nanoparticles under similar experimental conditions, which can be attributed to the diffusion of Zn ions occurring in some preferential directions [158]. High temperature (~1200 $^{o}$C) promotes the migration of grain boundaries and merges the small grains transforming them into the large ones. The elemental composition analyses (EDS) shows that the ratio of metallic (Al+Zn) to the oxygen atom decreases as the temperature increases, reaching the final ratio of 2.86 at 1100 $^{o}$C, **Table 3.8**.

**Table 3.8** EDS of nAlZn at various termination temperatures

| Exp. conditions | O | Al | Zn | (Al+Zn)/O |
|---|---|---|---|---|
| Temperature | Weight | Weight | Weight | - |
| °C | (%) | (%) | (%) | Ratio |
| 25 | 4.82 | 18.26 | 76.92 | 19.75 |
| 460 | 5.75 | 18.54 | 75.71 | 16.40 |
| 625 | 20.19 | 17.33 | 62.48 | 3.95 |
| 710 | 24.32 | 14.26 | 61.42 | 3.11 |
| 910 | 24.62 | 16.41 | 58.97 | 3.06 |
| 1100 | 25.90 | 16.68 | 57.43 | 2.86 |

### 3.4.3. Effect of Heating Rate

The TGA and DSC profiles under the entire heating rate, from 2 to 30 K/min, are given in **Figure 3.66**. It shows clearly that the scenario described above is applicable to all the other heating rates. The whole oxidation process can be still described by a three-stage scenario but with slight change of the temperature boundaries for different stages. The key features of oxidation at different heating rates are summarized in **Table 3.9-11**. **Table 3.9** shows the characteristics of the endothermic reactions, such as the characteristic temperature and enthalpy change; **Table 3.10** shows mass changed during various oxidation steps, and **Table 3.11** summarizes the exothermic reactions including the temperature and heat flow.

**Table 3.9** Key features of the endothermic reactions

| **Heating rate** | **1st Endothermic Peak** | | | | **2nd Endothermic Peak** | | | |
|---|---|---|---|---|---|---|---|---|
| β | $T_{pendo1}$ | $T_{OS1}$ | $O.S_1$ | $\Delta H_t$ | $T_{pendo2}$ | $T_{OS2}$ | $O.S_2$ | $\Delta H_f$ |
| K/min | ºC | ºC | J/g/ºC | J/g | ºC | ºC | J/g/ºC | J/g |
| 2 | 282 | 281 | -0.43 | 7.7 | 381 | 379 | -0.38 | 12.8 |
| 5 | 284 | 280 | -0.44 | 17.8 | 381 | 378 | -0.51 | 11.4 |
| 6 | 284 | 281 | -0.53 | 17.1 | 381 | 378 | -0.57 | 12.3 |
| 7 | 285 | 280 | -0.53 | 18.3 | 381 | 378 | -0.58 | 12.4 |
| 10 | 285 | 281 | -0.64 | 19.7 | 382 | 377 | -0.61 | 13.7 |
| 12 | 286 | 281 | -0.71 | 19.0 | 381 | 377 | -0.64 | 12.5 |
| 15 | 287 | 281 | -0.72 | 20.9 | 382 | 377 | -0.66 | 12.6 |
| 20 | 287 | 281 | -0.84 | 19.5 | 382 | 377 | -0.75 | 11.4 |
| 30 | 289 | 281 | -0.92 | 22.6 | 382 | 375 | -0.81 | 11.0 |
| Mean±SD | **285.4±2.1** | **280.8±0.4** | **-0.6±0.2** | **18.1±4** | **381.4±0.5** | **377.3±1.1** | **-0.6±0.1** | **12.2±0.8** |

Note:
$T_{pendo1}$, $T_{pendo2}$, are the peak values of temperatures of 1st and 2nd endothermic reactions; $T_{OS1}$, $T_{OS2}$ are the corresponding onset temperatures and $O.S_1$, $O.S_2$ are the onset slops of the endothermic peaks.
$\Delta H_t$ , $\Delta H_f$ are the enthalpy of phase transformation and the enthalpy of fusion for eutectic melting of the NA

**Table 3.10**. Mass changed during the various steps of reactions.

| B | $\Delta m_{1a}$ | $\Delta m_{1b}$ | $\Delta m_1$ | $\Delta m_2$ | $\Delta m$ |
|---|---|---|---|---|---|
| K/min | % | % | % | % | % |
| 2 | 12.4 | 9.2 | 21.6 | - | 29.07 |
| 5 | 12.6 | 8.6 | 21.2 | 3.7 | 29.37 |
| 6 | 12.5 | 8.3 | 20.9 | 3.9 | 28.6 |
| 7 | 13.1 | 7.9 | 21.0 | 4.8 | 29.2 |
| 10 | 13.1 | 8.3 | 21.4 | 5.5 | 29.15 |
| 12 | 13.0 | 8.0 | 21.1 | 6.0 | 28.61 |
| 15 | 13.1 | 7.8 | 20.9 | 5.8 | 28.52 |
| 20 | 12.1 | 8.2 | 20.3 | 6.4 | 28.01 |
| 30 | 12.2 | 7.9 | 20.1 | 6.4 | 27.91 |
| Mean± SD | 12.7 ± 0.4 | 8.2 ± 0.4 | 20.9 ± 0.4 | 5.3 ± 1.1 | 28.7 ± 0.5 |

Note:
$\Delta m_1$ is the mass changed during the first exothermic reaction. $\Delta m_{1a}$ and $\Delta m_{1b}$ are the mass changed during 2nd and 3rd substep of 1st exothemic reaction. $\Delta m_2$ is the mass changed during the second exothemic reaction. $\Delta m$ is the final mass of the sample

**Table 3.11** Key characteristics of the exothermic reactions on DSC curves

| $\beta$ | $T_{pendo1}$ | $h_{endo1}$ | $T_{pendo2}$ | $h_{endo2}$ | $T_{pexo1}$ | $h_{exo1}$ | $T_{pe1}$ | $h_{p1}$ | $T_{pexo2}$ | $h_{exo2}$ | $T_{pe2}$ | $h_{pe2}$ | $T_{pexo3}$ | $h_{exo3}$ |
|---|---|---|---|---|---|---|---|---|---|---|---|---|---|---|
| $Kmin^{-1}$ | °C | mW | °C | mW | °C | mW | °C | mW | °C | mW | °C | mW | °C | mW |
| 2 | 283 | -0.12 | 381 | -0.88 | 559 | 6.3 | 592.8 | 5.57 | 596 | 5.46 | missing | missing | missing | missing |
| 5 | 284 | 1.06 | 381 | 0.07 | 584 | 21.21 | 611 | 18.04 | 627 | 18.59 | 717 | 1.08 | 802 | 3.31 |
| 6 | 285 | 0.61 | 381 | -0.06 | 589 | 23.95 | 618 | 20.3 | 633 | 20.92 | 720 | 1.12 | 806 | 3.58 |
| 7 | 285 | 0.11 | 381 | -0.6 | 594 | 27.11 | 623 | 22.28 | 640 | 22.92 | 721 | 1.33 | 809 | 4.79 |
| 10 | 285 | 0.98 | 381 | 0.09 | 603 | 41.49 | 635.5 | 33.13 | 653 | 34.51 | 739 | 2.98 | 817 | 8.15 |
| 12 | 286 | -1.31 | 381 | -1.97 | 610 | 45.59 | 642 | 35.6 | 659 | 37.98 | 745 | 1.73 | 825 | 8.37 |
| 15 | 287 | -0.83 | 381 | -1.45 | 614 | 57.28 | 648 | 43.15 | 667 | 47.26 | 749 | 3.16 | 827 | 11.06 |
| 20 | 288 | 3.33 | 381 | 2.52 | 622 | 80.33 | 657 | 59.17 | 678 | 66.67 | 759 | 7.09 | 835 | 17.01 |
| 30 | 288 | 2.70 | 382 | 2.48 | 633 | 117.46 | 670 | 79.05 | 693 | 93.05 | 771 | 10.27 | 844 | 25.29 |
| **Mean** | **285.4±1.6** | **0.7±1.5** | **381.6±0.3** | **0.02±1.6** | **600.9±22.4** | **46.7±34.4** | **633.1±24.2** | **35.1±22.7** | **649.6±29.3** | **38.6±27.2** | **740.1±19.6** | **3.6±3.3** | **820.7±14.7** | **10.2±7.6** |

Note:

$\beta$ is the heating rate, $T_{pexo1}$, $h_{exo1}$, $T_{pexo2}$, $h_{exo2}$, $T_{pexo3}$, $h_{exo3}$, $T_{pendo1}$, $h_{endo1}$, $T_{pendo2}$, $h_{endo2}$ are the temperatures and corresponding heat flow on DSC curve for the first second and third exothermic and first and second endothermic peaks respectively. $T_{pe1}$, $h_{pe1}$, $T_{pe2}$, $h_{pe2}$, are the temperatures and heat flow where the curves attain the minima first and second time.

As descrbied earlier, the endothermic peaks are due to the phase transition and the descrbied earlier, the endothermic peaks are due to the phase transition and the eutectic melting. The mass changed during the first oxidation zone is found to decrease slightly with the increase of the heating rate. For instance at heating rate of 2 K/min its value is 21.6 %, which decreases to 20.1% at 30 K/min. Contrary to that, the mass increased during the second oxidation zone is proportional to the heating rate, e.g., its value is 3.72 % at the heating rate of 5 K/min and increases to 6.4 % at 30 K/min. The total mass gained during the whole oxidation process decreases slightly with the increase of the heating rates. The mean value of the mass gained during the whole oxidation process is 28.7 ± 0.5 %.

The XRD traces of nAlZn oxidized from room temperature to 1200 $^{o}$C under various heating rates (5, 10 and 20 K/min) are shown in **Figure 3.68**.

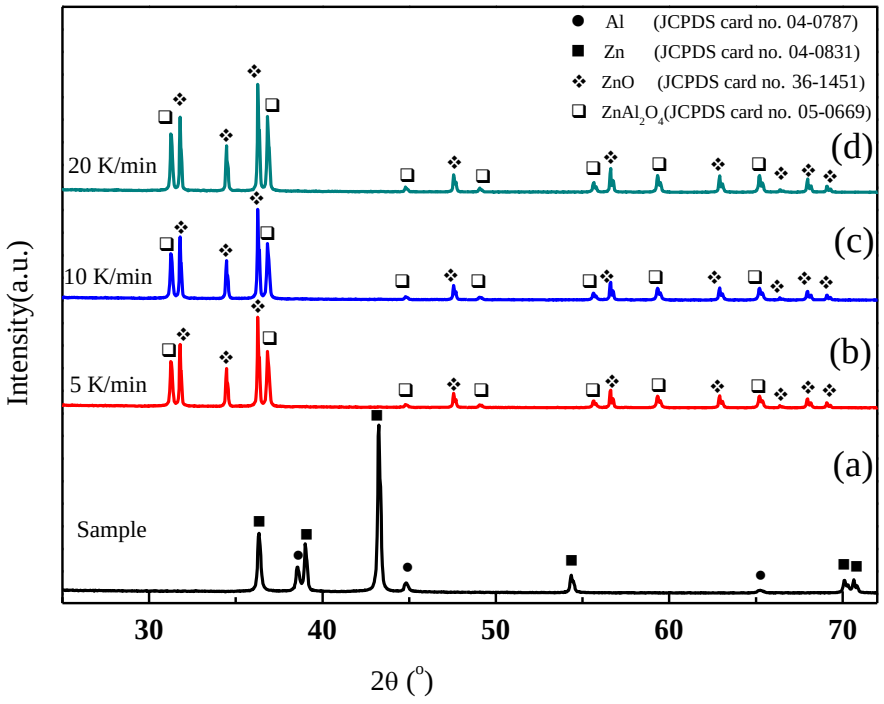


**Figure 3.68** XRD trace of nAlZn after oxidation under the heating rates of 5, 10 and 20 K/min

Similar elements and composition are shown regardless of the heating rates. The major end products of the oxidisation are ZnO and $ZnAl_2O_4$. Again no peaks of Al and Zn are seen, which suggests that the entire specimen have been oxidized.

The enthalpy analysis of different stages of oxidation at different heating rates is shown in **Figure 3.69**.

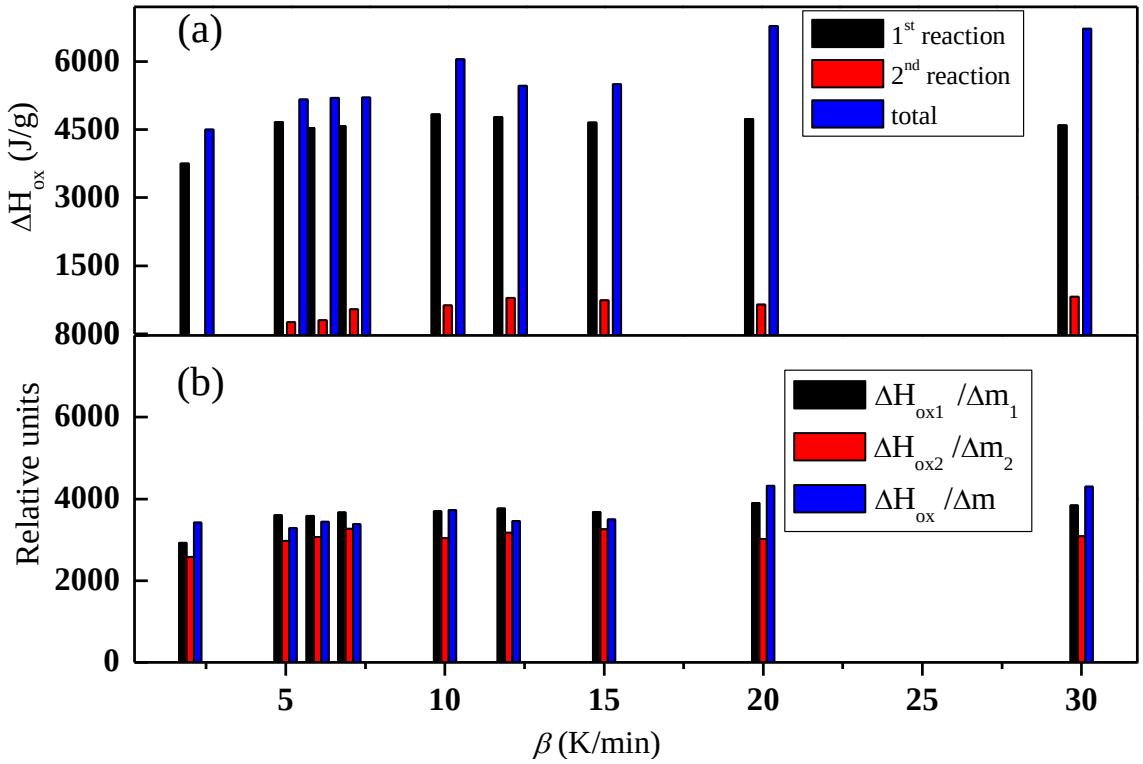


**Figure 3.69 (a)** Heat produced during the two-step exothermic reactions; **(b)** the relative thermal effect (specific heat) of the nAlZn during oxidation at various heating rates

It shows clearly that the energy produced during first and the second exothermic reactions (i.e., 2nd and 3rd stage) differs greatly from each other. For example, the heat produced during the first reaction is 4837 J/g at 10 K/min that constitutes 88.5 % of the total energy produced. On the other hand, its value for the second reaction is 630 J/g which is only 11.5 % of the total energy produced. The total mass changed during the

whole reaction is 26.6 %, out of which 21.4 % of mass increase is observed during the first reaction and only 5.5 % of the mass is changed in the second exothermic reaction. Clearly the energy produced during a specific oxidation step depends upon the metal content available for the reaction. During the first reaction Zn is in the molten form whereas complete melting of Al occurs after 635 $^{o}$C, which increases the rate of the oxidation process. This in turn increases the span of the reaction, resulting in more energy produced. During the second exothermic reaction, only a small amount of sample's mass is left. The total heat released of nAlZn is in the range of 4.5~7 kJ/g considering all the heating rates, which is consistent with thermodynamics values of the bulk materials.

The specific heat released ($\Delta H_{ox}/\Delta m$, rel. units) analysis is taken as ratio of the area under the DSC curve (thermal effect of oxidation) and the corresponding mass changed (on the TGA curve) [61]. This implies the relative thermal effect, i.e. the ability of energy release. **Figure 3.69(b)** shows the values of specific heat produced during the first, second stage of the exothermic and the whole oxidation process. The values are similar for all the stages and are weakly dependent on the heating rate.

## 3.5. Preliminary Combustion Analysis

The combustion of energetic metallic particles or particle suspensions have long been the area of interest in the combustion research community. Enormous research has been conducted to understand the mechanism of combustion of metallic particles either to improve the burning rate [44, 159, 160] or inhibit it for hazard prevention [64, 67]. Various techniques to initiate the ignition including lasers, shocks, flashes and gas burners [161-163] have been developed. The combustion history of the particles is often

tracked by the high speed cameras and the morphology is examined with the help of Electron Microscopes (EM) as well as using Particle Imaging Velocimetry (PIV) to measure the flame flow and analysing its characteristics [164].

As reviewed in **Chapter 1**, Glassman et al. [165] proposed that the combustion of conventional-sized aluminium particles is analogous to the combustion of hydrocarbon particles, and the burn time is related to the square of its diametric length, known as $d^2$ law. Many differences have been reported on the combustion behaviour of fine particles and that of conventional particles. The burning time of fine particles is a function of the particle morphology and the temperature and pressure of the environment [166]. Olsen and Beckstead [167, 168] observed that the burning time ($t_b$) of microsized particles (40-70 μm) was weakly related to the temperature of the surrounding gas. In the case of nanosized particles, Bazyn et al. [169] showed a strong dependence on the pressure of the surrounding gas, which concluded that the combustion process was kinetically controlled. Many studies [170-172] show that when the diameter of the particle becomes very small, the exponent of the conventional law of burn time, i.e., $t_b = \beta d^n$ becomes less than 2. However due to the agglomeration and non-uniform dimensions of these nanoparticles, a precise exponent number is not easy to find.

In this section, some preliminary combustion experiments are performed using a Bunsen burner in a particle-laden methane stream and the relationship of particle burning time with particle diameter is reported. The particles are characterised using DLS, SEM and EDS. A high speed video camera is used to capture the combustion process of the particles, and PIV technique is used to investigate the reactivities and the average velocity flow fields of the silicon, iron and aluminum particles.

### 3.5.1. Particle characterisation

Al, Si and Fe were used in the combustion experimentation. The physical characteristics of nAl have already been reported in the previous sections. Two types of Si particles were purchased from Nanostructure and Amorphous Materials Ltd (USA), with a nominal particle size of 50 nm and 1000 nm respectively. However the 50-nm nanoparticles come with heavy agglomerations. To reflect the particle morphology upon combustion, some Si samples were dispersed into ethanol without any mechanical or chemical aid, and its size distribution was measured by DLS, as shown in **Figure 3.70**. The particles size distribution is in the range of 600 to 1000 nanometer, peaking at ~ 720 nm, which is much larger than the primary particle size of ~50 nm. Iron powder having a grade Fe300 was purchased from William Rowland ltd. The Fe powder has diameter ranges from 45-75 μm and an average density of 2.8-3.0 g/cm$^3$. It was 99% pure and contained some trace elements likes C (0.01%), S (0.025%) and $O_2$ (0.15%). All the particles were mixed with natural gas ($CH_4$, 98%) and were combusted using a burner in the atmosphere of air. The particles were characterised with SEM and EDS employing the same methods discussed earlier.

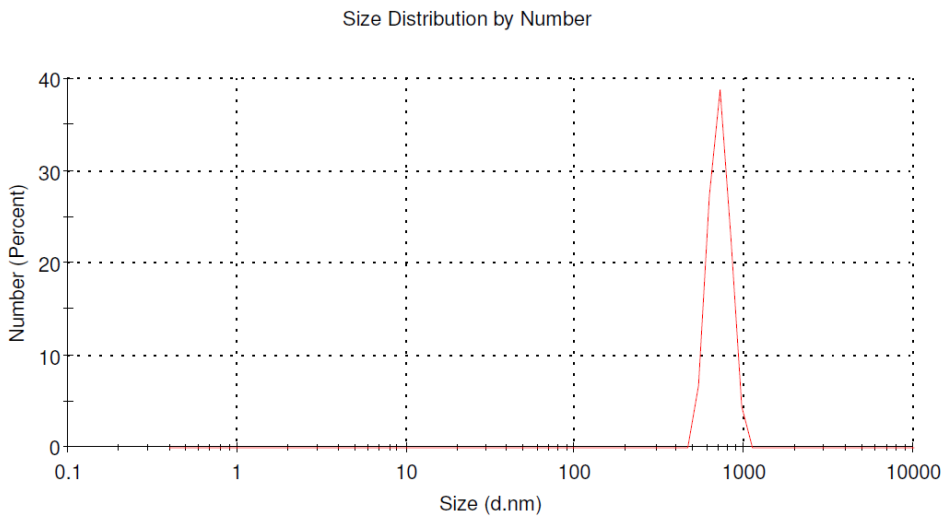


**Figure 3.70** Particle size ditribution (PSD) of Si (before combustion)

SEM images of the particles after their combustion are shown in **Figure 3.71** and EDS analyses are summarised in **Table 3.12**.

From the SEM images, it is observed that nanoparticles of Al and Si are still kept spherical. On the other hand, micrometric particles of Fe and Si are changed to big agglomerates of non-uniform shapes. Interestingly the EDS results of both nanometeric particles (Al and Si) show that it contains 55.46% (for Al) and 29.12% (for Si) of carbon. Contrary to that EDS of the micrometric particles does not show any signal of carbon. This means that during the experiment fewer Fe particles were burnt.

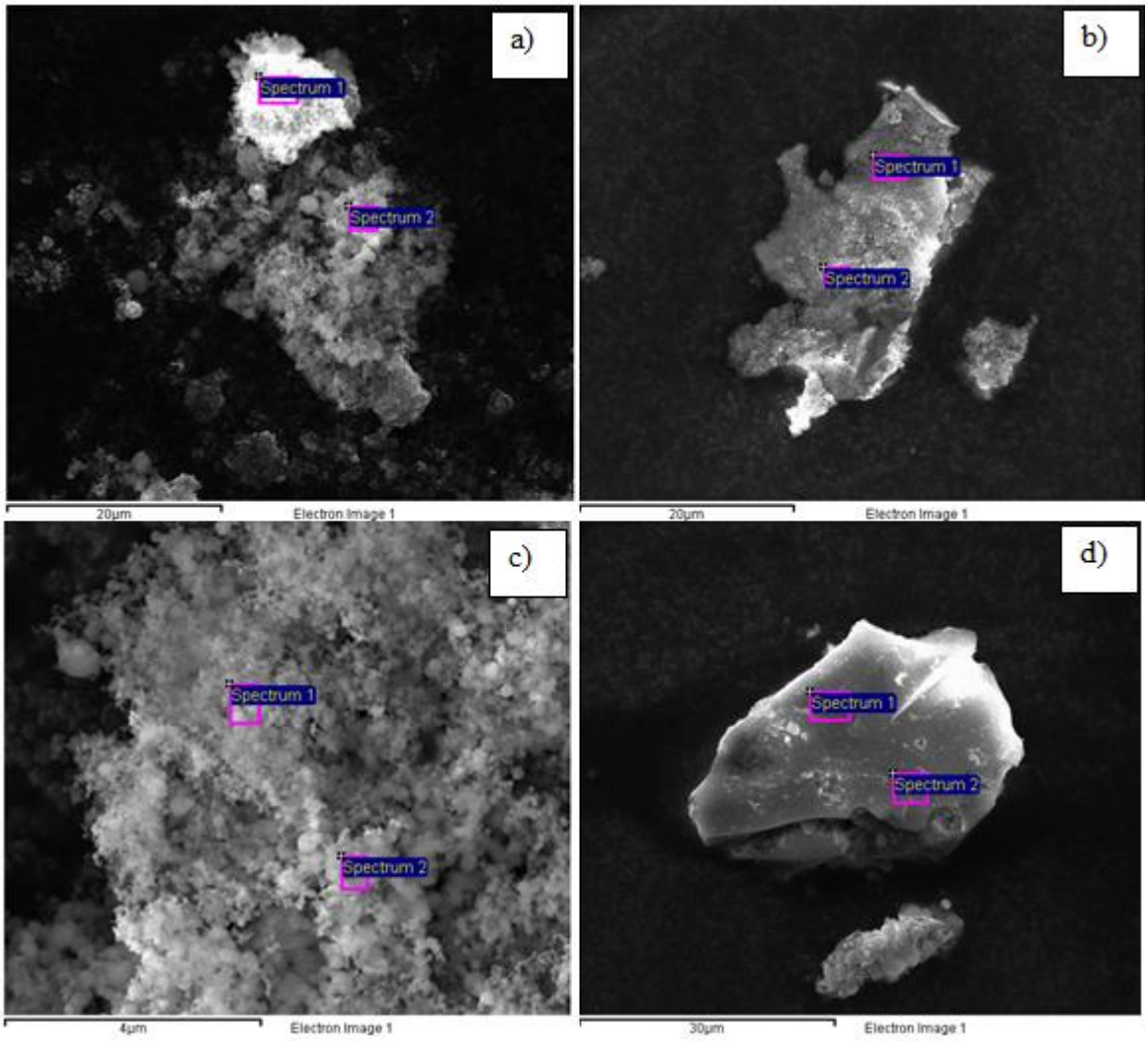


**Figure 3.71** Particles after their combustion, a) Al (150 nm), b) Fe, c) Si (720 nm) and d) Si (1 µm)

**Table 3.12** EDS analyses of various powders after combustion.

| **Samples** | **Products (%)** | | | | |
|---|---|---|---|---|---|
| | O | C | Fe | Al | Si |
| nAl | 15.3 | 55.46 | No signal | 29.1 | 0.26 |
| Fe | 30.0 | No signal | 68.8 | No signal | 0.60 |
| Si (720 nm) | 59.17 | 29.12 | No signal | No signal | 11.7 |
| Si (1 μm) | 54.67 | No signal | No signal | No signal | 45.3 |

## 3.5.2. Combustion experiments

The particles are ignited/ combusted at atmospheric conditions in the stream of natural gas/air using a conventional Bunsen burner, which is a simple system that allows greater control over the combustion parameters.

The particles are ignited after passing through the inner cone having the highest flame temperature. Typical particle combustion image showing distinct zones of the flame is presented in **Figure 3.72.**

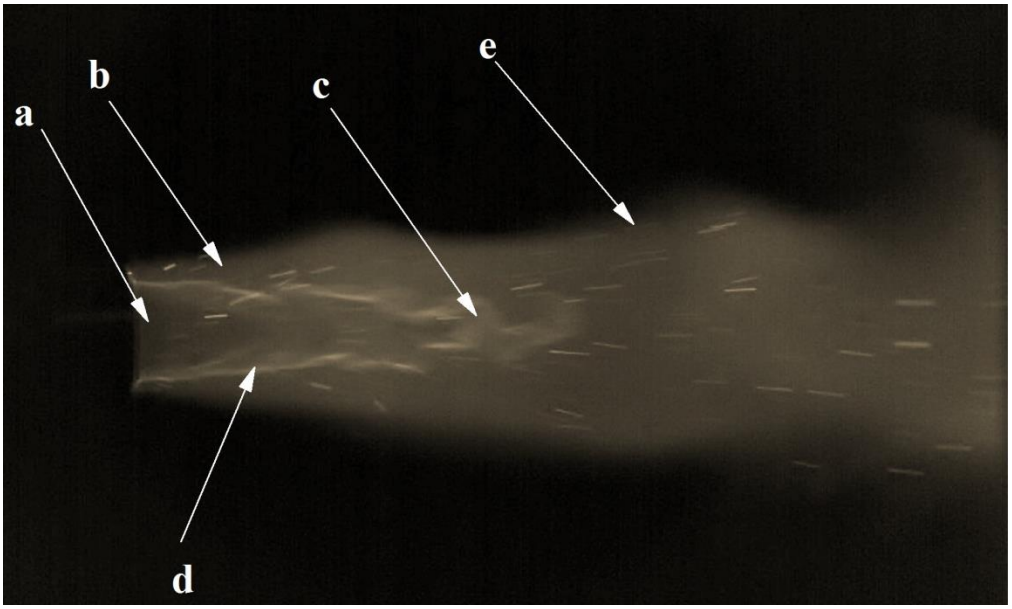


**Figure 3.72** Particle combustion in the stream of methane/air showing various regions of flame a) Cold flame zone; (b) Region of combustion; (c) Tip of inner cone, hottest flame zone; (d) Region of intense combustion, inner cone; (e) Outer cone-post flame region

### 3.5.3. Comparison of reactivities of Si particles

With the decrease of particle diameter, the specific surface area of the particle increases. This increases the contact points among the reactants and the particles. Consequently, the reactivity of the nano particles is higher than that of the micro particles. To reflect the particle morphology upon combustion, the peak particle size, i.e., 720 nm, rather than the primary particle size as supplied by the manufacturer. In the experiment particles of Si having 720 nm and 1 μm diameter are combusted at the same experimental conditions, and their combustion behaviour is compared in **Figure 3.73**.

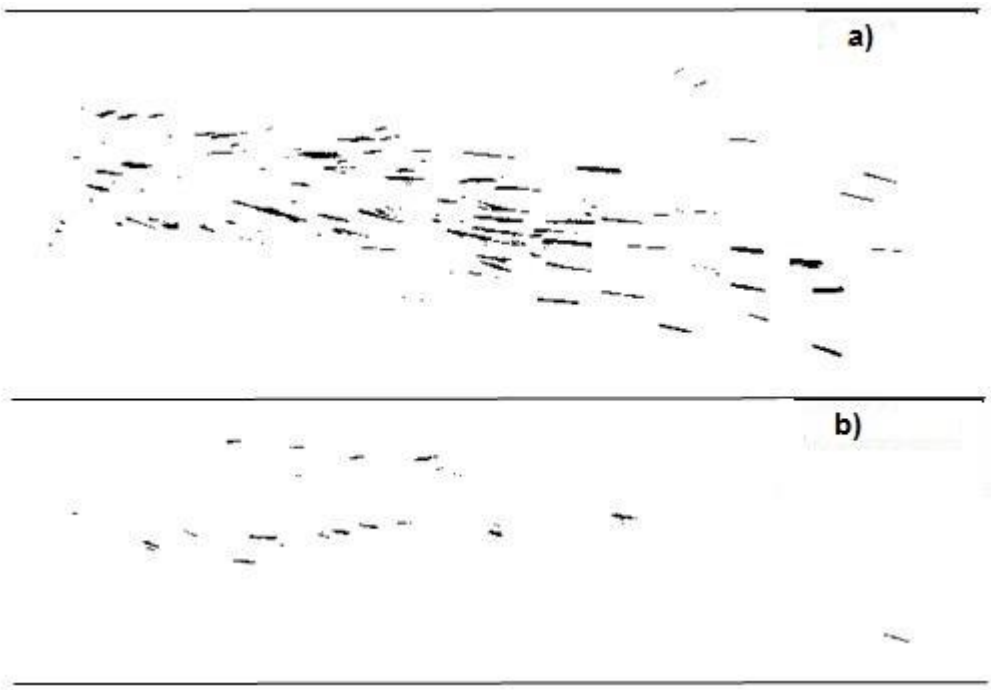


**Figure 3.73** Binarised images of the particles of Si (720 nm (a) and 1μm (b) ) showing the higher ignitibility (reactivity) of the particles having a smaller diameter.

The pin stubs for collection of the combusted particles were mounted over the flame. It can be easily discerned from **Figure 3.73** that the particles having a smaller diameter are characterised with higher reactivity as more particles are combusted during the combustion process. On the other hand, small number of particles (Si 1 μm) is combusted due to which the signal of carbon in the EDS results is missing.

### 3.5.4. PIV and extinction time results

It is very important to have detailed knowledge of particle combustion behaviour particularly its combustion velocity in relation to its ignition and burning time. PIV experiments are used to find out the velocity profiles of the burning particles. A series of PIV experiments were performed to calculate and compare the flow fields and speeds of the various particles, shown in **Figure 3.74** and **Figure 3.75**.

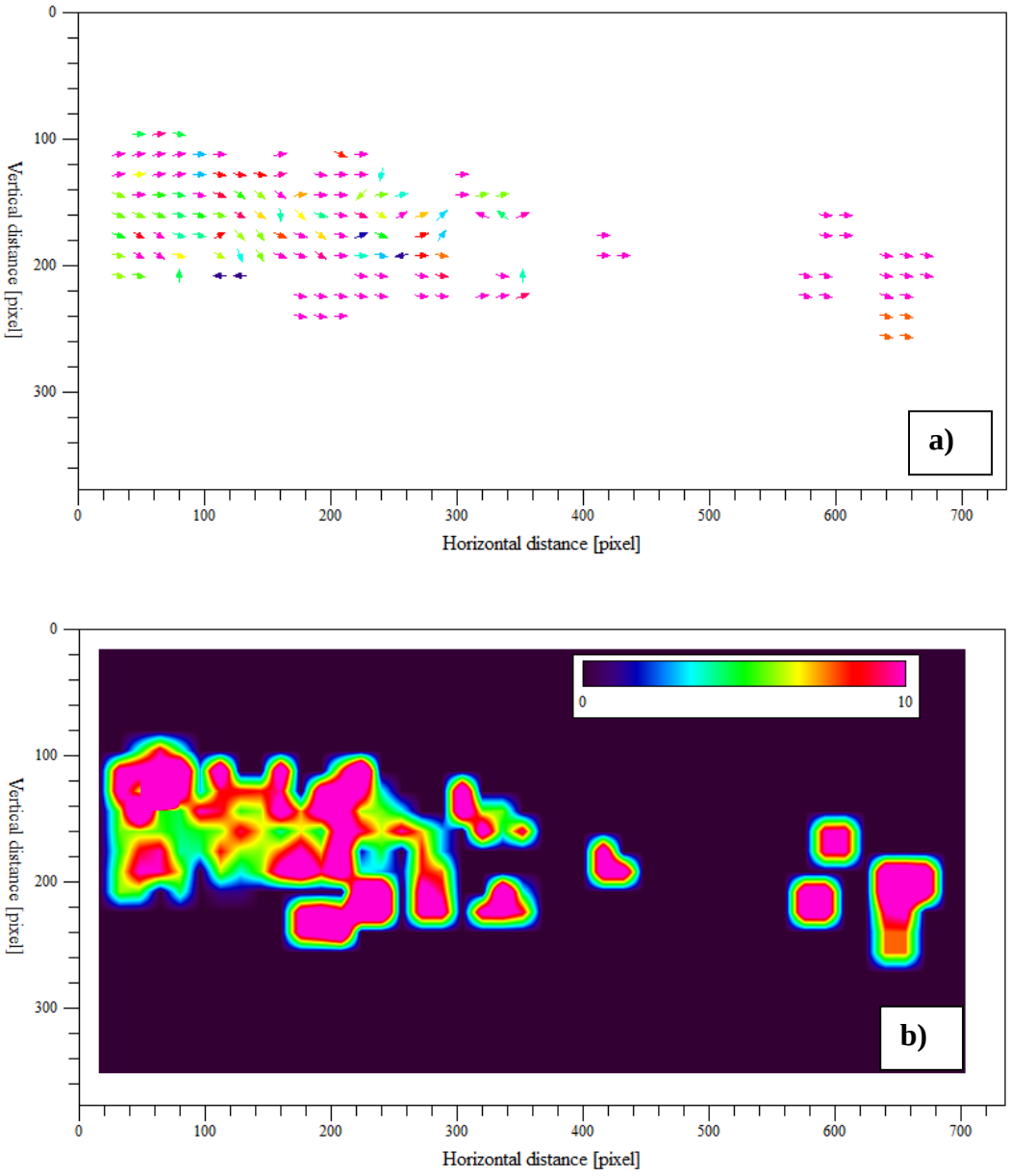


**Figure 3.74** Showing the results of PIV of an image pair of Si (720 nm) particles, a) velocity vector field; b) average axial components of velocity.

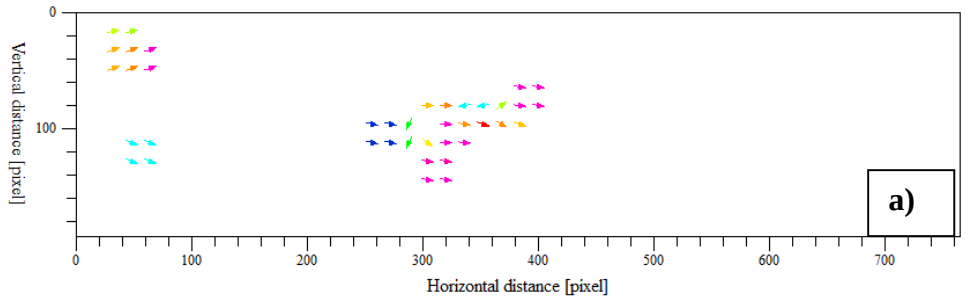

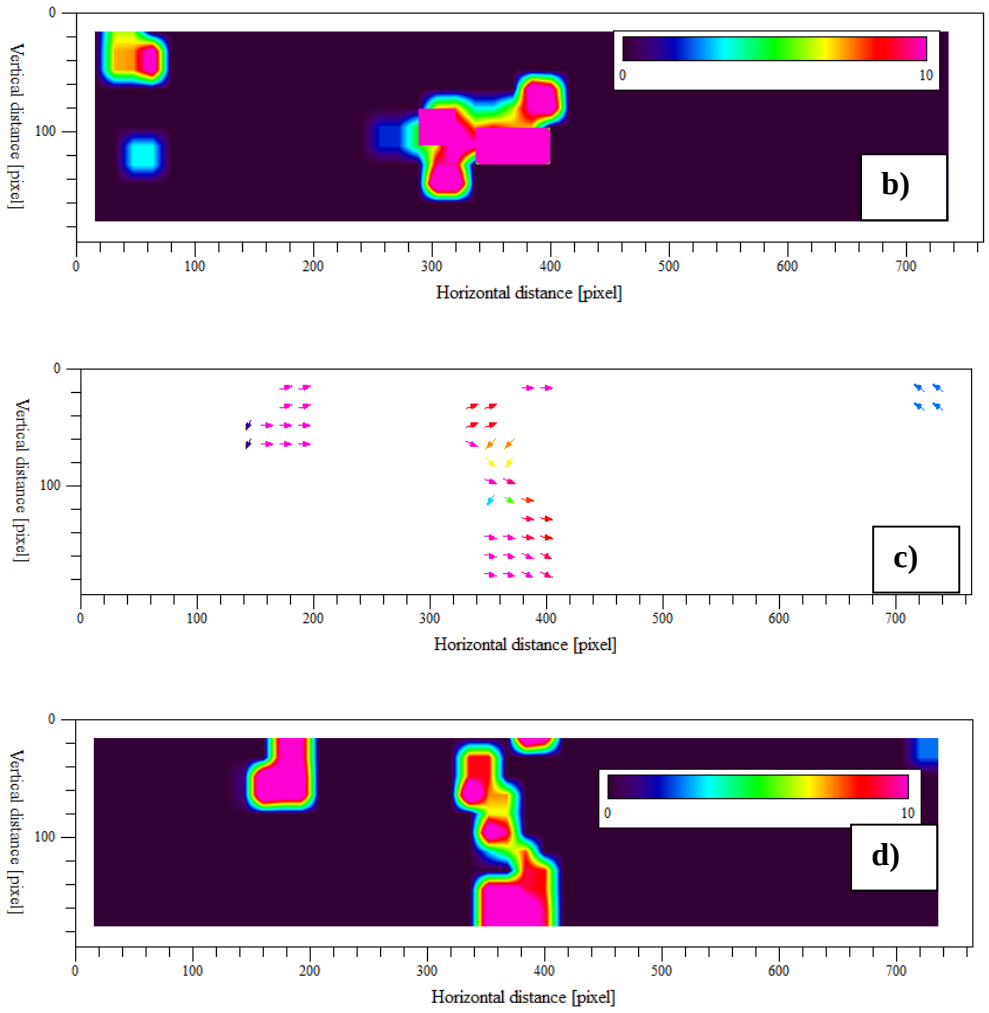


**Figure 3.75** Showing the PIV results of image pairs of Si (1000 nm) and Fe (45-75 μm) particles, a) velocity vector field of Si; b) average components of velocity of Si; c) velocity vector field of Fe; d) average components of velocity of Fe.

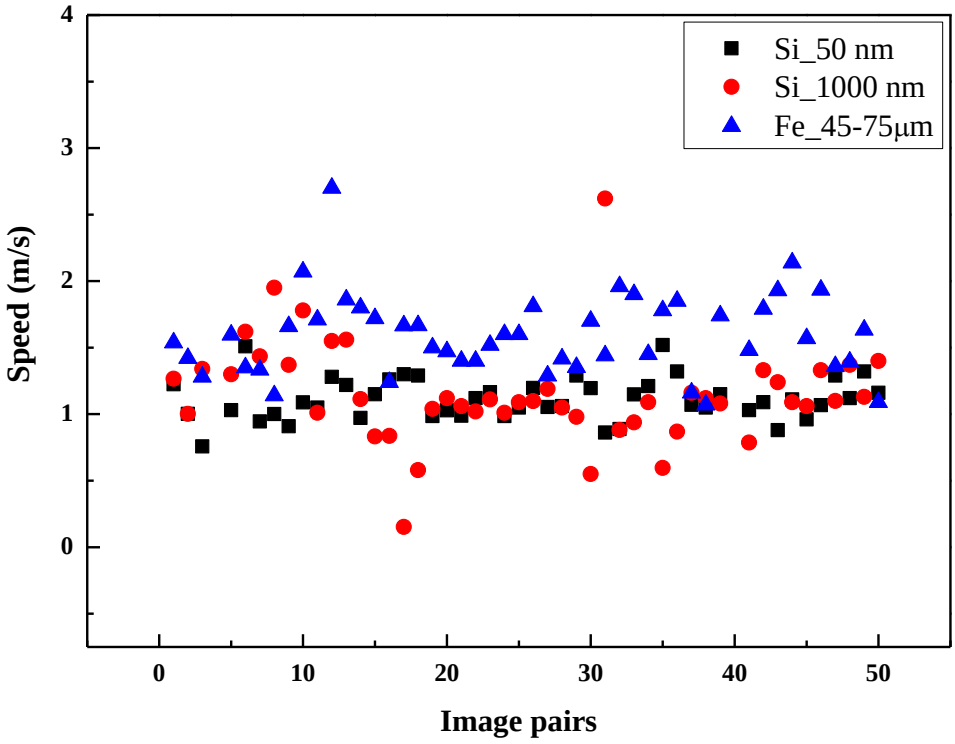


**Figure 3.76** Comparison of mean speeds of various particles by processing 50 image pairs.

From **Figure 3.74** and **Figure 3.75,** it can be observed that the ignitability/reactivity of the particles increase with the decrease of the diameter. The results of PIV profiles of Fe and Si having micrometric dimensions are similar to each other. It can be seen that the particles were ignited after passing through the tip of the internal cone which is the point of maximum temperature in the flame. In the post flame zone (outer cone) the particles extinct after travelling some distance. The mean speed profile of 50 image pairs are represented and compared in **Figure 3.76**. The average speeds of Si (720 nm), Si (1 μm) and Fe (45-75 μm) in the methane stream are 1.18 m/s, 1.15 m/s and 1.71 m/s, respectively.

The extinction times for 100 particles are calculated by tracking their motion. The average values of extinction time for Si (720 nm) and Si (1000 nm) are 11.4 ms and 17.2

ms, respectively. If assuming the extinction time as the burning time, the relationship of $t_b \sim d^{1.2}$ can be obtained. The exponent value is similar to that observed by Friedman and Maccek (1.2-1.5) [94].

The diffusion limited droplet combustion theory predicts that the combustion time is related to the square of particle diameter, i.e., $d^2$ law. However, with the decrease of particles size, the diffusion limited oxidation assumption becomes invalid and the oxidation transitions towards kinetically controlled. Various $d^n$ relationships are presented in the literature, depending upon the particles size, level of agglomeration, combustion and experimental conditions.

Such preliminary experiments demonstrate the large difference between conventional-sized particles and fine particles.

## 3.6. Chapter Summary

This chapter studies the exothermic reactions such as oxidation, ignition and combustion of nAl and its nanoalloys, i.e., nAlCu and nAlZn under controlled environments. The particles are oxidised under the heating rates of 2-30 K/min in a simultaneous TGA/DSC system in the atmosphere of air and nitrogen and thermodynamics, kinetics, morphological and structural characteristics of the particles along with the energy transfer and conversion processes at nanometer scale are explored. In the preliminary combustion analysis, the relationship of the combustion time with the diameter of the particles is also discussed. Some unique features of oxidation, ignition and combustion aluminum based nanomaterials are observed, as summarized below:

- In case of nAl, a three- stage oxidation scenario is observed under all heating rates: the main reaction occurs before the melting of nAl and other two occurs after.
- Early ignition of nAl is observed for heating rates higher than 8 K/min, which is characterized by a sudden temperature runaway, a fast mass gain and a rapid heat release. The ignition occurs before the bulk melting temperature of nAl, which is likely caused by the partial melting of the aluminum core and the phase transition during the rapid self-heating period. The ignition temperature increases approximately with the heating rates.
- XRD shows that there is a co-existence of different polymorphs of alumina after the first stage rapid oxidation, caused by the early ignition, which continues to the $2^{nd}$ stage, and all are converted to the stable alpha phase at the end of the oxidation. The early ignition is responsible for the co-existence of different polymorphs of alumina.
- When the particles are heated in the nitrogen atmosphere, no such ignition behaviour is observed.
- Different to the shrink-core model, a phenomenal model is proposed to explain the formation of hollow structure in aluminium nanoparticles, which is associated with the melting, phase transition of the oxides and the nanoscale Kirkendall effect.
- The unique step-wise cavity development in relation to the change of temperature and heating rates shows that after the first oxidation stage at ~600 $^{o}$C, the particles are still solid. The void is generated after the melting process, i.e., after 660 $^{o}$C, and the particles are a combination of solid and hollow structures at 700 $^{o}$C. The size of the void increases with the rise of the

temperature. The void development process completes at ~800 $^{o}$C where all the examined particles are hollow.

- It is also observed that at the higher heating rates when the early ignition phenomenon is observed, the size of the void is larger as compared to those oxidised without ignition, and the oxide shell thickness remains the same regardless of the heating rate.
- The oxidation, ignition and chemical kinetics of the nano alloy (NA) of Al and Cu are investigated from 2 to 30 K/min, up to 1200 $^{o}$C in the presence of air shows that the complete oxidation scenario of nano Al-Cu alloys can be characterized by two exothermic and two endothermic processes, associated with the melting and different reaction paths.
- A unique early ignition phenomenon was observed for nanoalloys (nAl-Cu) particles at heating rates $\beta > 7$ K/min, which is characterised with sudden change of mass and heat released, and the ignition temperature is identified in the region of 564.7 ± 10.8 $^{o}$C. The eutectic melting temperature found to be 545.6 $^{o}$C ± 1.4 $^{o}$C, similar to its bulk value, and played a key role for the early ignition of the NA.
- Complete reaction paths up to 1200 $^{o}$C for nano Al-Cu alloy are proposed in conjunction with the XRD analysis. The weak peaks of copper aluminate spinel $CuAl_2O_4$ in the diffractograms at 900 $^{o}$C suggest that its formation is not thermodynamically favourable due to the slow diffusion of metallic ions. The reduction of the weight at higher temperature ~1175 $^{o}$C is due to the liberation of oxygen gas during the reduction of CuO to $Cu_2O$.
- The thermal analysis combined with elemental, morphology and crystalline structure analysis of Zn and Al nanoalloys (nAlZn) having a BET equivalent

diameter of 141 nm elucidates that the complete oxidation of nAlZn in air can be characterised by a three-stage scenario, including two endothermic and three exothermic processes.

- The first stage occurs between room temperature and ~ 400 $^{o}$C, includes two endothermic reactions, which is due to the phase transformation and the eutectic melting.
- The second stage extends to ~750 $^{o}$C, involving the first and the second exothermic reactions, where the 2$^{nd}$ peak is associated with the melting of Al component.
- The third stage includes the third exothermic peak until the completion of the reaction at ~ 1050 $^{o}$C, and is associated with the conversion of the formed alumina to $ZnAl_2O_4$.
- The reaction pathways forming intermediate products of ZnO and $\gamma$-$Al_2O_3$ are proposed with the help of ex-situ XRD, leading to the end products of ZnO and $ZnAl_2O_4$.
- A preliminary investigation of the combustion characteristics of three particles, Al, Fe and Si, having variable dimensions in the methane/ air stream in a Bunsen burner setup shows that most of the particles are burned after passing through the inner flame cone. The chemical compositional analyses (EDS) show no carbon signals for the micrometric particle, which suggests small number of particles being burned during the experiment.
- The comparison of silicon particle with different sizes show that the reactivity of the particle increases with the decrease of the particle size and the conventional $d^2$ law is not applicable to fine particles.

# Chapter 4

# 4. Comparison between nAl and its alloys

## 4.1. Reactivity

The reactivity of the nano aluminium particles (nAl) having an average diameter of 150 nm and nano aluminum copper alloy (nAlCu) with 211 nm is investigated. The reactivity of the powders can be estimated by the onset temperature, the peak temperature, and the temperatures at which the rate of change of mass and heat produced are maximum [65, 83]. The DSC/TGA example curves are shown in **Figure 4.1**, where the particles are heated in the thermobalance from room temperature to 700 ºC.

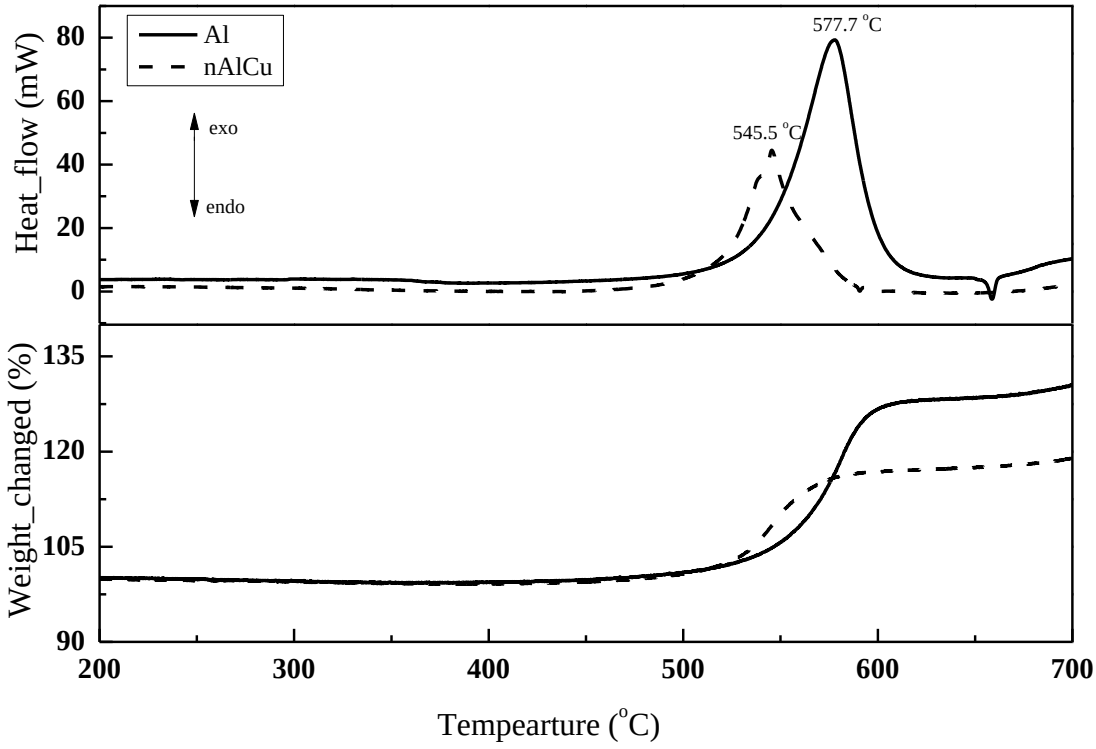


**Figure 4.1** TGA/DSC of nAl and nAlCu at a heating rate of 5 K/min showing nAlCu is more reactive than nAl

The reactivity parameters of both powders at 5 K/min are summarized in **Table 4.1** and **Table 4.2**.

**Table 4.1** Reactivity parameters of nAlCu and nAl at 5 K/min

| Sample | $T_{onset}$ | $T_{pexo1}$ | $T_{m1}$ | $T_{h1}$ |
|---|---|---|---|---|
| | $^oC$ | $^oC$ | $^oC$ | $^oC$ |
| nAlCu | 528 | 545.5 | 547 | 533 |
| nAl | 551 | 577.7 | 578 | 567 |

Note:
$T_{onset}$ is the onset temperature; $T_{pexo1}$ is the peak temperature of the first exothermic reaction, $T_{m1}$= $(dm/dT)_{max1}$ and $T_{h1}$= $(dh/dT)_{max1}$ are the temperatures where the rate of change of mass and rate of change of heat are maximum.

**Table 4.2** Comparison of Onset temperature, maximum heat flux and corresponding temperature of nAl and nAlCu

| β | $T_{onset}$ | | $T_{pexo1}$ | | $h_{pexo1}$ | | $T_{pexo2}$ | | $h_{pexo2}$ | |
|---|---|---|---|---|---|---|---|---|---|---|
| K/min | °C | | °C | | mW | | °C | | mW | |
| | **Al** | **AlCu** | **Al** | **AlCu** | **Al** | **AlCu** | **Al** | **AlCu** | **Al** | **AlCu** |
| 2 | 481 | 458 | 559.4 | 534.0 | 31.0 | 11.2 | 759.9 | 720.2 | 12.7 | 1.06 |
| 7 | 509 | 474 | 585.0 | 547.8 | 148.5 | 67.5 | 790.1 | 755.4 | 48.9 | 8.4 |
| 10 | 498 | 491 | 633.0 | 588.3 | 823.0 | 746.5 | 801.1 | 761.2 | 49.0 | 11.8 |
| 15 | 511 | 492 | 633.1 | 590.8 | 823.0 | 749.3 | 808.1 | 773.9 | 66.5 | 30.3 |
| 20 | 498 | 497 | 639.0 | 587.7 | 829.7 | 745.9 | 814.2 | 786.1 | 98.0 | 40.3 |
| 30 | 514 | 512 | 643.5 | 595 | 833.3 | 754.1 | 826.5 | 810.5 | 133.9 | 35.9 |

Note:
β is the heating rate, $T_{onset}$ is the extrapolated onset temperature, $T_{pexo1}$ and $T_{pexo2}$ are the peak exothermic temperatures for the first and second exothermic reactions, respectively and $h_{pexo1}$ and $T_{pexo2}$ are the corresponding peak heat values.

This clearly shows that the alloy particles are more reactive than the pure aluminum particles.

## 4.2. Ignition Temperature

The ignition temperatures of both powders under various conditions of the heating rate are calculated by the 2nd derivative of TGA and DSC curves. The ignition temperature of nAlCu at $\beta > 7$ K/min is $564.7 \pm 10.8\,^{o}C$. This temperature is similar to that observed by Stamatis et al. [9] in their study of ignition of Al-CuO nanocomposites. The ignition temperature of nAl under similar experimental conditions is $595.5 \pm 8.1^{o}C$. This suggests that the NA is more reactive than nAl as it is ignited at lower temperature. Ignition temperature curves of both samples are given in **Figure 4.2**.

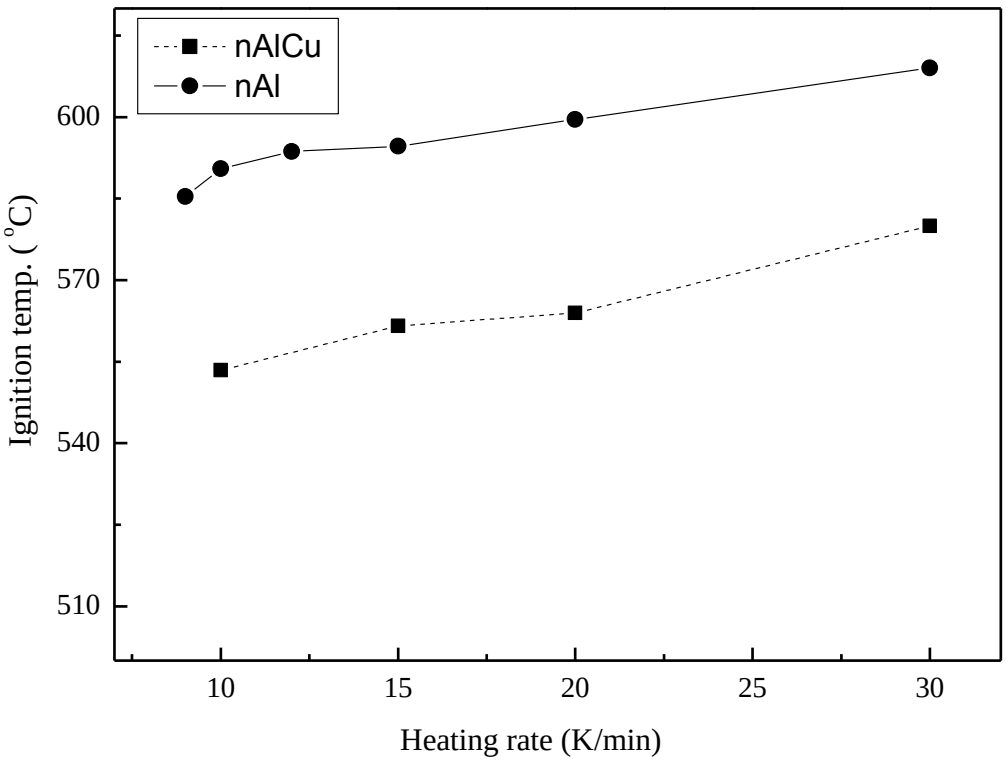


**Figure 4.2** Comparison of ignition temperatures of nAl with nAlCu showing nAlCu is ignited at lower temperature as compared to nAl under similar experimental conditions

Considering the eutectic melting temperature of the AlCu alloy, which has similar values at the bulk and nano-alloy level, i.e, 545~548 $^{o}$C, it is believed that the early melting of the aluminum part of the alloy is responsible for its high reactivity as well as early ignition.

## 4.3. Change of Mass and Heat Flux

In addition, **Figure 4.3** shows the general trend of the influence of the heating rate on the final weight increase and the maximum heat flux during with ignition reaction. Again similar patterns were observed for both materials. Under low heating rates (i.e. no ignition), the peak heat flux values change with the heating rate in a monotonous way. For nano-AlCu, it increases slightly from 11 mW at 2 K/min to ~70 mW at 7 K/min. However as the ignition reaction is observed, a large jump in its values is observed. The heat release rate remains a similar value and is in the region of 750 mW for all heating rates above 8 K/min. This suggests that the ignition event is similar under all these heating rates, and releases similar amount of heat. The heat release rate of nano-AlCu is smaller than the pure aluminum case. A nearly opposite trend is observed for the final weight increase. The heating rate influences little on the final weight change when there is no ignition. However as the ignition occurs, the final weight change generally decreases with the increase of the heating rate, which implies a kinetic process that higher heating rate leads to less time for the reaction to fully complete.

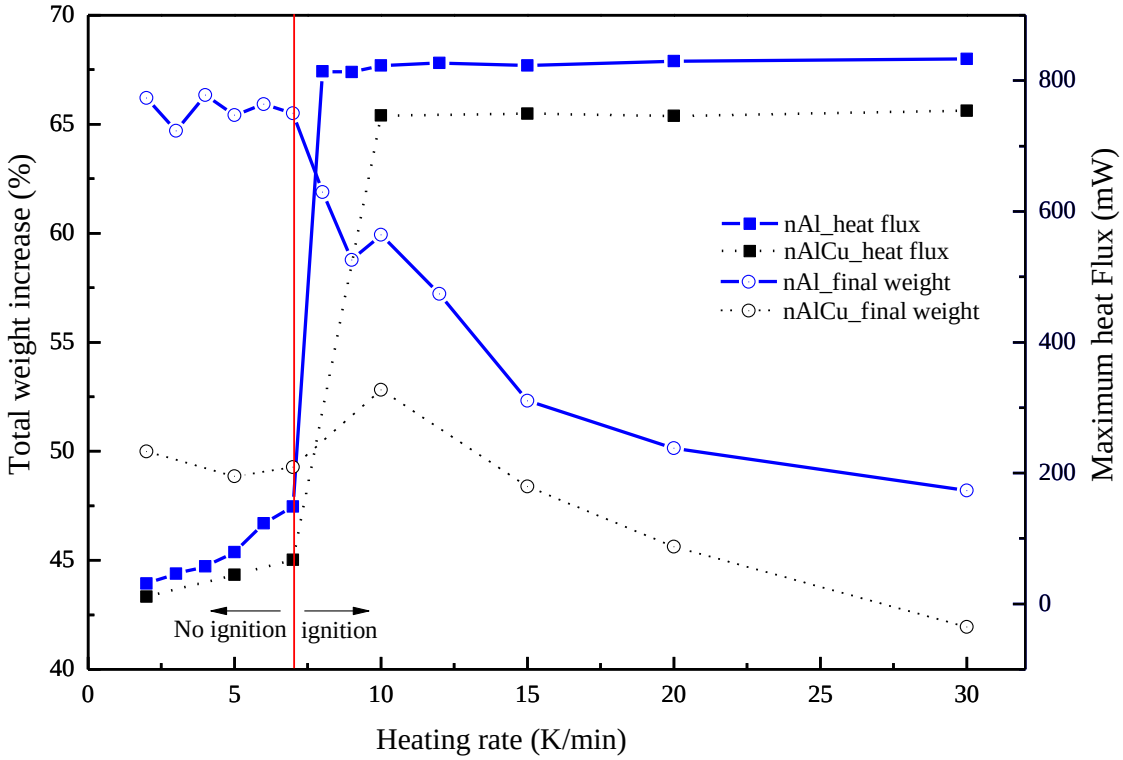


**Figure 4.3** Comparison of weight increase and peak heat flux of nAl with n-AlCu with ignition reaction

## 4.4. Comparison Between nAl and nAlZn

Conventionally the particle reactivity is described by its metal content, which is however not sufficient to quantify the reactivity for nanoparticles. Not only the metal content, the reactivity of nanoparticles depends upon also the particles size and distribution, the thickness and physiochemical characteristics of the passivation layers, and powder synthesis techniques. It is possible that the particles having similar metal content and/or similar diameters but behave differently in the oxidative environment. Four parameters, namely, the onset temperature ($T_{on}$), the temperature at which the maximum oxidation rate is achieved ($T_{01}$), the degree of oxidation ($\alpha$) up to a certain temperature, and the specific heat release ($\Delta H/\Delta m$), have been proposed to compare the reactivity of different nanoparticles [61, 65].

**Table 4.3**. Reactivity comparison of nAl and nAlZn under all heating rates

| Reactivity Parameters / Samples | $T_{on}$ °C | α % | $T_{01}$ °C | ΔH/Δm a.u. |
|---|---|---|---|---|
| Al (211nm) | 498.4±11 | 43.5±9.9 | 575.4±14.7 | 3994.7±418.7 |
| nAlZn (141nm) | 456.3±9.9 | 73.1±2.6 | 629.5±23.7 | 3649.1±393.6 |

Note:
Ton is the extrapolated onset temperature from TGA curve
α is the degree of conversion (up to 730 °C)
$T_{01}$ is the temperature at which the maximum rate of oxidation is achieved on TGA curve
ΔH/Δm is the specific heat effect

**Table 4.3** shows an example of the comparison between nAlZn and nAl with an average particle size of ~210 nm. As these values are insensitive to the heating rates, the numbers are averaged with a standard deviation reflecting the difference among the heating rates. Clearly nAl has a particle size ~1/3 larger than that of nAlZn, which has some disadvantages in the comparison. If neglecting the particle size effect for the time being, shows that nAlZn is more reactive if considering the onset oxidation temperature, and the degree of oxidation at the end of the major, i.e., the first exothermic reaction. UP to 73.1% was converted for nAlZn at 730 °C, whereas only 43.5% is observed for nAl, which is related to the smaller oxidation temperature of the zinc. However the temperature to reach the maximum oxidation rate is higher and the specific heat effect is slightly smaller for nAlZn, which implies that nAl is more reactive. It appears that different parameters should be used for different applications. For instance for applications considering the low temperature effect, the conversion ratio and onset temperature criterion should be used, whereas for applications focusing on the thermal effect, the relative specific heat effect should be used.

## 4.5. Chapter Summary

This work conducts a comparative study of the exothermic characteristics such as relative reactivities, ignition temperatures, change of mass and heat released under various heating condition on the basis of sizes as well as constitutional compositions of nanomaterials, aluminium nanoparticles (nAl), aluminum-copper (nano-AlCu) and aluminum-zinc (nano-AlCu) nanoalloys based on TGA/DSC studies. It is found that

- The general exothermic characteristics of nano-AlCu are similar to that of nAl. The complete reaction for both materials can be described by a three-stage reaction and an early ignition phenomenon is observed for both nAl and nano-AlCu under heating rate $\geq$ 8 K/min. The ignition temperature of nano-AlCu is higher than its eutectic melting temperature, and the melting is believed to be responsible for the early ignition.
- The comparison of the reactivity of both materials shows that nano-AlCu is more reactive than nAl under similar experimental conditions, showing increased reactivity through alloying.
- The comparison of reactivity of nAl and nAlZn suggests that different reactivity parameters should be used for different applications.

.

# Chapter 5

# 5. Conclusions and Future Work

This thesis conducts a systematic experimental investigation of the oxidation, ignition and combustion along with thermodynamics, kinetics, morphological and structural properties of nano aluminum (n-Al) and nanoalloys such as nano-AlCu and nano-AlZn under controlled exothermic reaction conditions. Such a study advances our understanding of the exothermic reaction of energetic nanomaterials, which is the key to control the energy transfer and conversion at the nanometer scale for many potential energy applications. The oxidation and ignition mechanisms of nano aluminum and its alloys are supported by the elemental, structural, and crystallography information. The thermal stabilities, the melting, the phase transformations, the intervening chemical reactions over a wide temperature range, and the reactivities of aluminum and its alloys were analysed and compared qualitatively and quantitatively to gain better understanding.

The major conclusions of the Thesis can be summarized as:

- The oxidation scenario of aluminum nanoparticles at heating rates of 2–30 K/min can be described by a three-stage reaction with the main reaction occurring before the melting of aluminum nanoparticles. A unique early ignition reaction characterized by a sudden temperature runaway, i.e., a fast mass gain and a rapid heat release, is observed when the heating rate is $\geq$ 8 K/min, and there is a co-existence of various polymorphs of alumina ($\gamma$–, $\delta$–, $\theta$–$Al_2O_3$) below the melting temperature of aluminum nanoparticles. Such an early ignition reaction is due to

a combined effect of solid phase transformation of the alumina shell and the early melting of the aluminium core, and is responsible for the co-existence of various polymorphs of alumina at the low temperature. When the particles are heated in the nitrogen atmosphere, no such ignition behaviour is observed.

- Contrary to the conventional shrink-core model, it is observed with ex-situ HRTEM that the aluminum nanoparticles form hollow structures in their central regions during the oxidation process. The particles remain solid after the first oxidation step (i.e., 600 $^{o}$C), ~25% develops hollow structures when the temperature is higher (i.e., 700 $^{o}$C) than the bulk aluminum melting temperature (i.e., 660 $^{o}$C), and nearly all observed particles develop hollow structures at 800 $^{o}$C when the second oxidation step is finished. It is also observed that the length of the voids increases significantly by the early ignition reaction whereas there is no effect on the shell thickness by such a reaction. It is proposed that the formation of hollow structure in aluminium nanoparticles is associated with the melting, phase transition of the oxides and the nanoscale Kirkendall effect.

- The oxidation, ignition and chemical kinetics of the nanoalloy (NA) of Al and Cu under different heating rates in the presence of air shows that complete oxidation scenario of nano Al-Cu alloys can be characterized by two exothermic and two endothermic processes. A unique early ignition of the nano alloy, in the temperature ~565 $^{o}$C, is found at heating rates $\geq$ 8K/min. The eutectic melting temperature of the nano alloy, which is identified at ~ 546 $^{o}$C, played a pivotal role for the early ignition. Despite the similar general exothermic characteristics, the comparison of nano-AlCu with nAl shows that the nanoalloy is ignited at

lower temperature than the pure aluminum nanoparticles under similar experimental conditions. This higher reactivity is associated with the alloying of aluminum. The weak peaks of copper aluminate spinel $CuAl_2O_4$, at ~900 $^oC$, suggest that its formation is not thermodynamically favourable because of the slow diffusion of metallic ions and the decrease of the sample weight at ~1175 $^oC$ is associated with the liberation of oxygen during the reduction of CuO to $Cu_2O$.

- The thermal analysis combined with elemental, morphological and crystalline structure analyses were conducted to elucidate the reaction mechanisms of nano alloy of aluminum and zinc. The complete thermal oxidation of nano AlZn in air could be characterised by a three-stage process. Two endothermic reactions occurring during the first stage are due to the phase transformation and eutectic melting. With the help of ex-situ XRD, different reaction pathways are proposed for different stages with the final oxidation products of ZnO and $ZnAl_2O_4$. The effect of heating rate and the comparison of aluminium nanoparticles showed that both had similar reactivities.

- A preliminary investigation of the combustion characteristics of three particles, Al, Fe and Si, having variable dimensions in the methane/ air stream in a Bunsen burner setup shows that most of the particles are combusted after passing through the inner flame cone and the ignitibility of the particles improves with the reduction of particle diameter. The analysis of particle burn time shows that the conventional $d^2$ law is not applicable to the fine particles.

Although the work presented in the thesis advances our understating of the fundamentals of oxidation, ignition and combustion of aluminum particles and its alloys for potential energy applications, there are some improvement that can be made by some future studies ,

- In this work, the experiments are performed in the heating range of 2-30 K/min for nAl, it would be interesting to perform more oxidation experiments at higher heating rates (i.e., 30 ~500 K/min) so that an appropriate model can be developed covering a wide range of conditions. In addition to this, particles having different sizes shall be investigated to gain insights on the particle size effect on the oxidation and ignition kinetics.

- TEM analysis was only conducted for aluminum nanoparticles, which reveals the development of hollow structures in the central particle region. It will be constructive to perform similar analysis for nano alloys (nAlCu and nAlZn), which will help extend the phenomenal model to the nanoalloys.

- It is found in the experiment that the reactivity of nano aluminum can be increased by alloying it with other metals such as copper but the alloys have fixed chemical compositions. It is of the interest to use alloys of variable chemical compositions so that the effect of individual element on the kinetic behaviours of alloys can be better understood. Moreover, extending the reactivity comparison of these nanoalloys to other elements, such as copper and zinc, will be useful.

- Due to the time constraint, only a preliminary combustion experiment is done by burning particles in a methane/ oxygen. Clearly more experiments and more image pair analysis shall be performed to provide a better

understanding of the combustion behaviour of nanoparticles, especially regarding the effect of particle size and the burning time comparison. Pure nanoparticle combustion experiments, i.e., without the support of a gaseous fuel, shall also be conducted to reveal the nanoparticle influence.

- Parallel to the experimental investigation, numerical simulation of the energy conversion process related to energetic nanoparticles shall be performed. The simulations shall relate the conversion process at single nanoparticle scale to that of the bulk scale, and produce predictive oxidation and ignition models for a wider application.

# References

[1] B.S.B. Reddy, K. Das, S. Das, A review on the synthesis of in situ aluminum based composites by thermal, mechanical and mechanical–thermal activation of chemical reactions, J Mater Sci, 42 (2007) 9366-9378.

[2] R.W. Conner, D.D. Dlott, Ultrafast Condensed-Phase Emission from Energetic Composites of Teflon and Nanoaluminum, The Journal of Physical Chemistry A, 114 (2010) 6731-6741.

[3] J.J. Granier, M.L. Pantoya, Laser ignition of nanocomposite thermites, Combustion and Flame, 138 (2004) 373-383.

[4] L. Zhou, N. Piekiel, S. Chowdhury, D. Lee, M.R. Zachariah, Transient ion ejection during nanocomposite thermite reactions, Journal of Applied Physics, 106 (2009) 083306-083306-083308.

[5] L. Zhou, N. Piekiel, S. Chowdhury, M.R. Zachariah, Time-Resolved Mass Spectrometry of the Exothermic Reaction between Nanoaluminum and Metal Oxides: The Role of Oxygen Release, The Journal of Physical Chemistry C, 114 (2010) 14269-14275.

[6] A. Prakash, A.V. McCormick, M.R. Zachariah, Aero-Sol−Gel Synthesis of Nanoporous Iron-Oxide Particles: A Potential Oxidizer for Nanoenergetic Materials, Chemistry of Materials, 16 (2004) 1466-1471.

[7] V. Rosenband, Thermo-mechanical aspects of the heterogeneous ignition of metals, Combustion and Flame, 137 (2004) 366-375.

[8] K. Sullivan, G. Young, M.R. Zachariah, Enhanced reactivity of nano-B/Al/CuO MIC's, Combustion and Flame, 156 (2009) 302-309.

[9] D. Stamatis, Z. Jiang, V.K. Hoffmann, M. Schoenitz, E.L. Dreizin, Fully Dense, Aluminum-Rich Al-CuO Nanocomposite Powders for Energetic Formulations, Combustion Science and Technology, 181 (2008) 97-116.

[10] G. Jian, S. Chowdhury, K. Sullivan, M.R. Zachariah, Nanothermite reactions: Is gas phase oxygen generation from the oxygen carrier an essential prerequisite to ignition?, Combustion and Flame, 160 (2013) 432-437.

[11] E.M. Hunt, M.L. Pantoya, Ignition dynamics and activation energies of metallic thermites: From nano- to micron-scale particulate composites, Journal of Applied Physics, 98 (2005) 034909-034909-034908.

[12] E.L. Dreizin, Metal-based reactive nanomaterials, Progress in Energy and Combustion Science, 35 (2009) 141-167.

[13] D. Wen, Nanofuel as a potential secondary energy carrier, Energy & Environmental Science, 3 (2010) 591-600.

[14] L.T. De Luca, L. Galfetti, F. Severini, L. Meda, G. Marra, A.B. Vorozhtsov, V.S. Sedoi, V.A. Babuk, Burning of nano-aluminized composite rocket propellants, Combust Explo Shock+, 41 (2005) 680-692.

[15] L. Meda, G. Marra, L. Galfetti, S. Inchingalo, F. Severini, L. De Luca, Nano-composites for rocket solid propellants, Compos Sci Technol, 65 (2005) 769-773.

[16] K.J. Klabunde, J. Stark, O. Koper, C. Mohs, D.G. Park, S. Decker, Y. Jiang, I. Lagadic, D.J. Zhang, Nanocrystals as stoichiometric reagents with unique surface chemistry, Journal of Physical Chemistry, 100 (1996) 12142-12153.

[17] R.A. Yetter, G.A. Risha, S.F. Son, Metal particle combustion and nanotechnology, Proceedings of the Combustion Institute, 32 (2009) 1819-1838.

[18] S. Schimpf, M. Lucas, C. Mohr, U. Rodemerck, A. Bruckner, J. Radnik, H. Hofmeister, P. Claus, Supported gold nanoparticles: in-depth catalyst characterization

and application in hydrogenation and oxidation reactions, Catalysis Today, 72 (2002) 63-78.

[19] M.W. Beckstead, Recent progress in modeling solid propellant combustion, Combust Explos Shock Waves, 42 (2006) 623-641.

[20] M.L. Pantoya, J.J. Granier, Combustion Behavior of Highly Energetic Thermites: Nano versus Micron Composites, Propellants, Explosives, Pyrotechnics, 30 (2005) 53-62.

[21] Y. Wang, W. Jiang, X. Zhang, H. Liu, Y. Liu, F. Li, Energy release characteristics of impact-initiated energetic aluminum–magnesium mechanical alloy particles with nanometer-scale structure, Thermochimica Acta, 512 (2011) 233-239.

[22] J.J.a.R.L.J. Riccardo Ferrando, Nanoalloys: From Theory to Applications of Alloy Clusters

and Nanoparticles, Chemical Reviews, 108 (2008).

[23] M. Schoenitz, E.L. Dreizin, E. Shtessel, Constant Volume Explosions of Aerosols of Metallic Mechanical Alloys and Powder Blends, Journal of Propulsion and Power, 19 (2003) 405-412.

[24] J. Jellinek, Nanoalloys: tuning properties and characteristics through size and composition, Faraday Discussions, 138 (2008) 11-35.

[25] M. Schoenitz, T.S. Ward, E.L. Dreizin, Fully dense nano-composite energetic powders prepared by arrested reactive milling, Proceedings of the Combustion Institute, 30 (2005) 2071-2078.

[26] S.M. Umbrajkar, M. Schoenitz, E.L. Dreizin, Exothermic reactions in Al–CuO nanocomposites, Thermochimica Acta, 451 (2006) 34-43.

[27] R.H. Chen, C. Suryanarayana, M. Chaos, Combustion Characteristics of Mechanically Alloyed Ultrafine-Grained Al-Mg Powders, Advanced Engineering Materials, 8 (2006) 563-567.

[28] Y.L. Shoshin, M.A. Trunov, X.Y. Zhu, M. Schoenitz, E.L. Dreizin, Ignition of aluminum-rich Al-Ti mechanical alloys in air, Combustion and Flame, 144 (2006) 688-697.

[29] F. René, Growth of thin, crystalline oxide, nitride and oxynitride films on metal and metal alloy surfaces, Surface Science Reports, 38 (2000) 195-294.

[30] C. Wagner, Z. Phys. Chem., B621 (1933) 25.

[31] B.N.C.A.N.F. MOTT, Theory of the oxidation of metals, Reports on Progress in Physics, 12 (1949).

[32] N. Eisenreich, H. Fietzek, M. del Mar Juez-Lorenzo, V. Kolarik, A. Koleczko, V. Weiser, On the Mechanism of Low Temperature Oxidation for Aluminum Particles down to the Nano-Scale, Propellants, Explosives, Pyrotechnics, 29 (2004) 137-145.

[33] M.A. Trunov, M. Schoenitz, E.L. Dreizin, Effect of polymorphic phase transformations in alumina layer on ignition of aluminium particles, Combustion Theory and Modelling, 10 (2006) 603-623.

[34] A. Rai, K. Park, L. Zhou, M.R. Zachariah, Understanding the mechanism of aluminium nanoparticle oxidation, Combustion Theory and Modelling, 10 (2006) 843-859.

[35] M.A. Trunov, M. Schoenitz, X.Y. Zhu, E.L. Dreizin, Effect of polymorphic phase transformations in Al2O3 film on oxidation kinetics of aluminum powders, Combustion and Flame, 140 (2005) 310-318.

[36] T.J. Campbell, G. Aral, S. Ogata, R.K. Kalia, A. Nakano, P. Vashishta, Oxidation of aluminum nanoclusters, Physical Review B, 71 (2005) 205413.

[37] I. Glassman, Combustion, Academic Press, Orlando, 1996.

[38] I. Glassman, Combustion of metals: physical considerations, Academic Press, New York, 1960.

[39] J.B.C. A.V. Von Grosse, Ind. Eng. Chem, 50 (1958) 663–672.

[40] M. Beckstead, Correlating Aluminum Burning Times, Combustion, Explosion, and Shock Waves, 41 (2005) 533-546.

[41] F.A. Williams, Some Aspects of Metal Particle Combustion, Physical and Chemical Aspects of Combustion: A Tribute to Irv Glassman, 1 ed., Taylor & Francis1997.

[42] M.R. Zachariah, S. Chowdhury, K. Sullivan, N. Piekiel, L. Zhou, Diffusive vs Explosive Reaction at the Nanoscale, J Phys Chem C, 114 (2010) 9191-9195.

[43] V.I. Levitas, B.W. Asay, S.F. Son, M. Pantoya, Melt dispersion mechanism for fast reaction of nanothermites, Appl Phys Lett, 89 (2006) -.

[44] V.I. Levitas, Burn time of aluminum nanoparticles: Strong effect of the heating rate and melt-dispersion mechanism, Combustion and Flame, 156 (2009) 543-546.

[45] S.F. Wang, Y.Q. Yang, H.N. Yu, D.D. Dlott, Dynamical effects of the oxide layer in aluminum nanoenergetic materials, Propell Explos Pyrot, 30 (2005) 148-155.

[46] V.I. Levitas, B.W. Asay, S.F. Son, M. Pantoya, Melt dispersion mechanism for fast reaction of nanothermites, Appl Phys Lett, 89 (2006).

[47] Y. Huang, G.A. Risha, V. Yang, R.A. Yetter, Effect of particle size on combustion of aluminum particle dust in air, Combustion and Flame, 156 (2009) 5-13.

[48] Y.F. Ivanov, M.N. Osmonoliev, V.S. Sedoi, V.A. Arkhipov, S.S. Bondarchuk, A.B. Vorozhtsov, A.G. Korotkikh, V.T. Kuznetsov, Productions of Ultra-Fine Powders and Their Use in High Energetic Compositions, Propellants, Explosives, Pyrotechnics, 28 (2003) 319-333.

[49] Kvartzkhava , Bondarenko V V, P.A.P.a.C.A. A, Oscillographic determination of the energy of electrical explosion of conductors, Zh. Eksp. Teor. Fiz. 1956, 31 745–51 (in Russian), (1956).

[50] Y. Kotov, Electric Explosion of Wires as a Method for Preparation of Nanopowders, Journal of Nanoparticle Research, 5 (2003) 539-550.

[51] P. Song, D. Wen, Experimental Investigation of the Oxidation of Tin Nanoparticles, The Journal of Physical Chemistry C, 113 (2009) 13470-13476.

[52] P. Song, D. Wen, Z.X. Guo, T. Korakianitis, Oxidation investigation of nickel nanoparticles, Phys Chem Chem Phys, 10 (2008) 5057-5065.

[53] L. Meda, G. Marra, L. Galfetti, F. Severini, L. De Luca, Nano-aluminum as energetic material for rocket propellants, Mat Sci Eng C-Bio S, 27 (2007) 1393-1396.

[54] D.S. Wen, Nanofuel as a potential secondary energy carrier, Energy & Environmental Science, 3 (2010) 591-600.

[55] B. Natan, S. Rahimi, The status of gel propellants in year 2000, Combustion of Energetic Materials, (2002) 172-194.

[56] P. Pranda, K. Prandova, V. Hlavacek, Particle size and reactivity of aluminum powders, Combustion Science and Technology, 156 (2000) 81-96.

[57] C.E. Johnson, S. Fallis, A.P. Chafin, T.J. Groshens, K.T. Higa, I.M.K. Ismail, T.W. Hawkins, Characterization of nanometer- to micron-sized aluminum powders: Size distribution from thermogravimetric analysis, Journal of Propulsion and Power, 23 (2007) 669-682.

[58] B. Rufino, F. Boulc'h, M.V. Coulet, G. Lacroix, R. Denoyel, Influence of particles size on thermal properties of aluminium powder, Acta Materialia, 55 (2007) 2815-2827.

[59] M.M. Mench, K.K. Kuo, C.L. Yeh, Y.C. Lu, Comparison of Thermal Behavior of Regular and Ultra-fine Aluminum Powders (Alex) Made from Plasma Explosion Process, Combustion Science and Technology, 135 (1998) 269-292.

[60] D.E.G. Jones, P. Brousseau, R.C. Fouchard, A.M. Turcotte, Q.S.M. Kwok, Thermal Characterization of Passivated Nanometer Size Aluminium Powders, J Therm Anal Calorim, 61 (2000) 805-818.

[61] A.P. Il'in, A.A. Gromov, G.V. Yablunovskii, Reactivity of Aluminum Powders, Combust Explos Shock Waves, 37 (2001) 418-422.

[62] Y.-S. Kwon, A.A. Gromov, A.P. Ilyin, Reactivity of superfine aluminum powders stabilized by aluminum diboride, Combustion and Flame, 131 (2002) 349-352.

[63] A. Dokhan, E.W. Price, J.M. Seitzman, R.K. Sigman, The effects of bimodal aluminum with ultrafine aluminum on the burning rates of solid propellants, Proceedings of the Combustion Institute, 29 (2002) 2939-2946.

[64] D.E.G. Jones, R. Turcotte, R.C. Fouchard, Q.S.M. Kwok, A.-M. Turcotte, Z. Abdel-Qader, Hazard Characterization of Aluminum Nanopowder Compositions, Propellants, Explosives, Pyrotechnics, 28 (2003) 120-131.

[65] A. Gromov, A. Ilyin, U. Förter-Barth, U. Teipel, Characterization of Aluminum Powders: II. Aluminum Nanopowders Passivated by Non-Inert Coatings, Propellants, Explosives, Pyrotechnics, 31 (2006) 401-409.

[66] A.A. Gromov, A.P. Il'in, U. Foerter-Barth, U. Teipel, Effect of the passivating coating type, particle size, and storage time on oxidation and nitridation of aluminum powders, Combust Explos Shock Waves, 42 (2006) 177-184.

[67] Q.S.M. Kwok, C. Badeen, K. Armstrong, R. Turcotte, D.E.G. Jones, V.Y. Gertsman, Hazard characterization of uncoated and coated aluminium nanopowder compositions, J Propul Power, 23 (2007) 659-668.

[68] L. Chen, W.L. Song, J. Lv, L. Wang, C.S. Xie, Effect of heating rates on TG-DTA results of aluminum nanopowders prepared by laser heating evaporation, J Therm Anal Calorim, 96 (2009) 141-145.

[69] A. Gromov, Y. Strokova, A. Kabardin, A. Vorozhtsov, U. Teipel, Experimental Study of the Effect of Metal Nanopowders on the Decomposition of HMX, AP and AN, Propellants, Explosives, Pyrotechnics, 34 (2009) 506-512.

[70] M.L. Pantoya, S.W. Dean, The influence of alumina passivation on nano-Al/Teflon reactions, Thermochimica Acta, 493 (2009) 109-110.

[71] A.C. Reber, S.N. Khanna, P.J. Roach, W.H. Woodward, A.W. Castleman, Reactivity of Aluminum Cluster Anions with Water: Origins of Reactivity and Mechanisms for H2 Release, The Journal of Physical Chemistry A, 114 (2010) 6071-6081.

[72] A.V. Korshunov, Influence of dispersion aluminum powders on the regularities of their interaction with nitrogen, Russ. J. Phys. Chem., 85 (2011) 1202-1210.

[73] S. Mohan, A. Ermoline, E. Dreizin, Pyrophoricity of nano-sized aluminum particles, Journal of Nanoparticle Research, 14 (2012) 1-6.

[74] A. Sossi, E. Duranti, M. Manzoni, C. Paravan, L.T. DeLuca, A.B. Vorozhtsov, M.I. Lerner, N.G. Rodkevich, A.A. Gromov, N. Savin, Combustion of HTPB-Based Solid Fuels Loaded with Coated Nanoaluminum, Combustion Science and Technology, 185 (2012) 17-36.

[75] J. Sun, M.L. Pantoya, S.L. Simon, Dependence of size and size distribution on reactivity of aluminum nanoparticles in reactions with oxygen and MoO3, Thermochimica Acta, 444 (2006) 117-127.

[76] V.I. Levitas, M.L. Pantoya, G. Chauhan, I. Rivero, Effect of the Alumina Shell on the Melting Temperature Depression for Aluminum Nanoparticles, The Journal of Physical Chemistry C, 113 (2009) 14088-14096.

[77] J. Sun, S.L. Simon, The melting behavior of aluminum nanoparticles, Thermochimica Acta, 463 (2007) 32-40.

[78] L. Chen, W.-l. Song, L.-g. Guo, C.-s. Xie, Thermal property and microstructure of Al nanopowders produced by two evaporation routes, Transactions of Nonferrous Metals Society of China, 19 (2009) 187-191.

[79] A. Pivkina, D. Ivanov, Y. Frolov, S. Mudretsova, A. Nickolskaya, J. Schoonman, Plasma synthesized nano-aluminum powders, J Therm Anal Calorim, 86 (2006) 733-738.

[80] M. Schoenitz, B. Patel, O. Agboh, E.L. Dreizin, Oxidation of aluminum powders at high heating rates, Thermochimica Acta, 507–508 (2010) 115-122.

[81] J. Wang, A. Hu, J. Persic, J.Z. Wen, Y. Norman Zhou, Thermal stability and reaction properties of passivated Al/CuO nano-thermite, Journal of Physics and Chemistry of Solids, 72 (2011) 620-625.

[82] Y.-S. Kwon, A.A. Gromov, J.I. Strokova, Passivation of the surface of aluminum nanopowders by protective coatings of the different chemical origin, Applied Surface Science, 253 (2007) 5558-5564.

[83] A. Ilyin, A. Gromov, V. An, F. Faubert, C. de Izarra, A. Espagnacq, L. Brunet, Characterization of Aluminum Powders I. Parameters of Reactivity of Aluminum Powders, Propellants, Explosives, Pyrotechnics, 27 (2002) 361-364.

[84] J.L. Cheng, H.H. Hng, H.Y. Ng, P.C. Soon, Y.W. Lee, Deposition of nickel nanoparticles onto aluminum powders using a modified polyol process, Materials Research Bulletin, 44 (2009) 95-99.

[85] M.A. Trunov, M. Schoenitz, X. Zhu, E.L. Dreizin, Effect of polymorphic phase transformations in Al2O3 film on oxidation kinetics of aluminum powders, Combustion and Flame, 140 (2005) 310-318.

[86] I. Levin, D. Brandon, Metastable Alumina Polymorphs: Crystal Structures and Transition Sequences, Journal of The American Ceramic Society, 81 (1998) 1995-2012.

[87] D. Meinkohn, Metal-particle ignition and oxide-layer instability, Combust Explo Shock+, 42 (2006) 158-169.

[88] B.J. Henz, T. Hawa, M.R. Zachariah, On the role of built-in electric fields on the ignition of oxide coated nanoaluminum: Ion mobility versus Fickian diffusion, Journal of Applied Physics, 107 (2010) 024901-024901-024909.

[89] D.A. Firmansyah, K. Sullivan, K.-S. Lee, Y.H. Kim, R. Zahaf, M.R. Zachariah, D. Lee, Microstructural Behavior of the Alumina Shell and Aluminum Core Before and After Melting of Aluminum Nanoparticles, The Journal of Physical Chemistry C, 116 (2011) 404-411.

[90] V.M. Boiko, S.V. Poplavski, Self-ignition and ignition of aluminum powders in shock waves, Shock Waves, 11 (2002) 289-295.

[91] K. Benkiewicz, A.K. Hayashi, Aluminum dust ignition behind reflected shock wave: two-dimensional simulations, Fluid Dyn Res, 30 (2002) 269-292.

[92] Y. Ohkura, P.M. Rao, X. Zheng, Flash ignition of Al nanoparticles: Mechanism and applications, Combustion and Flame, 158 (2011) 2544-2548.

[93] S. Yuasa, Y. Zhu, S. Sogo, Ignition and combustion of aluminum in oxygen/nitrogen mixture streams, Combustion and Flame, 108 (1997) 387-396.

[94] R. Friedman, A. Maček, Ignition and combustion of aluminium particles in hot ambient gases, Combustion and Flame, 6 (1962) 9-19.

[95] Y. Zhu, S. Yuasa, Effects of oxygen concentration on combustion of aluminum in oxygen/nitrogen mixture streams, Combustion and Flame, 115 (1998) 327-334.

[96] S. Mohan, M.A. Trunov, E.L. Dreizin, On possibility of vapor-phase combustion for fine aluminum particles, Combustion and Flame, 156 (2009) 2213-2216.

[97] Z.X. Yan, J.H. Wu, S. Ye, D. Hu, X.D. Yang, Shock-induced thermal behavior of aluminum nanoparticles in propylene oxide, Journal of Applied Physics, 101 (2007) 024905-024905-024905.

[98] S. Bau, O. Witschger, F. Gensdarmes, O. Rastoix, D. Thomas, A TEM-based method as an alternative to the BET method for measuring off-line the specific surface area of nanoaerosols, Powder Technol, 200 (2010) 190-201.

[99] P.S. Santos, H.S. Santos, S.P. Toledo, Standard transition aluminas. Electron microscopy studies, Materials Research, 3 (2000) 104-114.

[100] A.-W. B.D. Cullity, Elements of X-ray Diffraction, 2nd ed.1978.

[101] H. Fernandes, D. Tulyaganov, J.F. Ferreira, Al2O3/K2O-containing non-stoichiometric lithium disilicate-based glasses, J Therm Anal Calorim, (2012) 1-10.

[102] T. Uchikoshi, Y. Sakka, M. Yoshitake, K. Yoshihara, A study of the passivating oxide layer on fine nickel particles, Nanostructured Materials, 4 (1994) 199-206.

[103] M.A. Trunov, S.M. Umbrajkar, M. Schoenitz, J.T. Mang, E.L. Dreizin, Oxidation and melting of aluminum nanopowders, J Phys Chem B, 110 (2006) 13094-13099.

[104] Q.S. Mei, S.C. Wang, H.T. Cong, Z.H. Jin, K. Lu, Pressure-induced superheating of Al nanoparticles encapsulated in Al2O3 shells without epitaxial interface, Acta Materialia, 53 (2005) 1059-1066.

[105] M.A. Trunov, M. Schoenitz, E.L. Dreizin, Ignition of aluminum powders under different experimental conditions, Propell Explos Pyrot, 30 (2005) 36-43.

[106] S. Mohan, M.A. Trunov, E.L. Dreizin, Heating and ignition of metal particles in the transition heat transfer regime, Journal of Heat Transfer-Transactions of the Asme, 130 (2008).

[107] H. Dong, S. Zhumei, Study of the fast reaction characteristics of aluminized PETN explosive powders, Combustion and Flame, 105 (1996) 428-430.

[108] G.V. Ivanov, V.G. Ivanov, V.G. Surkov, O.V. Gawrilyuk, Nanosize electro-explosion powders: Assessement of safety in the production and application, Nato Sci S 1 Disarm, 26 (1999) 329-340.

[109] Y. Ma, K. Huo, Q. Wu, Y. Lu, Y. Hu, Z. Hu, Y. Chen, Self-templated synthesis of polycrystalline hollow aluminium nitride nanospheres, J Mater Chem, 16 (2006) 2834-2838.

[110] R. Nakamura, J.G. Lee, D. Tokozakura, H. Mori, H. Nakajima, Formation of hollow ZnO through low-temperature oxidation of Zn nanoparticles, Materials Letters, 61 (2007) 1060-1063.

[111] M. Kim, S.B. Yoon, K. Sohn, J.Y. Kim, C.-H. Shin, T. Hyeon, J.-S. Yu, Synthesis and characterization of spherical carbon and polymer capsules with hollow macroporous core and mesoporous shell structures, Microporous and Mesoporous Materials, 63 (2003) 1-9.

[112] Y. Sun, B. Mayers, Y. Xia, Metal Nanostructures with Hollow Interiors, Adv Mater, 15 (2003) 641-646.

[113] J.G. Railsback, A.C. Johnston-Peck, J. Wang, J.B. Tracy, Size-Dependent Nanoscale Kirkendall Effect During the Oxidation of Nickel Nanoparticles, ACS Nano, 4 (2010) 1913-1920.

[114] A. Cabot, M. Ibáñez, P. Guardia, A.P. Alivisatos, Reaction Regimes on the Synthesis of Hollow Particles by the Kirkendall Effect, J Am Chem Soc, 131 (2009) 11326-11328.

[115] H.J. Fan, M. Knez, R. Scholz, D. Hesse, K. Nielsch, M. Zacharias, U. Gösele, Influence of Surface Diffusion on the Formation of Hollow Nanostructures Induced by the Kirkendall Effect: The Basic Concept, Nano Lett, 7 (2007) 993-997.

[116] K. Brandstadt, D.L. Frost, J.A. Kozinski, Preignition characteristics of nano- and micrometer-scale aluminum particles in Al–CO2 oxidation systems, Proceedings of the Combustion Institute, 32 (2009) 1913-1919.

[117] J. Zheng, X. Song, Y. Zhang, Y. Li, X. Li, Y. Pu, Nanosized aluminum nitride hollow spheres formed through a self-templating solid–gas interface reaction, Journal of Solid State Chemistry, 180 (2007) 276-283.

[118] A.D. Smigelskas, E.O. Kirkendall, Trans AIME, (1947) 130.

[119] Y. Yin, R.M. Rioux, C.K. Erdonmez, S. Hughes, G.A. Somorjai, A.P. Alivisatos, Formation of hollow nanocrystals through the nanoscale kirkendall effect, 2004.

[120] T. Telbizova, S. Parascandola, U. Kreissig, R. Gunzel, W. Moller, Mechanism of diffusional transport during ion nitriding of aluminum, Appl Phys Lett, 76 (2000) 1404-1406.

[121] W. Wang, M. Dahl, Y. Yin, Hollow Nanocrystals through the Nanoscale Kirkendall Effect, Chem Mater, 25 (2012) 1179-1189.

[122] Y. Shoshin, E.L. Dreizin, Laminar lifted flame speed measurements for aerosols of metals and mechanical alloys, Aiaa Journal, 42 (2004) 1416-1426.

[123] Y.L. Shoshin, R.S. Mudryy, E.L. Dreizin, Preparation and characterization of energetic Al-Mg mechanical alloy powders, Combustion and Flame, 128 (2002) 259-269.

[124] L. Deng, H. Deng, S. Xiao, J. Tang, W. Hu, Morphology, Dimension, and Composition Dependence of Thermodynamically Preferred Atomic Arrangements in Ag-Pt Nanoalloys, Faraday Discussions, (2013).

[125] G. Rossi, R. Ferrando, C. Mottet, Structure and chemical ordering in CoPt nanoalloys, Faraday Discussions, 138 (2008) 193-210.

[126] Y. Aly, M. Schoenitz, E.L. Dreizin, Ignition and combustion of mechanically alloyed Al–Mg powders with customized particle sizes, Combustion and Flame, 160 (2013) 835-842.

[127] G. Singh, I.P.S. Kapoor, S. Dubey, Bimetallic nanoalloys: Preparation, characterization and their catalytic activity, Journal of Alloys and Compounds, 480 (2009) 270-274.

[128] M.S. Motta, P.K. Jena, E.A. Brocchi, I.G. Solórzano, Characterization of Cu–Al2O3 nano-scale composites synthesized by in situ reduction, Materials Science and Engineering: C, 15 (2001) 175-177.

[129] S.H. Kim, D.N. Lee, Fabrication of alumina dispersion strengthened copper strips by internal oxidation and hot roll bonding, Materials Science and Technology, 15 (1999) 352-354.

[130] K. Sullivan, G. Young, M.R. Zachariah, Enhanced reactivity of nano-B/Al/CuO MIC's, Flame, 156 (2009) 8-8.

[131] A.M.M. Gadalla, J. White, Equilibrium relationships in the system CuO-Cu2O-Al2O3, Trans. Br. Ceram. Soc., 63 (1964) 39-62.

[132] K.T. Jacob, C.B. Alcock, Thermodynamics of CuAlO2 and CuAl2O4 and Phase Equilibria in the System Cu2O-CuO-Al2O3, Journal of The American Ceramic Society, 58 (1975) 192-195.

[133] Y. Kumekawa, M. Hirai, Y. Kobayashi, S. Endoh, E. Oikawa, T. Hashimoto, Evaluation of thermodynamic and kinetic stability of CuAlO2 and CuGaO2, J Therm Anal Calorim, 99 (2010) 57-63.

[134] H.-S. Shin, B.-K. Lee, Agglomeration parameter, aggregation number, and aggregate porosity, J Mater Sci, 32 (1997) 4803-4806.

[135] K. Wieczorek-Ciurowa, K. Gamrat, Z. Sawłowicz, Characteristics of CuAl2-Cu9Al4/Al2O3 nanocomposites synthesized by mechanical treatment, J Therm Anal Calorim, 80 (2005) 619-623.

[136] T.B.O. Massalski, H.. Subramanian, P.R. Kacprzak,L., Binary Alloy Phase Diagrams, 2nd Edition ed., ASM Internationa1990.

[137] V.S.R. Murthy, Structure And Properties Of Engineering Materials, McGraw-Hill Education (India) Pvt Limited2003.

[138] U. Anselmi-Tamburini, F. Maglia, S. Doppiu, M. Monagheddu, G. Cocco, Z.A. Munir, Ignition mechanism of mechanically activated Me–Si(Me = Ti, Nb, Mo) mixtures, J Mater Res, 19 (2004) 1558-1566.

[139] M. Arjmand, A.-M. Azad, H. Leion, A. Lyngfelt, T. Mattisson, Prospects of Al2O3 and MgAl2O4-Supported CuO Oxygen Carriers in Chemical-Looping Combustion (CLC) and Chemical-Looping with Oxygen Uncoupling (CLOU), Energy & Fuels, 25 (2011) 5493-5502.

[140] T. Tsuchida, R. Furuichi, T. Sukegawa, M. Furudate, T. Ishii, Thermoanalytical study on the reaction of the CuO—Al2O3(η, γ AND α) systems, Thermochimica Acta, 78 (1984) 71-80.

[141] P.H. Bolt, F.H.P.M. Habraken, J.W. Geus, Formation of Nickel, Cobalt, Copper, and Iron Aluminates fromα- andγ-Alumina-Supported Oxides: A Comparative Study, Journal of Solid State Chemistry, 135 (1998) 59-69.

[142] C.-Y. Hu, K. Shih, J.O. Leckie, Formation of copper aluminate spinel and cuprous aluminate delafossite to thermally stabilize simulated copper-laden sludge, Journal of Hazardous Materials, 181 (2010) 399-404.

[143] M.M. Ba-Abbad, A.A.H. Kadhum, A. Bakar Mohamad, M.S. Takriff, K. Sopian, The effect of process parameters on the size of ZnO nanoparticles synthesized via the sol–gel technique, J Alloy Compd, 550 (2013) 63-70.

[144] C.H.-F. WEI Jian-Ning, GONG Chen-Li, ZHOU Zheng-Cun,, Grain Boundary Peak in a Foamed Zn-Al Eutectoid Alloy, Chin. Phys. Lett., 19 (2002) 381-384.

[145] N. Cabrera, N.F. Mott, Physics, 12 (1948) 163-184.

[146] M.M.Y. Mench, C L | Kuo, K K, Propellant burning rate enhancement and thermal behavior of ultra-fine aluminum powders (Alex), Energetic materials - Production, processing and characterization; Proceedings of the 29th International Annual Conference of ICT, Karlsruhe, Germany; GERMANY, 30-31 to 30-15.

[147] M.S. Aida, E. Tomasella, J. Cellier, M. Jacquet, N. Bouhssira, S. Abed, A. Mosbah, Annealing and oxidation mechanism of evaporated zinc thin films from zinc oxide powder, Thin Solid Films, 515 (2006) 1494-1499.

[148] H. Delalu, J.R. Vignalou, M. Elkhatib, R. Metz, Kinetics and modeling of diffusion phenomena occurring during the complete oxidation of zinc powder: influence of granulometry, temperature and relative humidity of the oxidizing fluid, Solid State Sci, 2 (2000) 229-235.

[149] Z. Zhou, J. Liu, S. Hu, Studies on the kinetics process of tetra-needle-like ZnO whisker growth, J Cryst Growth, 276 (2005) 317-320.

[150] Y.I. Alivov, A.V. Chernykh, M.V. Chukichev, R.Y. Korotkov, Thin polycrystalline zinc oxide films obtained by oxidation of metallic zinc films, Thin Solid Films, 473 (2005) 241-246.

[151] X. Ma, M.R. Zachariah, Oxidation Anisotropy and Size-Dependent Reaction Kinetics of Zinc Nanocrystals, The Journal of Physical Chemistry C, 113 (2009) 14644-14650.

[152] J.E. Flinn, Particle size measurements: (4th edition), by Terence Allen; Chapman and Hall; 1990; pp. 832, Materials Science and Engineering: A, 161 (1993) 309.

[153] Y.H. Zhu, F.E. Goodwin, Microstructures of thermomechanically treated eutectoid Zn–Al alloy (II), J Mater Res, 10 (1995) 1927-1932.

[154] S. Mey, Re-evaluation of the Al-Zn system, IInternational Journal of Materials Research, 84 (1993) 451-455.

[155] K.-L. Lin, L.-H. Wen, T.-P. Liu, The microstructures of the Sn-Zn-Al solder alloys, Journal of Elec Materi, 27 (1998) 97-105.

[156] W.R. Osório, C.M. Freire, A. Garcia, The effect of the dendritic microstructure on the corrosion resistance of Zn–Al alloys, J Alloy Compd, 397 (2005) 179-191.

[157] F. Noor, H. Zhang, T. Korakianitis, D. Wen, Oxidation and ignition of aluminum nanomaterials, Phys Chem Chem Phys, 15 (2013) 20176-20188.

[158] W.K. Tan, K.A. Razak, K. Ibrahim, Z. Lockman, Oxidation of etched Zn foil for the formation of ZnO nanostructure, Journal of Alloys and Compounds, 509 (2011) 6806-6811.

[159] S. Goroshin, I. Fomenko, J.H.S. Lee, Burning velocities in fuel-rich aluminum dust clouds, Twenty-Sixth Symposium (International) on Combustion, Vols 1 and 2, (1996) 1961-1967.

[160] A. Hahma, A. Gany, K. Palovuori, Combustion of activated aluminum, Combustion and Flame, 145 (2006) 464-480.

[161] A. Davis, Solid propellants: The combustion of particles of metal ingredients, Combustion and Flame, 7 (1963) 359-367.

[162] R.P. Wilson Jr, F.A. Williams, Experimental study of the combustion of single aluminum particles in O2/Ar, Symposium (International) on Combustion, 13 (1971) 833-845.

[163] R.W. Bartlett, J.N. Ong Jr, W.M. Fassell Jr, C.A. Papp, Estimating aluminium particle combustion kinetics, Combustion and Flame, 7 (1963) 227-234.

[164] D. Xu, J. Chen, Accurate estimate of turbulent dissipation rate using PIV data, Experimental Thermal and Fluid Science, 44 (2013) 662-672.

[165] T.A. Brzustowski, I. Glassman, H.G. Wolfhard, L. Green, Heterogeneous Combustion, 1964.

[166] Y. Huang, G.A. Risha, V. Yang, R.A. Yetter, Combustion of bimodal nano/micron-sized aluminum particle dust in air, Proceedings of the Combustion Institute, 31 (2007) 2001-2009.

[167] M.W. Beckstead, A Summary of Aluminum Combustion, Conference paper, ( JAN 200) 47.

[168] S. Olsen, M. Beckstead, Burn time measurements of single aluminum particles in steam and carbon dioxide mixtures, 31st Joint Propulsion Conference and Exhibit, American Institute of Aeronautics and Astronautics1995.

[169] P.L. Tim Bazyn, Herman Krier, Nick Glumac, Combustion Measurements of Fuel-Rich Aluminum and Molybdenum Oxide Nano-Composite Mixtures, Propellants Explos. Pyrotech, (April 08, 2009) 1 – 10.

[170] E.L. Dreizin, On the mechanism of asymmetric aluminum particle combustion, Combustion and Flame, 117 (1999) 841-850.

[171] Y. Shoshin, E. Dreizin, Particle combustion rates in premixed flames of polydisperse metal—air aerosols, Combustion and Flame, 133 (2003) 275-287.

[172] S. Rossi, E.L. Dreizin, C.K. Law, Combustion of Aluminum Particles in Carbon Dioxide, Combustion Science and Technology, 164 (2001) 209-237.